Novel Designs and Geometry for Mechanical Gearing

by

Erasmo Chiappetta

School of Engineering, Computing and Mathematics
Oxford Brookes University
In collaboration with Norbar Torque Tools ltd., UK.

A thesis submitted in partial fulfilment of the requirements of Oxford Brookes University for the degree of

Doctor of Philosophy

September 2018

Abstract

This thesis presents quasi-static Finite Element Methods for the analysis of the stress state occurring in a pair of loaded spur gears and aims to further research the effect of tooth profile modifications on the mechanical performance of a mating gear pair. The investigation is then extended to epicyclic transmissions as they are considered the most viable solution when the transmission of high torque level within a compact volume is required.

Since, for the current study, only low speed conditions are considered, dynamic loads do not play a crucial role. Vibrations and the resulting noise might be considered negligible and consequently the design process is dictated entirely by the stress state occurring on the mating components. Gear load carrying capacity is limited by maximum contact and bending stress and their correlated failure modes. Consequently, the occurring stress state is the main criteria to characterise the load carrying capacity of a gear system. Contact and bending stresses are evaluated for multiple positions over a mesh cycle of a contacting tooth pair in order to consider the stress fluctuation as consequence of the alternation of single and double pairs of teeth in contact. The influence of gear geometrical proportions on mechanical properties of gears in mesh is studied thoroughly by means of the definition of a domain of feasible combination of geometrical parameters in order to deconstruct the well-established gear design process based on rating standards and base the defined gear geometry on operational and manufacturing constraints only. From this parametric study, suitable suggestions for enhancing the load carrying capacity of the tooth flank are made by showing that the use of non-standard geometric parameters can improve the performance of gears.

As this study also aims to improve the performances of epicyclic gearings specifically for low speed-high torque operating conditions, the optimum parameters found in the preliminary parametric analysis were applied to this category of systems. The design procedure based on the area of existence of gear geometry was extended to this case which required the determination of the domain of feasible combination for gears in internal mesh with the addition of constraints addressed to epicyclic

configurations. Three epicyclic systems with same boundary design conditions but different combination of geometrical parameters have been modelled and analysed by means of quasi-static FEA. The results have shown that the improvements found for the case of two mating spur gears are also valid for the case of higher order systems in which multiple contacts are simultaneously occurring. Based on these results, suitable suggestions are made for the design of gears working in epicyclic systems for an enhanced torque capacity and a volume reduction for applications characterized by low speed and high loads conditions.

An alternative solution to geared systems that guarantees compactness and high torque transmission capabilities has also been investigated; it consists of a cycloidal transmission system. The parametric equations for the cycloidal profile have been determined and an executive design, then manufactured, has been produced. The preliminary quasi-static Finite Element analysis has predicted the load sharing and stress distribution among multiple components confirming the mechanical advantage of this category of transmission systems.

Acknowledgments

With sincere respect and gratitude, I would like to thank my principal supervisor Professor Denise Morrey for all the support, encouragement and most valuable guidance throughout the duration of the Ph.D.

To Norbar Torque Tools ltd. and particularly Neill Brodey, Managing Director, for supporting this work financially and Richard Radini, Engineering Manager, for providing the technical expertise and support.

I am grateful to my second supervisor, Professor John Durodola, for his helpful discussion and encouragement.

I would like to extend my thanks and appreciation to all my friends and colleagues at Oxford Brookes University. To Davide, Fabrizio, Miguel and Mohamed, you have been my family for these four unforgettable years that I will never forget; Thank you!

Special thanks are due to Peppe, Kara, Nino and Glenda for making me feel home with their warm friendship.

My deep love goes to my parents, my beloved grandparents and my friends Salvo, Mapi and Stella for their continuous support and motivation to believe in myself and give my best to bring this study to an end.

Finally, to my love Marghe, for all the understanding and the enduring and loving support.

Without the valuable contribution of each one of you this work would not have been possible.

Publications from this thesis

This research has produced a considerable amount of results on many design and performance aspects of mechanical transmission systems. The outcomes are currently being collated for publications.

Published Papers:

1. Chiappetta, E., Morrey, D., *Non-Standard spur gear tooth profiles for improved epicyclic gear system performance in low speed applications.* International Conference on Gears 2017. Technical University of Munich, Munich, Germany.

2. Chiappetta, E., Morrey, D., *High pressure Angle Spur Gears for epicyclic Gear Trains.* BGA – British Gear Association, GEARS 2016 - Technical Awareness Seminar, November 2016, Birmingham University.

Submitted Papers:

Chiappetta E., Morrey D., *Parametric FE Analysis of Tooth Contact Stress for a Spur Gear Pair.* Measurement, 2018.

Papers under preparation:

Parametric FE Analysis of Tooth Bending Stress for a Spur Gear Pair.

Design and analysis of a planetary gear set by means of blocking contour approach and numerical techniques.

Table of Contents

List of Figures

List of Tables

List of Symbols

Symbol	Description
α	Profile pressure angle at the pitch circle Angle [°]
θ	Involute rolling angle [°]
$Inv\alpha$	Involute function of angle α [°]
m	Module [mm]
d	Pitch circle diameter [mm]
r	Pitch radius [mm]
d_b	Base circle diameter [mm]
r_b	Base circle radius [mm]
h_a	Addendum factor
H_a	Addendum length [mm]
h_a^*	Rack cutter addendum factor
H_a^*	Rack cutter addendum length [mm]
d_a	Tip circle diameter [mm]
r_a	Tip circle radius [mm]
h_f	Dedendum factor
H_f	Dedendum length [mm]
h_f^*	Rack cutter dedendum factor
H_f^*	Rack cutter dedendum length [mm]
h	Tooth height [mm]
r_f	Dedendum circle radius [mm]
d_f	Dedendum circle diameter [mm]
h_w	Working tooth height [mm]

c	Root clearance [mm]
I	Moment of Inertia [kg m^2]
ρ	Density [kg/m^3]
p	Gear pitch [mm]
p_b	Base pitch [mm]
$ρ_f$	Cutter tip radius factor
$α_w$	Working pressure angle [°]
d_w	Working pitch diameter [mm]
r_w	Working pitch radius [mm]
a	Centre distance [mm]
a_w	Working centre distance [mm]
L	Gear facewidth [mm]
$α_a$	Profile pressure angle at the tip circle [°]
ε	Contact ratio
N	Number of teeth
x	Profile shift coefficient
X	Profile shift [mm]
m	mass [kg]
m_b	Tooth base thickness coefficient
s_a	Tooth tip thickness coefficient
S_a	Tooth thickness at the tip circle [mm]
S	Tooth thickness at the pitch circle [mm]
ω	Angular velocity [rad/s]
e_0	Eccentricity [mm]

i	Transmission ratio
int	Corner interference
σ_{H0}	Nominal contact stress [MPa]
σ_{H}	Calculated contact stress [MPa]
σ_{Hp}	Permissible contact stress [MPa]
σ_{Hlim}	Allowable contact stress [MPa]
σ_{F0}	Nominal bending stress [MPa]
σ_{F}	Calculated bending stress [MPa]
σ_{Fp}	Permissible bending stress [MPa]
σ_{Flim}	Allowable bending stress [MPa]
U_{tot}	Total deformation [mm]
σMX_{c}	Von Mises Contact stress [MPa]
σMX_{b}	Von Mises Bending stress [MPa]
A_{c}	Area of contact [mm^2]
N_{s}	Number of teeth of sun gear
N_{R}	Number of teeth of ring gear
N_{p}	Number of teeth of planet gear
β	Angle between adjacent planets [°]
R	Radius of curvature [mm]
F	Applied force [N]
b	Contact area width [mm]
r_{0}	epicycle radius [mm]
N_{l}	Number of lobes
r_{at}	Theoretical addendum circle radius [mm]

r_{dt}	Theoretical dedendum circle radius [mm]
r_{aw}	Working addendum circle radius [mm]
r_{dw}	Working dedendum circle radius [mm]
h	Tooth depth [mm]
r_{da}	Annulus dedendum circle radius [mm]
r_{aa}	Annulus addendum circle radius [mm]
d_h	output hole diameter [mm]
d_{op}	output pin diameter [mm]
r_c	Cutting instrument radius [mm]

Abbreviations

Abbreviation	Expansion
FEA	Finite Element Analysis
CAD	Computer Aided Design
FEM	Finite Element Method
HPSTC	Highest Point of Single Tooth Contact
LPSTC	Lowest Point of Single Tooth Contact
ISO	International Standards Organisation
AGMA	American Gear Manufacturer Association
DIN	German Institute for Standardization
DOF	Degree of Freedom

1 Introduction

In recent years, there has been an increasing desire to improve efficiency and reduce energy consumption for all manufactured products. Increasing efficiency is synonymous with better performance and since it often relies on multiple factors it can be achieved in different ways. For many products, improved handling involving reducing weight and volume is also critical.

This research work focuses on the performance analysis of mechanical power transmission systems, more commonly called speed reducers or torque multipliers, and covers the aspect of design and performance analysis of these categories of mechanisms. Norbar Torque Tools Ltd., the main sponsor of this work, worldwide market leader in the field of high quality mechanical transmission devices for hand tooling and machinery applications, has launched a campaign of innovation aimed at improving the mechanical characteristics of devices in their range of production.

1.1 Background

Norbar's product range is based on epicyclic spur gears systems (Norbar Torque Tools ltd., 2018). The main property of spur gears is the high load carrying capacity. The geometry on which any kind of gear tooth profile is based is the involute of a circle proposed by Leonhard Euler (Radzevich, 2012). The involute profile is universally used because of its advantageous characteristics both in terms of manufacturing and working conditions as it is able to deliver a constant transmission ratio also in presence of small manufacturing or assembling deviations. Gears are then assembled in order to create transmissions systems able to transmit power from a source to the user by performing a modification of speed and torque. Depending on the assembly arrangement different solutions can be found. The most traditional configuration involves gears mounted on parallel axis transmitting the power from one axis to the other. More complex arrangements exist as for the case of epicyclic configurations. Epicyclic systems are generally used when a high amount of power has to be transmitted in a limited

workspace. This typology of gearing systems is characterised by a concentric physical disposition that allows a reduction in terms of overall dimension compared to ordinary gear trains. Alternative mechanical solutions to geared mechanisms can be found in cycloidal drives. A cycloidal drive is a concentric axis device that use a cycloidal disk to transmit the power from the input to the output.

The mechanical advantage given by any transmission systems is their ability to vary the quality of the power that passes through them by converting a low torque input into a higher value at the output by operating a conversion of speed into torque. In order to operate such conversion a transmission ratio is required. Epicyclic gear train have successfully satisfied the need of high transmission ratios in constrained physical boundaries by ensuring a high level of reliability. High ratios are achieved with a series of multiple reduction stages that necessarily have effects on their physical footprint. If an even higher reduction ratio is required and the need of a compact form is of primary importance, cycloidal gear trains can be the most viable solution.

1.2 Technical terms

In the following chapters a large number of technical terms is used to describe and explain designs and processes related to gears. A list of these terms, supported by a brief explanation, is given in Table 1.1 to facilitate the reader's comprehension of the explained concepts.

Table 1.1 – Technical terms

Micro geometry	Refers to those aspects of the involute tooth profile that can be modified to connect unwanted phenomena during the meshing process. Tip relief and lead crowning are an example of micro geometry modifications.
Macro geometry	The combination of geometrical parameters that define the tooth profile geometry.
Design Space	An enclosed area delimited by contour lines representing geometrical boundaries and operational constraints.

Pitch Point	The point at which the pitch circles of a pair of mating gears are in mutual tangency.
Involute profile	The geometry of gear teeth that derives from the involute of a circle, universally adopted for gearing purposes.
Transmission ratio (*i*)	Is the value that indicates the speed conversion operated by the system between the input and output members.
Epicyclic gearing	An epicyclic gear train is a particular concentric axes arrangement in which one or more rotating gears revolve around a central gear.
Mesh cycle	Involves the entire action from the first to the last point of contact for a couple of mating teeth.
Rack cutter	The rack cutter is considered the reference generating system. It can be seen as a gear with an infinite number of teeth which makes it rectilinear with straight sides instead of curved profiles. The geometry is defined by geometrical parameters that are transferred to the generated gears.
Pressure Angle (α)	α is the angle between the tangent to any point of the involute curve and a radial line connecting the point with the gear centre. If the considered point of tangency lies on the pitch circle then α coincides with the angle of inclination of the cutter edges and is termed reference pressure angle.
Addendum (H_a)	Addendum is the distance between pitch and tip circle.
Dedendum (H_f)	Dedendum is the distance between pitch and root circle.
Cutter Tip Radius (ρ_f)	Is one of the parameters that define a rack cutter geometry. The cutter tip radius, is the fillet between the inclined and the straight side of the rack cutter and affects the tooth root geometry of the generated gear.
Profile Shift (X)	Profile shift is used to alter standard proportions of gears. It is a modification that consists in shifting the

	generating tool radially, so that the tooth profile will also be shifted towards the gear centre.
Manufacturing Parameters	Refers to all those parameters related to the manufacturing process. Profile shift can be considered one of these as it is applied at the manufacturing stage of the gear production.
Undercutting	Undercutting is an unwanted effect during the gear generation process. It happens when a condition of interference occurs between the cutter and the non-involute portion of the tooth. The effect is a removal of material at the root of the gear tooth.
Contact Ratio (ε)	Contact Ratio indicates the average number of teeth in contact during a mesh cycle. For standard gears, on pair of teeth is in contact for 100% of the time while another carries part of the load for a time determined by ε.
Internal Gears	Internal gear is a gear with its teeth cut in the internal surface of a cylinder pointing towards its centre.
Operational Parameters	This category contains all those parameters that affect the correct operation of a gear system. An example is: corner interference, minimum tooth tip thickness, and minimum contact ratio.
Corner Interference	Corner interference is when the tip of one of the gears interferes with a non-involute portion of the tooth profile of the mating gear that lies below the base circle.
Tooth Base Thickness (S_b)	The thickness of the portion of a tooth at the root circle.
Top land thickness (S_a)	The thickness of the top portion of a tooth.
Contact stress	Contact stress occurs at the point of contact where the two active flanks are transmitting the force. It is of primary importance as represents the major cause of failure in gears.
Pitting	Pitting refers to the mechanism of surface fatigue failure of gears. It occurs due to repeated loading with the contact stress exceeding the surface fatigue strength of the material.

Bending stress	Bending stress in gears occurs at the tooth root as consequence of the action of the force applied on the tooth flank.
Load Sharing Ratio	Is the amount of Load shared between multiple tooth pairs in contact related to the maximum load transmitted by a single toot pair.
Symmetric Profile	Refers to a tooth profile in which the active and unloaded sides have the same geometry.
Asymmetric Profile	Asymmetric gear tooth profile has the two sides generated with two different values of pressure angle. Generally the active flank has an higher pressure angle than the unloaded side which guarantees an improved load carrying capacity.
Base pitch	The base pitch is equal to the circular pitch of the gear on the base circle and must be a common dimension to both members of a pair of properly mating spur gears.
Quasi static FEA	Quasi-static refers to the method used for the numerical analyses and implies the solution of Dynamic problems by means of static Loads.
Time-Varying Stress	Contact and Bending stresses in gears have a variable nature. The Time-Varying Stress refers to the full spectrum of stresses generated during the mesh cycle of two or more mating gears.
Arc of action	The arc on the pitch circle through witch a tooth travels from the first point of contact with the mating gear tooth to the point where the contact ends. The Arc of action is divided in arc of access and Arc of recess.
Line of contact	The point of contact, while the two gears rotate, moves along a line tangent to the base circles of the mating gears and passes through the pitch point. This is the line of contact also called line of action along which the transmitted forces are directed.
Power/Torque density	This quantity indicates the amount of Power and torque that a transmission system is able to deliver in relation

	to its physical volume. The lower the volume the higher the density for the same amount of Power/Torque.
Cycloidal profile	The cycloidal profile derives from the epicycloid curve and is adopted for cycloidal transmissions.

1.3 Motivation

The aim of this industry funded PhD project is to investigate the mechanics of gearing in order to enhance compactness and performance of gearing systems. Epicyclic gear trains find application in the field of hand torque multipliers in which Norbar Torque Tools Ltd. is leading the worldwide market.

Epicyclic transmission systems have been the focus of much interest in recent years mostly because they represent a viable solution for all applications in which limited weight and compactness are primary aspects of a design choice. Despite the large amount of literature available on epicyclic transmissions, there is very little information about applications with low rotational speed and high levels of transmitted torque. For these specific conditions, the only standard entirely dedicated to Epicyclic gearboxes available confirms the knowledge gap, underlining the necessity of undertaking a detailed engineering study in order to satisfy the requirements for the design of epicyclic devices (ANSI/AGMA 6123-B06, 2006).

The design of gears traditionally follows rigid rules imposed by the available design standards such as the ones published by ISO and AGMA. The aim of standards is simplifying the design process by reducing the number of parameters to define and have as result a standardisation of the gear geometry and quality. Such approach brings a balance of performance based on an acceptable compromise for the vast multitude of working condition to which a gear can be subjected to.

In the last years, thanks also to the advent of new production techniques that allow the manufacture of almost any kind of geometry and shape, gear design engineers are inclined to exploring non-standard combinations of parameters in order to develop custom products built to satisfy the requirements of specific applications. This introduces the necessity of detailed studies oriented to understand and evaluate the

effect that individual geometrical parameters have on gear performance and evaluate the optimal combination in relation to the working condition in which the gear system will operate.

The continuous request of compactness and space reduction expressed by Norbar has motivated the research of an alternative transmission system with similar characteristics to the traditional epicyclic but with an improved power to volume ratio, in order to minimise the size of their devices for hand tooling applications.

1.4 Research Objectives

Increasing market requirements for compactness and enhanced performance of mechanical components, introduces, in the field of transmission systems, the concept of high torque density (Kapelevich, 2013). The consequent reduction in size of components naturally implicates overloading conditions that result into premature failures. Gears generally fail when the tooth stress overtakes the material safe limit. The failure mechanisms for gears are related to the applied load which, combined with geometrical characteristics, determines the local stress distribution. Tooth breakage occurs when the generated stresses are exciding the endurance strength of the material. In order to limit the chances of mechanical failure both material and geometry can be improved.

The main objective of this thesis was to find an appropriate combination of gear design parameters that would enhance the mechanical properties of epicyclic gear trains under low speed and high torque working conditions. To investigate the contact stress distribution occurring on gear tooth flank and bending stress distribution at the tooth base, numerical methods have been adopted and results compared with the available rating standards. The steps taken to fulfil the requirements of the research are described as follows:

- A geometrical analysis has been carried out to assess the physical boundaries of the feasible combinations of parameters that define the geometry of a pair of spur mating gears in order to separate the design process from the existing design standards.
- The definition of the domain boundaries as for above, for the case involving two

spur gears in internal mesh.

- The understanding of the effect on gear performance of each geometrical parameter. Gear performance in this case is evaluated in terms of stress magnitude and distribution during the entire mesh cycle of a contacting tooth pair.
- Evaluate the effect of modified geometrical parameters on a higher order system, namely the epicyclic gear train, by investigating the stress distribution occurring on the multiple mating teeth for the entire duration of a mesh cycle.
- Determine the parametric equations for generating the cycloidal profile disk and the mating components with the aim of designing a cycloidal transmission with a 15:1 ratio.

1.5 Research Methodology

The research methodology undertaken is based on numerical and analytical methods. While the numerical approach has been used with the purpose of researching and analysing novel combinations of parameters that result in non-standard involute tooth shapes, the analytical approach, based on international design standards, has been carried out as validation methodology for numerical data. The analyses focus on a single pair of mating gears, considered a low order model, and on higher order model, with multiple gears in mesh, such as planetary gear trains. Force interactions and contact deformations can be numerically determined using Finite Element Analysis (FEA) software packages such as ANSYS® (2016). With the aid of CAD geometry, FEA studies can be performed and the results of which can be compared with analytical results. A comprehensive analysis of the involute profile geometrical parameters has been performed by means of Finite Element Methods capable of modelling gear pairs and gear systems and simulating their working conditions. Gear teeth are subjected to different loads during their mesh cycle. As the point of contact changes its position along the tooth flank while gears rotate, the effect of the applied load on different portion of the tooth generates a stress distribution that varies with gear's rotation. In order to gain information on the time-varying stresses for the entire mesh cycle a quasi-static Finite Element Methodology is considered appropriate as shown by Zhan et Al. (2016). The

gear models are generated in accordance with the domain of feasible combination of geometrical parameters determined by applying the blocking contour technique. Such technique was also applied for the first time to the case of internal mating spur gears and it was further developed by considering the existing relations and constraints of epicyclic gear trains.

The parametric equations for the design of the cycloidal disk profile have been derived starting from the definition of the epicycloidal curve. The generated model was analysed by means of 3D quasi-static finite element analysis in order to evaluate the distribution of the stress among the simultaneous multiple contact. The amount of load carried by each pin in the system has also been evaluated.

The results of the applied methodology have shown good agreement with analytical results obtained from the application of the design standard for the case of a spur gear pair and epicyclic systems. Since there is no standards available for the design of cycloidal devices, experimental results from the ongoing testing will be compared with the ones resulting from the application of numerical techniques.

1.6 Originality and contribution of this research

The originality and major contributions of this work are presented in the following section.

The definition of a domain of feasible combination of parameters is of fundamental importance for the design of non-standard gears. The multi parametric design space has been obtained by the superimposition of lines that have the physical meaning of extreme values for the gear geometry and work as limit of the feasible area.

To the knowledge of the author, for the first time the concept of a multi parametric design space has been applied to spur gears in internal mesh. In this case, manufacturing, operational and geometrical constraints addressed to internal mating gears have been determined and applied in order to define the area of feasible combination of parameters.

And even more, the multi parametric design space has been applied for the design of epicyclic gear models. Assembling relations, typical of epicyclic arrangement, have been considered in the definition of the design space. The result is a design tool that allows the user to define any combination of parameters suitable for an epicyclic transmission.

In order to evaluate the performance of a spur gear pair in mesh, the contact stress state occurring at the tooth flank has been evaluated by means of a 2D quasi-static Finite Element Method. The effect of the contact formulation on the quality of result has been extensively discussed and the optimum formulation found represents a novelty in the field.

The time-varying stress distribution for the evaluation of contact and bending stress occurring respectively at the tooth flank and at the tooth base has been evaluated for a copious number of models that differ one from the other by the modification of a single parameter such as pressure angle, profile shift, addendum and dedendum factors. In total 17 different geometrical configurations were analysed for the evaluation of contact stress and how it is affected by geometrical parameters. Similarly, 21 geometrical configurations were investigated in order to quantify the variation of bending stress with geometrical parameters. This has resulted into a comprehensive analysis of the stresses related to the gear geometry that was not available in literature.

The developed design method for planetary gear trains was applied to a case study in which three epicyclic transmissions with different parameters were designed and analysed by means of FEA. Gears with high values of pressure angle, found beneficial for the reduction of stress in the previous analysis, were applied to epicyclic systems and compared to a case standard. There is no mention in the available literature of planetary systems designed with a working pressure angle beyond 25°. The case under investigation with $\alpha_w \approx 28°$ represents a novelty.

The design of a cycloidal transmission is a complex task given that no standards and or design guidelines are available. A model capable of a transmission ratio 15:1 has been generated and then manufactured for testing purposes. The 3D digital model has been the subject of quasi-static FEA analysis in order to evaluate the time-varying stress

distribution during an entire mesh cycle. The stress distribution at the interface pin-cycloidal disk has been evaluated along with the amount of load simultaneously shared between multiple pins. To the knowledge of the author a detailed study of the time-varying stress distribution occurring on the contacting components of a cycloidal transmission is not available in literature.

1.7 Thesis Outline

This thesis focuses on the research performed on mechanical transmission systems in eight chapters. The following outlines the content of each chapter.

Chapter 1 presents a general introduction of the topic and introduce the reader to the sphere of mechanical transmission systems along with the concept of performance analysis associated to this class of devices. It outlines the objectives of this research as well as the methods taken to conduct the study. Finally, the major contributions to the field of gear design are outlined and the layout of the thesis is described.

Chapter 2 provides an extensive survey of the existing literature currently available about the design and performance analysis of gearing systems. The chapter proceeds by discussing the concept of design space and the various techniques adopted for its determination. It follows with the description of performance analysis associated with the stress distribution. A review of the numerical methods adopted for the analysis of gears and gear trains is also done. The survey continues with the epicyclic gear trains along with the alternative category of cycloidal transmissions.

Chapter 3 gives the basic concept of the involute profile. The construction method of the involute curve is determined in a parametric form. As gear geometry is function of multiple parameters, a detailed analysis of the effect caused by the modification of each parameter is given. Furthermore, the background theory of the finite element method used in this thesis, focusing in particular on the solution of non-linear problems such for the case of gears is explained.

Chapter 4 focuses on the concept of area of feasibility of a rack based design process. The chapter describes the technique used to create a parametric multi-dimensional

design space by taking under consideration the factors that define the gear profile geometry.

Chapter 5 provides an extensive description of the analysis conducted for the evaluation of the performance of a spur gear pair. The chapter content of the chapter spans from the generation of the models to the detailed settings for the numerical analysis along with the evaluation of the time-varying stresses for a number of gear configurations in the design space previously determined.

Chapter 6 introduces the epicyclic transmission systems by describing their geometrical arrangement, meshing and assembling requirements. Successively, a design technique based on a multi-dimensional design space was developed also for the case of epicyclic gear trains. The characteristics of gears in internal mesh have been coupled with the constraints imposed by the epicyclic configuration. A case study consisting in the analysis of three different planetary gear sets has been conducted starting from the early stages of design up to the performance analysis and the definition of an optimum geometry for the application in low speed high torque working conditions.

Chapter 7 deals with the design of a cycloidal transmission with the scope of finding an alternative solution to the more traditional epicyclic transmission. The parametric equations of the cycloidal profile have been determined and a model of the entire transmission has been designed and successively manufactured. By means of finite element method a performance analysis has been attempted.

Chapter 8 summarises the general conclusion of the thesis and outlines the main contribution to the area of design and performance analysis of spur gears, epicyclic gear trains and cycloidal transmission systems.

2 Literature Review

Gear and gear trains play a critical role in the family of mechanisms and machines since they were invented thousands of years ago. Dudley (1969) in his “evolution of the gear art” has classified the development of gears and gearing starting from mechanisms used in ancient populations and explains the development of gears in a chronological order from pre-Christian times, around 3,000 B.C. till modern times. Primitive form of gears consisted of wooden pins arranged on the periphery of a wooden wheel to drive the mating member, as shown in Figure 2.1. The historical change of tooth form is mainly accounted for by development in manufacturing technologies; the developments of new production methods have permitted the evolution from wooden pin toothed wheels to modern gears with involute profiles.

Figure 2.1 - Ancient form of geared transmission consisting in wooden gear in mesh with a pin toothed wheel (Dudley, 1969).

The beginning of modern gearing is dated between 1600 and 1800 A.D. when the involute curve was first postulated. According to Dooner (2012), the involute curve was first introduced by Philip de la Hire in 1669, but it was later, in the eighteenth century that the Swiss scientist Leonard Euler developed the mathematics to describe the involute curve and then introduced the involute of a circle as a viable geometry for tooth flank profiles.

In recent times, gear design has become a complex subject that has to deal with many aspects of engineering. The main goal of a gear train is the transmission of power but restrictions such as maximum overall dimension, reduction in vibration and noise emission, low maintenance requirements, are some of the considerations that a modern

gear designer has to take into account, as well as minimum possible manufacturing costs (Maitra, 2012).

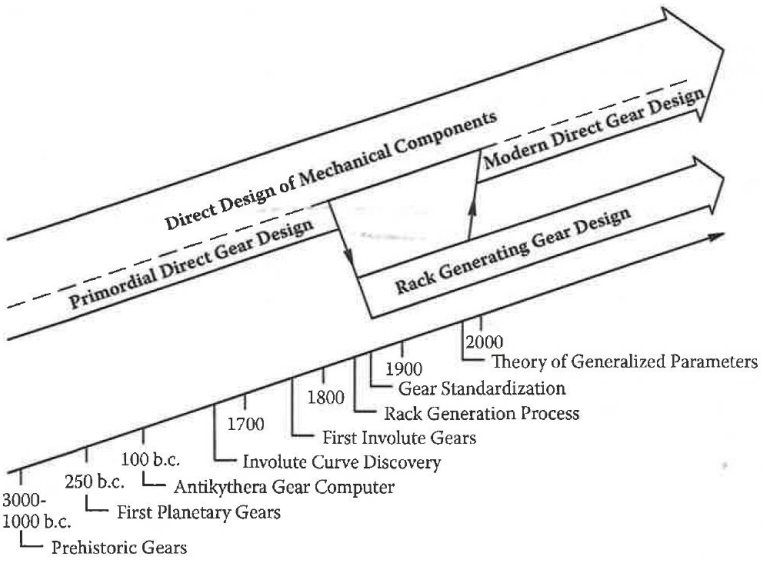

Figure 2.2 - Evolutionary steps of gear design from the prehistoric form of gears to the gear standardization and the newly developed direct gear design (Kapelevich, 2013).

Kapelevich (2013) summarises the evolutionary steps of gear design in the diagram given in Figure 2.2. In particular, he points out the way that gears were categorised and designed in the past, before gear standardisation appeared. For ancient engineers the manufacturing process was the second step of the gear design process and it was only taken into consideration when the gear design data were already known. Historically gears were produced for a particular application based on the performance requirements, often as one off production components. This is conceptually different and in contrast with what happens for the majority of the gear production after the introduction of gear standardisation based on the rack generation process.

The concept of standardisation in gear design has meant that the established standard manufacturing process imposes the geometry of gears. In coincidence with the industrial revolution and the exponential increase in the demand of transmission components for all kinds of mechanisms and machines, the standardisation of gears began.

The invention of hobbing machines as a more efficient manufacturing process was based on the application of the tooling rack for gear manufacturing. The size and proportion

of the cutting tool were standardised. In Figure 2.3 the main factors subjected to standardisation such as addendum h_a, dedendum h_f, cutter tip radius ρ_f, pressure angle α, and the radial clearance coefficient c, are shown. These parameters with the scale factor m, the module, completely define the geometry of the corresponding gear profile.

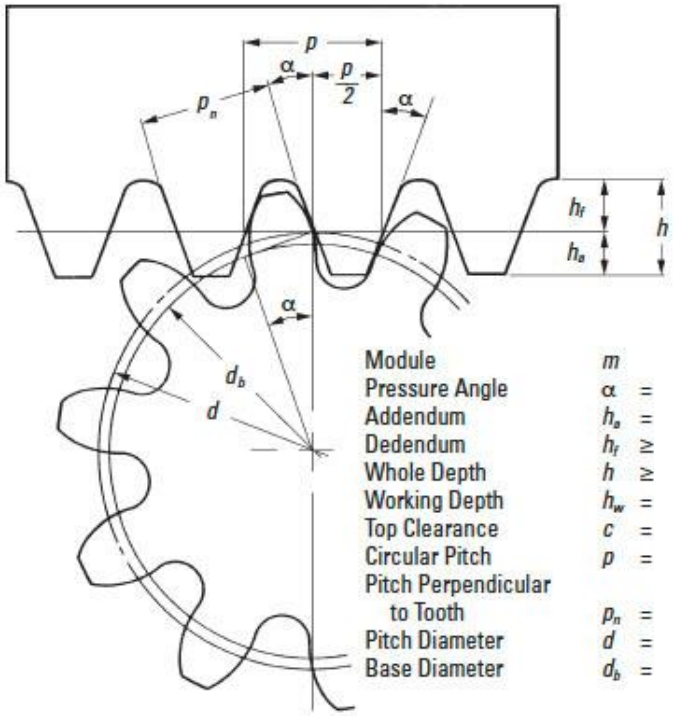

Figure 2.3 - Tooth profile and dimention of standard rack cutter (KHK, 2015).

A standardization of the gears in the first instance was required to guarantee the interchangeability of gears made by different manufacturers, but also for the use in different applications. The resulting design is a solution of compromise for the majority of applications. On the other hand, this standardisation can be seen as a limit for a further development of gear technology. It has simplified the design of gears making the process indirect and dependent on the standard geometry of the manufacturing tool (Kapelevich, 2013). Designs based on the standard basic rack provide a satisfactory solution in terms of strength and life, but also vibration and noise emission. However, an average solution might not work for applications in which an optimization of a specific characteristic is required, or a high performance application. The majority of the research done on gear technology is based on the optimization of the *micro* geometry of gear profiles. This means that gear researchers and engineers have mainly focused on

the optimisation of those aspects of gear profiles generated with standard parameters without exploring the possibilities of new feasible proportions that define the *macro* geometry of gears.

With the help of mathematical models, the use of computer-aided design software and finite element analysis, the exploration of new proportions of involute profiles is made more approachable (Amani et Al., 2017; Goldfarb et Al., 2005; Kapelevich et Al., 2013). Paired with new production technologies, this allows optimized solutions to be found for specific applications.

2.1 Design Space

The exploration of the design space includes the feasible geometries for gears in mesh and has been an area of particular focus in recent years.

The design of gears and gear trains, even for the simplest case of two spur gears in mesh, is complex due to the number of parameters involved. By considering that, for a single gear, module, addendum, dedendum, pressure angle, cutter tip radius, face width and profile shift coefficient have to be determined and that each parameter can be chosen independently between the two gears in mesh, the problem already has a significant degree of complexity (Amani et Al, 2017). To combine the parameters listed above, their interaction has to be taken under consideration to identify the domain of feasible combinations. Amani et Al. (2017) presented a multi-parametric design space by considering manufacturing and geometrical limitations. In their research, the authors investigated the occurrence of undercutting and corner interference by combining values of pressure angle, module, number of teeth, cutter tip radius, dedendum, addendum and tooth thickness of two spur gears in mesh. As the study was focused on geometrical compatibility, the effects of the analysed design choices on stress and load carrying capacity were not considered. In their geometrical analysis they have stated that the condition for a correct mesh is not necessarily dependent on the condition of equal pressure angle of the two mating profiles, but rather on the condition of base pitch compatibility (Kapelevich, 2013; Spitas et Al., 2014). The outcomes of the geometrical study highlighted that addendum and dedendum combinations correlate directly to radial interference. Changes to the pressure angle modifies the tooth

thickness by increasing the tooth base and reducing the width at the tip. The limitation is due to the condition of tip pointing. Dedendum, cutter tip radius and pressure angle have a combined effect on the occurrence of undercutting. Equations for the already mentioned geometrical and manufacturing constraints are given by the authors, and a large family of combinable plots has been presented for a pair of mating spur gears with regards to manufacturing feasibility and geometrical compatibility. The authors found that an increase in pressure angle reduces the feasible design space when the other factors under consideration are cutter tip radius, dedendum and cutter tip radius coefficients. Regarding the condition of interference, a combination of number of teeth, pressure angle, dedendum and cutter tip radius coefficients has been investigated and the result suggests that larger module and high pressure angles are more prone to interference problems. Regarding the undercutting limitation, by increasing the number of gear teeth, dedendum coefficient and pressure angle, the design space for non-undercutting will be increased. Furthermore, suggestions about the design of high pressure angle and high contact ratio non-standard tooth forms that are already in use for high performance gear applications such as in automotive and aerospace industry are given. To the knowledge of the authors, the design of non-standard profiles is still at the stage of trial-and-error in industry practice.

Goldfarb et Al. (2015) have introduced the concept of Dynamic Blocking Contours in gear design as a tool for designers to predict the gear's quality at the initial stage of its design. The blocking contours are used to choose profile shift modifications for the pinion and gear. In this way, a specific profile shift coefficient is selected to obtain specified gear properties. With this approach, the rack parameters, including the number of teeth, have to be fixed leaving as the only independent parameter the profile shift. Given that the area restricted within isograms fulfils the conditions imposed by compatibility and manufacturing processes, all the possible combination of profile shifts for the two gears in mesh are feasible. In their work the authors give an example of a contour plot for a couple of spur gears respectively with 22 and 35 teeth, with 20° pressure angle and addendum coefficient, h_a=1. They also assume a predetermined centre distance a_w=58.5 mm. Given that such a centre distance is indicated by a line that crosses the design space, all the points that lie on that line are feasible combinations of profile shifts. They

also found optimum design choices for high contact ratio and the same specific sliding. Even though this work is comprehensive and covers the main aspects of gear design, it does not consider internal gearing, and does not give an indication of the resulting gear performance.

In 2013 Kapelevich (2013) introduced the “area of existence of the gear pair” generated by means of the direct design method. The author considers the area of existence a research tool that allows engineers to explore “exotic” gear mesh solutions other than the ones commonly used, and to find a gear pair with certain characteristics that satisfies the required performance of a specific application. Figure 2.4 shows an example of area of existence for a pinion and a gear compared with the blocking contours of a gear pair generated with standard proportioned racks and three different pressure angles 20°, 25° and 28°.

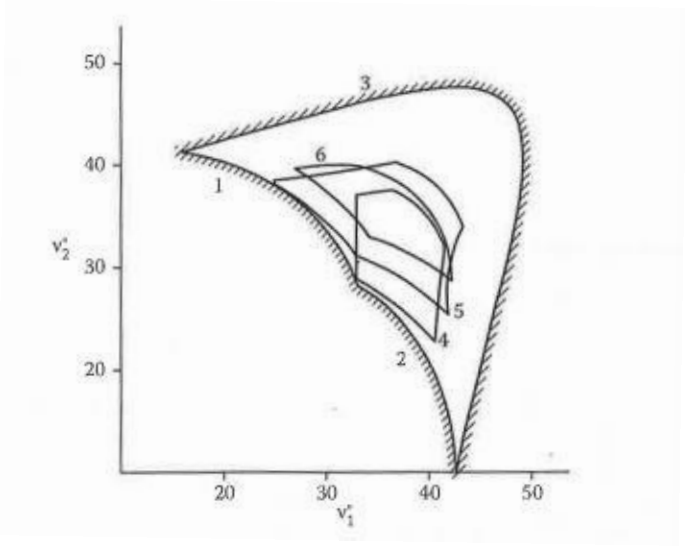

Figure 2.4 - Area of existence of a gear pair as function of profile angle at the tooth tip for the two mating gears $v_{1,2}$. Lines 1,2 and 3 are respectively pinion root interference, gear root interference and minimum contact ratio while 4, 5 and 6 determine the area of feasible combinations for a rack-based design with pressure angles 20°, 25° and 28° respectively Kapelevich (2013).

The area of existence for a gear pair is still a confined space within a blocking contour in which all the combinations of parameters are feasible and covers all the possible gear pair combinations that could be generated by any possible rack. Gear tooth profiles, in general, depend on preselected and standard set of parameters of the basic rack that

are all related to the manufacturing tool. With the direct design approach, tooth profile geometry is based on new independent parameters directly connected to the involute geometry such as number of teeth, base diameter, tip diameter and base tooth thickness. Kapelevich et Al. (2010) describe the construction of each isogram that defines the area of existence by considering the gear mesh characteristics including operational parameters such as corner interference, minimum tooth tip thickness, and the minimum contact ratio. Unlike design block contours, where profile shifts of the two gears in mesh are used as coordinates of the area of existence, this method uses the tooth base thicknesses of pinion and gear called respectively m_{b1} and m_{b2} in Figure 2.5. It is interesting to notice that the tooth fillet profile is not included in the geometry definition process as typically happens with the rack generation. In this case the tooth fillet profile is added in a second step and is shaped by the trajectory of the mating gear tooth tip. This second step completes the gear tooth geometry definition.

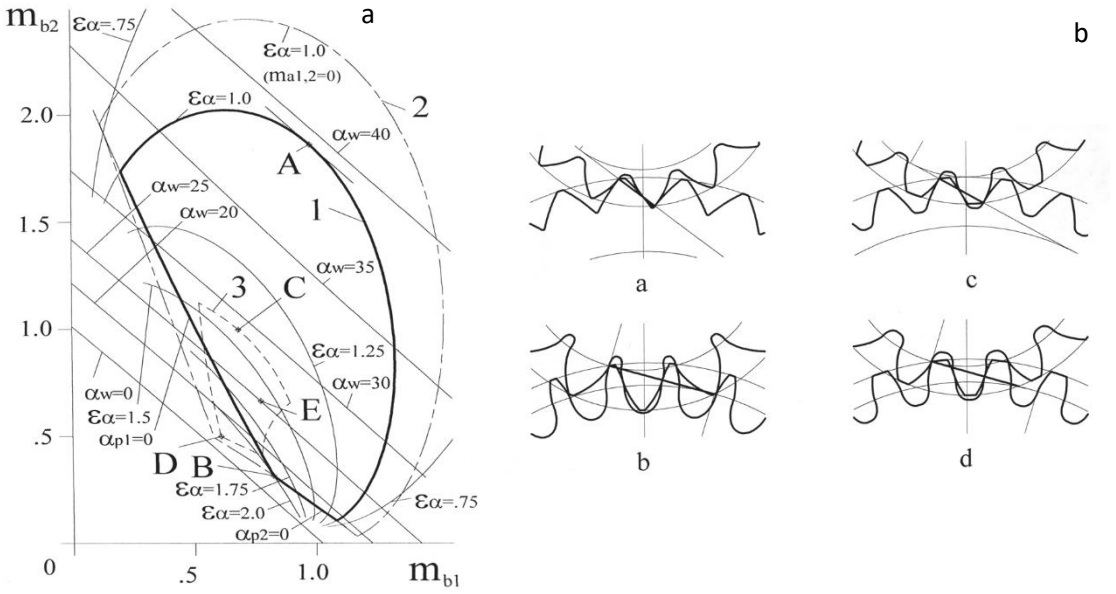

Figure 2.5 - a) area of existence for a gear pair with N_1=14 and N_2=28. Iso-working pressure angle lines and iso-contact ratio curves are shown as function of tooth base thicknesses m_{b1} and m_{b2}. Point A indicates α_{wmax}=39.5° and ε=1; point B indicates α_w=16.7° and ε_{max}=2.01; oint C indicates α_{wmax}=29.6° and ε=1; point D indicates α_w=15.9° and ε_{max}=1.64. b) Tooth profile geometries corresponding to the points A,B,C,D of Figure 2.5 a (Kapelevich, 2013).

In Figure 2.5 the area of existence for an external spur gear pair with number of teeth of pinion N_1=14, and gear N_2=28, is shown. In this figure the above mentioned isograms are plotted and characteristic points corresponding to different tooth geometries are indicated. The non-standard gear pair tooth profiles corresponding to the specific points are shown In Figure 2.5 b. The drawback of this methodology is that manufacturing of the gears is not considered during the design process and it does not rely on the standard and most commonly used production methods. This aspect means that Direct Gear Design is still of great interest for research and custom products, but it does not find application in large volume gear production.

Another technique to design involute spur gear drives is presented by Alipiev (2011) and is based on the concept called the Generalised Basic Rack. The proposed approach follows the traditional principle of defining the gear geometry from the rack cutter proportions, but in this method, eight independent parameters have to be determined to completely define the basic rack geometry compared to the four of the traditional basic rack. Furthermore, a characteristic of this model is that gears are simultaneously modified in the radial and tangential directions; this influences thickness and profile of the cut teeth. The generalised basic rack determines the geometry of two different rack cutters one for the pinion and the other for the gear teeth. Alipiev has applied this design method to symmetric and asymmetric gears with such a small number of teeth that cannot be obtained by using the traditional geometric design due to the occurrence of low contact ratios. To satisfy the necessary condition of contact ratio $\varepsilon>1$ that guarantees the continuous transmission motion from one gear to the other, the author introduced the Realized Potential Method in which the contact ratio of the gear drive is always the maximum achievable.

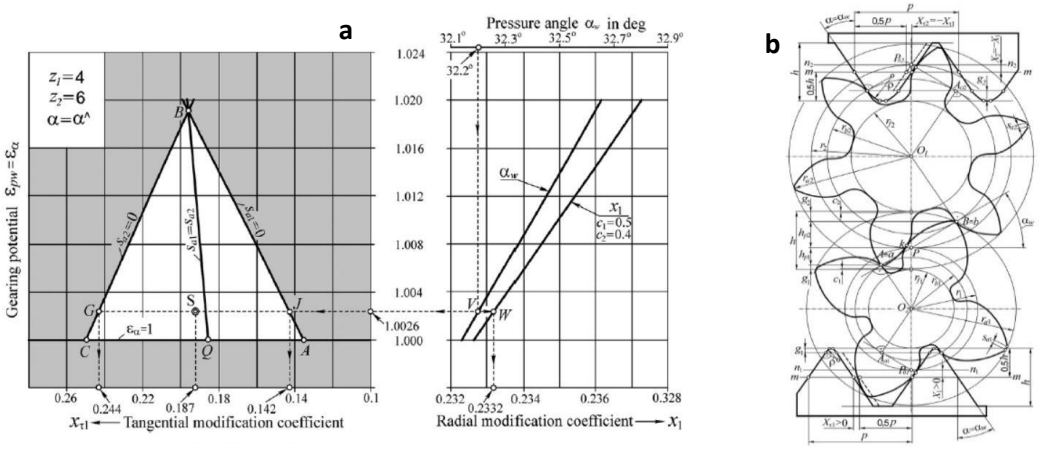

Figure 2.6 - a) Area of the realised potential of symmetric meshing with number of teeth N_1=4 and N_2=6. b) Corresponding geometry of pinion and gear in simultaneous mesh with rack cutters and mating gear (Alipiev, 2011).

Figure 2.6 a shows the parametric area of gears with symmetric teeth generated with the Realized Potential Method. Each point in this area corresponds to a gear train with a specified geometry for which the contact ratio is always maximum and >1. In the example with N_1=4, to fulfil the condition of ε>1, N_2 must be greater than or equal to 6 otherwise, for a smaller number of gear teeth the area does not exist. Once module, number of teeth for pinion and gear, pressure angle and fillet radii of the rack cutter have been chosen, the generated area allows the tangential and radial modification needed for the pinion to achieve the desired tooth tip thickness for the predetermined contact ratio to be determined, and gives the indication of the resulting pressure angle. Both radial and tangential modifications for the gear, have reciprocal values to the ones applied to the pinion. The obtained geometric models including the rack cutters are shown in Figure 2.6b in which is noticeable the difference compared to standard profiles. The pinion teeth are thicker than the gear ones because of the opposite modifications in the radial and tangential directions. The authors state that only when N_1 is specified, the Realized Potential Method allows N_2 to be determined for ε>1. To this end it is necessary to draw the areas for different combinations of N_1 and N_2 to find the desired condition.

Regalado (2007) evaluates the effects on the performance of gears as consequence of nonstandard proportions of the gear geometry. The author analyses individual

manufacturing and operational parameters and shows how a profile shift affects them. Firstly, he correlated profile shift with pressure angle and number of teeth, to find the minimum profile shifting to avoid undercutting. On the other hand, the occurrence of the condition of pointed tooth tip imposes an upper limit to the variation of the profile shift. These two conditions are plotted together and define a feasible manufacturing area. To follow, the analysis is extended to two mating external spur gears. The author does not consider the condition of radial interference but considers the operational interference occurring between the tip and the root of the mating gear asserting that if the two gears in mesh are generated using a hob or a rack without the occurrence of undercutting, this guarantees the nonexistence of operating interference. Contact ratio has been studied in relation to centre distance and pinion profile shift. A reduction in centre distance and a negative profile shift produce an increased contact ratio in the gear set. The author has included in the study the geometry factors for bending and contact stress defined by the American Gear Manufacturers Association. He has observed that for enhanced pitting strength, an extended centre distance and a positive profile shift in the pinion are recommended without affecting the contact ratio. To improve the bending strength of the gear, a positive profile shift and an increased centre distance are needed.

Several other works are related to gear design space boundaries, geometrical and operational parameters and their effect on gear proportions and gear drives performance.

Alipiev et Al. (2013) proposed a generalized approach for defining the undercutting of involute teeth. The authors developed a new approach for the determination of the undercutting condition taking into account the rack cutter tip radius. Compared to the traditional approach, described by Litvin et Al. (2004), they added to the typical undercutting condition one called type I, and two other conditions of undercutting called type II_a and II_b. In the traditional approach the tip radius of the rack cutter is not considered. When this radius reaches a certain value, the traditional condition of non-undercutting is satisfied but a portion of the root fillet still experiences a loss of material. The author describes the boundaries to the case of undercutting by providing the equations to generate the curves that represent the above mentioned limits. For the

type I undercutting condition, the limit has been defined as a function of profile shift by defining a minimum value, X_{min}, that corresponds to the boundary case. For the other two conditions it has been shown how the boundaries vary for different values of pressure angle α and number of teeth N. In order to check the validity of the proposed model the authors manufactured three prototypes of undercut teeth and defined quantitative radial and tangential indices of the undercutting to specify the amount of material removed from the involute teeth profile in both directions.

Miler et Al. (2017) have studied the influence of profile shift on the gear pair volume. By using a genetic algorithm, they created an automated five-variable optimization process that includes module, pinion tooth number, face width and profile shifts for the two mating gears. Tooth root strength and surface durability, calculated with the ISO 6336 method B, were used as constraints for the analysis (ISO 6336, 2006). Boundaries of the explored domain were defined by the authors in relation to the ISO standard and based on practical considerations such as the tooth thickness at the tip diameter. Results of the genetic algorithm formulation gave an indication that increasing the module and profile shift, and simultaneously reducing the facewidth rather than balancing the two gives the best results in terms of volume optimization. Optimized results have also shown that profile shift reduced the volume of the gear pair by 30% compared with a pair without the modification applied. This effect is explained by considering the influence that a positive profile shift has on tooth profile proportions. A larger tooth radius of curvature is beneficial for contact and root bending stress. Results were compared with those from the commercial software KISSsoft (2017) where the optimization criterion was focused on weight reduction.

Rameshkumar et Al. (2010) studied the relation between addendum factor and contact ratio of a gear pair. By increasing the addendum factor from the standard 1 to 1.25, they raised the contact ratio of a standard gear pair to a value above 2. The normal contact ratio and the high contact ratio gear pairs were compared in terms of contact and bending stress. A 2D Finite Element Analysis was carried out for all the gear mesh positions with angular increments of 0.5°. The load sharing ratio has shown that while the normal contact ratio carries 100% of the load in the area of single tooth pair in contact, and 57% each when two pairs are in contact, instead the maximum transferred

load for the high contact ratio gear pair is 57% of the total. The variation of bending stress follows the same trend as the load sharing ratio, and results in a value 18% lower in the high contact ratio HCR compared to the normal contact ratio NCR gears. The tooth contact stress was analysed using the Hertz formula and using the loads from the previous analysis. Contact stress was reduced by 19% compared to the unmodified design. In summary, the authors stated that the load carrying capacity of their modified design was increased by 18% compared to the standard case.

In recent years there has been a heightened level of interest in gear profiles with increased values of pressure angle. Studies on high pressure angle gears have been carried out by Handschuh et Al. (2010) for space mechanism applications, and have revealed the benefits of such design choice. The authors made considerations on the limits imposed by manufacturing and operational parameters on the increase of pressure angle. Pointed tooth top land and minimum contact ratio are both limiting factors for a higher pressure angle design choice. To avoid those conditions, the number of teeth for the 35° pressure angle gear was increased and the module reduced. In order to compare the influence of pressure angle on gear performance, two other designs with 20° and 25° pressure angles respectively were made. The common parameters between the three models were centre distance, gearing ratio and facewidth. By means of finite element analysis and analytical calculations, it was found that sliding velocity, which is proportional to gearing losses and wear rate, was considerably smaller for the non-standard profile. On the other hand, the separating forces acting on the bearings doubled with the high pressure angle design. Stress analysis results from the finite element analysis have shown fairly good agreement, with a lower bending stress for the 20° pressure angle, and a lower contact stress for the 35° pressure angle design. In a companion paper, the authors have reported their testing carried out on the previously mentioned models. In particular, high-speed and a low-speed test modes were run. For the first case, by measuring the temperature of the lubricant which is a function of the gear meshing losses, a lower temperature change across the gearbox was found for the high pressure angle model. A further surface analysis has also shown the absence of any kind of contact failure after $3x10^8$ cycles at 10,000 rpm. For the second case study, the applied rotational speed was 150 rpm for $5x10^5$ cycles, and gears were lubricated with

grease. A difference in weight before and after the test was taken as an indication of wear rate. Also in this case, high pressure angle gears performed better than the other two designs under investigation, with less than half of the mass loss for the 25° pressure angle, and about a quarter of the mass loss for the 20° pressure angle gears. As a result, Handschuh et Al. (2012) stated that high pressure angle gears have shown an improved efficiency and lower wear rates compared to standard gear profiles.

Miller (2017) has shown the mathematical calculations needed to determine the geometrical parameters of a gear pair with a high pressure angle. The method presented by the author considers the pressure angle as a final result of the calculation procedure and is a function of minimum top land thickness, whole tooth depth, contact ratio and cutter tip radius. Three configurations with 33.5°, 35° and 36° pressure angles were analysed and compared to a 25° gear profile considered as baseline. All the parameters involved in the design of a gear pair were kept constant. Stress results calculated using AGMA standards have shown a significantly reduced bending and surface contact stress for the higher pressure angle gears. The author suggested the application of high pressure angle gears where high power density and high gear tooth strength are required. Moreover, because of the higher separating forces due to the higher radial component of the applied load, it is suggested these are used in planetary applications as they are self-balanced systems.

The improved effects of higher pressure angles were also studied for asymmetric gear design. Marimuthu et Al. (2016), by means of direct gear design, have created the area of existence for symmetric and asymmetric gears with similar parameters. The first part of the study was a comparison between symmetric spur gear models directly designed and conventionally designed respectively. The two models differed only in that the pressure angle was 25° for the first case and 28° for the second. Results have shown an 8.4% bending stress reduction and 5.5% contact stress reduction for the higher pressure angle configuration compared to standard tooth proportions. A similar reduction was also shown in the case of asymmetric profiles. The root bending stress for loading applied to the high pressure angle side was approximately 8% lower than that for loading applied to the low pressure angle side. With regards to contact stress, the reduction was approximately 15%. Based on those findings, the authors suggested the use of higher

pressure angles on the loaded side of asymmetric teeth to enhance the load carrying capacity of a gear drive. Another consideration regarded the contact ratio, and the conclusion was that smaller contact ratios are preferred to improve the performance of the gear drive. Similar results were found by Olguner et Al. (2014); in their study on the design of symmetric and asymmetric external spur gears for pump applications. Their work focuses on various combinations of drive and coast side pressure angles and different profile shifts have been tested and compared. Also in this case, the results have shown that increasing the drive side pressure angle and the profile shift reduces tooth contact stress and bending stress significantly. Tooth stress was reduced by 20% by increasing the pressure angle from 20° to 40° respectively. For symmetric 20° pressure angle profiles a 15% reduction in contact stress was seen by increasing the profile shift coefficient from 0 to 0.6. The reductions were also confirmed for the root bending stress by the same amount and for the same geometrical modifications. Also for this case study, gears with larger pressure angles and positive profile shifts made a considerable contribution in increasing the load carrying capacity.

2.2 Stress Analysis of gears

Stress analysis of gears has been developed over the years with different calculation methods and approaches. Analytical formulations have been developed and constantly updated to more accurately predict the stress state occurring in gears and gear trains. The complexity of the gear geometry, dynamics and kinematics are all factors that contribute to the stress development, and make the results hard to predict. In this context, the advantages of FEA became apparent and in the years have almost entirely substituted the experimental methods based on photoelasticity. Coy et Al. (1985), Kawalek et Al. (2006), Spitas et Al. (2007) and many other authors have recognised the importance of Finite Element for the analysis of gears to the point that they claimed FEM being the most powerful method to accurately determine stress and deflection in gears. However, Coy pointed out critical aspects for a valuable and accurate analysis such as mesh quality, boundary conditions and geometry definition.

2.2.1 Root bending stress analysis

Root bending stress is a concentrated stress at the base of the tooth. If the gear tooth, according to Lewis' analysis (Lewis, 1893), is considered a cantilever beam, the highest stress concentration will occur at the root fillet. When bending takes place, the tooth base experiences a tensile stress on the side where the load is applied whereas the other side experiences a compressive stress. High root stress levels exceeding the allowable material limits lead to tooth breakage and consequent failure of gear transmission. The study of tooth root stress is of fundamental importance in the determination of gear performance, and in assessing the effectiveness of a gear design.

Until the mid-20th century all the gear calculations were based on the considerations developed by Lewis about the relation between tooth geometry and bending strength. To estimate the strength of the teeth under load, Lewis inscribed a parabola of uniform strength within the tooth form, and at the point of tangency between the tooth and the parabola, the weakest cross-section has been determined.

Latterly, Dolan et Al. (1942) have focused attention on localized stresses due to abrupt changes in the section of a stressed member. They found that the form factor for gear teeth based on the Lewis' equations did not take into account important geometrical factors such as the sharpness of the root fillet, which influences the generated stresses at the weakest section. Based on this assumption, the authors started a campaign of research by means of photoelastic techniques to clearly understand the effect of some geometrical variables on bending strength. Following this research, stress concentration factors were introduced to adapt the stress value calculated by means of Lewis equation to those measured experimentally.

The current trend of gear design focuses on minimizing the root bending stresses with the ability to accurately model spur gears and obtain accurate bending stress results.

Andrews (1991) was one of the first to apply the finite element method to the study of spur gears. The author focused on the validity of finite element gear analysis compared to the semi-empirical formulae generally adopted by the gear design standards, or those based on photoelastic experiments. Given that such technique requires the use of

physical models, it is impossible to analyse every proposed gear design to develop an accurate formulation that represents the actual stress state under load. Therefore, the author has proven the validity of the finite element method by making a direct comparison with photoelastic experimental results. Due to the limited computational power at this time, the model included a whole tooth and two halves of the adjacent teeth. The involute geometry has been generated by using the rack-gear meshing equations that determine three distinct portions of the tooth geometry: the involute portion, the trochoidal fillet and the root circle. The model was fully constrained and the load was applied in six different positions from the tip to the root. As the loading point moves along and descends down the flank, the tensile fillet stresses were decreasing due to the smaller bending moment associated with lower load application points. The trend changed for load positions closer to the root fillet. Due to the application of the load, an additional tensile component superimposes the stress at the fillet determining a “proximity effect”. The direct comparison between the results obtained by photoelastic experiments and those yielded by numerical analysis had shown a good agreement establishing the ability of the finite element to accurately represent the behaviour of a loaded gear.

Kawalec et Al. (2006) provided a comparative analysis of tooth root strength between ISO 6336 (2006) and ANSI/AGMA 2101/D04 (2016) standards. Results were compared to FEM with the aim of understanding the existing limitations of the current gear standards. The authors conducted a comprehensive analysis of the impact of geometrical, manufacturing and operational parameters on gear performance. Gear design variables such as number of teeth, pressure angle and profile shift were studied in relation to the generated root stress state. Calculations were also performed for gears manufactured with rack cutters and gear cutting tools. Moreover, the influence of the location of load application was investigated. Stresses determined in accordance with ISO and AGMA were compared with results of finite element analysis of the corresponding gear models. The study revealed that the two standards tend to give different results due to their differences in the calculations of critical section parameters. An increase of pressure angle from 15° to 25° has resulted in a considerable root stress reduction for both ISO and AGMA. The increase of profile shift coefficient

from –0.5 to +0.75 has also determined, for the case of AGMA calculations, a reduction in root bending stress. The decreasing trend was confirmed by FEA but with a smaller percentage of reduction. ISO showed a minimum for x=0 and an increasing trend towards high profile shifts. An increase in normal module has also shown a stress reduction and in this case the three methods were in agreement both for load applied at the tip and at the highest point of single tooth contact (HPSTC). In all the calculations performed, tooth root stresses according to the ISO standard were showing greater values than that calculated according to AGMA while stress values computed with the use of FEM were generally in between the two. The difference was smaller, but still visible, in the case of load applied at the HPSTC compared with the load applied at the tip. In the case of gear profiles generated with racks, stresses computed with FEA were closer to the ISO results, whereas in the case of profiles generated with gear tools, these were closer to AGMA. The same comparison with the addition of experimental results was done by Lisle et Al. (2017); the authors introduced an experimental technique based on strain gauge technology to validate the accuracy of ISO, AGMA and FEA for gear stress analysis. The comparison was made for large 50 mm module single tooth geometry with strain gauges positioned at the tooth root. The applied load was normal to the tooth flank surface and positioned at the tooth tip. The stresses established from the strain gauge experiments have shown a minimal difference (0.5% on average) with those produced using FEA. Also, in this case, ISO was more conservative than AGMA for the estimation of root bending stress while FEA gave the most accurate result, perfectly aligned with the experimental findings. Both Kawalek and Lisle stated that FEA is the most accurate stress analysis technique compared to ISO or AGMA.

Spitas et Al. (2007) have developed an optimization procedure to reduce the root bending stress on a spur gear pair. The maximum tensile stress at the root fillet was calculated with boundary elements and validated through a photoelastic investigation. The optimization routine required constraints to reduce the domain of existence for the gear pair to existing values. The given active constraints were based on kinematic, manufacturing and geometrical limitations, and dictated by commercial standards or common practice in manufacturing. Since the aim of the study was the optimization of the gear pair for bending resistance, contact pressure (proportional to pitting resistance)

was also included in the constraints to ensure that the optimized design was not inferior in that respect. By comparing the results, it was noticed that the optimum solution was found for the case of an equal stress state on pinion and gear. This result was achieved by increasing the profile shift on the pinion and decreasing the corresponding profile shift on the gear. As the centre distance was constrained a reciprocal modification was applied. The photoelastic experimental results have confirmed the numerical predictions, assuring a decrease of the maximum fillet stress up to 8%.

Dai et Al. (2015) have performed a static and dynamic tooth root strain analysis for symmetric and asymmetric spur gear profiles. Their analysis is based on a finite element/contact mechanics approach with an extensive use of experimental data to validate the numerical results for an accurate prediction of the tooth root strain. The authors have focused on the shape of the dynamic and static strain curves and its relation with tooth geometry in the presence of profile modifications. Their model includes two full body gears in mesh in relative rotation and the contact area on the active flank is captured using a semi-analytical formulation. This configuration allowed the authors to keep the mesh relatively coarse near the tooth surface resulting in high computational efficiency. For the experiments, strain gauges were applied to the roots of five consecutive teeth, and tooth root strains were measured under static and dynamic conditions. For the case of static tooth root strain, the finite element approach used has accurately predicted the amplitude and the distribution of the static strains during the mesh cycle compared with experimental results. The authors have also explained the transition between single and double pairs of teeth in contact and its effect on the root strain and consequent stress. With regards to dynamic tooth root strains, the gear pairs were tested experimentally to validate the numerical models. Also in this case, the FEA model has predicted the root strain amplitude and shape for the entire duration of the mesh cycle. For the two cases considered, static and dynamic root strains are similar except for speeds close to resonance. When resonance occurs, due to large amplitude vibration, the strain curve showed multiple peaks during the mesh cycle, with a maximum strain about 50% higher than the corresponding static value.

2.2.2 Tooth flank contact stress analysis

Contact stress in gears is generally known as Hertzian stress. Gear teeth undergo compression due to the pressure generated in the region where contact occurs. According to Juvinall et Al. (1983), While the bending stress is dependent on the geometry and shape of the gear tooth, contact stress is a function of the curvature, material surface, hardness and elasticity. Contact pressure at the point of mesh between a gear and pinion is of great importance for the estimation of gear resistance and durability. According to Kapelevich et Al. (2013) and Gopinath et Al. (2016) contact stress is the main cause of surface failure of gears. This is due to the extremely high contact pressure that is generated at the interface between the two tooth flanks in contact. The shared load is distributed over a limited area of contact within which contact stresses can reach values above the permissible limit. More than twenty different forms of tooth flank failures have been reported according to ISO 10825 (1995). A summary of gear failure methods was done by Gopinath et Al. (2016) and presented in a flowchart in figure 2.7.

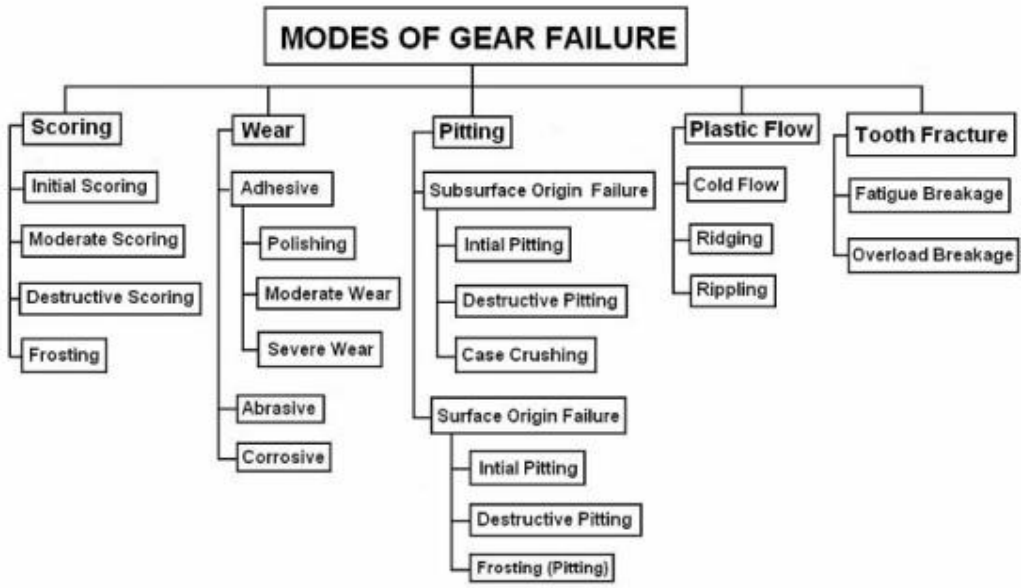

Figure 2.7 - Flowchart representing the modes of gear failures (Gopinath et Al., 2016).

The calculation of contact pressure and related stress is based on the theory developed by Enrich Hertz for two elastic cylinders in contact which was further developed by Archard (1953). It is clear that a proper evaluation of flank contact stress is one of the

most critical parameters to minimize in order to improve gear transmission durability and performance. Several research works have investigated the contact stress distribution of mating gears by means of analytical, numerical and hybrid methods. The available contents relevant to this study are summarized in the following paragraph.

Hwang et Al. (2013) presented a contact stress analysis by means of FEA for a pair of mating gears. The model consists of three teeth from the pinion, and one tooth from the gear, in relative rotation to each other. The model was loaded with a torque on the pinion with the mating gear allowed to rotate by 27.4° in order to cover the full mesh cycle of a tooth pair. With this configuration the analyses were performed at different contact positions during the relative rotation to investigate the variation of contact stress along the line of contact. The authors made the assumption that the load is perfectly split in half when two pairs of teeth are in contact. By calculating analytically, the position of the highest and lowest points of single-tooth contact, they applied the full load and half of the load depending on the position of the contact point. The finite element results in the area of single pair of teeth in contact showed an increasing trend with the maximum contact stress occurring around the lowest point of single tooth in contact. The results were compared with the contact stress calculated with the application of the AGMA standard. The analytical value matched exactly the FEA result at the highest point of single tooth contact. This value was not the overall maximum for the case of the finite element stress. By comparing the two maximum stress values the computed stresses were more severe than that of the AGMA standard. Similarly, Olguner et Al. (2014) have applied both analytical and numerical approaches to determine the contact stress on involute spur gear teeth. The authors developed a 2D finite element model of a three teeth pinion and gear by assuming a uniform load distribution along the facewidth. By creating three tooth gear model, the authors did not make any assumptions of the load distribution among tooth pairs in a simultaneous mesh. This configuration increased the fidelity of results. The variation of FEA contact stress during a complete mesh cycle was compared with AGMA analytical results showing a substantial similarity between the two except for the first point of contact where the radii of curvature are small and possibly the Hertzian theory deduced from two elastic cylinders in contact is not precise enough. The authors extended the analysis

to the effect of gear ratio on the generated contact stress. By increasing the number of teeth of the driven gear, three different contact ratios were achieved. The results have shown that an increase in the number of teeth of the gear significantly reduces the tooth contact stress.

Gurumani et Al. (2011) have made a comparison between a standard external spur gear and two differently crowned spur gears for stress and tooth contact analysis. The crowning was applied longitudinally across the full facewidth. The authors described the contact stress distribution and its relation with the generated contact area. They also explained that while for standard involute profile the contact between two involute flanks can be considered equivalent to those of two cylinders with same radii of curvature, for the case of crowned profiles this assumption does not reflect the actual contact state. Instead this can be assumed as the contact between two spheres of different diameter. For the first case the contact stress is uniformly distributed along the facewidth on a rectangular area, and for the second case, the uniform distribution does not occur given that the contact area assumes an elliptical shape with higher contact stress at the centre and progressively lower contact stress towards the edges. The tooth contact analysis undertaken by the authors is based on the Hertz theory and is compared to numerical results. Also in this case a three teeth 3D model was used in order to consider the effect of adjacent teeth in the stress distribution. The authors considered the load applied at the pitch diameter and uniformly distributed on a line for the case of a standard profile, and concentrated at the point of contact in the case of crowned gears. The Von Mises stresses at the critical contact points were analytically calculated and compared with FEM results. The results showed a more severe stress state for the case of analytical calculations of 21% for the case of unmodified profile, 28% for the case of circular crowning, and 32% for the involute crowning modification.

Ristivojević et Al. (2013) have carried out a theoretical and experimental study to more accurately model the tooth flank contact stress and the load distribution in spur gears considering the influence of the manufacturing accuracy and the influence of the tooth geometry. The manufacturing accuracy was modelled by varying the base pitch of one of the two gears in mesh and for the tooth geometry, positive and negative profile shift coefficients were used for the driving and driven gear respectively. The authors found

that the base pitch difference in meshed teeth has an influence on the load distribution of meshed pairs only for a low magnitude of applied load. Once the load increases, the load distribution factor tends to a constant value which corresponds to the case of equal base pitch for the two gears in mesh. A numerical analysis of the flank contact stress was also presented by considering both manufacturing and geometrical deviations. For the case of zero profile shift, maximum contact stress occurs when only one pair of teeth is in contact. In the region where two pairs of teeth are in contact the maximum contact stress occurs at the first and last point of contact. For the case of profile shifted profiles, contact stress is the highest at the last point of contact of the entire cycle. This, for the authors, is the result of an unfavourable geometry of the mesh profile. The variation of base pitch only lightly affected the distribution of contact stress for the case of gears without profile shift applied. For the case of profile shifted teeth, the presence of manufacturing errors affected the contact stress distribution from the point of single tooth pair in contact (STPC) to the last point of contact of the meshing cycle. The degree of influence was proportional to the error.

Ye et Al. (2016) have studied the contact characteristics of a high contact ratio spur gear pair. Influence factors such as axis misalignment and tooth flank modifications have been taken into consideration and studied by means of analytical tooth contact analysis and the finite element method. The authors described the influence of tooth contact at the tip edge. The FEA model consist of a 3D full body gear pair in mesh in which the pinion is located axially and radially and can only rotate about its axis, and the gear is fixed in all six directions for each time sub-step. For the case of unmodified profiles, the ellipse-type stress distribution is evenly distributed along the facewidth, and for the case of lead crowned profiles, the ellipse is located at the centre and does not extend towards the edges. In this case the stress level is higher due to the smaller contact area and the increased curvature. In presence of axis misalignment, the lead crowning avoids the occurrence of edge contact at the face-end, and the consequent non-Hertzian contact stress, by relocating the point of contact towards the centre. For the case of pinion tip relief, while the contact stress mesh cycle for the unmodified profile showed a spike in the region of first contact due to tip corner impact, in the case of tip relief, the concentrated contact stress is avoided, but an increased amount of stress is shown in

the central area of the mesh cycle with a variation tendency similar to a gear pair with normal contact ratio.

2.2.3 Combined Contact and Bending analyses

Other studies have focused on a coupled analysis of contact and bending stress.

Zhan et al (2015) have studied the time varying load capacity of a spur gear system through a quasi-static finite element analysis by means of the commercial software Ansys (2016). The quasi-static analysis allowed the estimation of the induced contact stress and bending stress as a function of contact position. The choice taken by the authors to use quasi-static analysis is justified by the slow rotational speed involved, as the inertial effect can be neglected. The 3D model includes the full body geometry of the two gears. All the degrees of freedom have been constrained except for the rotation, and a rotational velocity of 0.55 [rad/s] and a torque of 276 [N] were applied to the driving and driven gear respectively. The authors described in detail the approach they have followed to get these results and avoid the convergence difficulties due to normal contact stiffness, interface treatment, mesh density and non-linear contact characteristics. For the same gear design and load conditions the AGMA standard was applied to estimate both contact and bending stress in order to compare and verify the numerical methodology (ANSI/AGMA 2101/D04, 2016). Contact stress and bending stress have shown a variation as function of the contact position with a sudden increase at the point when a single tooth pair is in contact. The FEA methodology has shown also the ability to consider deformations and deflections due to the load applied and its effect on the stress state. The comparison made has shown a good agreement with AGMA for the case of contact stress with a difference of 2.5% for the peak values. On the other hand, numerical bending stress results were more severe than that of AGMA with a difference at the peak value of 77% which makes the two results incomparable. The FEA result has been taken as the most reliable by the authors, and the large difference has been explained by taking into consideration that the AGMA standard is based on uniform beam theory which is far from the involute geometry of a gear tooth.

Similarly, Lias et Al. (2017) developed a quasi-static model based on Ansys to conduct the analysis of time-varying strength of spur gears, and to compare the results to the analytical ratings. For the authors, the complexity of the tooth geometry limits the

accuracy of analytical results due to the imperfection of the assumption needed. The physical model used for the quasi-static analysis was a 3D three tooth gear pair model allowed only to rotate about the central axis. The equivalent Von Mises stress criterion was used to evaluate the time-varying surface contact stress for a time interval of 0.6 s and a 30° rotation of the pinion. The performed analysis showed the variation of tooth surface contact stress for different contact positions along the line of contact with an increase in magnitude of 26% when the engagement moved from a double tooth pair in contact, to a single tooth pair in contact, where the maximum stress condition was recorded. For the case considered, the contact stress predicted by the AGMA standard was 8% lower compared to the numerical analysis. A similar behaviour of a time-varying nature was shown for the case of tooth root bending stress for which the variation of number of teeth simultaneously in contact causes a fluctuation in the bending stress values. The worst loading condition was recorded at the HPSTC both for the pinion and the gear. In this case, the comparison made with the AGMA standard has shown a more severe result of 10% when compared to FEA.

Sánchez et Al. (2017) have developed an analytical model applied to internal spur gears based on the Minimum Elastic Potential Energy. The authors have computed their model accordingly with the ISO 6336 standard to calculate load sharing ratio, contact stress and bending stress for an internal gear pair. The model was able to estimate the variation of load sharing ratio and contact and bending stresses along the path of contact. Results are shown for a standard profile and a profile with a reduced addendum. The evolution of the contact stress along the path of contact was predicted and the critical point was found at the first point of contact where the radius of curvature of the involute profile has the minimum value. The evolution of the bending stress instead has shown a maximum located at the outer point of the interval of single pair tooth contact of the pinion i.e. HPSTC. These results have been validated by means of FEA through a 3D model included the external pinion and the internal gear in mesh. Values of stresses have been calculated for multiple position of the gear mesh by means of multiple static analyses. For each relative position, the gear was prevented from rotating while the pinion was delivering the torque. The analytic results showed higher values of bending stress compared to FEA. This effect was attributed to the fact that the

ISO standard only considers the tangential component of the force. The radial component, which in fact generates a compressive stress state around the root area, reduces the tensile stress state. On the other hand, contact stress was in good agreement with FEA. The authors have further developed their model including the contact stiffness for the calculations. In this case the model was applied to a couple of external spur gears in mesh and for a standard and high contact ratio configuration. Results of contact stress were showing that the critical stress can be located either at the HPSTC or at the first point of contact depending on the geometry for standard contact ratio spur gears. For the case of high contact ratio gears critical points were found at the first point of contact of the mesh cycle, or at the beginning and at the end of the interval with three teeth in contact. Tooth root stress was also computed and the evolution along the full arc of action has been shown for both normal and high contact gears. In this case the maximum was shown at the HPSTC for standard contact ratio gears and within the second interval of two pair tooth contact for high contact ratio gears. Also for this study the authors validated their model with FEA. The results show very good agreement with the analytical calculations except for the stress state at the first point of contact, for which the developed model tends to show a more severe stress state compared to FEA. This small discrepancy is accounted by the authors to the added stiffness to the FEA model due to the constraints applied.

2.3 Coaxial drives: epicyclic and cycloidal systems

This section provides the available literature on epicyclic and cycloidal drives. It includes an overview of designs from the first patents to the current design practice, followed by the literature review based on current scientific and industrial Research.

High speed reduction ratios cannot be achieved using only single pairs of internal or external gears. Coaxial drives are the most viable solution for applications that require high speed ratios and compactness at the same time. Thanks to their physical disposition with concentric axes and the combination of internally and externally toothed gears they are able to provide weight reduction and compactness, typical properties for applications in which high power density is required (Höhn et Al., 2013a; Kapelevich et Al., 2011). Given that the pinion and gears can be combined in different

ways, Yu (1987) has classified a vast family of epicyclic gear trains by giving an appropriate nomenclature based on their physical arrangement.

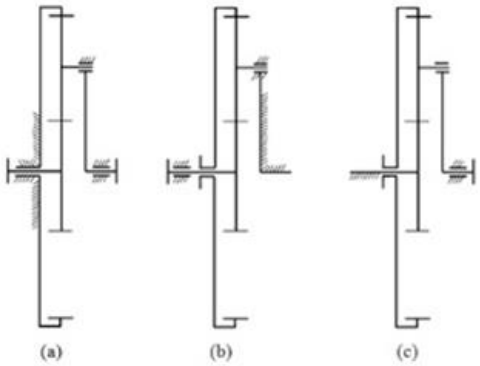

Figure 2.8 - Schematic of single epicyclic gear layouts: a) Planetary gear; b) Star gear; c) Solar gear (Yu, 1987).

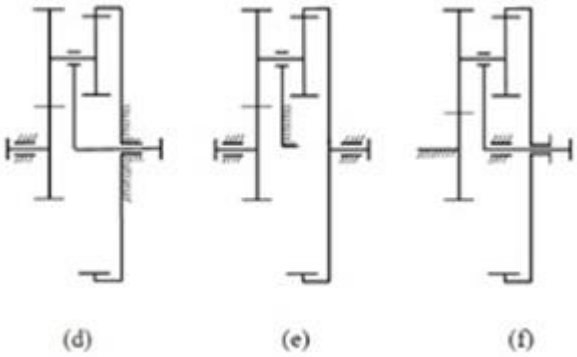

Figure 2.9 - Schematic of compound epicyclic gear layouts: d) Compounded Planetary gear; e) Compounded Star gear; f) Compounded Solar gearing systems; (Yu, 1987).

In epicyclic gear trains, the desirable high ratios are achieved by the compounded motion of gears and pinions that consist of a combined movement of the planet gears. The planets spin around their own axis and simultaneously revolve around the central axis of the gear train, for this reason Yu suggests using the term “moving axis gearing”. Figure 2.8 a) shows the planetary system, where the planet gears orbit around a central sun gear. Figure 2.8 b) and 2.8 c) show a star and solar gearing system where the planet axis and the sun axis are fixed respectively. Figure 2.9 d), 2.9 e) and 2.9 f) show the same configuration as before with compound planets, one side in mesh with the sun and the other in mesh with the ring or annulus. Of the 6 combinations, Yu considers only 4 as

'moving axis gearing' because he does not consider as epicyclic gears the arrangements in which the planet axis (planet carrier) is fixed. A further generalization of epicyclic gear trains is based on the sign of the speed ratio. The negative or positive signs indicate the sign of the realized speed ratio. Two main categories have been reported by the author, called 2K-H(-) and 2K-H(+).The term "2K" means two coaxial central gears either internally or externally toothed. "H" denotes the planet carrier and so the moving axis and the (-) or (+) is the sign of the resulting speed ratio. The basic 2K-H(-) arrangements are shown in figure 2.10 where all the systems have two central axis gears 2K and a planet carrier H.

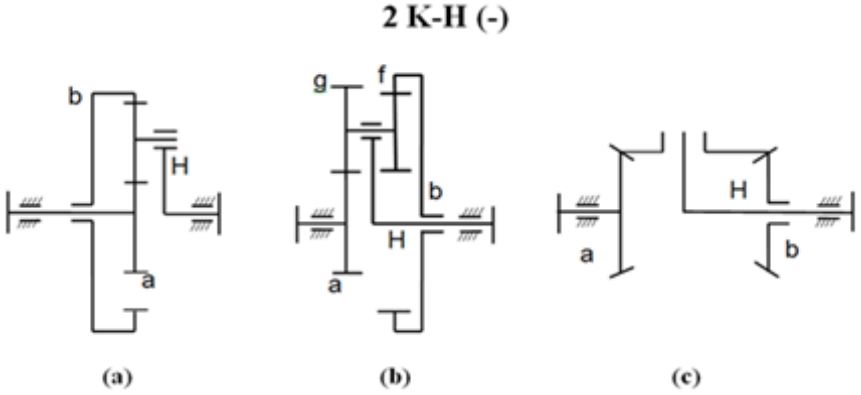

Figure 2.10 (a, b, c) – Schematic layouts of 2K-H(–) type (Yu, 1987).

Similarly, in Figure 2.11, members of 2K-H(+) are shown. In this case the systems also consist of two central gears and one carrier but the speed ratio is positive.

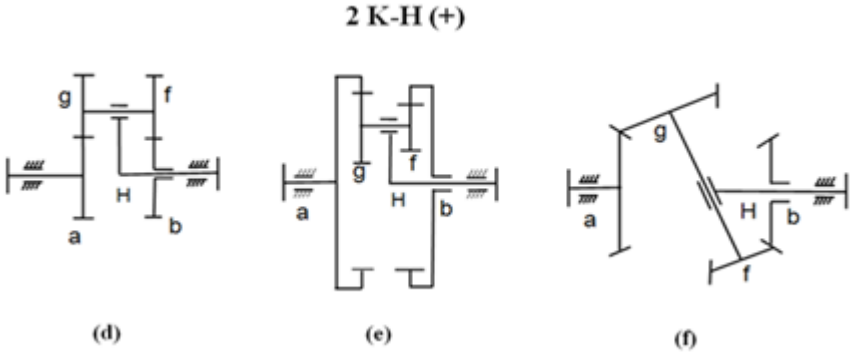

Figure 2.11 d, e, f) - Schematic layouts of 2K-H(+) type (Yu, 1987).

Yu has developed empirical formulae for the efficiencies of each family and conclude that 2K-H(–) can achieve high efficiency with a limited maximum speed ratio (similar to that for a pair of external spur gears). On the other hand, 2K-H(+) type can achieve high

speed ratios in a compact size at the expense of efficiency. The author proposed the hybrid KHV combines the high efficiency and the high speed ratio in a relatively compact volume. The KHV system has the same basic layout of the current Cycloidal drives and is able to provide a speed ratio in a single stage between 40 and 200 with efficiency up to 92%. The physical realisation sees a single central gear (K), a planet and an Eccentric shaft which also functions as a planet carrier (H). The planet gear, carried by the eccentric shaft is in mesh with the central gear (ring), and experiences wobbling and rotating motions. To convert the compound motion and transmit the rotation and the power of the planet to an output shaft coaxial with the central axis, Yu introduced an equal angular velocity mechanism (V). In Figure 2.12, a version of the V mechanism called a 'Plate-shaft' type equal velocity mechanism is shown. The output shaft flange is composed of pins that are turned by oversized holes radially placed on the planet gear. The differential motion of the planet turns the cranks at reduced speed and high torque. To dynamically balance the system, two or more planets (cycloidal gears) are generally used. At high speeds the wobbling masses, a consequence of the compound motion, balance the centrifugal forces.

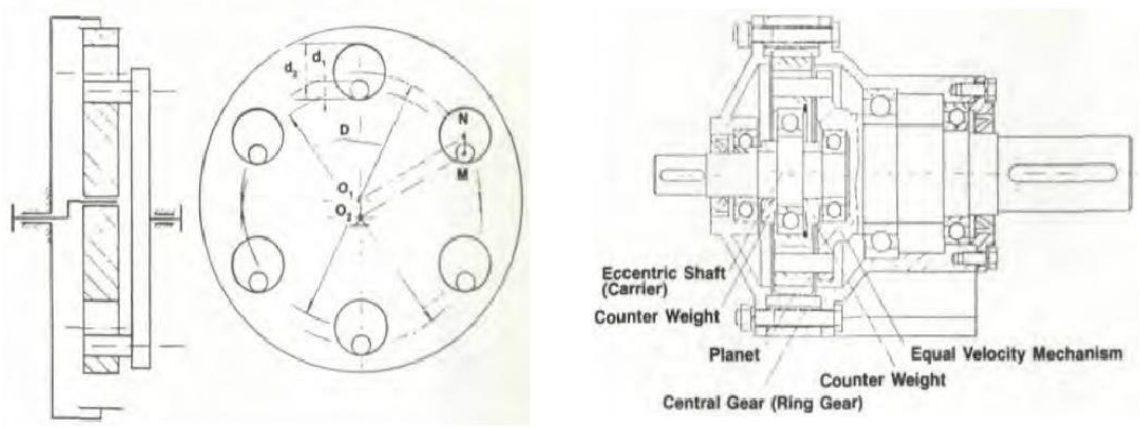

Figure 2.12 - a) Schematic representation and b) Longitudinal section view of a Plate shaft (KHV) Equal Angular Velocity mechanism (Yu, 1987).

A comparison of the physical size of Cycloidal drives with equivalent conventional drives is made by Botsiber et Al. (1956) as shown in Figure 2.13. They state that to achieve a speed ratio of 75:1, three reduction stages of conventional gear trains are

required. Sizes of gear drives are determined by the load applied to the teeth and by the desired velocity ratio. Cycloidal drives are more compact than conventional gear trains with same capacities. Figure 2.13 shows a comparison between systems with a 75:1 velocity ratio and same output power. As seen, the housing size for the differential gearbox is very much larger than the Cycloidal drive, even though their capacities are the same.

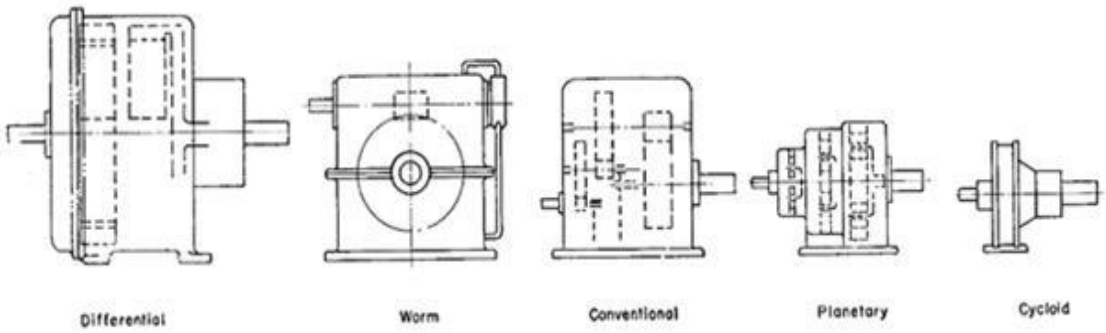

Comparison of four reduction units with 75:1 speed ratio. Rated horsepower = 25; input speed = 1000 rpm

Figure 2.13 - Size comparison between different speed reduction units (Botsiber et Al., 1956).

2.3.1 Planetary drives

Planetary or Epicyclic gear trains have been invented and used since the first kind of transmission systems appeared. Dudley (1969) reports on the most ancient mechanisms created in China in about 3000 B.C., consisting in a complex differential gear system. For this reason, it is impossible to place in history the precise time of its invention.

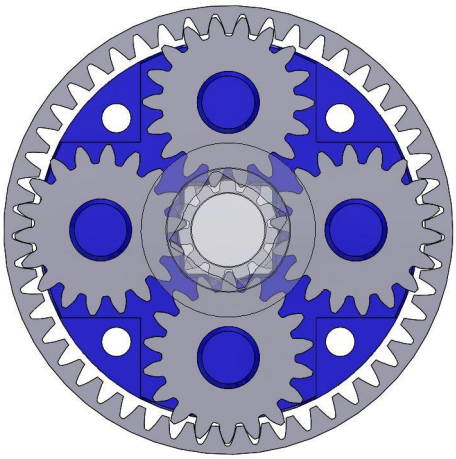

Figure 2.14 - Frontal view of a four planets epicyclic transmission system.

A simple planetary system as the one shown in Figure 2.14, can be connected in six different ways creating a different velocity ratio for each configuration. To determine the kinematics of the system two components can be controlled and the output is a function of these two inputs. Ferguson (1983) presented a governing kinematic equation that yields all possible velocity ratios and allows the evaluation of torque and efficiency of the system for any given planetary configuration. The governing kinematic equation for *n* independently controlled components is presented in the form:

$$\omega_{E1} = k_1\omega_{E2} + k_2\omega_{E3} + \cdots + k_n\omega_{E(n+1)} \qquad 2.1$$

where ω_{En} is the angular velocity of a given independently controlled component, and E_n and k_n are constants that depend on the planetary gear geometry. Another method to calculate the velocity ratio is the most common tabular method explained by ANSI/AGMA 6123-B06 (2006) and Maitra (2012).

The main characteristic of planetary drives is the ability to transmit high amount of power within compact volumes. Kapelevich et Al. (2011) presented an approach to optimize the gearbox arrangement and the gear geometry to increase the transmission density. This approach is based on the definition of a volume function. The maximization of the number of planets in an epicyclic gear stage reduces the volume function and increases the compactness of the gearbox. The authors applied the volume function to three different multi-stage arrangements: two stars, two planetary and a differential first stage followed by a star arrangement with a stationary carrier. Of the three, the volume function showed a minimum for the arrangement that includes the differential stage because part of the power is transmitted directly from the first stage to the output, hence loading the second stage less. In another research work, Novikov et Al. (2008) have further developed the double-stage gear train that includes the differential by adding asymmetric tooth gears. The system, composed by three planets at the first stage and five planets at the second, found application in a turboprop engine gearbox and provides the highest power transmission density for the required gear ratio. The design concept of asymmetric gears for applications in epicyclic transmissions with singular planet gears is based on the equalization of the contact stress safety factors as the two flanks of a planet gear tooth are simultaneously in contact with the sun gear in the

external mesh and with the ring gear in the internal mesh, where because of the convex/concave surfaces on contact, the stress level is lower.

Höhn et Al. (2013) compared the volume, weight and efficiency of three one degree of freedom planetary transmissions. The aim was to find the configuration that maximizes the power density. The gears were designed in accordance with ISO 6336, with optimized parameters to reduce gear losses and increase the efficiency. The authors describe the geometrical constraints that determine the correct assembly of a certain number of planets within the sun and the ring gears. The number of teeth is determined by satisfying the geometrical constraints and, on the other hand, the desired reduction ratio and the requirements of reduced weight and volume. Regarding the design of low-loss gears, the authors give suggestions about the positive influence of an increased pressure angle, a reduced module and a low contact ratio. As result, volume and weight are proportional to the gear ratio instead of centre distance that has a quadratic influence on volume and weight.

Rameshkumar et Al. (2010) applied the concept of high contact ratio gearing to increase the load carrying capacity in a planetary gear train used in a military vehicle final drive. In order to increase the power density of the original gear drive the contact ratio was modified from 1.343 to 2.0106. To achieve this result, number of teeth, addendum factor h_a, module and profile shift of the three gears were changed accordingly, with the initial assumption of maintaining the same centre distance. By means of a quasi-static Finite Element analysis, the authors made a comparison between the replaced normal contact ratio and the newly designed sun and planets in terms of bending stress, contact stress and deflection. FEA results revealed a considerable 25% reduction of bending and contact stress for the case of high contact ratio that imply an increased load carrying capacity of 25% for the same weight and volume.

Kalyanshetti et Al. (2014) investigated the stress state on a loaded ring gear. Both bending stress and stresses developed across the thickness of the ring gear have been evaluated through a 3D FEA static model and experimental measurements. The rim thickness of the ring gear plays a crucial role in the reduction of volume and mass and hence power density. The experimental setup consisted of a three-planet planetary

drive with strain gauges applied on the outer surface of the ring gear in proximity to the meshing position between planet and ring. Tests and computational analyses were run for different input torque levels. Experimental stress values and numerical results were in strict agreement.

Prueter et Al. (2011) have studied the root strain of the ring gear for a flexible-pin multi stage planetary drive for wind turbine applications by using 3D finite element and full scale system experiments. The system is composed of three stages as follow: one fixed-carrier planetary stage, one differential planetary stage, and a third traditional helical pinion and wheel. The input torque goes into the system via the ring gear of the first stage and is also connected to the carrier of the second stage. The sun of the first stage is connected to the ring of the second stage. The sun gear of the second stage connects to the helical pinion of the third stage. The root strain at eight strain gauge locations placed across the facewidth was compared with the one obtained from FEA. The finite element technique used in this work is a hybrid combination of finite element and semi-analytical to increase the computational efficiency due to the large dimension of the model. Strain data from the finite element model and data from the experiments were in close agreement. Maximum values of strain were measured both for experimental and computational strains near the constrained end of the ring. On the free end side, the peaks of strain are not visible because the body is allowed to deform in that area. Based on this result, and after the computational model was validated against experiments, the authors decided to test a more flexible ring gear. For the configuration with more compliance, a noticeable improvement was seen. The sharp spike disappeared also on the side of the constrained end, due to more deflection and a consequent improved load distribution across the facewidth.

2.3.2 Cycloidal drives

Cycloidal drives can be considered an alternative solution to epicyclic transmissions due to the fact that both have concentric input and output shafts. In fact, also the cycloidal transmission is an epicyclic-kind system and while its components and geometrical arrangement are different they have in common the same working principle with load shared between multiple components in simultaneous mesh.

The Cycloidal drive was invented by Lorenz Konrad Braren (1928) and presented in his patent in 1928US Patent # 1,694,031 of which the introductory page is shown in Figure 2.15.

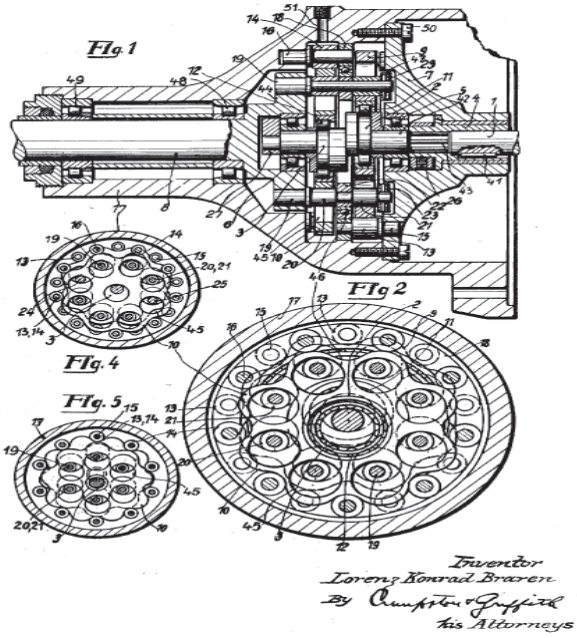

Figure 2.15 - Lorenz K. Braren "Gear Transmission", (Braren, 1928)-US Patent # 1,694,031.

The design of current cycloidal drives is based on Braren's design concept. The working principle is based on conjugate surfaces that meshing with each other are able to transmit the load from a member to the other. In Braren's design the conjugate surfaces consist of a cycloidal disk, defined by the author "intermediate" and a number of pins placed circumferentially around the disk and hold in place by the annulus that works as housing of the system as shown in Figure 2.15. A primary role in the cycloidal transmission is played by the cycloidal disk. The geometry of this component presents complex epicycloidal tooth profiles as shown in Figure 2.15.

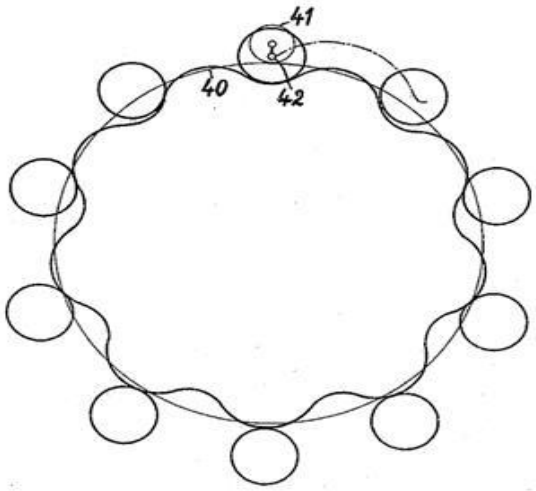

Figure 2.16 - Braren's tooth profiles in 'Gear Transmission', (Braren, 1932)– US Patent # 1,867,492: a)epitrochoid tooth profile.

Braren (1932) describes the construction method of the epicycloidal profile used for the cycloidal disk and appropriate for a mechanical transmission. The curve generated by a point fixed inside a rolling circle designated as '41' in Figure 2.16. When the circle rolls without slipping on the outer periphery of a fixed pitch circle, marked '40' in Fig. 2.16, the path traced by the point '42' in Fig. 2.16 within the rolling circle describes a curtate epicycloid. According to Braren (1932) and Beard et Al. (1992), different curves can be generated depending on the distance between point 42 and the centre of circle 41; when such distance is shorter than the radius of circle 41 then the defined curve is called curtate. If point 42 lies on the perimeter of circle 41 the curve is defined normal otherwise, if the distance is greater than the radius of circle 41, the created curve is a prolate epicycloid. The speed ratio of the transmission is independent from the position of point 42 as it defined by the ratio of the diameter of the pitch circle 40 to that of the rolling circle 41. Such ratio should be a whole number, otherwise the locus of the point 42 would not form a closed profile and the resulting geometry would be unusable for mechanical applications (Braren, 1932). In Braren's design an equidistant curve to the original curtate profile is used in order to generate a prolate curve that represents the actual tooth working profile. The parameter defined "equidistant" corresponds to the annulus pin radius as shown in Figure 2.16 and is chosen such that the profile of the curve generated causes an appropriate tooth profile to mesh with the pins of the ring gear. Braren used the prolate form of the curve because of its advantageous geometry

given by the absence of cusps and consequently the absence of single line contacts between the tooth profile and its conjugate pin.

Annulus pins are cantilever beams type with one end secured to the annulus member and the other end free for meshing with the tooth profiles of the cycloidal discs as shown in Figure 2.15. A support ring between the two discs is recommended for higher loads to assist in balancing the load on the pins (Braren, 1928).

Although other patents have been published, Braren's design still represents a valid guideline for the design of cycloidal transmission systems. An increasing number of research works have been conducted in order to define the geometrical and performance characteristics of cycloidal drives.

With regards to the geometry of cycloidal drives, Litvin gave a major contribution to the field by writing rigid body equations using coordinate transformation (Litvin, 1989; Litvin et Al., 1998; Litvin et Al., 2004). This method has been utilised by several researchers for generating meshing equations and determine the actual cycloidal profile by taking under consideration annulus pins and eccentricity which guarantees an interference-free geometry. Litvin (2004) named the geometrical configuration of cycloidal gearing as "overcentrode cycloidal gearing" by the fact that cycloidal disk lobes are displaced with respect to the gear centrodes. In another publication Litvin et Al. (1996) covered the generation of cycloidal gearings geometry and focuses on the characteristics of such geometry in order to avoid profile and surface singularities. The determination of the cycloidal curve is indirectly determined by considering simultaneously the mating surface and the equation of meshing; from this, the curve conjugate to the annulus pins is determined. The authors investigated the presence of singularities in the cycloidal profile as they represent an unacceptable condition for working applications. The proposed mathematical formulation enables to determine the limiting value of the radius of curvature in order to avoid profile singularities.

Yan et Al. (2002) have used the approach proposed by Litvin for the design of a cycloidal gear train with cylindrical tooth profile. By means of coordinate transformation and the equation of meshing the most appropriate geometry for the annulus/internal gear was defined and used for the generation of a solid model.

Hwang et Al. (2006) have illustrated the envelope theorem for the geometric design of a cycloidal speed reducer. The mathematical model for the pin-wheel meshing has been formulated using coordinate transformation and the envelope theorem. The curvature of the epicycloidal profile was analysed by first considering the curvature of the prolate epicycloid and then deriving the equation of curvature for the cycloidal wheel profile. The authors in a companion research work (Hwang et Al. (2007) have investigated the presence of singular points and the presence of undercutting on the cycloidal wheel profile. This approach has allowed the authors to determine a preliminary feasible design region of which the boundaries consist of undercutting curve and line of maximum pin radius.

With regards to the definition of the lobe profiles Shin and Kwon proposed an analytical approach based on the principle of the instant velocity centre and the homogeneous coordinate transformation. Their calculations are based on Kennedy's theorem (Shigley et Al., 2003) and determine the condition of absence of sliding between bodies in relative motion. The presence of sliding, as asserted by Hwang (2007), is indication of undercutting. By applying the method of instant velocity centres Shin et Al. (2006) were able to determine a limiting condition for the eccentricity e_0 so that:

$$e_0 < \frac{r}{N_p} \qquad 2.2$$

The developed design methodology has then been implemented in a computer-aided design program and different examples of cycloidal drives have been presented.

The review of the available literature on cycloidal drives continues by focusing on the performance analysis of this category of devices. The most relevant content is summarised below.

Hwang et Al. (2006) have used an analytical approach to define the forces shared between annulus pins and cycloidal wheel at the contact interface. The authors assert that the contact forces between annulus pins and cycloidal wheel are oriented in the direction of the common normal to the contacting surfaces. Moreover, even if all the annulus pins are in tangency with the cycloidal wheel at the same time, only half can be under load and if tolerances and manufacturing/assembling deviations are considered,

less than half would be able to transmit the load. The effect of tolerances on the contact force distribution among pins has been further investigated by Blagojevic (2014). The author proposed an analytical procedure for the calculation of the maximum deformations experienced by the cycloidal disk subjected to load. Based on the direct proportion between contact force and amount of deformation, considerations on the effect of clearances between the cycloidal disk and the annulus pins on shared loads and total number of pins in simultaneous contact were made. The results have shown that the amount of deformation experienced by the cycloidal disk is inversely proportional to the facewidth. Deformation is a periodic function of time given the meshing process of mating components; the number of pins in contact is inversely proportional to the amount of clearance applied and decreases if clearance increases. A similar study was conducted by Tsetserukou et Al. (2015 in which the effect of machining tolerances on the contact force distribution was evaluated. The results of the study show that the most loaded pin, in the case of applied tolerances, is subjected to a 42% increase of normal force compared to the case of nominal profile.

Once the force distribution acting on the cycloidal disk has been assessed the natural consequence is the analysis of the stress state occurring on loaded components for a performance evaluation. Blagojevic et Al. (2014) have investigated the stress state of the cycloidal disk using numerical and experimental methods. The stress state analysis was realised using Finite Element Method. As the analysis regarded only the cycloidal disk, fixed supports were applied at the centre and a Force was applied normally to the convex portion of the cycloidal profile. The applied loading simulated a single tooth meshing condition which never happens in reality for this category of devices. Maximum Equivalent stress occurred in the area where the force was applied and it was almost entirely addressed to contact stress to the point that bending stress was neglected. This was addressed to the favourable geometry of cycloidal disks with a large tooth base thickness and a high radius of curvature. Numerical stress values were validated with experimental tests on a cycloidal disk model. Numerical and experimental results have resulted being in very good agreement.

Jiang et Al (2015) have modelled a cycloidal transmission by means of the commercial

Finite Element software Ansys® (2016). The authors aimed to analyse the load carrying capacity of a cycloidal drive by evaluating the stress distribution and the maximum value of stress occurring on the mating components. To do so, a 3D model including the cycloidal wheel and the annulus pins was created and subjected to applied loads and boundary conditions. In order to simplify the simulation, the movement of the cycloidal disk was approximated with simple rotation, neglecting the effect given by the eccentric input shaft. Results have shown a distribution of stress in the area where multiple pin contact occurs with maximum values always below the allowable strength of the material. Accuracy of results in this case is affected by the applied boundary conditions which not represents the real kinematics of the system.

Another research work based on the numerical analysis of a cycloidal transmission was made by Thube et Al. (2012) at Sumitomo Drive Technologies. The paper discusses the stress distribution occurring on the cycloidal disk and annulus pins for nominal and shock loading conditions. In this case the model was constrained such a way that the cycloidal disk was able to replicate the characteristic wobbling motion due to the interaction with the eccentric shaft and the annulus pins. A constant input speed of 1800 rpm and a moment of 135 Nm were applied to the input shaft. The time duration of the simulation was set for 360° rotation of the input shaft and the time duration was divided in time increments in order to achieve a resolution of 2° rotations. Results have shown that the cycloidal disk shares load with 5 over a total 16 annulus pins. For shock loading conditions of 500% the nominal load, the maximum stress value recorded results only 38% higher than the one evaluated for nominal conditions. The reaction forces acting on the annulus pins have shown that with a higher load applied more pins are in simultaneous contact. This confirm the ability of cycloidal drives to withstand shock loading conditions. Results show the general trend over the entire mesh cycle; due to the low resolution they are not able to capture variation of load and stress within small intervals.

Cycloidal drives are currently becoming more popular in industrial applications, due to the ease of production of complex curves with Computer Numerically Controlled (CNC) machines. Some manufacturers have included the Cycloidal drive transmissions in their product range.

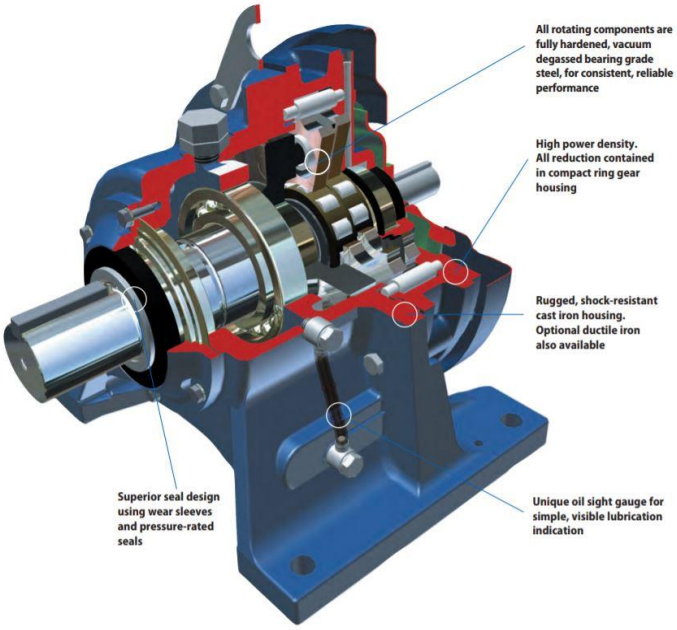

Figure 2.17 - Sumitomo's "Cyclodrive"; section view of a single stage "Cyclo 6000" transmission (Sumitomo Drive Technologies, 2017).

Sumitomo Heavy Industries is a well-known producer of Cycloidal drives and Cycloidal gear motors. General purpose Cycloidal drives are sold by Sumitomo under the commercial terms "Cyclo" and an example is shown in Figure 2.17. Cycloidal drives are available with speed ratios in the range of 6:1 to 119:1 for single stage reduction units. Ratios in a range of 104:1 and 7569:1 are presented in double stage Cycloidal reduction units. The entire product range spans 23 sizes with torque ratings between 55 lb in and 603000 lb in.

Several advantages of cycloidal drives are listed below:

- High Efficiency: SM Cyclo is reported to have about 95% efficiency rating for a single stage unit and about 85% for a double stage configuration. The reason is addressed to the pure rolling contact between internal components with consequent reduction of friction and operating wear.
- Compact Size: since the Cycloidal drive is a high ratio drive, very high ratios can be easily achieved in single stage configurations. The small number of parts involved in the Cycloidal drive mechanism limits the overall size making cycloidal as very high torque density speed reducers.
- Sumitomo claims that Cycloidal drives are able to withstand 500% Shock over loading conditions. This is addressed to the multiple contacts

occurring between at least 30% of the lobes with the mating annulus pins. Moreover, the components are loaded in compression rather than in tension, which eliminates the possibility of tooth shearing due to shock overload.

- Overall economy: Cycloidal drives offer several advantages starting from a low initial cost, high reliability, working life up to 50,000 hours of operation with negligible component wear, minimum maintenance.
- Capacity for frequent Start-Stop and severe reversing: The low inertia makes the drive respond quickly to changing loading conditions. Shear free profiles have less wear rate.
- Silent operating conditions due to the reduced speed of internal components combined with rolling motion with minimal or no sliding.
- All are grease lubricated for life except a few high torque versions which need regular re-greasing.

Similar characteristics to the ones listed above are given by other cycloidal drives manufacturers such as Nabtesco and Darali confirming the mechanical advantages provided by this class of transmission devices (Nabtesco Corporation, 2016; Sumitomo Drive Technologies, 2017).

2.4 Available Design Standards

Many international standards have been published to guide gear design and manufacturing procedures. Gear design and analysis methods are standardised by many international Organisations such as AGMA (American Gear Manufacturers Association), ISO (International Standard Organization), JIS (Japanese Industrial Standard) and DIN (Deutsches Institut fur Normung) to standardise the various aspects of gear design. Currently the most popular are those published by the International Standard Organization (ISO) developed over the years in Europe, and by the American Gear Manufacturer Association (AGMA) developed in the US (ANSI/AGMA 2101/D04, 2016; ISO 6336, 2006). ISO 6336 standard was first published in 1996 and then has been revised on several occasions and republished in 2006 with considerable improvements.

ISO 6336 consists of the following parts: 6336-1:2006 Basic principles, introduction and general influence factors 6336-2:2006 Calculation of surface durability (pitting) 6336-3:2006 Calculation of tooth bending strength 6336-5:2003 Strength and quality of materials 6336-6:2006 Calculation of service life under variable load. AGMA published the first standard in 1982. The content has continuously been updated and revised until the last edition AGMA 2101-D04 of 2016. Both the standards provide formulas applicable for rating the pitting resistance and bending strength of internal and external spur and helical involute gear teeth operating on parallel axes. The formulas estimate gear tooth capacity as influenced by the major factors which affect gear tooth pitting and gear tooth fracture at the critical section. The models described in ISO and AGMA present some similarities but are not identical. Both are based on theoretical and experimental research but also industrial practice in the field. The two standards have critical geometrical and performance parameters different from each other and also the estimation of those parameters is based on different assumptions and mathematical relations. These differences determine a discrepancy of results obtained according to the ISO and the AGMA standards under the same conditions as revealed by Kawalec et Al. (2006) and Lisle et Al. (2017). Both the standards indicate the finite element method as the most precise way to compute gear tooth strength.

The design of epicyclic gear trains is guided by the ANSI/AGMA 6123-B06 (2006) a dedicated design standard published by AGMA and titled Design Manual for Enclosed Epicyclic Gear Drives. The European Organisation ISO gives indications for the design of epicyclic gear trains in the ISO 6336 (2006) standard dedicated to spur and helical gears.

Cycloidal drives are relatively new in the field of mechanical transmission. The only standard for Composite Cycloidal toothed gears (watch gears) is under the British Standard BS978 Part 2 1984: Specification for fine pitch gears – Cycloidal type gears (BS 978 - 2 1984:978).

2.5 Knowledge gaps in literature review

In the undertaken literature review it has emerged that the research on gears geometry and performance mainly follows two different currents; while one focuses on the effect of macro geometrical factors such as module or number of teeth, the other aims to

improve the tooth mesh characteristics by applying micro modifications such as profile relief and crowning. In the vast literature available, a considerably small number of works focuses on the modification of the tooth profile geometry. This can be addressed to the reluctance of gear designer and manufacturer to move away from the established standards and develop new and custom products with enhanced performance suited to the specific applications.

The recent advent of asymmetric gears has brought to attention the beneficial effect of high pressure angle gears compared to the standard 20° or 25°; contact and bending stress are drastically reduced with the use of high values of pressure angles and gear performance increase as a direct consequence. Despite this, the use of high pressure angles in symmetric spur gears is not common and few research works have been published on the topic. Other geometrical factors such as addendum and dedendum and their effect on gear performance has rarely been taken under consideration. In the available literature, researchers are prone to alter more parameters per time limiting the understanding of the properties of each single geometrical parameter. This suggested the need of a comprehensive analysis of the effect that geometrical profile modifications have on gear performance.

Epicyclic gear configurations have been the focus of much research given the favourable mechanical characteristics of such systems. Despite the large amount of literature available on epicyclic transmissions, there is very little information about applications with low rotational speed and high levels of transmitted torque. For these specific conditions the only dedicated design standard ANSI/AGMA 6123-B06 (2006) confirms the knowledge gap, underlining the necessity of undertaking a detailed engineering study to satisfy the requirements for design of epicyclic devices. In the literature available on the topic, the time-varying stress distribution on the epicyclic gear train components has not been found. Moreover, there is no mention regarding the use of symmetric gears designed with non-standard parameters for the use in epicyclic drives. A design tool that allows the designer to select the most appropriate profile geometrical parameters for the use in epicyclic arrangements is missing.

With regards to cycloidal transmissions, the literature survey has shown that while some works have been done with regards to the geometry definition and geometrical characteristics of the cycloidal profile, very few publications are available addressing static and dynamic problems of cycloidal transmissions. The available literature on the topic focuses on the force distribution and the evaluation of stresses acting on the cycloidal disk and annulus pins. In general, the amount of available material is very small compared to the vast amount of documents available for gears and gear transmissions. These considerations suggest the necessity of undertaking research campaigns focused on the statics and dynamics of cycloidal devices in order to gain the necessary knowledge for further develop this class of devices with such unique characteristics.

3 Gear tooth geometry

The tooth profiles in reciprocal mesh need to have certain geometrical characteristics in order to guarantee a constant and smooth energy transfer while rotating. At the base of a gearing concept is the need to transfer power from one member to the other by maintaining a constant velocity ratio. A couple of friction disks would ensure a smooth and accurate transmission with the angular velocities inversely proportional to the diameters of the cylinders. This arrangement has an obvious limit with regards to the transmitted power and the occurrence of slippage. Similar to the friction disks, mating gears roll without slipping on their pitch diameters producing a pure rolling motion. Since the contact occurs between mating teeth, their geometry has to be designed so that a constant velocity ratio is maintained during meshing; this condition is achieved only if the profiles in contact satisfy the law of gearing. To this end, the common normal to the tooth profiles at the point of contact must pass through the pitch point of the two mating surfaces (Litvin et Al., 2004). The curves that satisfy such a condition are called conjugate profiles. Within the vast range of possible curves that satisfy this condition, the involute geometry has been almost universally utilised for geared applications. The reasons for its diffusion are addressed to the ease in manufacturing, and more importantly to the singular property of this geometry to guarantee a constant ratio even in presence of an alteration of distance between the mating surfaces. In order to explain the contact action between conjugate surfaces, the geometry shown in Figure 3.1 will be considered as follows:

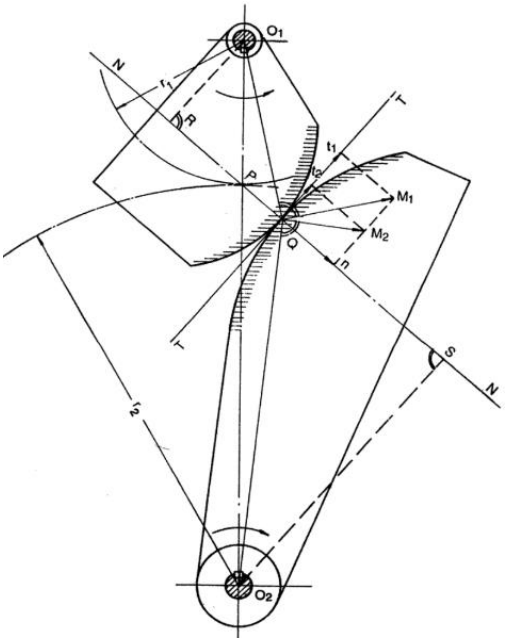

Figure 3.1 – Contact between two rigid bodies with conjugate surfaces realising the fundamental law of gearing (Maitra, 2013).

The rigid bodies of Figure 3.1, which rotate about fixed centres O_1 and O_2 with angular velocities ω_1 and ω_2, touch at the instantaneous point of contact, C, where the two surfaces are tangential to each other. From there, the common tangent $\overline{TT}$ and the common normal $\overline{NN}$ at C can be drawn. As the transmission of forces takes place along $\overline{NN}$, this line is also called the line of action. $\overline{NN}$ Intersects the line that connects the fixed centres $\overline{O_1O_2}$ at point P. P is the pitch point where the pure rolling motion occurs. For a constant angular velocity ratio, P stays stationary at a fixed point and the line of action, for every instantaneous point of contact, passes through P. In the case of involute profiles all the points of contact take place on the line of action $\overline{NN}$ during the mesh cycle. Since all the normals to the tooth profiles coincide with the line $\overline{NN}$, the law of gearing is satisfied. According to the Lewis theorem (Litvin et Al., 2004; Radzevich, 2012), P divides the line of centres into two segments $\overline{O_1P}$ and $\overline{O_2P}$ that determine the velocity ratio *i* as follows:

$$\frac{\overline{O_2P}}{\overline{O_1P}} = \frac{\omega_2}{\omega_1} = i \qquad 3.1$$

Segments $\overline{O_1P}$ and $\overline{O_2P}$ are also the radii of two circles having centres at O_1, and O_2, called pitch circles, that work as reference parameters of the two gears. Although the

gear mesh is kinematically equivalent to two friction disks, the gear teeth actually move with a combined rolling and sliding motion. Vectors $M_1=\omega_1 r_1$ and $M_2=\omega_2 r_2$ represent the instantaneous velocity vectors of which t_1, t_2 and n_1, n_2 are tangential and normal components. Since the two bodies are rigid, the velocity along the line of action has to be the same so that $n_1=n_2=n$. While n has a constant value during the mesh cycle, components t_1 and t_2 vary with the position of point Q along $\overline{NN}$ and their difference t_1-t_2 gives the amount of relative sliding velocity between tooth flanks in contact. It is interesting to notice that when the contact occurs at the pitch point so that Q≡P, M_1= M_2 and consequently t_1-t_2=0 indicating pure rolling motion between the two gears (Maitra, 2012; Radzevich, 2012).

3.1 Involute tooth geometry

The tooth profile can be considered as the combination of four curves as shown in Figure 3.2. The part of the tooth flank where contact occurs has an involute shape that is limited by the tip circle at the intersection with the outer diameter, and by the trochoidal fillet at the form diameter where the transition between the usable involute profile and the fillet of the tooth occurs (Gerpen et Al., 1989; Thurman, 1999). The fillet has a trochoidal shape and is delimited by the involute curve on one side and by the root circle on the other. During the generation of the envelope of the two conjugate surfaces, i.e. the cutting tool and the gear blank, the straight side of the rack generates the involute curve, and the rack fillet generates the gear fillet. Moreover, the dedendum circle is generated by the straight line consisting of the rack tooth tip while the addendum circle, if full length profiles are considered, is automatically generated as result of the enveloping process.

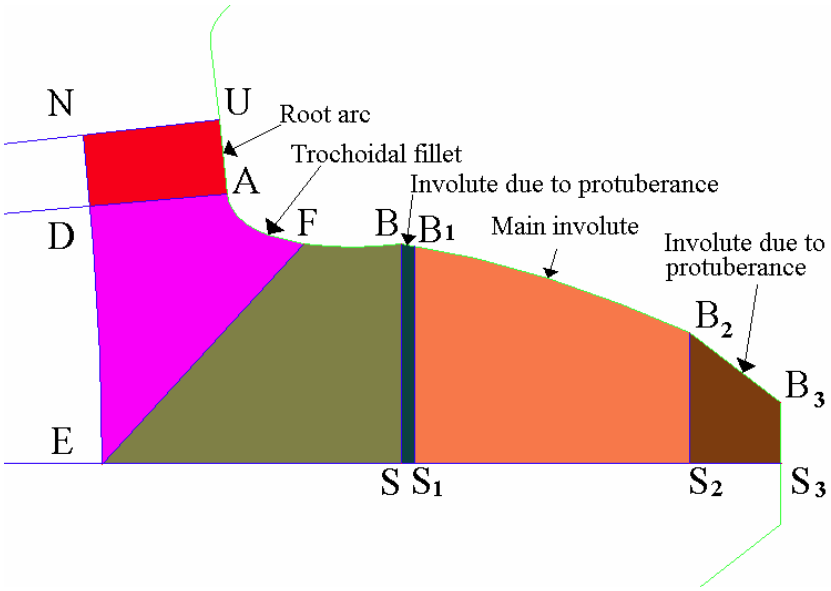

Figure 3.2 - Sequence of curves that generate a spur gear tooth profile (Bonori, 2005).

3.1.1 Involute curve

The geometry of involute curves is a particular case of conjugate profiles and is described by the trajectory of a point lying on a string that rolls without slipping on a circular geometry called the base circle (Maitra, 2012). For manufacturing purposes, the process has been engineered by means of a rack cutter having straight sides that rolling without slipping on the gear blank generates the gear profile as shown in Figures 3.4 and 3.5. At the common point of tangency, the two surfaces experience a pure rolling motion so that an amount of rotation for the gear corresponds to an amount of translation of the rack cutter. The rack cutter pitch line is in continuous tangency to a point of the gear blank that satisfies the condition of enveloped surfaces.

Figure 3.3 shows a graphical representation of the geometrical construction of the involute curve starting from the base circle of radius r_b being generated by the pure rolling motion of the string $\overline{cb}$ on r_b.

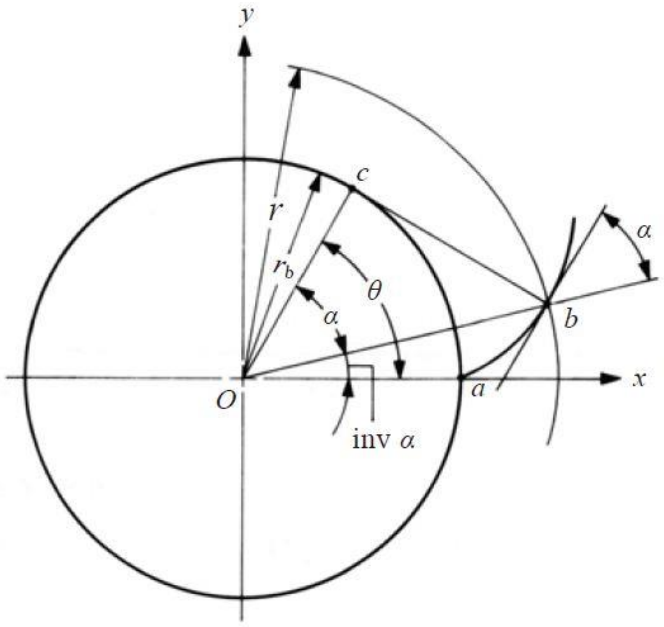

Figure 3.3 – Geometrical construction of an involute curve (KHK, 2015).

In order to derive the analytical description of the involute curve, the function represented by $inv\alpha$ in Figure 3.3 has to be defined. Starting with a point b on the tooth profile that lies on the pitch circle of radius r, and by connecting b with point c, results in a line $\overline{bc}$ being always tangential to the base circle while the angle of rotation, θ varies from 0 to θ_{max}. The rotation angle relative to point b is a variable that allows to describe the involute curve. By considering the triangle $\widehat{Ocb}$ and the parameter θ, trigonometric considerations yield:

$$\overline{Ob} = \overline{Oc} + \overline{cb} \tag{3.2}$$

$$x_c = r_b \cos\theta \tag{3.3}$$

$$y_c = r_b \sin\theta \tag{3.4}$$

$$x_b = x_c + \overline{cb} \sin\theta \tag{3.5}$$

$$y_b = y_c - \overline{cb} \cos\theta \tag{3.6}$$

For the peculiar property of involute curves, $\overline{cb} = \widehat{ca}$ in length and by geometrical considerations relative to Figure 3.3 the following relation can be written:

$$\overline{cb} = \widehat{ca} = r_b\theta \tag{3.7}$$

$$x_b = r_b \cos\theta + \overline{cb} \sin\theta \tag{3.8}$$

$$y_b = r_b \sin\theta - \overline{cb} \cos\theta \tag{3.9}$$

and a Cartesian representation of point b can be calculated:

$$x_b = r_b \left[\cos\theta + \theta \sin\theta\right] \tag{3.10}$$

$$y_b = r_b \left[\sin\theta - \theta \cos\theta\right] \tag{3.11}$$

In order to find the expression of the involute angle $inv\alpha$ relative to point b, the relation between $\overline{cb}$ and α has to be considered:

$$\overline{cb} = \widehat{ca} = r_b \tan\alpha \tag{3.12}$$

And by considering Equation 3.7 and that $\theta = \alpha + inv\alpha$ this yields:

$$r_b(\alpha + inv\alpha\ ) = r_b \tan\alpha \tag{3.13}$$

hence:

$$inv\alpha = \tan\alpha - \alpha \tag{3.14}$$

Other expressions of the involute curve can be determined by using the involute function $inv\alpha$ and the variable parameter α in Figure 3.3 as follows:

$$x_b = \frac{r_b \cos inv\alpha}{\cos\alpha} \tag{3.15}$$

$$y_b = \frac{r_b \sin inv\alpha}{\cos\alpha} \tag{3.16}$$

From an engineering point of view, for the application of involutes in gears, it is interesting to note that the segment $\overline{bc}$ represent the instantaneous radius of curvature

along the tooth flank and α is the pressure angle at the considered point. If point b lies on the pitch circle then α is the reference pressure angle.

3.1.2 Trochoidal curve

The fillet of a gear tooth has a trochoidal profile generated by the tip corner of the rack cutter during the envelope of rack and gear blank. The root fillet does not take part in the kinematics of the gears but does play a fundamental role for the strength of the gears. The root fillet is the area of maximum bending stress where stress concentration factors, due to the highly curved profile, occur. An accurate representation of the root fillet is necessary to numerically predict the strength of loaded gears. Two reference systems have to be defined, x_0, y_0 attached to the rack cutter in order to define coordinates of the cutter profile with respect to the pitch point P and another, x,y attached to the centre of the gear, as shown in Figure 3.4. By considering the position of point Q on the rack tool which is offset from P by x_0 and y_0, in the reference system x,y connected to the gear blank, it yields:

$$x = r + x_0 \tag{3.17}$$

$$y = rt + y_0 \tag{3.18}$$

which implies the condition of pure rolling motion at point P.

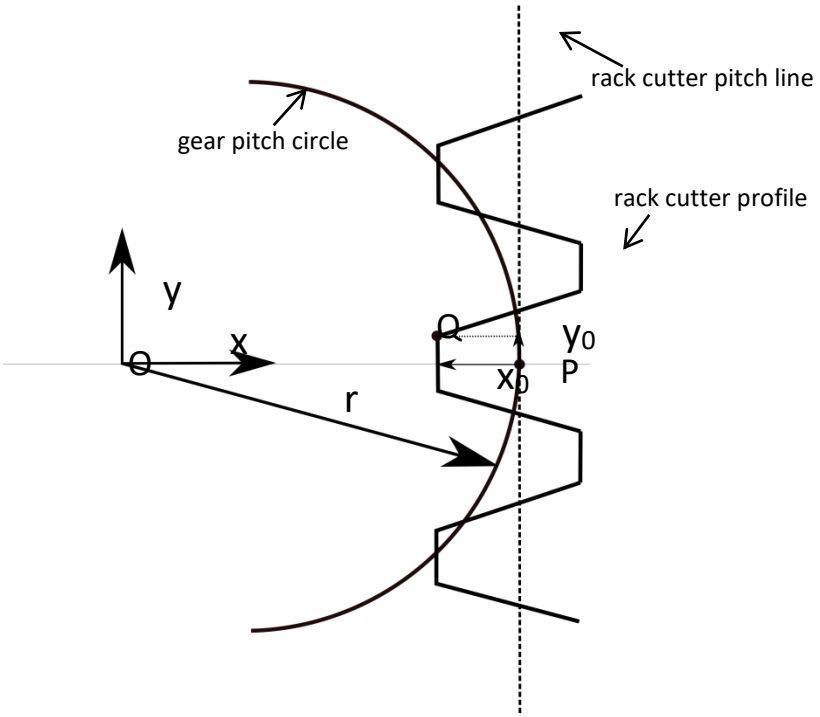

Figure 3.4 – Simplified geometry of the rack tool with the pitch line tangent to the pitch circle of the gear being cut at the starting position.

The trochoidal geometry of the tooth root is determined by tracing the trajectory of any point that lies on the edge of the rack cutter. For its generation, the enveloping motion described above for the involute profile, can be simplified with a rotation/translation of the rack cutter. The translation rt of the rack cutter and the rotation angle t of the gear blank in Figure 3.5a are simplified by only moving the rack cutter with a rotation/translation compound motion. To do so, the entire system is rotated about the origin O by an angle t. As a result, the gear returns to its default position while the rack

rolls without slipping around the stationary gear's pitch circle as shown in Figure 3.5b.

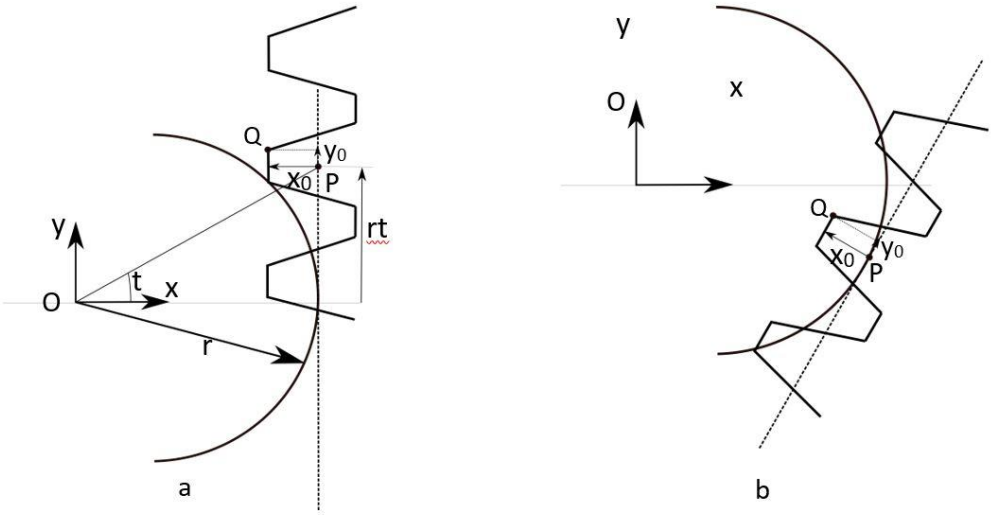

Figure 3.5 – a) first motion of the system: translation of the cutter and rotation of the gear blank; b) second component of motion: the whole system is rotated about the origin O of an angle t.

To find the position of point Q in the new configuration it is necessary to multiply Equations 3.10 and 3.11 by a clockwise rotation matrix (Litvin et ALl., 2004):

$$\begin{bmatrix} \cos t & \sin t \\ -\sin t & \cos t \end{bmatrix} \tag{3.19}$$

And considering the local coordinates of point Q:

$$x_0 = -1.25\,m \tag{3.20}$$

$$y_0 = -\frac{1}{4}\,\pi m + 1.25\,m\,\tan\alpha \tag{3.21}$$

the final parametric equation for the trochoidal fillet curve is:

$$x(t) = (r - 1.25m)\cos t + \left(rt - \frac{1}{4}\pi m + 1.25m\tan\alpha\right)\sin t \tag{3.22}$$

$$y(t) = -(r - 1.25m)\sin t + \left(rt - \frac{1}{4}\pi m + 1.25m\tan\alpha\right)\cos t \qquad 3.23$$

The involute and fillet tooth profile equations can be found in a number of references (Alaci et Al., 2008; Anon, 2014; Fetvaci, 2012; Litvin, 1989; Litvin et Al., 1998; Litvin et Al., 2004; Litvin et Al., 1993; Litvin et Al, 1996; Moya et Al., 2009; Simionescu, 2008).

3.2 Spur gear design parameters

The gear generating process based on the rack cutter implies the dependency of the generated tooth profiles on the geometry of the cutting tool shown in Figure 3.6. Within the involute system many variations of tooth form are possible by varying the proportions of the rack tooth profile. Each side of the rack geometry is a straight line which is a unique case of the involute curve with an infinite base circle diameter.

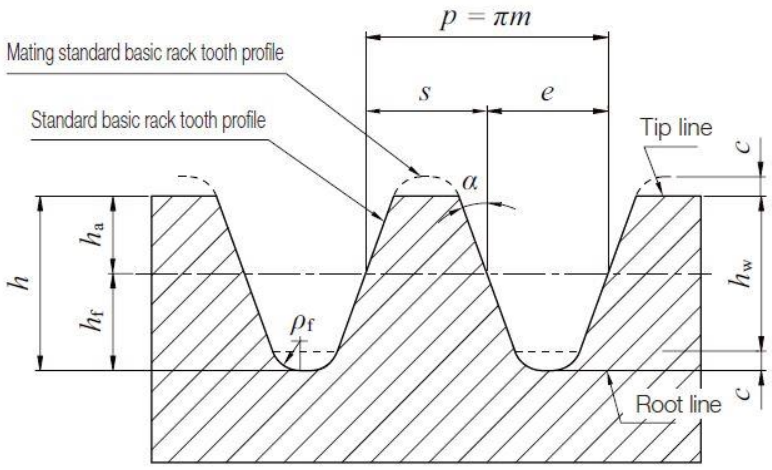

Figure 3.6 – Basic metric rack geometrical parameters (KHK, 2015).

Gear design in the metric system is based on modular proportioning which takes the module as the main parameter and relates all the relevant dimensions to it. The module refers to the gear tooth size and is defined as the ratio between the circular pitch at the reference diameter and π:

$$m = \frac{p}{\pi} \qquad 3.24$$

where the circular pitch p is:

$$p = \frac{2\pi r}{N} \tag{3.25}$$

It follows that the reference diameter d is:

$$d = mN \tag{3.26}$$

In the modular proportioning system, the quantities such as addendum, dedendum and cutter tip radius are expressed by coefficients related to the module. In this way m works as a scale factor for the geometry of the cutter (Figure 3.7), and hence for the gear that derives from it. Standard values for the module are available in ISO 54 (1996). This International Standard specifies the values of normal modules for straight and helical gears for general engineering and for heavy engineering.

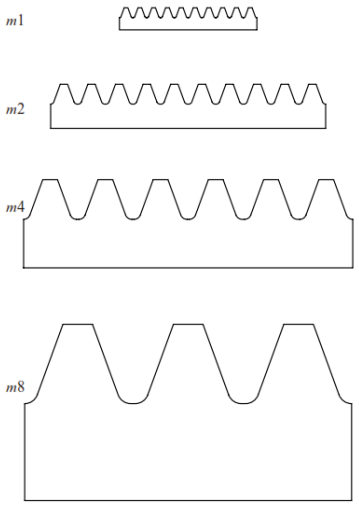

Figure 3.7 – Basic rack geometries as function of the module (KHK, 2015)

Tooth profiles are limited by the external circle of radius r_a at the tip and the internal circle of radius r_f at the root. Given the pitch circle that is considered and the reference geometry, the radial distance between the tip and pitch circle is called addendum and is defined as h_a. On the other hand, the radial distance between the pitch and root circles is called the dedendum and defined as h_f. The values of addendum and dedendum have been standardised with the following quantities:

$$h_a = m \qquad h_f = 1.25\, m \tag{3.27}$$

The complete geometry of an involute profile needs the specification of a pressure angle α and cutter tip radius coefficient ρ_f. Values of pressure angle commonly used in industry are 14.5°, 20° and 25° with the 20° being the most popular. The two extreme choices give a solution respectively for applications where high contact ratio (less noise production), or high strength (high power transmission) are required, while the 20° solution is an acceptable compromise between the two. Regarding cutter tip radius, the standard ISO 53 (1998) reports three standard profiles with different tip radius coefficents, ρ_f as follows:

1.25/0.38/1 ISO 53: 1998 Profile A

1.25/0.30/1 ISO 53: 1998 Profile B

1.25/0.25/1 ISO 53: 1998 Profile C

As specified in the ISO 53, small cutter tip radii are for fine pitch gears with modules below 1.25 while for coarse pitch gears a value of 0.38 is recommended. These values are given only for a pressure angle of 20° while there is no mention for other pressure angle. Figure 3.8 shows the mentioned parameters.

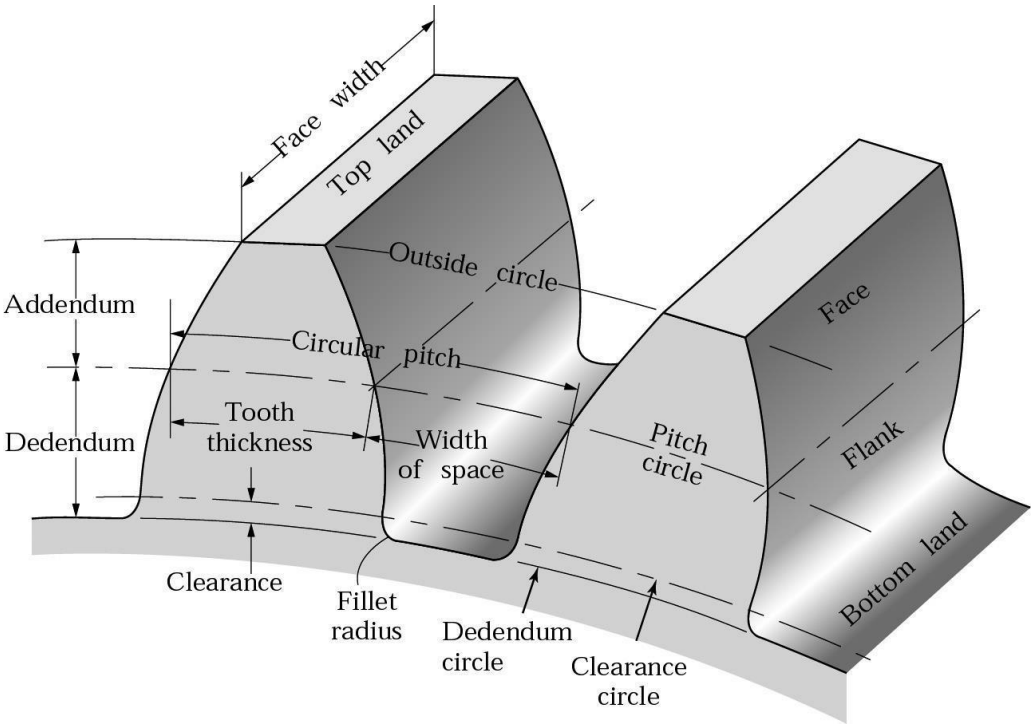

Figure 3.8 – Nomenclature of a spur gear (Shigley et Al., 2003)

When a modification to one of the values listed above is introduced the tooth profile is not considered standard anymore and is termed as corrected.

In the following sections a detailed description of the geometrical values relevant to this study is given. It should be pointed out that cutter tip radius does not take part in this work given that tooth profiles here have circular root fillets.

3.2.1 Addendum factor

The variation of the addendum length can be considered as a pure geometrical alteration. The tooling cutter has to be designed with the required addendum factor, h_a, in order to produce a longer or shorter tooth in the region above the pitch circle. The effective addendum modification in mm H_a is the product of the factor, h_a, and the module m. For standard proportions $h_a=1$ and so $H_a=m$. A modification to the addendum determines a variation of the tip circle diameter as the involute portion above the pitch circle is prolonged or shortened respectively for $H_a>m$ or $H_a<m$. Figure 3.9 shows a comparison between tooth profiles generated with the same proportions, but with variations in the addendum factor. It can be seen that tooth thickness is constant for any of the addendum factors used while it varies in relation to the tip geometry. By

increasing h_a the top land thickness s_a decreases resulting in a more pointed geometry. On the other end, a decrease of h_a determines a thicker profile at the tip as a portion of the involute curve has been truncated.

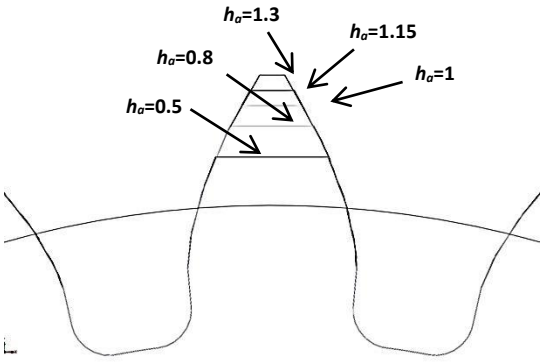

Figure 3.9 – Effect of addendum factor h_a modification on the tooth geometry.

3.2.2 Dedendum factor

Dedendum modification can be considered the reciprocal of addendum modification as in this case the alteration involves the part of the involute below the pitch circle. The tooling cutter geometry is modified in order to increase or reduce the depth of the cut on the gear blank. As for the case of the addendum, the effective dedendum length in mm H_f is the product of a factor h_f times the module m. For standard proportions h_f=1.25, that yields $H_f=1.25*m$. While the addendum modification operates on the tip diameter, the dedendum modification affects the other boundary that defines the tooth profile, the root circle. An increase of h_f determines a deeper cut and consequently a reduction of the root diameter. Inversely, for values of Hf<1.25*m the cut would be less pronounced and the root circle diameter bigger. Figure 3.10 shows a comparison between three profiles with different dedendum modifications. It can be seen that while the geometry of the upper part of the tooth remains unchanged, as H_f varies from H_f=1*m to H_f=1.5*m, the tooth section in proximity of the root becomes narrower. This modification does not affect the involute length because it occurs below the start of the active profile.

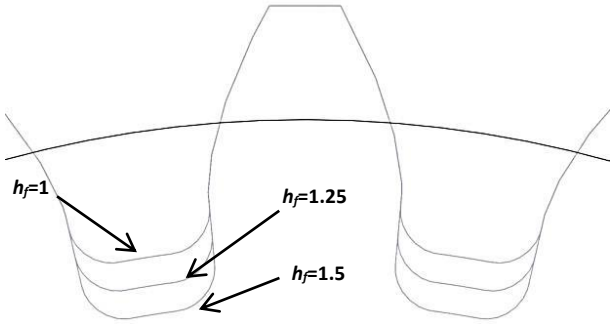

Figure 3.10 – Effect of dedendum factor h_f modification on the tooth geometry.

3.2.3 Profile shift (X)

Profile shift is the most common modification feature in gear production and is applied at the manufacturing stage without requiring a specific cutting tool. Profile shift is generally called addendum modification due to its effect on the outside diameter of gears. In reality both addendum and dedendum are simultaneously affected by applying a so called profile shift, whether positive or negative. The effective length in [mm] of the two quantities follows the relations:

$$H_a = m * (h_a + x) \qquad H_f = m * (h_f - x) \tag{3.28}$$

Profile shift is used to alter standard proportions of gears, namely gear thickness. In gear design, profile shift is mainly used to adjust centre distance, avoid the undercutting condition, and balance the stress levels between pinion and gear. The actual quantity in [mm] of profile shift is given by *X* and is determined by the dimensionless profile shift coefficient *x* times module *m*. The modification consists in shifting the generating tool radially, so that the tooth profile will also be shifted towards the gear centre; this means shifting the pitch line with respect to the reference pitch line. In this new configuration the gear pitch circle rolls without slipping on a new pitch line, parallel to the reference one with a X=*x*m* [mm] offset. A shift in the direction of bigger radii is defined positive, inversely it is defined negative. By shifting the teeth outward or inward, the active profile lies on a different portion of the involute generated from the same base circle. Figure 3.11 shows side by side a standard gear and a modified profile created with a positive profile shift.

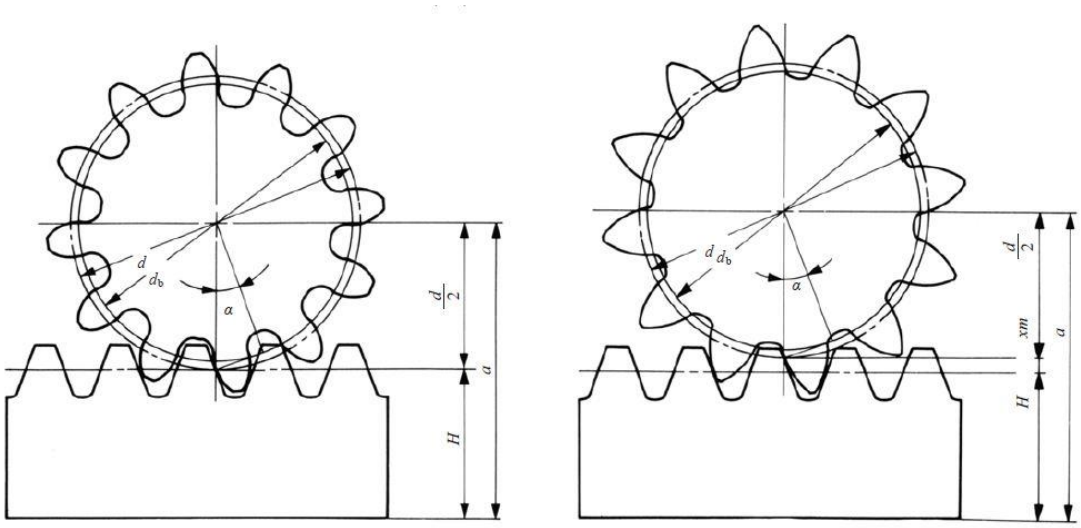

Figure 3.11 – Comparison between a) standard gear-rack mesh and b) with a positive profile shift applied; source (KHK, 2015).

The main change due to the profile shift is related to the variation of the tooth thickness that will be increased for positive shifts and reduced for negative shifts. The tooth thickness at the new generating pitch circle becomes:

$$S = \frac{m\pi}{2} + 2xm\tan\alpha \qquad 3.29$$

Such a variation implies the shift of the mating gear centre in order to compensate for the tooth thickness variation and allow a correct mesh. This condition makes the two modified gears work on a different diameter called the operating diameter. In Figure 3.12 a tooth profile with a positive modification is compared with a standard profile. Since the profile pressure angle varies continuously along the tooth flank, the pressure angle at the operating diameter is different than the one at the reference diameter and is called the operating or working pressure angle α_w. Moreover, an increase in the radius of curvature as the diameter changes from reference to operating is seen in Figure 3.12. The modified radius of curvature R', between the point of tangency T and A' that lies on the operating pitch circle is longer than the radius of curvature, *R*, that occurs for standard profiles. The calculation of the profile shift coefficient is strictly related to the gear geometry and application. The two standards ISO/TR 4467 (1982) and ISO 21771 (2007) give indications on the amount of profile shift and its distribution among the two mating gears depending on geometry and loading conditions.

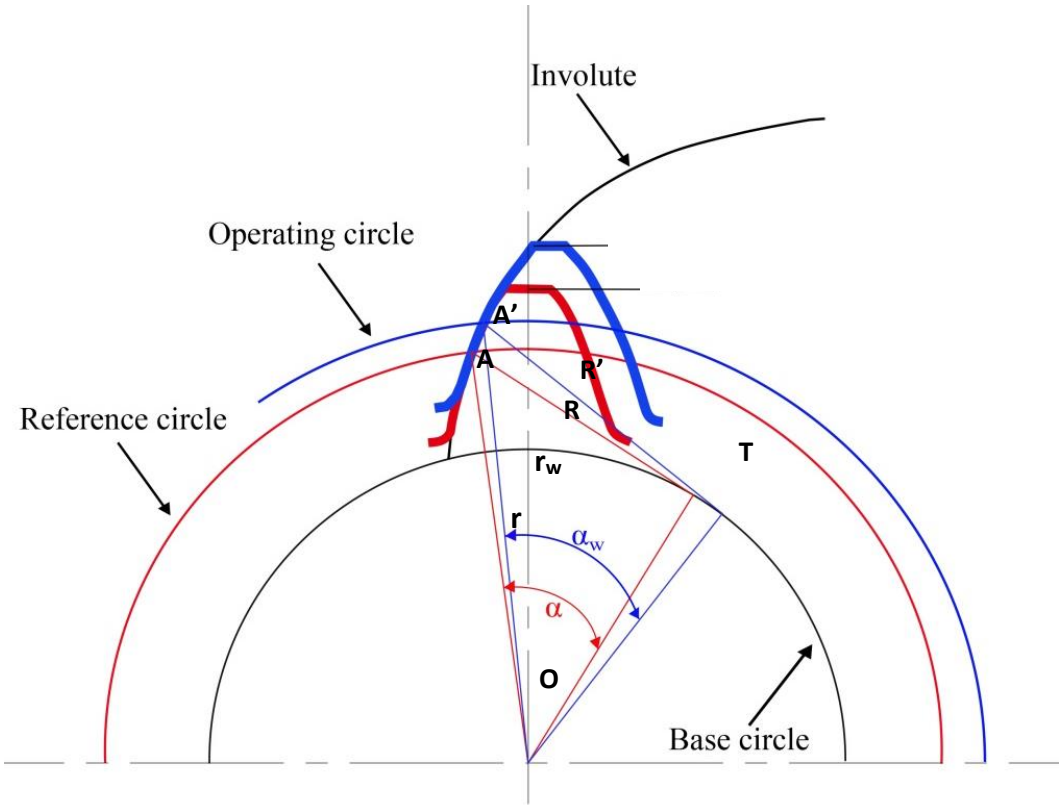

Figure 3.12 – Comparison between a standard tooth profile (X=0) and a X=0.5 mm shifted profile. The diagram shows the pitch circle radius r and the radius of the operating or working pitch circle r_w. The instantaneous radii of curvature R and R' at the pitch points A and A' of working and modified profiles are also shown.

It has to be specified that in the case of two mating gears with a balanced profile shift where $x_{1,2} = -x_{2,1}$, the increase in diameter of one gear is balanced by the decrease of diameter of the other, with the result of an unchanged centre distance. This condition is also translated into the working pressure angle that, for such cases, is equal to the reference value. The applicability of a balanced profile shift is verified by the inequality:

$$N_1 + N_2 > 2N_{min} \qquad 3.30$$

where $N_{1,2}$ is the number of teeth of pinion and gear respectively and N_{min} is the minimum number of teeth that do not produce undercut as expressed in Equation 3.44.

If the condition above is not verified, reciprocal modifications cannot be used. This indicates a deviation of centre distance (a_w) from the nominal value a. In this case, the modified centre distance a_w changes the inclination of the line of action with a consequent variation of the pressure angle into α_w. In order to find the working pressure

angle, an iterative process is needed. The inverse involute function that allows the value α_w to be determined from $inv\alpha_w = tan\alpha_w - \alpha_w$, cannot be solved in a closed form, and therefore an iterative process is needed. Based on geometrical considerations from Figure 3.12, $inv\alpha_w$ can be expressed in terms of α, $x_{1,2}$ and $N_{1,2}$ as follows:

$$inv\alpha_w = \frac{m(x_1 + x_2)\tan\alpha}{m\frac{(N_1 + N_2)}{2}} + inv\alpha \qquad 3.31$$

In the example below (KHK 2015), iterations are performed by applying the Newton-iteration method. The calculation starts with α_w=1 rad and the quantity $inv\alpha_w$ derived from Equation 3.31 and is iterated until the solution does converge to a stable value of α_w.

$$\alpha_{w1} = 1 + (inv\alpha_w - \tan 1 + 1)/\tan^2 1$$

$$\alpha_{w2} = \alpha_{w1} + (inv\alpha_w - \tan\alpha_{w1} + \alpha_{w1})/\tan^2\alpha_{w1}$$

$$\alpha_{w3} = \alpha_{w2} + (inv\alpha_w - \tan\alpha_{w2} + \alpha_{w2})/\tan^2\alpha_{w2} \qquad 3.32$$

...

...

$$\alpha_{wx} = \alpha_{x-1} + (inv\alpha_w - \tan\alpha_{x-1} + \alpha_{x-1})/\tan^2\alpha_{x-1}$$

Figure 3.13 shows how the working pressure angle α_w varies as a function of profile shift. x, that varies in the range -1 to 1, has only been applied to the driven gear for a fixed number of teeth N. It can be noticed that for x=0 the working pressure angle coincides with the reference angle α=20° and then increases or decreases for positive or negative profile shifts respectively.

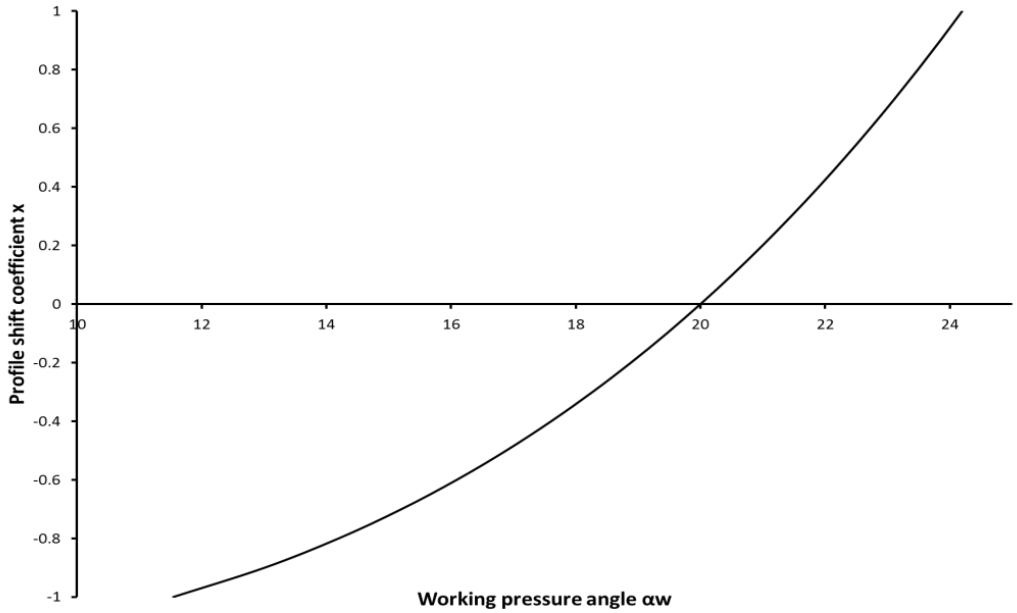

Figure 3.13 - Working pressure angle as function of profile shift coefficient for $-1 \leq x_2 \leq 1$; z1=20, z2=40, α=20°.

As described above in this paragraph, the application of a profile shift changes the pitch circle diameters and consequently the centre distance. From Figure 3.12, the working pitch radius can be found as follows:

$$r_{w1,2} \cos \alpha_w = r_{b1,2} \tag{3.33}$$

$$r_{w1,2} = \frac{r_{1,2} \cos \alpha}{\cos \alpha_w} \tag{3.34}$$

Once the working pitch radii are known, the working centre distance is calculated as follows:

$$a_w = (r_1 + r_2) \frac{\cos \alpha}{\cos \alpha_w} \tag{3.35}$$

$$a_w = a \frac{\cos \alpha}{\cos \alpha_w} = m \frac{(N_1 + N_2)}{2} \frac{\cos \alpha}{\cos \alpha_w} \tag{3.36}$$

Working centre distance is a fundamental parameter for the design of transmissions, as it is a basic constraint that comes from the layout of the gearbox.

3.2.4 Pressure angle (α)

Pressure angle is usually associated with the cutting edge inclination of the rack cutter as visible in Figure 3.6. In general, if a tangent to any point of the involute curve is considered and a radial line connecting the centre of the gear with the considered point of tangency, the angle between these two lines is the pressure angle at that point as shown in Figure 3.14. This implies that pressure angle varies continuously along the tooth flank. If the considered point of tangency lies on the pitch circle, then α assumes its reference value and coincides with the angle of inclination of the cutter edges. The reference pressure angle α is one of the most important specification factors in the design of an involute gear.

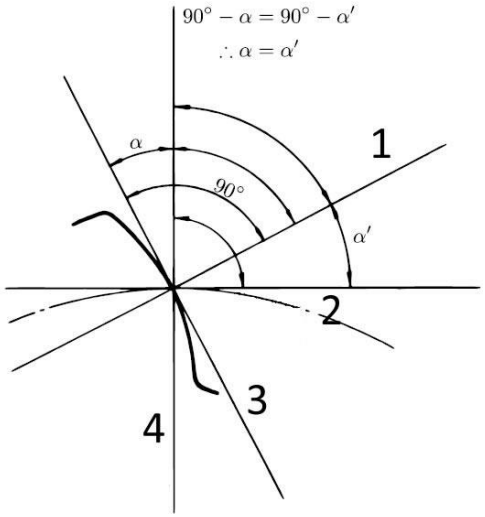

Figure 3.14 – Profile Pressure angle; source (KHK, 2015).

The main effect of α on the involute geometry is due to its influence on the base diameter, such that an increase in the generating pressure angle results in a reduction of the base diameter according to the following equation:

$$d_b = d \cos \alpha \qquad 3.37$$

The involute geometry is strictly related to its base diameter. A change of d_b results in the creation of a different involute curve. Figure 3.15 shows a comparison between two profiles with α values of 20° and 30°, and their associated base circles. The two profiles have the same tip and root diameters and the same reference diameter. In this context it is important to notice the variation in length of the instantaneous radius of curvature

consequent to an increase of the pressure angle. An increased radius of curvature, at the instantaneous point of contact, creates a larger area on which the contact force is distributed that returns a reduced contact stress.

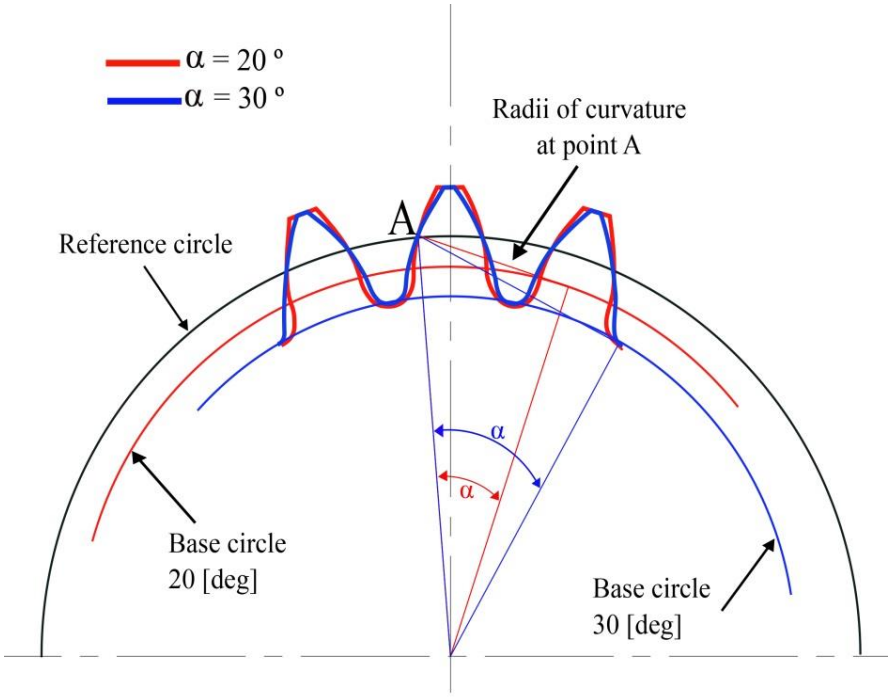

Figure 3.15 – Comparison between two profiles with different reference pressure angles: α=20°; α=30°.

3.2.4.1 Instantaneous radius of curvature

As explained in the paragraphs above, pressure angle and profile shift both change the tooth flank curvature, and hence its behaviour under load. Variation of the reference pressure angle results in a change of the base diameter, and consequently the generation of a different involute, whilst a profile shift modification results in the working profile being part of a different portion further along the same involute. The instantaneous radius of curvature for any point of the involute curve can be determined by using the parametric Equations 3.10 and 3.11 and considering the generation process of the involute curve described earlier. As explained by Patrick (Patrick, 2009) the radius of curvature R of any point on a curve is given by:

$$R = \frac{\left[\left(\frac{dx}{d\theta}\right)^2 + \left(\frac{dy}{d\theta}\right)^2\right]^{3/2}}{\frac{dy}{d\theta}\frac{d^2x}{d\theta^2} - \frac{dx}{d\theta}\frac{d^2y}{d\theta^2}} \qquad 3.38$$

where:

$$\frac{dx}{d\theta} = -r_b \sin\theta + r_b \sin\theta + r_b\theta \cos\theta = r_b\theta \cos\theta$$

$$\frac{dy}{d\theta} = r_b \cos\theta - r_b \cos\theta + r_b\theta \sin\theta = r_b\theta \sin\theta$$

$$\frac{d^2x}{d\theta^2} = r_b \cos\theta - r_b\theta \sin\theta \qquad 3.39$$

$$\frac{d^2y}{d\theta^2} = r_b \sin\theta + r_b\theta \cos\theta$$

that yields:

$$R = \frac{[r_b^2\theta^2 \cos^2\theta + r_b^2\theta^2 \sin^2\theta]^{3/2}}{r_b\theta \sin\theta\,(r_b \cos\theta - r_b\theta \sin\theta) - r_b\theta \cos\theta\,(r_b \sin\theta + r_b\theta \cos\theta)} \qquad 3.40$$

and after rearranging the equation gives:

$$R = r_b\theta = r_b \tan\alpha \qquad 3.41$$

that confirms what already stated with the geometrical construction in Equation 3.12. The radius of curvature varies continuously with θ. This is an important conclusion due to the effect that the profile curvature has on the area of contact and consequently the contact stress. Given that the curvature radius increases (curvature decreases) as the generating point moves away from the base circle, but also with an increase of α, less curved tooth flanks are generated with positively modified profiles and hence higher pressure angles. These two aspects will be extensively studied in the following chapters.

3.3 Manufacturing and operational boundaries

Non-standard proportions can be used to improve gear performance and make custom products optimised for a specific application. In order to produce tooth profiles with specific characteristics, the parameters listed above have to be modified with proportions different from the standard. However, the range of variation for each geometrical parameter is limited by manufacturing and operational boundaries. The

first category is addressed to the manufacturing process by means of the viability of the rack cutter geometry. On the other hand, operational boundaries relate to the meshing process between mating gears. Moreover, the way that these parameters affect both geometry and performance is not independent, and the effect can be either concurrent or divergent on the result. This condition introduces the existing relations between parameters and their mutual influence on the definition of boundaries that define an area of feasibility of involute spur gear profiles. Undercutting and pointed tooth conditions are constrained by the manufacturing process while tip/root interference and contact ratio are constrained by working or operational considerations.

3.3.1 Undercutting

Undercutting is a phenomenon that can occur during the manufacturing process due to a combination of factors. If gears are produced by a generation process that involves the meshing between the cutting tool and the gear blank, then the profiles potentially can be undercut. While the gear teeth are generated, if the cutter addendum extends beyond the base circle of the gear being cut, an extra amount of material will be removed at the root of the gear tooth creating a recess in the area. This effect produces a reduction of the gear thickness in proximity of the root that already is the weakest part in relation to bending. Clearly undercutting is an unacceptable condition due to the produced weakened geometry as shown in Figure 3.16.

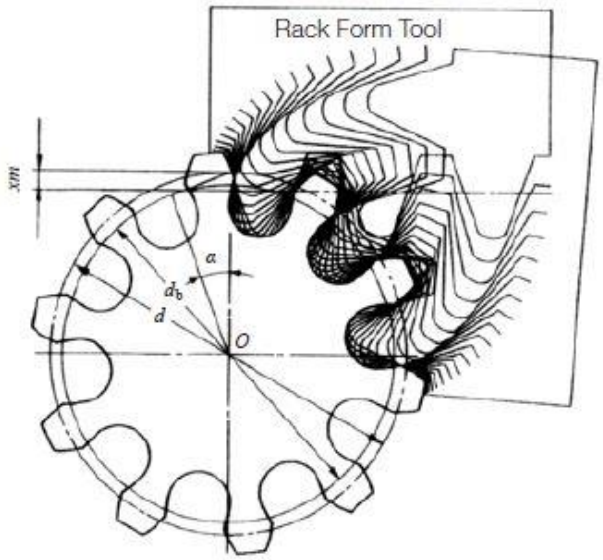

Figure 3.16 – Undercut tooth profiles due to a negative profile shift. Gear parameters: alpha=20°, N=10, x=-0.5 (KHK, 2015).

The condition of undercutting occurs when the cutter addendum line is below the point of tangency between the normal to the rack profile at the pitch point and the base circle. By referring to Figure 3.17, if line AA is below a parallel line passing through point N then undercutting occurs.

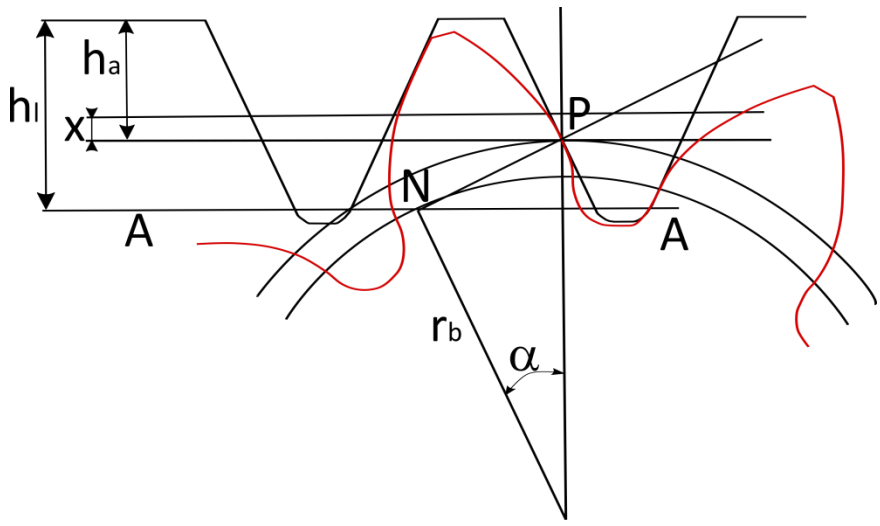

Figure 3.17 – Limiting condition for the occurrence of undercutting.

The configuration schematised in Figure 3.17 represents the condition limit with the two lines being coincident. By considering the geometry of Figure 3.16, it is possible to express the limiting condition for non-undercutting as follows:

$$r \sin\alpha \ \sin\alpha = h_a^* m - xm \tag{3.42}$$

which yields:

$$\frac{mN}{2}\sin^2\alpha = (h_a^* - x)m \tag{3.43}$$

and expresses the undercutting avoidance condition as function of *N, α, m,* h_a and *x.* Equation 3.43 can be modified in order to find the minimum number of teeth for a given set of parameters. By turning Equation 3.43 into the following inequality and converting *N* into N_{min} we get:

$$N_{min} \geq \frac{2(h_a^* - x)}{\sin^2\alpha} \tag{3.44}$$

In Figure 3.18 the relation expressed in 3.44 is plotted between the minimum number of teeth on the limit of undercutting and the pressure angle α for a standard non-shifted spur gear. The graph shows an exponentially decreasing trend for minimum number of teeth as the pressure angle increases. An increase in pressure angle, as explained in detail in section 3.2.4, causes a reduction in the base diameter (equation 3.37) which also causes the point N to drop below the line AA, hence preventing undercutting (Figure 3.17).

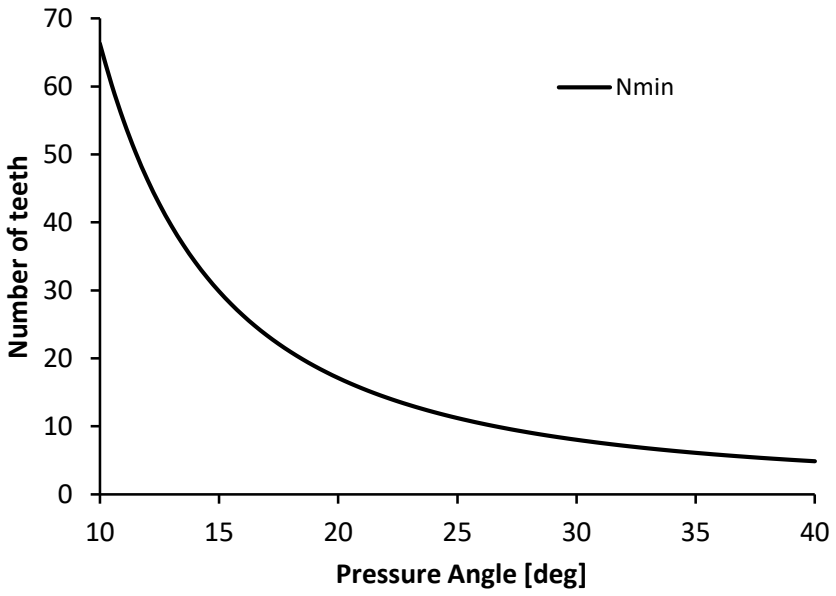

Figure 3.18 – Minimum number of teeth in absence of undercutting as function of pressure angle α for x=0.

In order to explain the effect of pressure angle and profile shift on the minimum number of teeth, a standard gear with a pressure angle α=20° is considered. For this configuration, from Figure 3.18, the minimum number of teeth without undercutting is given as 17. For applications that require the use of gears with smaller number of teeth, a solution with non-standard parameters and correction coefficients has to be considered in order to overcome the manufacturing limitation and still ensuring correct mesh operation. For example, a pinion with α=35° has a bottom practical limit of 7 teeth, for the same value of module. This results in a much smaller outside diameter compared to the previous case with α=20°. Nevertheless, by taking into account the profile shift modification it would possible to achieve the same bottom limit N_{min}=7 even with α=20°. As already described in section 3.2.3, a positive profile shift moves the actual cutter pitch line radially outwards. This allows the addendum line AA to stay above point N in Figure 3.17 which represents the undercutting boundary. By rearranging Equation 3.44 in terms of *x* as function of N_{min} for fixed α, the necessary amount of profile shift coefficient to avoid undercutting for a given pressure angle and rack cutter addendum coefficient can be found as follows:

$$x = h_a^* - \frac{N}{2}\sin^2\alpha \qquad 3.45$$

The graph plotted in Figure 3.19 indicates the required amount of profile shift coefficient for a given number of teeth and profile pressure angle in order to avoid undercutting. From Figure 3.19 it can be seen that a standard gear with α=20° and *N*=7 requires a profile shift *x*= +0.6 to avoid the condition of undercutting. On the other hand, for the same number of teeth, a gear with α=35° can tolerate a negative profile shift up to *x*=-*0.18* without presenting undercutting.

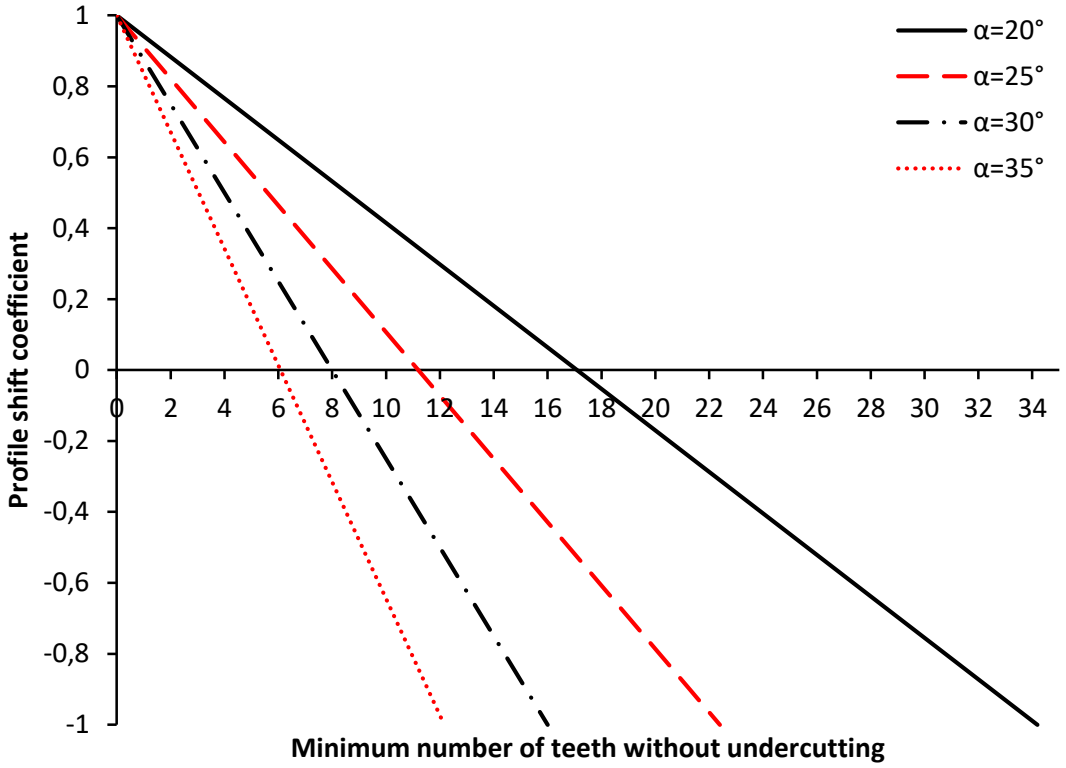

Figure 3.19 – Minimum number of teeth without undercutting as function of profile shift coefficient for a range of pressure angles α.

3.3.2 Top land thickness

In the previous paragraph it has been shown that values of pressure angle and profile shift have a bottom boundary due to the occurrence of the phenomenon of undercutting. For the range of variation of α and *x* also an upper boundary exists and occurs due to the condition of pointed teeth. If the intersection point between the two involute tooth flanks lies on a circle smaller or coincident with the tip circle, the top land thickness is zero and the tooth shows a pointed profile. This represents an unwanted

condition particularly for hardened gears, because a hardened pointed tooth tends to be brittle and an early breakage due to shock loads can occur. The tooth thickness at the tip circle can be found by geometrical considerations according Figure 3.20.

The value of the profile pressure angle at the tip circle α_a is derived from the following relation between tip and base radii:

$$r_a \cos \alpha_a = r_b \tag{3.46}$$

$$\cos \alpha_a = \frac{r \cos \alpha}{r_a} \tag{3.47}$$

which yields:

$$\alpha_a = \cos^{-1}\left(\frac{Nm}{d_a}\cos \alpha\right) \tag{3.48}$$

Through the profile angle σ, it is possible to relate the tooth thickness at the pitch circle (Equation 3.29 and Figure 3.8) to the tooth thickness on the tip circle:

$$\sigma = \frac{S}{2r} + inv\alpha = \frac{S_a}{2r_a} + inv\alpha_a \tag{3.49}$$

From this equation, the top land thickness S_a is defined as follow:

$$S_a = 2r_a\left(\frac{S}{2r} + inv\alpha - inv\alpha_a\right) \tag{3.50}$$

And by substituting Equations 3.46 and 3.48 into 3.50, the tooth thickness at the tip circle is given by:

$$S_a = d_a\left\{\frac{\pi}{2N} + \frac{2x}{N}\tan \alpha + inv\alpha - inv\left[\cos^{-1}\left(\frac{Nm}{d_a}\cos \alpha\right)\right]\right\} \tag{3.51}$$

As for the other parameters in the metric gear system, also the thickness can be defined in terms of the module in order to create a non-dimensional factor s_a. Recommended values of top land thickness are given by the standard AGMA 2101/D04 (2016) and span from 0.2 to 0.6. IS 3756 (2002) recommends thickness should be at least 0.4*m for

hardened gears and for exceptional cases can be reduced to 0.25*m. Kapelevich et Al., (2002) suggests a window of proportional values calculated as top land thickness divided by the base pitch between 0.06 and 0.12.

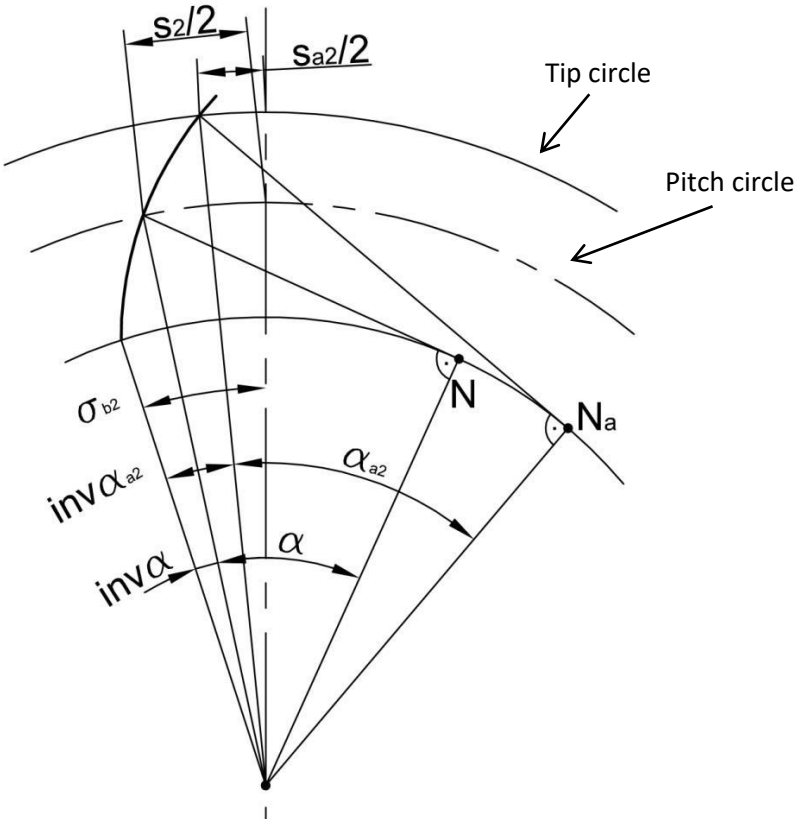

Figure 3.20 – Schematic diagram for the calculation of the top land thickness S_{a2}. α is the profile angle at the pitch circle; α_{a2} is the profile angle at the tip circle.

For positive values of addendum modification, the top land thickness becomes smaller and eventually results in a pointed tip. On the other hand, a negative profile shift has the opposite effect by making the top land thickness thicker as the addendum modification decreases. A similar effect is given by the pressure angle variation. Both positive profile shifts and increasing pressure angles push the active involute portion farther away from the base circle than for a standard gear making the resulting geometry thinner at the tip and thicker at the root (Goldfarb et Al., 2005). In order to evaluate the individual and combined effect of the two parameters, the variation of S_a as function of x and α has been plotted in Figure 3.21. It can be seen that for a fixed number of teeth, for a given profile shift as the pressure angle increases the top land

thickness decreases up to values below the practical limit of S_a=0.25*m (red line). For a standard gear with N=20 and m=1, the boundary occurs for α=31°, while for a negatively corrected geometry with x=0.5 and the same value of pressure angle, S_a=0.596 mm, which is way above the imposed limit. On the other hand, by applying a positive addendum modification (*x=0.5*), the limit is reached for α=24° and presents the condition of pointed tooth for α=28°.

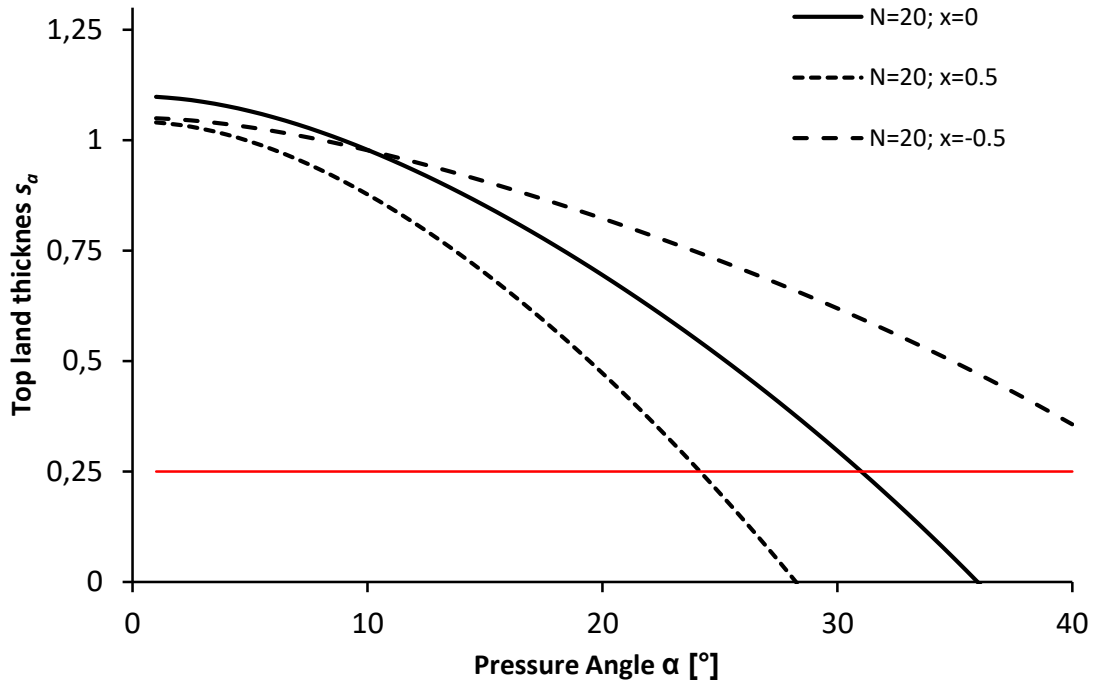

Figure 3.21 – Top Land Thickness as function of pressure angle α for constant profile shifts; N=20; m=1.

To conclude, the concurrent use of positive addendum modifications and increased pressure angles anticipates the occurrence of the pointed tooth condition. This suggests, for certain combination of parameters, the need of a balanced design choice to overcome the occurrence of undercutting without reaching the limiting condition of a peaking tooth tip.

3.3.3 Tip/root interference

The interference between tip and root of two mating gears is similar to the undercutting condition described earlier. While in the previous situation, the interference occurred between the cutter tip edge and the tooth root, in this case the tip of one of the gears

interferes with a non-involute portion of the tooth profile of the mating gear that lies below the base circle. The contact would result in a non-conjugate action i.e. due to interference, the tip of one gear would clash onto the flank of the mating gear in the region between the base and the root circles, impeding the gears from properly meshing.

The path of contact is a portion of the line of contact limited by the points of first and last contact of two mating teeth. By definition, the line of action is tangential to the base circles of the mating gears and determines two limiting points of the path of contact corresponding with the points of tangency T_1 and T_2, as shown in Figure 3.22. Given that the involute does not exist below the base circle, each mating point that exists outside the segment $\overline{T_1T_2}$ implies a non-conjugate action because one of the two mating surfaces is not an involute curve. The limiting condition of interference implies that points A and D must coincide with T_1 and T_2. If A and/or D are external to $\overline{T_1T_2}$ it means that at the points of tangency the tip of one gear is still below the base circle of the other. This condition is equivalent to the one shown in Figure 3.17 in regards to the limit of undercutting where the cutting edge of the tool lies on the base circle of the gear being produced. By considering the limit of undercutting related to the manufacturing process, it is possible to derive the equation for interference by imposing the equivalence between the length of the path of contact and the condition of non-undercutting. By referring to Figure 3.22, where the tip of the driven tooth comes in contact within the segment $\overline{T_1T_2}$, the limiting interference condition for the pinion can be expressed as follows:

$$a_w \sin \alpha_w - r_{b2} \tan \alpha_{a2} = r_1 \sin^2 \alpha - (h_{a1}^* - x_1)m \qquad 3.52$$

Similarly, for the gearwheel we get:

$$a_w \sin \alpha_w - r_{b1} \tan \alpha_{a1} = r_2 \sin^2 \alpha - (h_{a2}^* - x_2)m \qquad 3.53$$

And by substituting equations 3.36, 3.43 and 3.44, into 3.53 yields:

$$(N_1 + N_2)\cos\alpha\tan\alpha_w - d_{b2}\tan\alpha_{a2} = N_1\sin^2\alpha - 2\,(h_{a1}^* - x_1) \quad 3.54$$

$$(N_1 + N_2)\cos\alpha\tan\alpha_w - d_{b1}\tan\alpha_{a1} = N_2\sin^2\alpha - 2\,(h_{a2}^* - x_2) \quad 3.55$$

Equation 3.54 and 3.55 express the interference limit for the pinion and gear respectively as function of α, *x* and h_a^*.

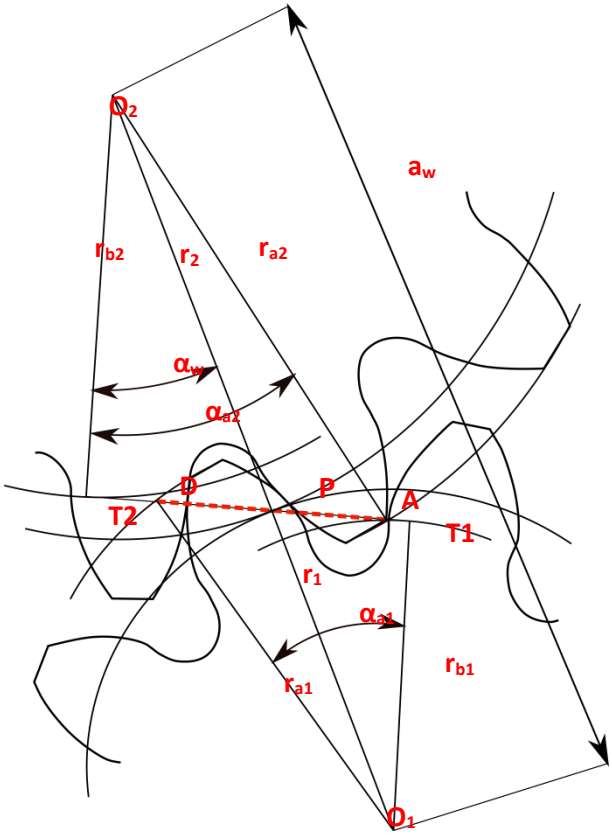

Figure 3.22 – Geometrical description of Tip/Root interference condition.

3.3.3.1Path of contact

The path of contact is a portion of the line of contact and can be defined as the geometrical locus of points on which contact occurs during the relative rotation of one gear to the other. At the intersection between the line of contact and the tip circles of the mating gears, two characteristic points are determined: A, the first point of contact that occurs at the intersection between the line of action and the gear tip circle; D, the last point of contact, located at the intersection between the line of action and the pinion tip circle. In order to calculate the length of the path of contact $\overline{AD}$ in Figure 3.22,

working centre distance, tip and base circles radii must be known. For the calculation of the radii, accordingly to the geometrical configuration of Figure 3.22 we get:

$$\overline{T_1 \mathrm{A}} = \mathrm{a}_w \sin(\alpha_w) - \sqrt{\mathrm{r}_{\mathrm{a}2}^2 - \mathrm{r}_{\mathrm{b}2}^2} \tag{3.56}$$

$$\mathrm{r}_{\mathrm{A}} = \sqrt{\overline{\mathrm{T}_1\mathrm{A}^2} - \mathrm{r}_{\mathrm{b}1}^2} \tag{3.57}$$

$$\overline{\mathrm{T}_2\mathrm{D}} = \mathrm{a}_w \sin(\alpha_w) - \sqrt{\mathrm{r}_{\mathrm{a}1}^2 - \mathrm{r}_{\mathrm{b}1}^2} \tag{3.58}$$

$$\mathrm{r}_{\mathrm{D}} = \sqrt{\mathrm{T}_2\mathrm{D}^2 - \mathrm{r}_{\mathrm{b}2}^2} \tag{3.59}$$

The length of the contact segment AD, can be calculated once base radii and tip circles radii are known as follows:

$$\mathrm{AD} = \sqrt{\mathrm{r}_{\mathrm{a}1}^2 - \mathrm{r}_{\mathrm{b}1}^2} + \sqrt{\mathrm{r}_{\mathrm{a}2}^2 - \mathrm{r}_{\mathrm{b}2}^2} - \mathrm{a}_w \sin(\alpha) \tag{3.60}$$

As the path of contact is the locus of points where contact occurs, some other characteristic points with specific properties can be found. Firstly, the Pitch point, P, that lies on the point of tangency between the operating pitch circles of the mating gears and is defined by the intersection between the line of action and line connecting the centres of the two wheels. Pitch circle radius $r_{1,2}$ is one of the basic gear dimensions and is determined by equation 3.26. Points B and C represent the meshing positions at which the number of teeth in contact changes. Starting with two pairs of teeth in contact between A and B, when the contact point reaches B the first pair of teeth disengages and only one pair of teeth is in mesh. From C to D a new pair engages and again two couples are in contact at the same time as shown in Figure 5.14.

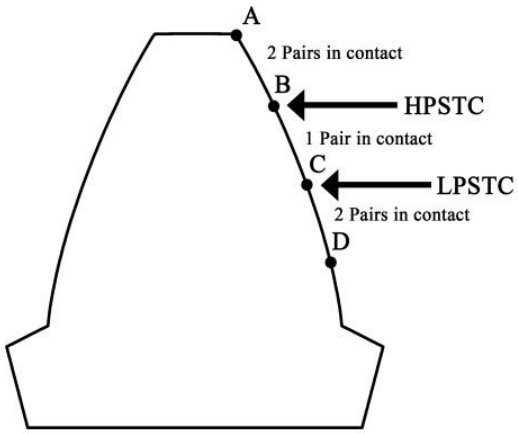

Figure 3.23 – Distribution of the tooth pairs in simultaneous contact along the tooth flank for a complete mesh cycle.

Figure 3.23 shows the distribution of the pair of teeth in simultaneous contact along the tooth flank and the limiting points of the single pair of teeth in contact. Point B lies on the largest radius at which a single tooth pair is in contact and is generally referred as HPSTC acronym of Highest Point of Single Tooth Contact. On the other end, point C lies on the smallest radius of single contact and is called LPSTC or Lowest Point of Single Tooth Contact (Raptis et Al., 2012). The following relations, based on Figure 3.22 allow $\mathbf{r_B}$ and $\mathbf{r_C}$ to be found for both pinion and gear:

$$\overline{T_1B} = a_w \sin(\alpha_w) - \overline{T_2D} - \frac{2\pi r_{b1}}{N_1} \tag{3.61}$$

$$r_B = r_{LPSTC1} = \sqrt{\overline{T_1B} - r_{b1}^2} \tag{3.62}$$

$$\overline{T_2C} = a_w \sin(\alpha_w) - \overline{T_1A} - \frac{2\pi r_{b2}}{N_2} \tag{3.63}$$

$$r_C = r_{LPSTC2} = \sqrt{\overline{T_2C} - r_{b2}^2} \tag{3.64}$$

$$\overline{T_1C} = \overline{T_1A} + \frac{2\pi r_{b1}}{N_1} \tag{3.65}$$

$$r_C = r_{HPSTC1} = \sqrt{\overline{T_1C^2} - r_{b1}^2} \tag{3.66}$$

$$\overline{T_2B} = \overline{T_2D} + \frac{2\pi r_{b2}}{N_2} \tag{3.67}$$

$$r_B = r_{HPSTC2} = \sqrt{\overline{T_2B} - r_{b2}^2} \tag{3.68}$$

Where $\frac{2\pi r_{b1,2}}{N_{1,2}}$ are the base pitches of pinion and gear respectively. The geometrical approach used here can also be found in Niemann (1982).

3.3.4 Contact ratio

In order to ensure a continuous tooth action and a continuous power transmission, as one pair of teeth is approaching the point of disengagement, a succeeding pair must already have been engaged. Considering two gears in mesh, the value of contact ratio, ε, indicates the average number of teeth in contact during a mesh cycle and has a great influence on the correct working condition of the transmission. The contact ratio, for spur gears, is usually in the range between 1 and 2 and is function of the quantities AB, CD and BC of Figure 3.23.

The geometrical explanation of the contact ratio is given in Maitra (2012). In this approach the contact ratio ε is defined by the ratio between the angle of action and the pitch angle and is calculated as follows in this paragraph. By considering the initial and end point A and B of the path of contact in Figure 3.24, it is possible to derive the position of points a and b that lie on the base circle by following the involute trace of the tooth flank. Moreover, given that A and B lie on the tangent to the base circle, from the properties of the involute curve, the following relation can be determined:

$$\widehat{T_1a} = \overline{T_1A} \tag{3.69}$$

$$\widehat{T_1b} = \overline{T_1B} \tag{3.70}$$

and subtracting one from the other yields:

$$\widehat{T_1b} - \widehat{T_1a} = \overline{T_1B} - \overline{T_1A} = \widehat{ab} = \overline{AB} \tag{3.71}$$

This means that the arc length $\widehat{ab}$ is equal to the length of the path of contact $\overline{AD}$, already known from Equation 3.60. Since the angle θ subtended by the arc ab at the centre O_1 is equal to the angle subtended by the arc a^1b^1 to the centre O_1, where a^1 and b^1 are traced from points a and b along the involute to the pitch circle, then the following relations can be determined:

$$\widehat{a^1b^1} = r_1\theta \tag{3.72}$$

$$\widehat{ab} = r_1\theta\cos\alpha \tag{3.73}$$

Which yields:

$$\widehat{a^1b^1} = \frac{\widehat{ab}}{\cos\alpha} \tag{3.74}$$

The contact ratio is given by:

$$\varepsilon = \frac{\theta}{\varphi} \tag{3.75}$$

Where θ is called angle of action and can be calculated from the equations above as:

$$\theta = \frac{\widehat{a^1b^1}}{r_1} = \frac{\widehat{ab}}{r_1\cos\alpha} = \frac{\overline{AB}}{r_1\cos\alpha} \tag{3.76}$$

And φ is the pitch angle:

$$\varphi = \frac{\pi m}{r_1} \tag{3.77}$$

Which yields:

$$\varepsilon = \frac{\overline{AB}}{r_1\cos\alpha}\frac{r_1}{\pi m} = \frac{\overline{AB}}{\pi m\cos\alpha} \tag{3.78}$$

And by considering equation 3.60 becomes:

$$\varepsilon = \frac{\sqrt{r_{a1}^2 - r_{b1}^2} + \sqrt{r_{a2}^2 - r_{b2}^2} - a_w \sin \alpha_w}{\pi m \cos a} \qquad 3.79$$

From Equation 3.79 it can be noticed that if the path of contact $\overline{AB}$ is equal to the base pitch p_b, *the* contact ratio would be 1. This happens because only one tooth and the adjacent vain would fit the entire path of contact and so only one pair of tooth would be in contact during a complete mesh cycle.

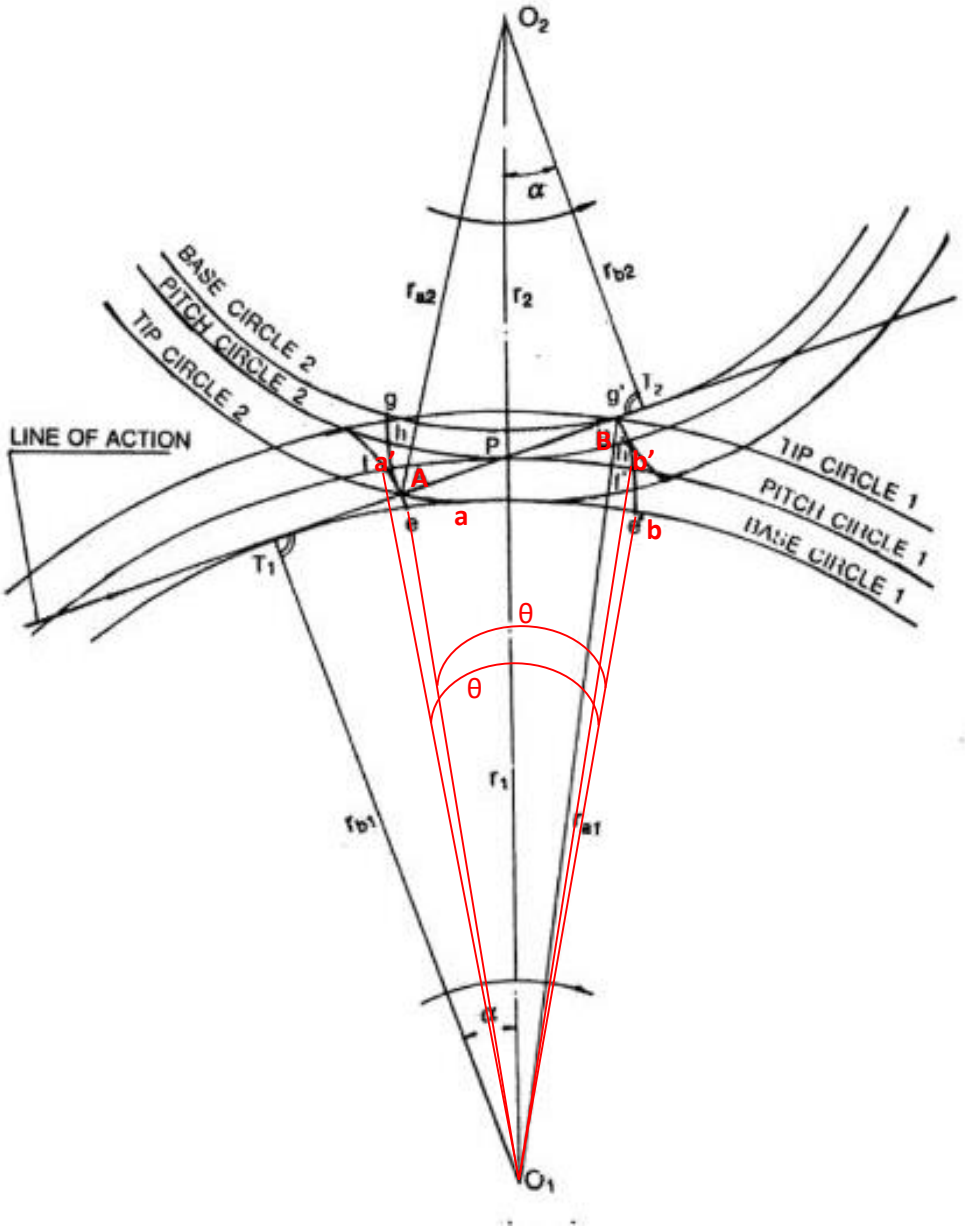

Figure 3.24 – Geometrical description of contact ratio as function of the path of contact and base pitch (Maitra, 2013; modified by the author).

For values of ε<1 the basic requirement of a constant transmission ratio is not satisfied. The pulsating torque delivery and the impacts between teeth would be an unacceptable solution for any transmission system. By taking into account manufacturing and assembling deviations, the limit for ε is increased to a minimum of 1.2 with typical values ranging from 1.4 to 1.6 (Goldfarb et AL., 2005; Kapelevich, 2013; Maitra, 2012). The physical meaning of a contact ratio, for example 1.6, is that during the period of engagement one pair of tooth is permanently in contact, while during the same period, another pair is also in mesh for 60% of the time only. The contact ratio, as defined above, is function of both working pitch and base circle radii and working pressure angle.

For conventional gears with a number of teeth above the limit of undercut, an increase in pressure angle determines a consequent reduction in contact ratio as shown by the solid line in Figure 3.25. Nevertheless, for gears with a small number of teeth in which the undercutting condition occurs, increasing the pressure angle has a positive effect (dashed line in Figure 3.25) on contact ratio.

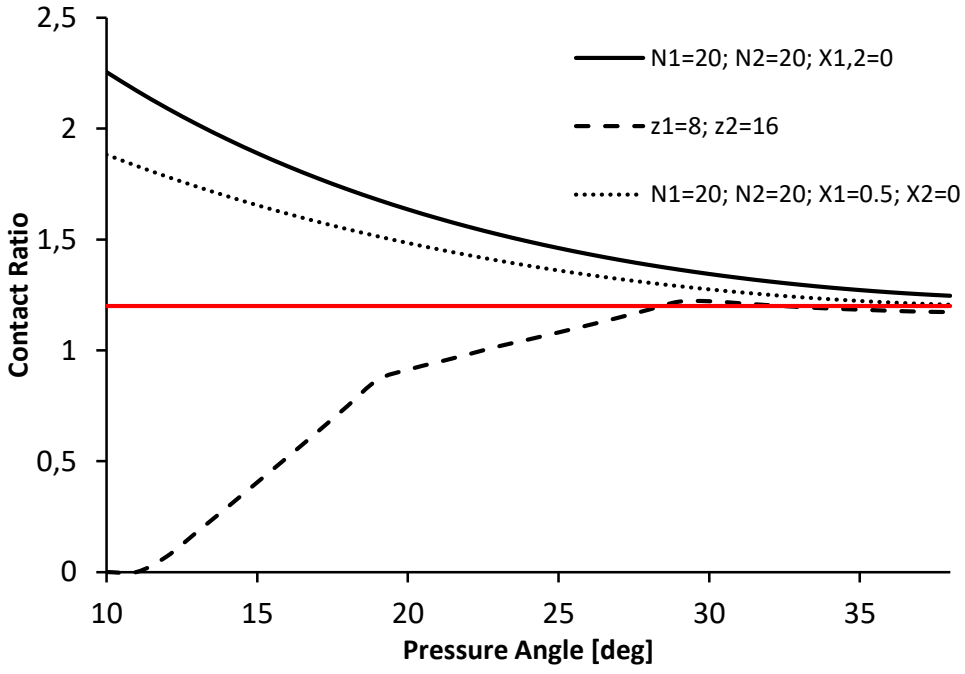

Figure 3.25 – Contact ratio variation as function of pressure angle for constant profile shifts and fixed number of teeth.

3.3.5 Summary

The interaction between geometrical parameters explained above can be summarised in a chart in which the influence of each modification on the described boundaries and how the tooth profile geometry would be affected are considered.

As already discussed, increasing the pressure angle over the standard α=20° has a positive effect on gear performance thanks to an increased thickness at the tooth base and a reduced profile curvature of the tooth flank. Another main advantage is preventing the occurrence of undercutting due to the reduction of the base diameter. A similar effect is with regards to the tip/root interference in which an increased α pushes the limit further way. On the other end, by increasing α profiles become more prone to the tip pointed condition. Moreover, a reduction of contact ratio is experienced. Pressure angle only affects the base diameters that decreases as α increases. Tip and root diameters stay constant as well as the centre distance.

Similarly, to pressure angle, a positive profile shift variation from the standard x=0 has a positive effect on the undercutting and tip/root interference. In this case the reason is not addressed to the base diameters that stays constant but rather to the shift of the pitch line/circle compared to the standard condition. Reduced top land thickness and reduced contact ratios are the negative effects. Vice versa, if the modification is negative with x<0, the effects are reciprocal to the ones already described. Centre distance, tip and root diameters change accordingly with x by increasing or decreasing whether x is positive or negative.

Addendum factor h_a is the parameter that defines the length of the tooth portion above the pitch circle. Since it refers to the gear geometry it does not influence undercutting which is, in fact, affected by the rack cutter addendum h_a^*. As the Tip/Root interference is function of the addendum length of the mating gears, with an increased h_a the gear addendum can result being below the line of action at the extreme point of the path of contact generating interference. However, before the limit for interference occurs, a longer addendum determines an increase of contact ratio given that the path of contact becomes longer without changing the base pitch. On the other hand, by elongating the tooth length outwards from the gear centre, the two sides of a tooth profile become

closer with a consequent reduction of the tooth thickness. With a variation of h_a the outside diameter is the only geometry that varies.

Dedendum coefficient, H_f is the parameter that indicates the length of the tooth portion below the pitch circle. Dedendum factor h_f, strictly relates to the condition of undercutting given that in order to generate a tooth profile with a longer dedendum the cutter needs a longer H_a^* that can eventually generate undercut profiles. In general, as H_f increases the tooth thickness at the tooth root is reduced with a consequent reduction of the load carrying capacity. A dedendum variation do not affect the active portion of the tooth profile as it acts at the tooth root by only affecting the root diameter of the gear.

The Interaction between geometrical parameters and their mutual effect on limiting manufacturing and operational conditions is shown in the diagram below.

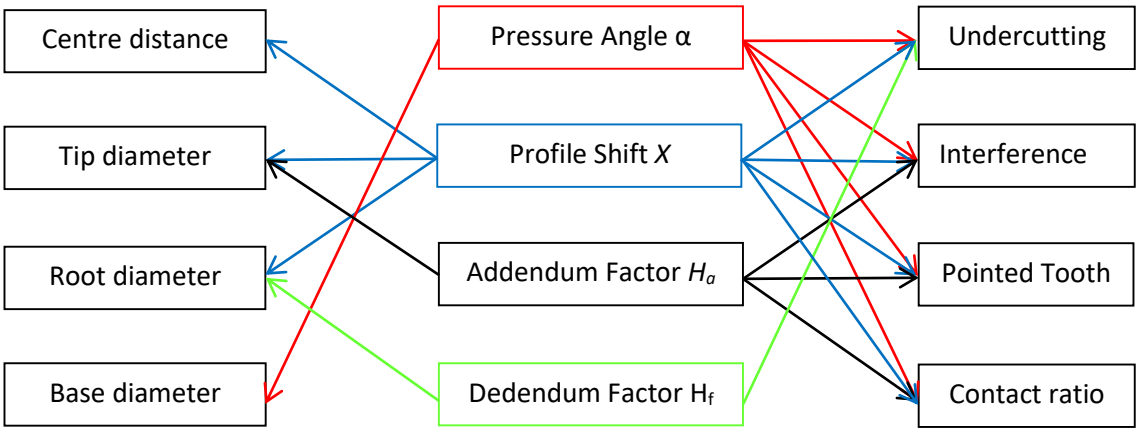

Figure 3.26 – Interaction between geometrical parameters and their mutual effect on limiting manufacturing and operational conditions.

3.4 FEA Background

Structural analysis can be divided in two macro areas: Analytical or modelling methods and Experimental methods. Finite element method (FEM) belongs to the first category and consists of the solution of partial differential equation systems. It only requires a digital representation of the model to be analysed, and some computational resources to find a solution to an engineering problem. Alternatively, experimental methodologies require the production of physical models and all the necessary equipment for data

acquisition and analysis. This “ease” in performing structural analysis with just computational resources, combined with a proved reliability of results, has made the finite element method the most used structural analysis technique, often leaving to the experimental methodology the role of validating the results achieved at the last stage of the design process.

The Finite Element Method is a numerical technique to solve boundary value problems. Its basic concept is the hypothetical decomposition of a system in a continuous number of sub-systems called elements as shown in Figure 3.27. Each element defines a small region but does not introduce any discontinuity such as cracks or surfaces within the continuum of the system.

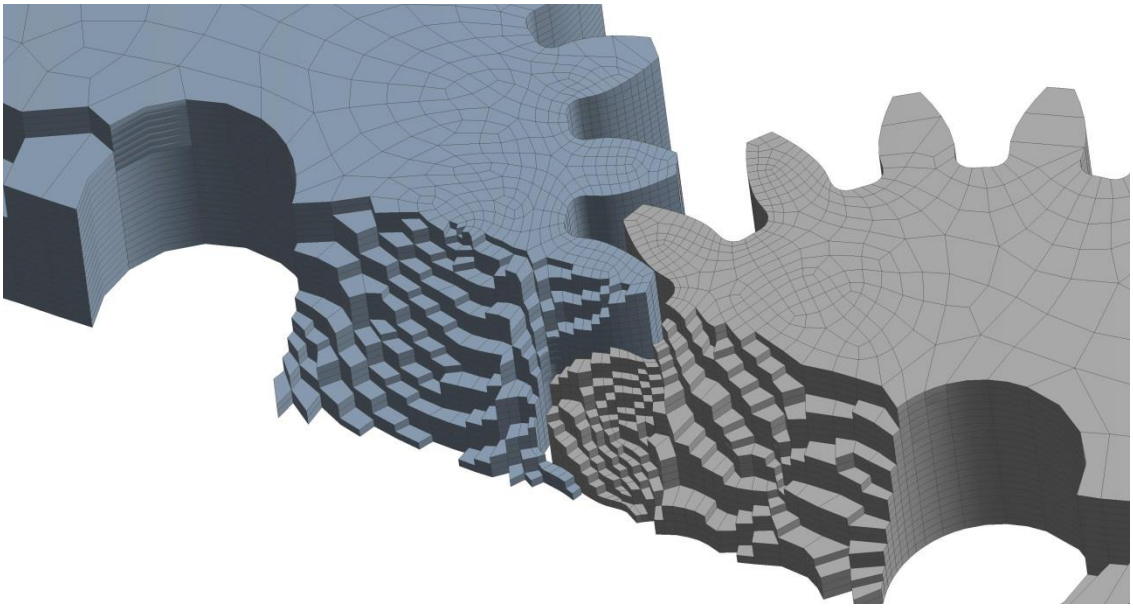

Figure 3.27 - Discretization of a 3D gear pair solid body with hexahedral elements.

Elements are characterized by a certain number of nodes, each one with a finite number of degrees of freedom. Nodes also act as joints between adjacent elements. Once the position of nodes is determined, the combination of elements and nodes determines a network, called a mesh, through which mutual nodal information are shared.

The real distribution of a field variable throughout a physical system is generally an unknown continuous function. The basic building block of Finite Element Analysis is the definition of a shape function that defines the properties of each element. The shape function is a mathematical formulation that correlates the considered field variable at

the nodes and its distribution within the element by performing numerical interpolations. The interpolation order can be a constant, linear or quadratic approximation of the real distribution, and certainly determines the quality of the analysis as shown in Figure 3.28. The order is determined by the number of nodes used in the element; the higher the order of the elements that describe the system, the lower is the degree of approximation, and the increase in the computational requirements.

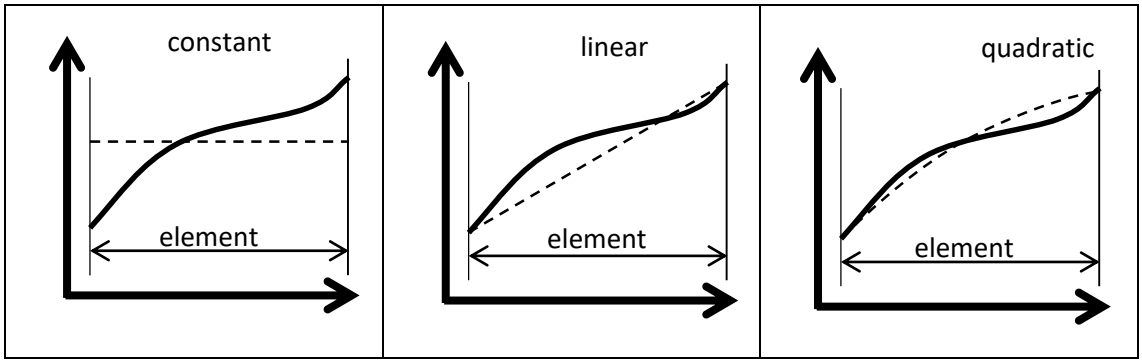

Figure 3.28 - Approximation of a generic displacement function by means of a) constant; b) linear; and c) quadratic shape function.

Figure 3.29 shows the shape and nodal position for the most common elements used in structural analysis. Generally, elements that have nodes only at their corners are known as first-order or linear elements. Those with mid-side nodes are quadratic or second-order elements.

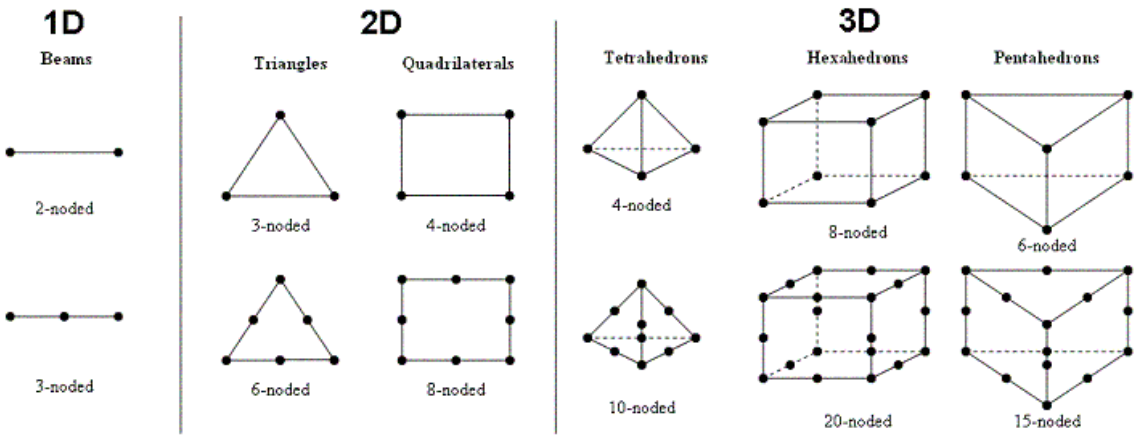

Figure 3.29 - Graphical representation of FEA elements (image source Studioseed.net).

To calculate the distribution of a field variable within a system, it is a commonly accepted procedure in structural FEA to first determine the nodal displacements and then use

displacements to derive the required field variable. For the case of stress analysis, displacements are used to find strains, and then elemental stresses, by applying constitutive relations. The displacement field which is assumed within each element is written in terms of nodal displacements in the form:

$$\{u\} = [N]\{d\} \tag{3.80}$$

where $\{u\}$ is the unknown displacement field within the element, $\{d\}$ is the vector of nodal displacements and $[N]$is the shape function. By considering that strain is defined as a variation in length compared to the original length, in matrix form this can be expressed as shown in Equation 3.81

$$\{\epsilon\} = [\delta]\{u\} \tag{3.81}$$

In which $[\delta]$ is a partial differential operator matrix used to convert the displacement vector $\{u\}$ into the required strains vector$\{\varepsilon\}$. By combining the Equations 3.80 and 3.81 we get Equation 3.82

$$\{\varepsilon\} = [\boldsymbol{\delta}]\{u\} = [\delta][N]\{d\} = [B]\{d\} \tag{3.82}$$

where $[B] = [\delta][N]$ is called strain-displacement matrix. By applying Hooke's law in which $[E]$ is a symmetric matrix that contains the material stiffnesses, stresses are derived from strains as follows:

$$\begin{aligned}\{\sigma\} = [\boldsymbol{E}]\{\varepsilon\} \rightarrow \{\sigma\} &= [E][\delta][N]\{d\} \\ &= [E][B]\{d\}\end{aligned} \tag{3.83}$$

From Equations 3.83, strain and stress vectors can be calculated once the displacement vector $\{u\}$ is known.

After model discretisation, the calculation of governing equations for each element is required. Once the element type and the formulation to describe the shape function have been chosen, the stiffness matrix for each element is computed. By calculating the work done by the external forces applied to the system as in Equation 3.84

$$W_e = \frac{1}{2}\{d\}^T[K_e]\{d\} \tag{3.84}$$

and the virtual internal work made by the internal forces as in Equation 3.85

$$W_i = \frac{1}{2}\int_A \{\varepsilon\}^T[\sigma]dA \tag{3.85}$$

Applying the principle of Virtual Work that imposes equality between external and internal work done we get:

$$\frac{1}{2}\{d\}^T[K_e]\{d\} = \frac{1}{2}\int_A \{\varepsilon\}^T[\sigma]dA \tag{3.86}$$

Equation 3.86 allows the stiffness matrix for each element of the system to be determined as:

$$\{d\}^T[K_e]\{d\} = \int_A \{d\}^T[B]^T[E][B]\{d\}dA \tag{3.87}$$

Rearranging Equation 3.87, the element stiffness matrix is determined as follows:

$$[K_e] = \int_A [B]^T[E][B]dA \tag{3.88}$$

After individual element stiffness matrices in the system are computed the next step is to assemble them into a form of global stiffness matrix $[K]$ that represents the whole body. The matrix assembly process results in a system of algebraic equations that include element stiffnesses, nodal displacements and loading/boundary conditions. Equation 3.89 is the one to be solved in the case of static analysis is expressed in the form:

$$[K]\{d\} = \{F\} \tag{3.89}$$

where $[K]$is the global stiffness matrix, $\{d\}$ is the nodal displacement vector that refers to the whole system and $\{F\}$ is the vector that contains external forces applied to the nodes. After boundary conditions are applied to the relevant nodes, the nodal displacement solution involves the inversion of the stiffness matrix in Equation 3.89:

$$\{d\} = [K]^{-1}\{F\} \tag{3.90}$$

The solution process explained above is defined implicitly and requires the inversion of the stiffness matrix in order to solve the unknown displacement vector (Gavin, 2016).

The full process of Finite Element Analysis can be divided in three different steps that require the geometry definition and material characteristics at the first step. Once the geometry is defined, boundary conditions and constraints involving supports and external loads are applied to the model. The last step of the pre-processing phase is the mesh generation, after the element type has been chosen. Once this step is accomplished, the Solution phase described above takes part and ends with the stress evaluation. The last phase, called post-processing, consists of a critical analysis of the obtained results. This can then either lead to a reiteration of the whole process to improve a specific aspect of the analysis, or the acceptance of the outcomes.

3.4.1 Static and Quasi-static analyses

A static analysis calculates the effects of *steady* loading conditions on a structure, while ignoring inertia and damping effects, such as those caused by time-varying loads. As a consequence, static analysis is generally used to calculate the system response caused by loads that do not induce inertia and damping effects. To achieve this condition, the basic assumption is that the applied loads and the structure's response do not vary with respect to time. If the loading conditions are varying slowly, such that inertial and damping effects are considered negligible, then they can be considered as quasi-static loads. Quasi-static formulations are governed by the static equilibrium equation as applied for static analyses (Zienkiewicz et Al., 2000). For the case of the gear meshing process, which includes relative motion of gears in mesh, the problem can be approached as quasi-static by conducting a series of FEA calculations at different relative positions of the gears. Each position is determined by a fixed angular displacement for the driven gear and an external load being "statically" applied to the driving gear. In a problem conditioned such as this, the equilibrium conditions have to be verified at each predetermined analysis step by applying the static analysis formulation written in a way that takes into consideration the dependency of the stiffness matrix on the unknown DOF values:

$$[K_t]\{d_t\} = \{F_t\} \tag{3.91}$$

Therefore, even though the applied loads and boundary conditions (except for contact boundaries defined later) are known for the entire time domain, the stiffness matrix $[K_t]$

depends on the unknown displacements $\{d_t\}$ due to the change in geometry of the system. This non-linear condition is defined as geometrical nonlinearity and will be explained in more detail in the next section.

A description of geometrical and contact non-linearity is provided in the following section along with a description of the Newton-Raphson iterative procedure used to solve non-linear problems. Due to the importance that contacts play in the analysis of gear systems a further explanation is given in the next paragraph.

3.4.2 Non-linear structural analysis

One of the first studies about computational procedures applied to the analysis of static and dynamic response of non-linear structures was carried out by Mondkar et Al., 1977. The main reasons for non-linearity in structural analysis are because of material behaviour, large deformations and contact conditions. Material non-linearity occurs when materials with a load-dependent response are used. In this case the solution of the analysis relies on the actual loading history. Geometric non-linearity is introduced when large displacements are encountered during the analysis. To handle analysis of systems that behave in such way, the current nodal coordinates are used in the element stiffness matrices, so that the analysis becomes position dependent. Contact non-linearity or boundary non-linearity arises for contact conditions between parts. Contacts can be regarded as discontinuous boundary conditions that depend on the actual system's configuration and applied loads. When contact occurs, the applied loads and generated displacements are not linearly related.

3.4.3 Non-linear structural solution method

A Quasi-static finite element formulation is defined by the set of matrices in Equation 3.91.This expresses the equilibrium condition at a specific time increment, t, through the stiffness matrix$[K_t]$, between the applied load vector $\{F_t\}$, and the unknown nodal displacements, $\{D_t\}$. As force and displacements are not linearly related, the system of resulting equations are non-linear. For such problems, Equation 3.91 can no longer be solved with a single solution based on the initial stiffness matrix $[K]$ due to the dependency of the non-linear stiffness matrix, $[K_t]$, on displacements, material and contact conditions (Nielsen 2013). In order to achieve a solution, an iterative process

with a series of linear approximations is needed. The iterative process solved with Newton-Raphson method implies the division of the load into multiple steps defined as load increments. Inside each load increment there are iterations based on results of the previous increment (Equation 3.92).

$$\left\{d_{t+\Delta t}^{(i)}\right\} = \left\{d_{t+\Delta t}^{(i-1)}\right\} + \left\{\Delta d^{(i)}\right\} \quad 3.92$$

Displacements and reaction forces are evaluated by applying the static formulation as follows:

$$[K_t]\left\{\Delta d^{(i)}\right\} = \{F_{t+\Delta t}\} - \{R_{t+\Delta t}\} \quad 3.93$$

in which the stiffness matrix $[K_t]$ is updated at the beginning of each load increment and $\left\{\Delta d^{(i)}\right\}$ is the nodal point vector of incremental displacements corresponding to iteration (i).

The second part of equation 3.93 represents the out of balance forces between the external nodal applied forces $\{F_{t+\Delta t}\}$, and the internal forces representing the system response $\{R_{t+\Delta t}\}$. The iterations continue until the difference between internal and external forces $\{F_{t+\Delta t}\} - \{R_{t+\Delta t}\}$ is within an imposed tolerance determined by the convergence criterion used. Convergence is an indication of how well equilibrium is satisfied.

The schematic of the Newton-Raphson method applied to the solution of a one DOF problem is represented in Figure 3.30 where the iterative solution of a non-linear force-displacement function requires four equilibrium iterations before achieving convergence.

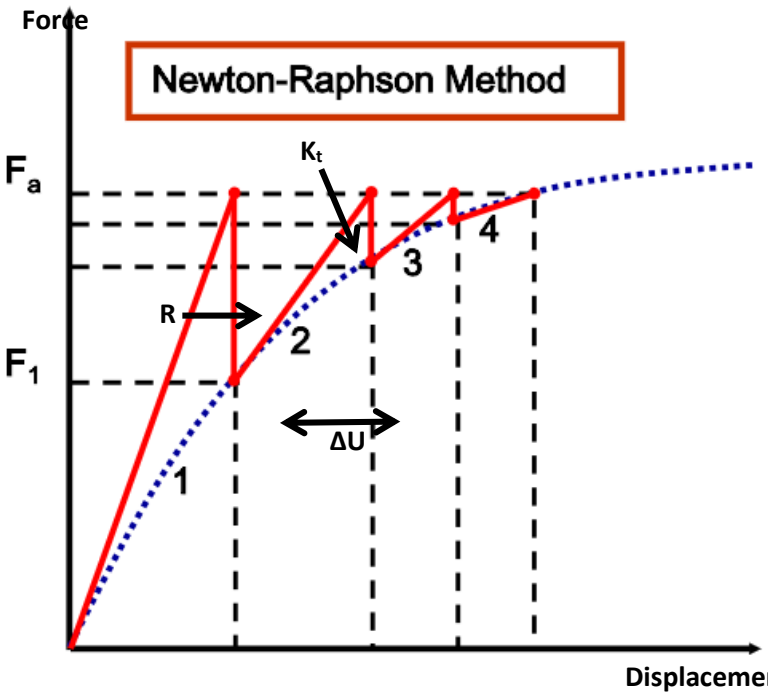

Figure 3.30 – Newton-Raphson iterative solution, (ANSYS®, 2016; ANSYS 15.0, 2015).

The iteration method starts with setting up the stiffness matrix $[K_t]$ for the first iteration by using the initial conditions imposed to the system. After the first iteration, with the stiffness matrix $[K_t]$ represented by segment 2 in Figure 3.30 and the internal forces $\{R\}$, it is possible to determine the Incremental displacements {ΔD} that have to be added to the previous displacement solution. Equilibrium iterations are performed at each load increment until the difference between external and internal loads is within the accepted tolerance. Typical values for force convergence criteria range from 0.1 to 0.5% of the applied load.

3.4.4 Solution of Structural Contact Problems

The interaction between structural parts plays a crucial role in the analysis of mechanical systems. Mechanical problems that involve contacts are inherently non-linear due to the produced change in status of the system. Depending on the contact condition between parts, the stiffness of the whole system can experience an abrupt change resulting in a highly non-linear behaviour (Konter, 2000). Because of the variable nature and the number of relevant factors involved, solution of contact problems is a difficult task. Contact conditions depend on the material properties, applied loads and boundary conditions that determine deformations, and eventually contact when two separate

surfaces become mutually tangent. Due to the highly non-linear dependency with the above mentioned parameters an iterative solution scheme is required to conduct contact analyses (Oysu, 2007).

Contact can be considered as a discontinuous constraint that is only applied when the actual interaction between mating parts occurs. In the areas where contact is expected, special elements have to be defined in order to include the relevant formulation. Contact elements conform to the underlying geometry and existing mesh and add contact compatibility conditions to the local and global stiffness matrices. An element's formulation is modified by taking into account the contact force (F_c) as an external force acting on the system as indicated by Equation 3.94

$$[K_t + K_C]\{\Delta d^{(i)}\} = \{F_{ext}\} - \{F_c(d)\} - [K]\{d\} \qquad 3.94$$

The non-linear Equation 3.94 is an extended version of Equation 3.93 and includes an extra term for the stiffness matrix that takes into account the influence of contact on system's response as well as the contact force applied from one body to the other, to avoid inter-penetration at the contacting interface. This prevention of inter-penetration is defined as contact compatibility enforcement, and is performed by penalty-based contact formulations. For such formulations contact force is expressed by Equation 3.95

$$\{F_C\} = [K_C]\{x_p\} \qquad 3.95$$

where $[K_C]$ is the contact stiffness that depends on the material stiffness of contacting bodies and $\{x_p\}$ indicates the amount of penetration as shown in Figure 3.31

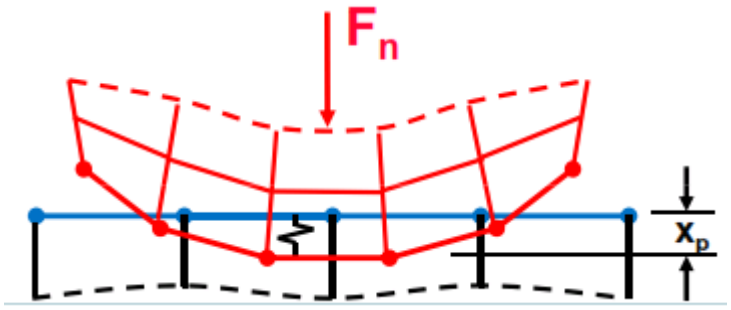

Figure 3.31 - Two bodies in contact that experience penetration (ANSYS®, 2016).

Penalty-based formulations tolerate a small amount of interpenetration in order to increase the robustness of the solution. This allows the contact to be stable avoiding the oscillatory effect due to a sudden change between penetration and presence of gap.

Given that both force and displacement on the contact boundary are unknown, a contact search is necessary at each iteration to find nodes that violate the impenetrability condition and apply a correction force (contact force) to re-establish compatibility. The two-step contact formulation process is shown in Figure 3.32 where violated nodes (B) within contact element candidates (A) are found and a contact force is applied to re-equilibrate the system.

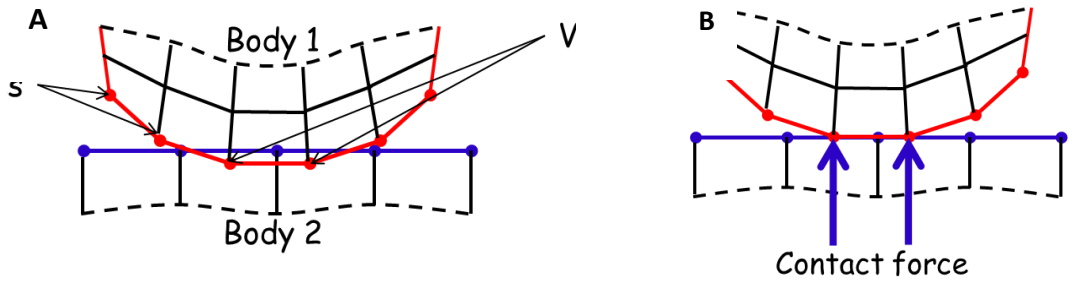

Figure 3.32 - Schematics of the process to re-establish compatibility and the applied contact force (ANSYS®, 2016).

Contact is not necessarily detected at nodal locations; penalty-based formulations use a number of virtual integration points in order to increase the number of sensible points on the element area as shown in Figure 3.33. In Equation 3.96 the resultant contact force F_c is the result of the sum of smaller contact force components acting at the integration points.

$$F_C = \sum_{i=1}^{N_n} F_{ci} \qquad 3.96$$

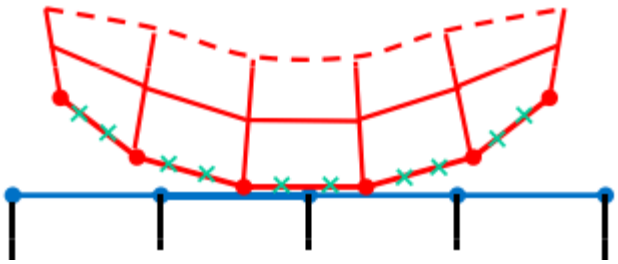

Figure 3.33 - Virtual integration points for contact detection (ANSYS®, 2016).

If, as for the case of gears in mesh, there is friction between the two bodies in relative motion a contact force in the tangential direction also exists. Similarly, for the impenetrability condition, in the tangential direction a sliding condition is imposed. The formulation is equivalent to the one explained above for normal contacts and is expressed with Equation 3.97 as follows

$$\{F_f\} = [K_f]\{s\} \tag{3.97}$$

where $\{F_f\}$ is the friction force that is generated when two bodies stick, $[K_f]$ is the tangential stiffness that relates to the shear strength of the contacting bodies material and $\{s\}$ indicates the sliding distance. On the other end, for the case of frictional contacts that allow sliding and relative motion, the Coulomb friction force is expressed as follows:

$$\{F_f\} = [\mu]\{F_C\} \tag{3.98}$$

In Equation 3.98 $[\mu]$ represents the friction coefficient and is function of material properties and surface roughness, and $\{F_C\}$ is the normal contact force that balances the external loads.

3.5 Conclusion

The construction method of the involute tooth profile geometry is given in a parametric form. As gear geometry is function of multiple parameters, a detailed analysis of the effect caused by the modification of each parameter is done in this chapter. To this follows the analytical definition of geometrical, manufacturing and operational boundaries used in the following chapter for the determination of design domains of spur gear pairs. Furthermore, the background theory of the finite element method used in this thesis, focusing in particular on the solution of non-linear problems such for the case of gears has been treated in detail.

4 Parametric multi-dimensional design space

Conventional gear design is based on a standard rack cutter of which size and proportions such as addendum, dedendum, cutter tip radius and pressure angle have standard values and completely define the rack geometry. Standardization has also been adopted to simplify the gear design process and hence reduce the number of parameters to define. In fact, once the number of teeth is defined in accordance with the desired transmission ratio, the design choice changes from being multi-parametric to mono-parametric with the only variable left to be determined being the profile shift. To ensure correct meshing, the geometry of tooth profiles has to be carefully determined. As the number of possible independent design parameters, even for the simplest case of a spur gear, is sizeable, there is the necessity to control the synergic effect of design parameters and identify a practical range of values that leads to the definition of a confined domain (Amani et Al., 2017). The domain boundaries are determined by the limiting conditions imposed by manufacturing processes and geometrical compatibility, and delimit an area that contains all the feasible combination of parameters that fulfil the pre-imposed geometrical requirements. A graphical study of the imposed limiting conditions determined in the previous chapter by Equations 3.44, 3.51, 3.55, 3.79, finds a useful graphical representation with the use of two dimensional blocking contours as described by (Goldfarb et Al., 2005; Kapelevich, 2013). This technique uses a number of multi-level curves representing the aforementioned manufacturing and operational conditions for the mating gears. The graphical representations of Equations 3.51, 3.54, 3.55, 3.79 describing top land thickness, corner interference and contact ratio are surfaces in the x_1x_2 domain as shown in Figures 4.1, 4.2, 4.3. Although any set of variables could have been used for the two axes, $x_{1,2}$ were used due to the vast use of profile shift in industry in order to facilitate the comprehension of the generated domains. The range of variation for x_1 and x_2 from -3 to +3 displays the geometrical functions in their entirety but does not represent the practice in which the actual range is considerably smaller.

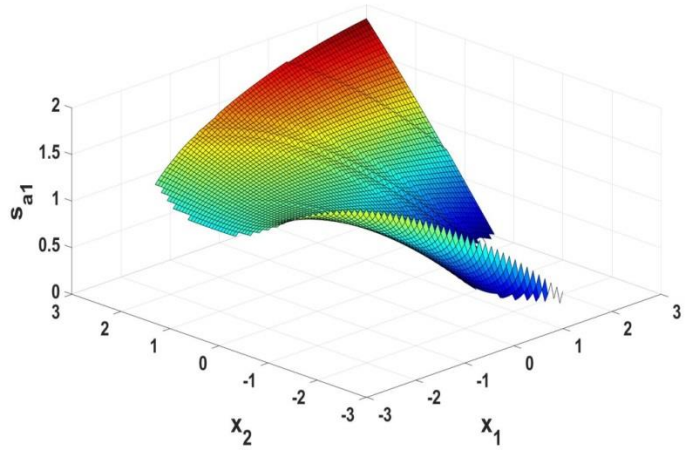

Figure 4.1 - Graphical representation of the top land thickness function in the x_1x_2 domain for gears with $N_{1,2}$=20, α=20° and m=1 mm.

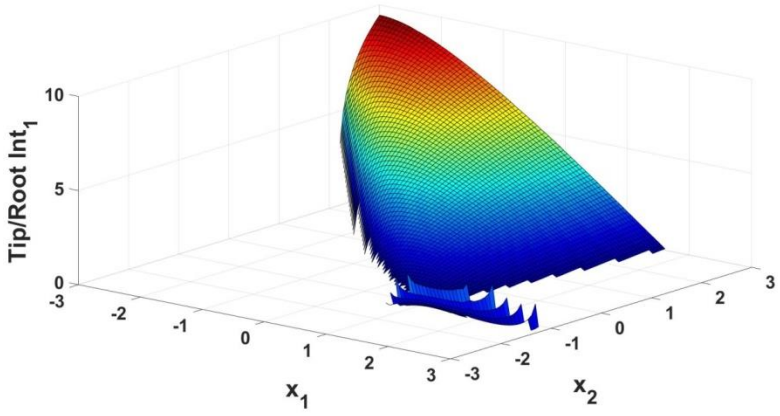

Figure 4.2 - Graphical representation of the corner interference function in the x_1x_2 domain (for $N_{1,2}$=20 α=20° and m=1 mm).

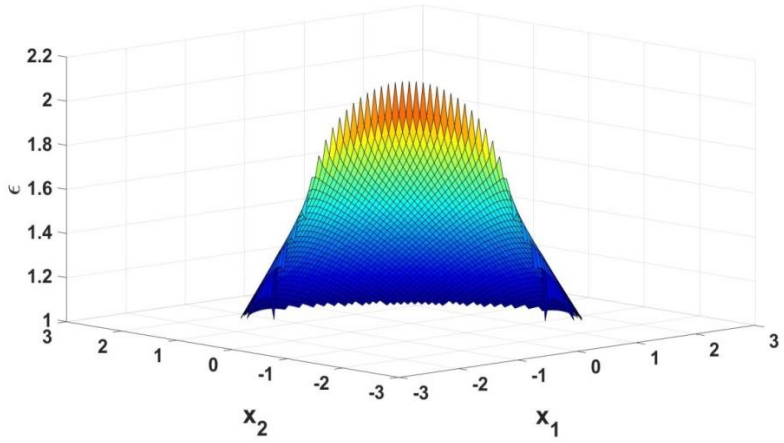

Figure 4.3 - Graphical representation of the contact ratio function in the x_1x_2 domain (for $N_{1,2}$=20, α=20° and m=1 mm).

The intersection of the surfaces with a planes parallel to x_1x_2 and placed at a certain height corresponding to the value of interest for the variable under consideration gives the limiting curves of a design space shown singularly in Figures from 4.4. to 4.7 and in the form of a design domain shown in Figure 4.8.

A Matlab® script (appendix A) has been written in order to generate an enclosed area delimited by contour lines corresponding to the geometrical boundaries and operational constraints such as Tooth tip thickness, Undercutting, Contact Ratio and Tip/Root Interference.

Figure 4.4 shows the limiting lines for tooth thickness at the addendum circle. The lines plotted in Fig 4.4 lie on three different levels of the vertical axes in Figure 4.1 and represent the minimum allowable top land thickness $s_{a1,2}$=0.2 determined from practice, the generally used $s_{a1,2}$=0.4 and the theoretical minimum for $s_{a1,2}$=0 corresponding to pointed gear teeth. It can be seen that by increasing the tooth thickness at the addendum circle the area left between the opposite curves is reduced.

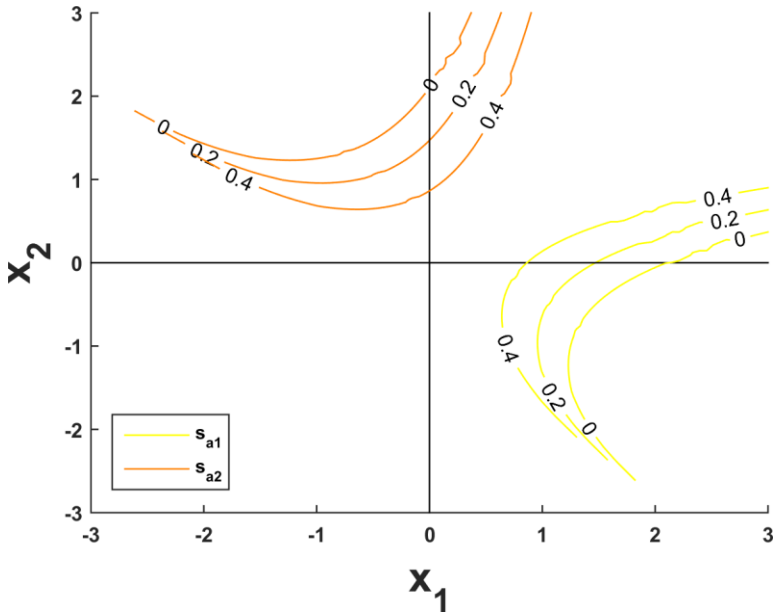

Figure 4.4 - Top land thicknesses in the $x_{1,2}$ domain for a spur gear pair with α=20°, N1,2=20, m=1 and standard profile parameters according to ISO 53 A.

Figure 4.5 shows the lines that determine the absence of interference for correct meshing. The limiting condition of interference is defined at the level $Int_{1,2}$=0 of Figure 4.2 when the tooth tip is tangent to the root fillet of the mating gear. In Figure 4.5, the

conditions of interference for the pinion and gear defines an enclosed area within which only positive values are present. Inside the lines, the mating gears are not interfering making any combination of profile shifts possible.

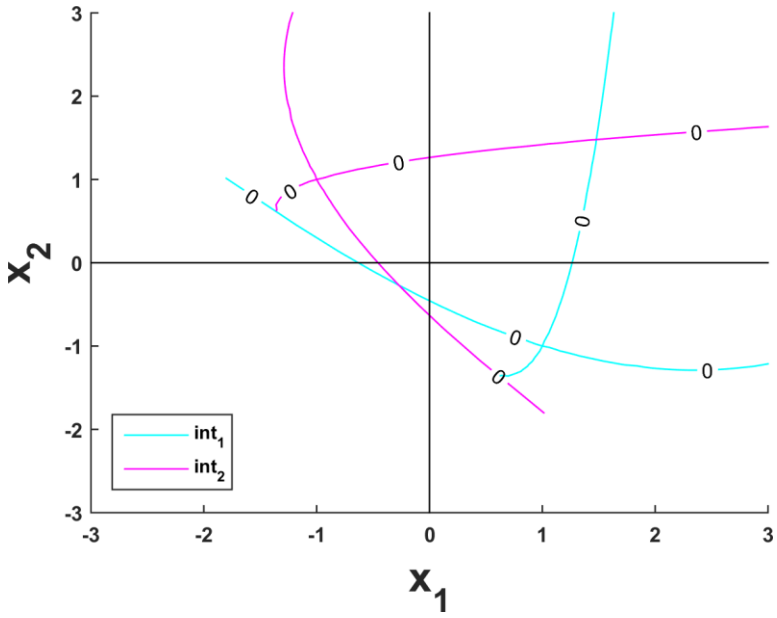

Figure 4.5 - Tip/root interference limit in the $x_{1,2}$ domain for a spur gear pair with α=20°, N1,2=20, m=1 and standard profile parameters according to ISO 53 A.

The third operation criterion considered is the Contact ratio shown in Figure 4.6. Also in this case the curve is the surface profile plotted in Figure 4.3 at the levels of interest. Contact ratio has a theoretical limit ε =1 in order to ensure a constant velocity ratio. This value has to be increased to ε =1.2 if manufacturing and assembling deviations are considered. Standard values of ε for normal contact ratio gears span from 1.4 to 1.6. By increasing the limit for ε, the limiting curves move towards the centre limiting the use of high values of profile shift coefficients as shown in the figure below.

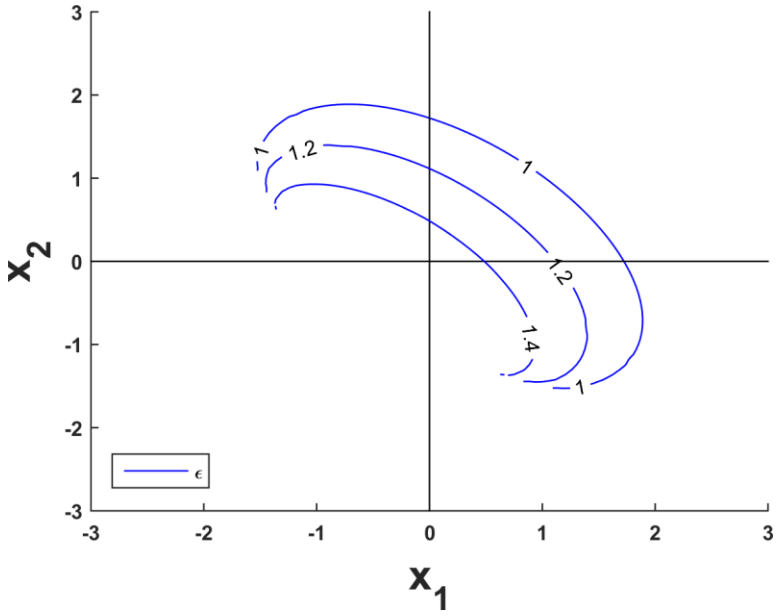

Figure 4.6 - Normal contact ratio in the $x_{1,2}$ domain for a spur gear pair with α=20°, N1,2=20, m=1 and standard profile parameters according to ISO 53 A.

In addition to the cases already considered it is necessary to add the limiting condition for undercutting. The minimum amount of profile shift to use in order to avoid undercutting is expressed by equation 3.45 and is shown in Figure 4.7 represented by two straight lines for x_1 and x_2.

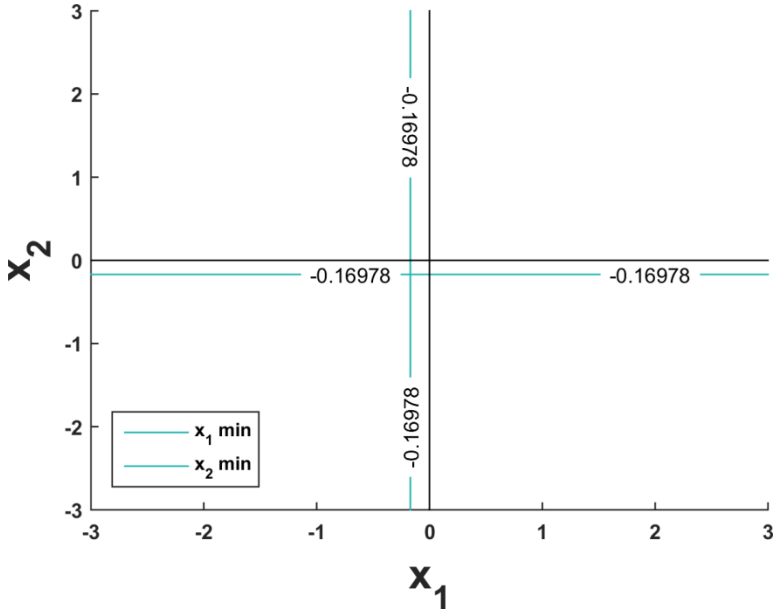

Figure 4.7 - Undercutting limits in the $x_{1,2}$ domain for a spur gear pair with α=20°, N1,2=20, m=1 and standard profile parameters according to ISO 53 A.

The intersection between the above-mentioned limiting curves defines an enclosed region that allows any combination of profile shifts for the given geometrical parameters. For a spur gear pair, the domain boundaries depend on the desired gear ratio and so the number of teeth of the mating gears and on initial basic rack parameters such as module, pressure angle and addendum factor. Moreover, they depend on the pre-defined value imposed by the designer, whether based on standards or practical considerations for the case of custom/non-standard designs or for research purposes.

4.1 Multi-dimensional contour plots

The superimposition of the limiting conditions shown in the previous paragraph leads to the definition of an enclosed area defined by the intersection of lines representing operational and manufacturing limits.

Figure 4.8 shows the area of feasible values for a standard spur gear pair of parameters $N_{1,2}$=20, $h_{a1,2}$*=1, α=20°, m=1 of which, the considered limits assume their minimum possible value in accordance with practical considerations to maximise the size of the internal area. The point corresponding to the combination of x_1 and x_2 must lie within the area in order to fulfil the criteria stated above. However, Figure 4.8 includes additional lines in the plane x_1 x_2 that have a peculiar physical meaning. The actual centre distance lines a_w are plotted as they represent, with the gear ratio, basic requirements usually predetermined at the beginning of the design process.

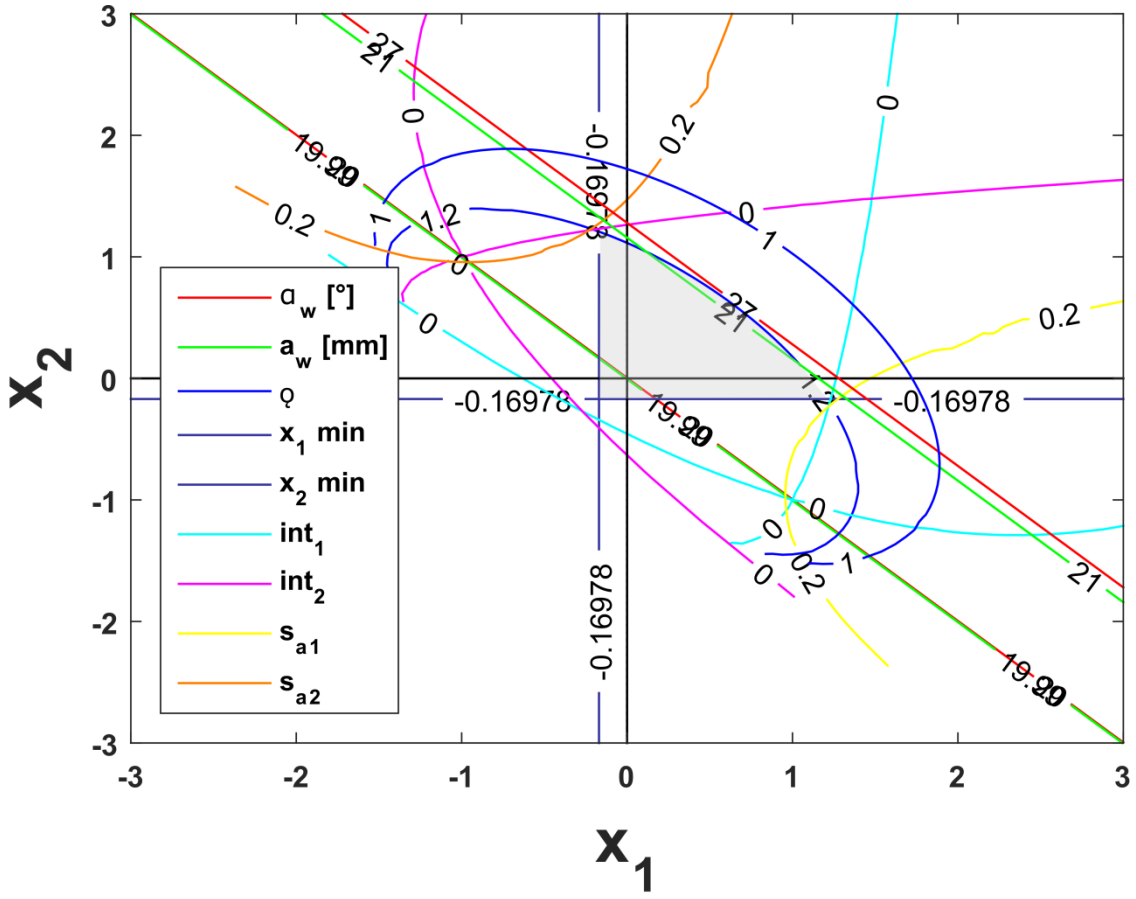

Figure 4.8 - Multi-dimensional design space in the $x_{1,2}$ domain for a spur gear pair with α=20°, $N_{1,2}$=20, m=1 and standard profile parameters according to ISO 53 A.

The area of possible combination, for the set of parameters used, is limited in the first quarter by the minimum contact ratio and for the remaining part by lines that indicate the occurrence of undercutting for the pinion and gear. The point of coordinates x_1=-0.169; x_2=1.242 lies at the intersection between minimum top land thickness and corner interference for the gear, the undercutting limit for the pinion and minimum contact ratio. Similarly, the point with coordinates x_1=1.242; x_2=-0.169 is at the intersection of the minimum top land thickness and interference for the pinion, the limit of non-undercutting for the gear as well as minimum contact ratio. Furthermore, two green lines with constant centre distance a_w are shown: one is passing through the centre of the plot and corresponds to the condition of balanced profile shift with a null overall value such that $\sum x_{1,2}$=0; the other is a tangent to the minimum contact ratio ε=1.2 that limits the region of possible combination in the first quarter. In red are shown the lines that represent the working pressure angle α_w: one passing through the centre and the

other tangential to the limit condition imposed by the contact ratio. If the sum of profile shifts is null, then the working centre distance and the working pressure angle would coincide with the reference values. In this case, the two line passing through the centre are coincident and with values a_w=a=20 mm; α_w=α=20° (a_w=19.99 is only for display reasons otherwise the two lines would have been indistinguishable). The other set of lines indicate the maximum value of centre distance and consequently working pressure angle achievable by applying a positive profile shift combination. In this case a_w=21.09 mm and α_w≠α=26.9°. As they both are directly interconnected, a line representing a_w or α_w is always coincident with the line representing the other parameter of the two. If those lines cross the area of feasible combinations, then it is possible to choose the corresponding profile shift coefficients for any point that lies on them.

4.1.1 Influence of pressure angle

A further evolution of the domain is made by taking into account a third fundamental design variable, the profile pressure angle α. While the application of profile shifts does not involve the modification of the cutting tool, varying the geometrical proportion of the tooth profile would determine a deviation from the standard rack geometry. If pressure angle α is the considered variable, the combination of x_1, x_2, and α give singular kinematic and load carrying characteristics while fulfilling the required manufacturing and operational requirements. This enables the design of custom non-standard gear drives based on the requirements of a specific application.

In order to study the effect of modifying α, the evolution of the feasible domain is shown across a number of plots for different pressure angles in Figure 4.9. For all the plots, the only geometrical parameter that has been varied is α while $N_{1,2}$=20 and the other parameters are in accordance with ISO 53 Profile A. Starting with a value of α=20°, the same as the one plotted above, it can be noticed that the domain of interest becomes smaller when the pressure angle increases. The first effect produced is that the limit of undercutting increases and lets other boundary conditions to limit the area. From the second plot, for α=22.5°, minimum top land thickness and interference occur in the

second and fourth quarters while in the third quarter the limit for undercutting is replaced by corner interference.

The condition described becomes more evident for a further increase in pressure angle to the point that for α=32° the area of existence does not include any positive value of profile shift as the minimum top land thickness lines are intersecting at $x_{1,2}$=0. For this condition only a narrow range of negative profile shifts is usable before the interference limit occurs. As already seen in section 3.3.4, an increase of pressure angle determines a reduction of contact ratio; this is shown in the plots with the curves of ε=1.2 getting closer to the centre, reducing the feasible domain. In the last plot, for α=32°, the contact ratio does not work as a limiting condition because of the occurrence of the s_a limit. For that condition, due to the primary influence of minimum top land thickness, the maximum possible contact ratio is given by the curve that passes through the interference point $s_{a1,2}$ and is equal to 1.29. A variation of profile pressure angle also limits the centre distance to be increased and consequently the maximum achievable α_w. Maximum centre distance occurs at the intersection with ε_a=1.2 and is equal to 21.09 mm, which corresponds to a maximum working pressure angle of 26.9°. For α=22.5° the maximum a_w decreases to 21.02 mm and for that configuration α_w assumes a value of 28.48°. For α=25° maximum a_w drops below 21 mm and at the point of tangency is equal to 20.94 mm while α_w=30.05°. The trend explained can be followed in Figure 4.9 by tracking the line of a_w=21 mm in all the plots. It is important to notice that as pressure angle does not alter the centre distance for any value of α, the lines corresponding to the reference centre distance (20 mm in this case) in accordance with module and number of teeth pass through the origin $x_{1,2}$=0 and are always coincident with the lines of reference pressure angle α that varies for any plot.

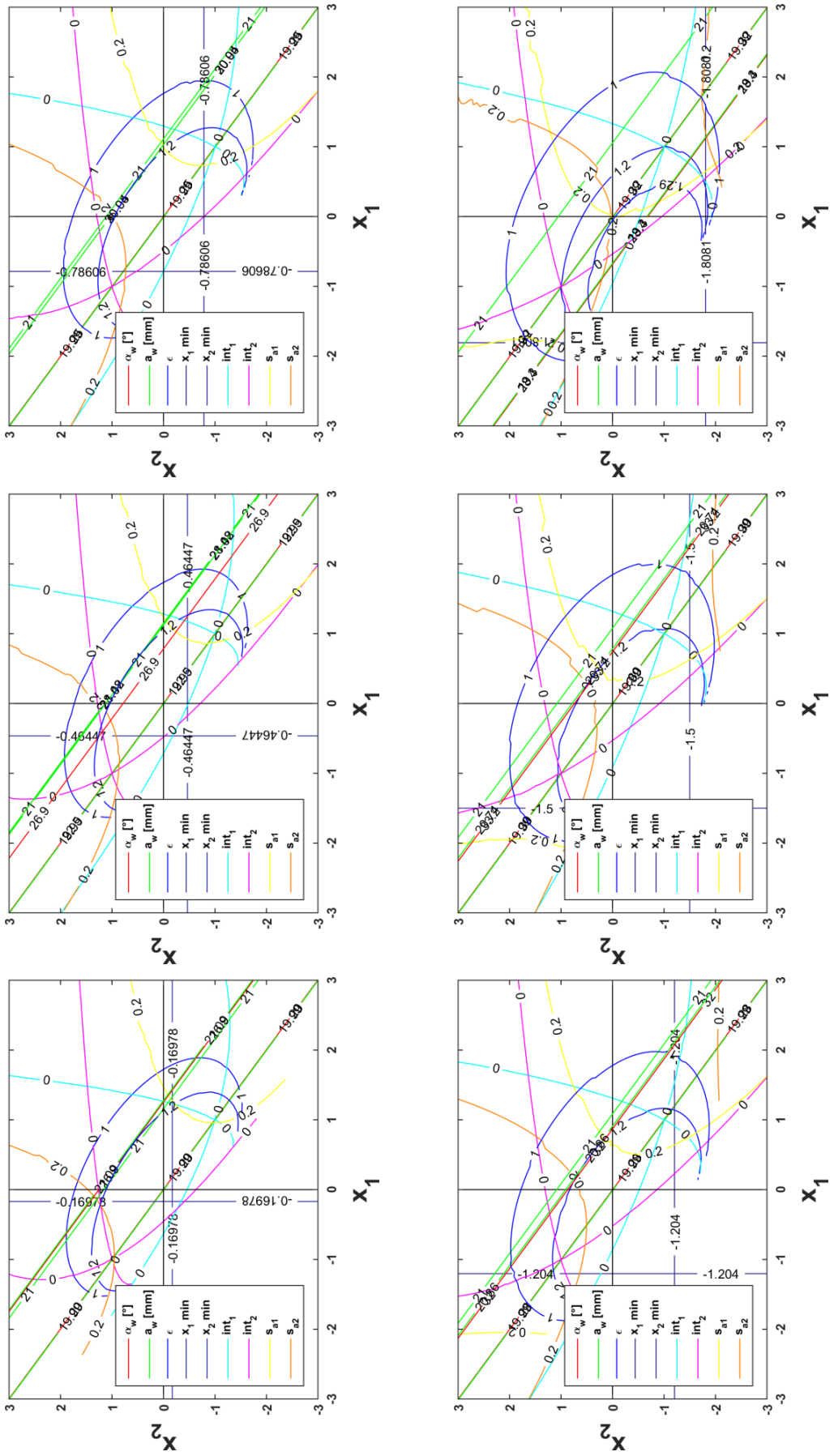

Figure 4.9 - Evolution of the feasible domain as function of profile shifts $x_{1,2}$ and pressure angle α.

4.1.2 Influence of addendum length

Similarly, to what explained with regards to pressure angle, the influence of the addendum length on the x_1x_2 domain is carried out in the following Figure 4.10, where a number of pinion geometrical configurations with different addendum lengths, h_{a1} are plotted. The basic rack addendum factor (Figure 3.6 in section 3.2) is one of the main parameters that defines the overall tooth geometry and has been standardized with a value of 1. Other values are used in practical applications where a deep tooth form or short cut toothing is used. In order to achieve a modification of the addendum length of the actual gear, the base rack addendum h_{a1}^* needs to be adjusted by the quantity $h_{a1}^*=h_{a1}$. A variation of the addendum length does not cause an alteration of the undercut limit as the modification occurs above the pitch circle and so $x_{1,2\,min}$ is the same for any value of h_a^*. As the modification is applied to the pinion while the gear has standard proportions, only the top land thickness of the pinion s_{a1} changes while s_{a2} is constant. Corner interference occurs at the upper portion of the gear fillet with the tip of the pinion clashing on the non-involute portion of the gear; for this reason, by modifying h_{a1} the limit for interference affected is the one occurring at the gear fillet int_2. Contact ratio is simultaneously affected by the geometry of the two gears and so varies as function of h_{a1}. Also in this case, $N_{1,2}$=20 and α=20° determine a centre distance of 20 mm and a working pressure angle of 20° for $x_1=x_2$=0 and $\sum x_{1,2}$=0. Starting with the standard tooth geometry (h_{a1}=1), also shown in Figure 4.10 and extensively described above, a reduction in the addendum length for gear 1 creates a smaller x_1,x_2 domain due to the limitation imposed by the contact ratio. For the set of parameters used here, h_{a1}=0.5 is the minimum usable addendum length for $x_1=x_2=0$; for any smaller addendum length the plot centre would lie in the domain of contact ratios < 1.2. The area in this case is delimited by ε and $x_{2\,min}$ in the second quarter, by $x_{1\,min}$ and x_{2min} in the third and by ε and x_{1min} in the fourth quarter. The imposed tooth thickness for the pinion s_{a1}=0.2 is far from the delimited area. By increasing h_{a1} to 0.8 the contact ratio increases and, at the same time, the interference limit for the gear becomes closer to the area as well as to $s_{a1}=0.2$. For $h_{a1}=1.15$, above the standard value $h_{a1}=1$, the condition of corner interference starts to delimit the area in the first, second and fourth quarter in conjunction with contact ratio and undercut limits. The limit condition is reached for

h_{a1}=*1.3* for which a very narrow window of possible x_1x_2 in between int_2 and s_a is shown placed almost entirely in the first quarter of the plot. Finally, in the plot for h_{a1}=*1.4,* an area cannot be determined due to the fact that s_a=0.2 crosses the curve of int_2 cancelling out the area shown for h_{a1}=*1.3.*

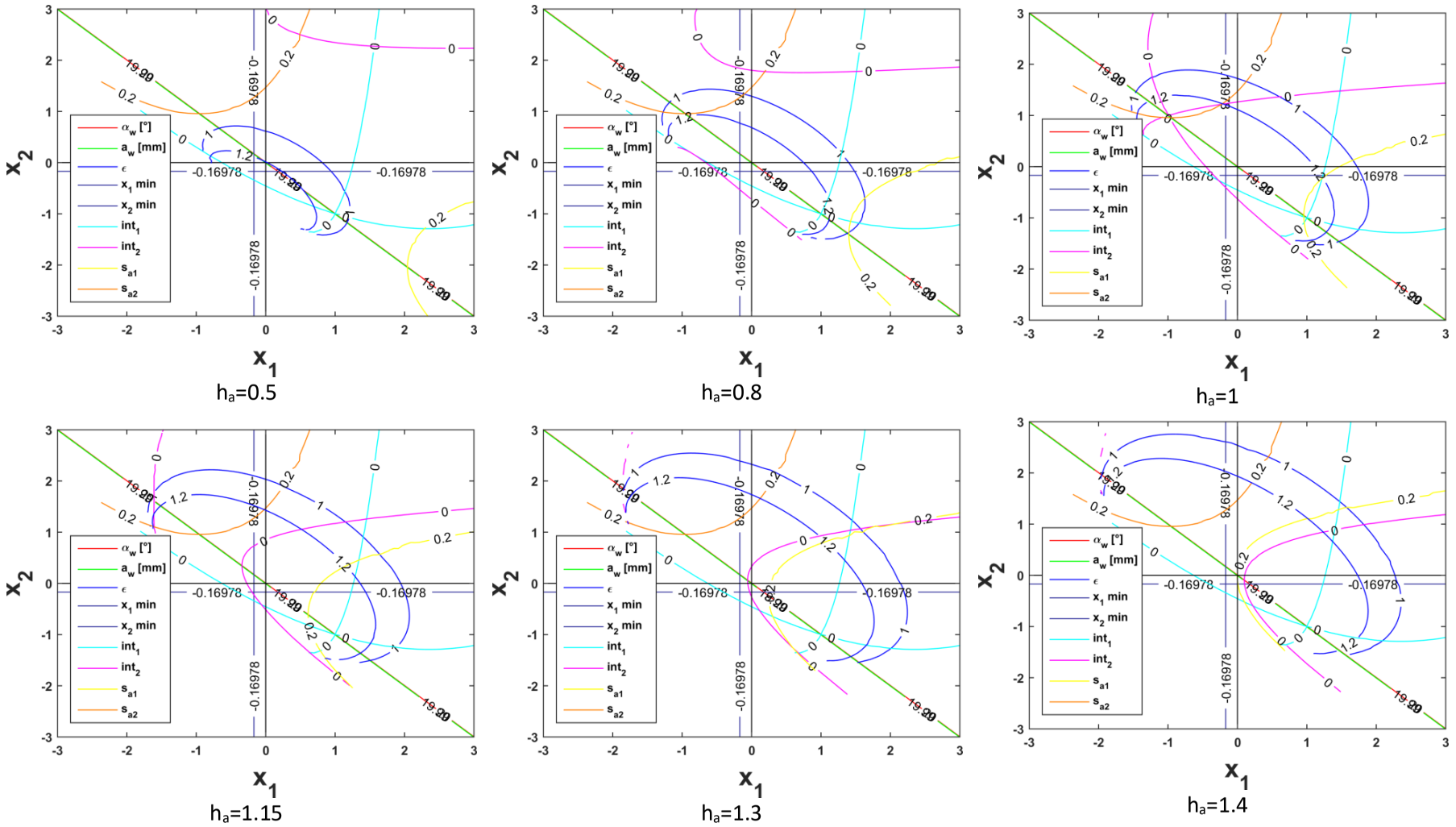

Figure 4.10 - Evolution of the feasible domain as function of profile shifts $x_{1,2}$ and pinion addendum length h_{a1}..

4.2 Conclusion

The domain of feasible combination of geometrical parameters allows the limiting conditions for a given selection of involute profiles to be defined and visualized, and allows the location of the feasible gear pairs that fulfil the manufacturability and geometrical compatibility limitations. The multi-parametric model considers the simultaneous effect of pressure angle, module, addendum and dedendum length and number of teeth of the mating gears. Production limitations in terms of tooth pointing and undercutting were considered as well as geometrical compatibility and generated contact ratio. The multi parametric design approach shown above can be adopted for the study of any dependent or independent geometrical parameters. It allows the analysis of multiple possible gear combinations in order to find the most suitable solution for the application requirements. This implies an advantage in performance that consequently increases the competitiveness of the products to the point of justifying the extra cost for custom cutting tools. For advanced engineering products such as gearboxes used in aviation and automotive the application of non-standard geometries is the norm given that the maximization of the transmitted power within a lighter and smaller size is of main importance (Kapelevich et Al., 2002).

5 Spur gear pair performance analysis

In this chapter numerical analyses of spur gear pair with different geometrical characteristics are presented and results elaborated in detail. Contact and bending stresses have been evaluated by means of the Finite Element Method and the mechanical characteristics for each geometrical configuration have been estimated and compared to a baseline with standard parameters. Several driving/driven gear models were considered and of the two gears in mesh, only the geometry of the driven gear has been changed so that the effect of the modification is isolated and not compensated with a corresponding profile alteration on the mating gear. For the case of pressure angle the modification was applied to both gears in order to ensure regular meshing. The stress state is evaluated for 100 contact location points along the gear tooth flank and compared with the one corresponding to the stress state of a reference profile tooth: ISO 53.2 Profile A (hf 1.25/ ρf 0.38/ ha 1.25), α=20° and x=0 (ISO 53, 1998). To reduce the number of parameters studied, the number of teeth, module and root fillet radius have been fixed accordingly to Table 5.1. The range of variation for the modified parameters was imposed by functional and manufacturing limitations as described in Chapter 3 and 4.

Table 5-1 – Gear parameters for driving and driven gears

Parameter	Driving	Driven
Number of teeth N	20	20
Module [mm]	1	1
Dedendum factor. h_f	1.25	$1<h_f<1.5$
Root fillet radius coeff. ρ_f	0.38	0.38
Addendum factor. h_a	1	$0.5<h_a<1.3$
Pressure angle α [°]	20<α<32	20<α<32
Profile shift coeff. x	0	-0.2<x<0.5

A graphical representation of the tooth profiles affected by the considered geometric parameters is given in Figure 5.1 where the extreme cases of the parameters range of variation are shown. The standard ISO 53.2 Profile A, with α=20° and x=0 (blue) is compared with: α=32° tooth profile in green, and x=+0.5, and x=-0.2, in red and black respectively, and in yellow a profile with h_a=1.3.

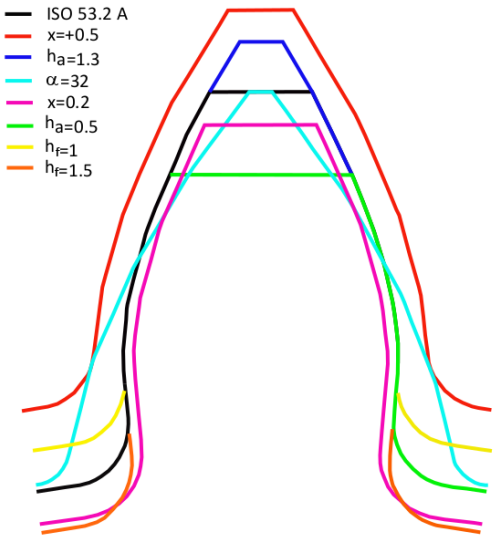

Figure 5.1 – Comparison between tooth profile outlines including the standard ISO 53.2 A against non-standard profiles in which only one parameter per time is modified.

This chapter also introduces the machine design software KISSsoft®, through which all the gear models for this study are created. KISSsoft® was also used for the performance calculations in accordance with the rating standard ISO 6336 method B (2006). In the next paragraphs, there follows a detailed explanation of FEA settings for the solution of gear problems in order to achieve convergence and perform the most accurate results possible in relation to the applied loads and constraints; the description focuses on mesh modelling, contact modelling, and analysis settings. In the end, in-depth analyses and explanations of performance results supported by graphical displays are given and justified.

5.1 KISSsoft®

Traditionally, the design of gears and transmissions requires an in depth knowledge of the rating standards in the field. Despite that, the high amount of technical considerations coupled with the considerable number of iterations needed to reach a result with an acceptable compromise of performance intended as strength, life, weight, or efficiency can be extremely long. This happens even more for complex systems such as planetary gear trains where multi-mesh conditions occur.

KISSsoft®, developed by KISSsoft AG., is one of the most frequently used computer programs for the design of machine components. The software is specifically developed for the sizing of gears, shafts and bearings, screws, springs, joining elements, and belts and in general all the components that are found in a transmission system. Optimization routines are also implemented in order to optimize existing designs or fine tune the design for a specific requirement. The software includes a library of the currently valid rating standards (ISO, AGMA, DIN) and performs the calculations according to them. Geometry of components can be evaluated and customized on the base of the user requirements. Strength calculations, safety factors, fatigue life and many other performance parameters can be calculated and easily exported in a detailed report. Graphical animations and display are also features offered by KISSsoft that allow comparison between different design solutions. Gear tooth profiles can be modelled in accordance with the standards or customized by varying each single parameter that defines the tooth shape. The modifications can be applied both to the cutting tool and to the final tooth profile by using the "constructed involute" function. Usefully, any determined geometry can be exported into the 3D CAD software Solidworks®. The direct associative interface between the two software ensures that the real tooth form is maintained in the file transfer which guarantees accuracy in the following analysis or in the manufacturing stage.

In this thesis KISSsoft (2017) has been largely used for the generation of gear models to be exported into the FEA environment. The software has also been used to perform analytical calculations based on the current standard ISO 6336 Method B (2006) for all the geometries studied. Results were used as guideline and were compared with Finite Element Analysis in order to find the level of agreement between numerical and analytical methods used for validation.

5.2 Gear Modelling

One of the critical aspects in the numerical analysis of mechanical systems is the creation of the solid model. Geometry clearly plays a crucial role on the accuracy of results so it is of fundamental importance that the mechanical component is modelled as accurately

as possible. In this study the gear models are generated in two consecutive steps; first, to generate gear profiles, the KISSsoft constructed involute function, that allows a full customization of the involute profile, has been used. The second step sees the geometry data transfer from KISSsoft through a direct associative interface to SolidWorks. 3D models are automatically created in the CAD environment when the export function in KISSsoft is used. Even for the case of a multiple-gear system, gear models are generated individually.

If the purpose is to study the gear system in its interity, then the assembly process is required. SolidWorks allows the user to create multi-body systems through “mate” functions in order to place bodies in the space in relative positions and replicate real world constraints. For a gear system this translates into the definition of the position of gear centres by applying the working centre distance value and the tooth mesh positioning in order to avoid any gap or superposition between solid parts (mating teeth) as shown in Figure 5.2.

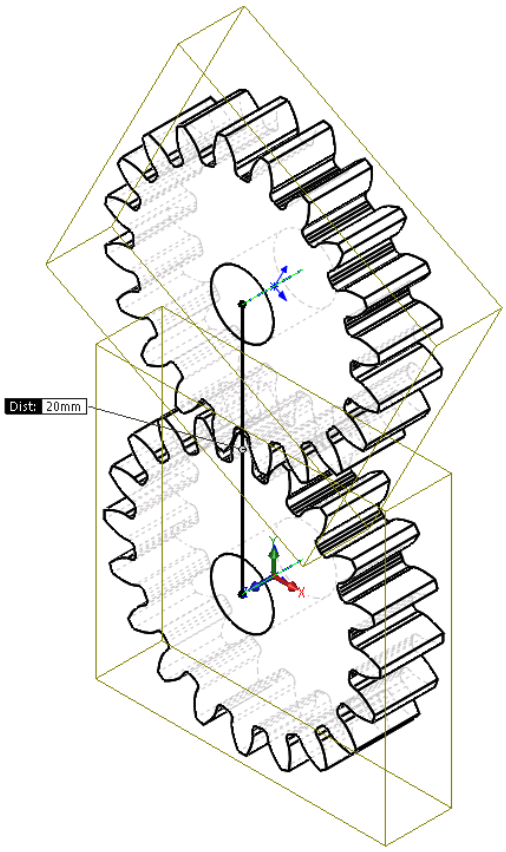

Figure 5.2 – Assembling procedure in SolidWorks of a 3D spur gear pair.

From this, all the models are exported, again through a direct associative interface, into the FEA environment for the final numerical analysis. Due to a lack of computational resources, the problem has been downgraded and treated as a 2D analysis in order to reduce the solution time. To obtain this conversion, an extra step is needed. The 3D models previously assembled are treated in the ANSYS built-in CAD environment 'DesignModeler' for surface extraction. Due to the axisymmetric shape of the gear bodies, the "mid-surface" corresponding to the central cross section has been extracted and used for the subsequent 2D numerical analyses.

The process described above ensures that the geometrical details of the original model are maintained without losing any accuracy. The process is also interactive as any upstream modification is automatically implemented in the following stages.

5.3 ISO 6336 Method B

As already introduced in the literature survey chapter, ISO 6336 (2006) is composed of five parts. Part 1 covers the basic principles of gearing and provides the general influence factors; part 2 and 3 cover the calculations respectively for surface durability and bending strength; part 5 covers the aspects related to materials and allows to establish limit stress numbers; Part 6 provides the information necessary for the calculation of the service life of gears subject to variable loading.

The analytical calculations according to ISO 6336 Method B were performed in KISSsoft for all the considered geometries and a brief description of the ISO calculation procedure including the main analytical expressions and the factors of influence is given below. Starting with the calculation of maximum and permissible contact stress, these two quantities are based on Hertzian contact theory adjusted by modification factors. The three main fundamental stress equations 5.1, 5.2, 5.3 given below allow to calculate the quantities σ_{H0}, σ_H and σ_{HP} respectively nominal contact stress, calculated contact stress and permissible contact stress.:

$$\sigma_{H0} = Z_H Z_E Z_\varepsilon Z_\beta \sqrt{\frac{F_t}{d_l b}\frac{u+1}{u}} \qquad 5.1$$

$$\sigma_H = Z_B \sigma_{H0} \sqrt{K_A K_V K_{H\beta} K_{H\alpha}} \leq \sigma_{HP} \quad 5.2$$

$$\sigma_{HP} = \frac{\sigma_{Hlim} Z_{NT}}{S_{Hmin}} Z_L Z_V Z_R Z_W Z_X \quad 5.3$$

The relations between the calculated quantities are such that contact stress σ_H must be less than the permissible contact stress σ_{HP} for preventing failure and verify the design. In equation 5.3, the term σ_{Hlim} is the allowable contact stress number described in ISO 6336 part 5, and is based on a contact pressure that may be sustained for a specified number of cycles without the occurrence of progressive pitting. The factors used in equations 5.1, 5.2 and 5.3 can be distinguished in two categories: Z-factors are determined by gear geometry, material and lubricating conditions; K-factors are related to conditions of general influence. Since the values used in this work for comparison and reference reasons are the ones relative to nominal contact stress, a general description of the factors in Equation 5.1 only is given hereafter:

- Z_H is defined as zone factor and takes into account the effect of flank curvature at the pitch point on the Hertzian pressure. It transforms the tangential load at the reference cylinder to tangential load at the pitch cylinder.
- Z_E is the elasticity factor and takes into account the influence of material properties such as moduli of elasticity and Poisson ratios of the mating gears.
- Z_ε is the contact ratio factor and accounts for the influence of the effective length of the lines of contact on the load capacity of cylindrical gears.
- Z_β is the helix angle factor which accounts for the influence of the helix angle on the load capacity of helical gears. For spur gears Z_β=1.

Description and calculation methods for any other geometric factor can be found in (ISO 6336-2, 2006) while general influence factors are described in (ISO 6336-1, 2006).

Similarly, to surface load capacity, the calculation of tooth bending strength involves the calculation of nominal, actual and permissible stresses. The actual stress is calculated as the product of the nominal root bending stress σ_{F0} and a number of stress correction factors to take into account various aspects of loading condition. σ_F needs to be smaller or at least equal to the permissible stress in order to consider the design valid. To follow,

the equations to calculate the root bending stresses are given and the factor of main importance are briefly described.

$$\sigma_{F0} = \frac{F_t}{bm_n} Y_F Y_S Y_\beta Y_B Y_{DT} \quad 5.4$$

$$\sigma_F = \sigma_{F0} K_A K_V K_{F\beta} K_{F\alpha} \quad 5.5$$

$$\sigma_{FP} = \frac{\sigma_{Flim} Y_{ST} Y_{NT}}{S_{Fmin}} Y_{\delta relT} Y_{RrelT} Y_X = \frac{\sigma_{FG}}{S_{Fmin}} \quad 5.6$$

σ_{F0} in Equation 5.4 is the nominal tooth root stress also defined as the maximum local principal stress produced at the tooth root for the case of an error-free gear pair is loaded by the static nominal torque. The error free condition involves the absence of any production and assembling errors. σ_{FP} is the permissible bending stress and represents the limit value of tooth root stresses after taking into account material characteristics and gear dimensions. The term σ_{Flim} represents the nominal bending stress number determined by testing reference test gears which takes into account influences of material, heat treatment and surface roughness. Values of σ_{Flim} are available in ISO 6336 part 5 (2006) in tabular and graph forms. Stress correction factors, also in this case are divided into two categories: Y-factors are related to the gear geometry and material and their calculation methods can be found in ISO 6336 Part 3 (2006) and ISO 6336 Part 5 (2006); K-factors instead are factors of general influence mainly related to loading conditions. Also for the case of root bending stress, values from numerical analyses are compared to the nominal stresses. The influence factors in σ_{F0} (Equation 5.4) are briefly described as follows:

- Y_F is the form factor which takes into account the tooth form when the load is applied at the point of single tooth pair in contact.
- Y_S converts the nominal tooth root stress to the local root stress by taking into account the curvature radius of the root fillet.
- Y_β is the helix angle factor which accounts for the reduced bending moment as a consequence of the oblique line of contact in helical gears. For spur gears Y_β=1.
- Y_B is the rim thickness factor which takes into account the extra stress due to thin rimmed gears.

- Y_{DT} is the deep tooth factors which adjusts the calculated tooth root stress for the case of high contact ratio gears with $2 \leq \varepsilon \leq 2.5$.

Description and calculation methods for other geometric factors can be found in ISO 6336-3 (2006) while general influence factors are described in ISO 6336-1 (2006).

S_{Hmin} and S_{Fmin} are the minimum safety factors that have to be considered for the design and follow considerations based on the risk analysis by taking into consideration the consequences caused by a possible failure.

The factors in the ISO standard can be calculated by three methods A, B or C. In method A, the factors are derived from full-scale testing. This is clearly the least used method because of the amount of resources needed to perform the tests. Method B is based on analytical calculations and allows deriving factors with reasonable accuracy for most gear geometries. Method C is similar to Method B but involves some simplifications and approximations for the evaluations of the relevant factors.

For the purpose of this study, KISSsoft has been set up to perform calculations according to Method B. Factors of general influence are set equal to 1. The Nominal values of analytical contact and bending stress are compared to the numerical results, as the FEA analysis tend to simulate the system in its integrity without taking into account adjustment coefficients and safety factors.

5.4 FEA methodology and analysis settings

The main goal of modelling a spur gear pair by means of the Finite Element Method is the evaluation of contact and bending stresses, the principal causes of failure in gears according to ISO 10825 (1995). The simulation of a mating gear pair is a hard task to solve with general purpose FEA software such as ANSYS due to the high level of non-linearity of the system. Specific analysis settings are required in order to overcome the convergence difficulties and obtain accurate results from the analyses.

Two gears in mesh are considered highly non-linear and the reasons are:

- geometrical nonlinearities given that the structure geometrical configuration changes continuously during the relative rotation, and experiences a large global deformation;
- contact non-linearity due to the non-linear Hertzian contact deflection and the variation of the area of contact as function of the radii of curvature of the tooth profiles.

An example of the non-linear response of a mating gear pair is shown in Figure 5.3 where the normalised tooth flank contact stress for the entire mesh cycle is plotted as a function of the applied torque. In this case a linear increase/decrease of the applied load does not result in a linear response of displacements and stresses.

Geometrical nonlinearities are considered in ANSYS with the option “large deflection” that accounts for changes in the geometry during the course of the analysis.

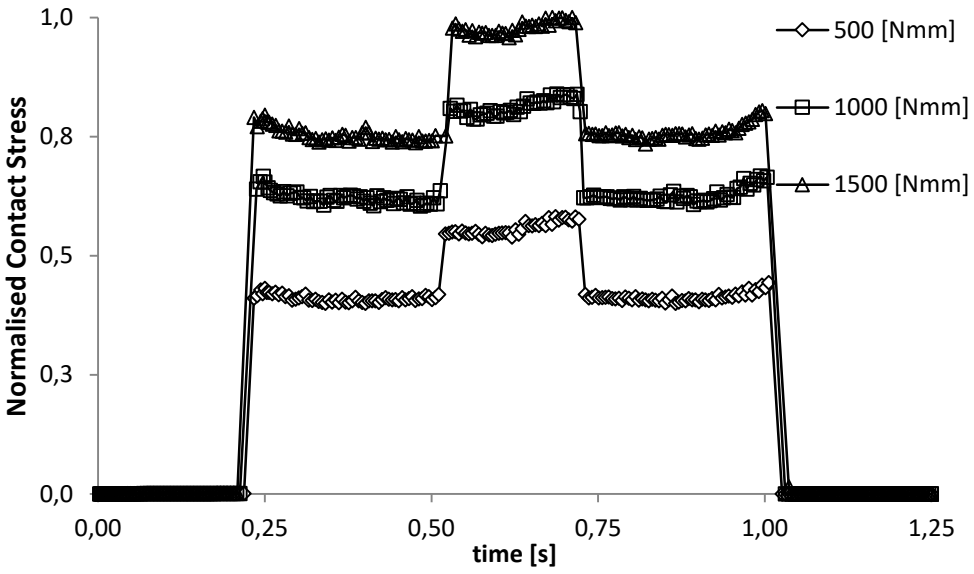

Figure 5.3 - Predicted normalised tooth flank Contact Stress for three Torque levels

The model used for the following parametric study is a two-degree of freedom spur gear pair in which shafts and bearings are considered as rigid entities. Another simplification regards the condition of perfect mesh: all the possible inaccuracies derived from manufacturing and/or assembly processes are considered negligible in this study. Furthermore, for the following analysis, in order to justify the quasi-static assumption,

low speed rates have been used so that the inertial effect produced in the gear pair is modest and can therefore be ignored.

5.4.1 Load Inertia

To support the assumption made in this work that inertial forces and the associated dynamic effects are negligible in the relevant cases and that, for those cases a quasi-static FEA approach can be appropriate to represent the time-varying stress distribution for a spur gear pair in low speed operating conditions, actual values of load inertia are calculated.

Inertia is the property of an object to resist change in acceleration and for a rotational body represents the resistance to angular accelerations about a given axis. As stated by Roos et Al. (2004) the inertia of a spur gear can be reasonably approximated using the equations for a cylinder with the external diameter equal to the pitch diameter. The sum of the products of each element of mass in the body and the square of the element's distance from the axis of rotation gives the wanted value of inertia as in equation 5.10.

$$I_i = \frac{1}{2} m_i r_i^2 \qquad 5.10$$

For a gear system composed of a spur gear pair, the Moment of inertia of gear 1 (input) is calculated as follows:

$$I_1 = \frac{1}{2} m_1 r_1^2 \qquad 5.11$$

that, with a mass of 22.558 g and a pitch radius of 10 mm is equal to 1.128E-06 kg m^2.

Another parameter to take into account when a certain load is transmitted by means of a mechanism such as a gear train is the reflected inertia; this means reflecting the inertia of the driven component back to the input member. Mazurkiewicz (1995) states that for any transmission system, the load inertia reflected to the motor is a squared function of the speed ratio which, in this case, gives:

$$I_r = \frac{\frac{1}{2} m_2 r_2^2}{i^2} \qquad 5.12$$

The total inertia of the gear train to be considered is then:

$$I_t = I_1 + I_r = \frac{1}{2} m_1 r_1^2 + \frac{\frac{1}{2} m_2 r_2^2}{i^2} \qquad 5.13$$

and is equal to 2.2558E-06 kg m^2.

In order to determine the actual force of inertia acting against the input torque, the moment of inertia I has to be multiplied for the angular acceleration experienced by the gear body. By considering, as described in the previous paragraph, two time-steps of 0.25 and 1 s within which a rotation of 9 and 36 ° is applied, the gear body accelerates in the first time step with a constant angular acceleration of 2.513 rad/s^2 generating a load inertia of 0.00567 Nmm. In the second time step, the constant rotational velocity does give 0 inertia. The calculated load inertia results either 0 or a value five orders of magnitude lower than the applied torque (500 Nmm) which makes it negligible and supports the initial assumption made.

5.4.2 Plane stress/strain

The simulation of the gear models has been treated as a 2D analysis in order to reduce the requirement for high computational resources and time. This decision involves the approximation of the actual 3D stress condition at the area of contact, and in proximity of the tooth root, with a 2D model that can be either plane stress or strain. In two dimensional models one of the principal stresses is assumed to be zero, as given in Equation 5.7 where the stress state is perpendicular to the z axis.

$$\begin{cases} \sigma_z = \tau_{xz} = \tau_{yz} = 0 \\ \gamma_{xz} = \gamma_{yz} = 0 \end{cases} \qquad 5.7$$

As a general rule, based on the elasticity theory, components with an axial dimension considerably smaller than the other two in-plane (x-y) loading and boundary conditions can be considered to be under a plane stress state (Richards, 2001) for the calculation of displacements and stresses. In the 2D study of gear models, Wang et Al. (2006) found the plane stress state to be more accurate for small thicknesses while plane strain and plane stress approximations were produced equivalent results when applied to geometries with thicker bodies. The thickness variation in their study spans from 5 to 300 mm. Conrado et Al. (2007) confirmed the validity of the approximations by saying that the plane strain or plane stress model can be used without approximations only in the case of infinite, or infinitesimal, facewidth. Several examples of models based on the plane stress assumption are presented by some authors (Arafa et AL., 1999; Lewicki et

Al., 1997), whilst other authors present those based on plane strain theory (Kuang et Al., 1992; Sirichai, 1997). Based on these previous considerations and given the gear facewidth of the models in this study being under 5 mm, the same as the one studied by Wang et Al. (2006), the plane stress approximation was considered the most appropriate. If the problem is well conditioned and the assumption made is appropriate, the distribution and magnitude of stress and strain are the same for both 3D and 2D plane stress analysis.

5.4.3 Finite Element Mesh

Nodal displacement is the primary unknown when a finite element solution is attempted. The finite element method uses the approximate solution for displacement to evaluate approximate values of stress and strain that may be considered as second order unknowns. Ideally the computed FEA displacement converges to the exact value as the size of the discretized elements tends to zero. If the value of those displacements calculated during the FEA analysis is either too high or too small compared to a range of reasonable values based on material, loading and constraints characteristics, then the solver experiences convergence difficulties. Lepi (1998) defines the convergence of displacement as:

$$displacement\ convergence = \frac{e_2}{e_1} = \left(\frac{h_2}{h_1}\right)^{p+1} \qquad 5.8$$

where the convergence is defined as the ratio between errors e_1 and e_2 associated with two solutions, where h_1 and h_2 are the largest element size in each model and p is the order of the interpolation function. Similarly, strain or stress convergences are defined as:

$$higher\ order\ convergence = \frac{e_2}{e_1} = \left(\frac{h_2}{h_1}\right)^{p+1-r} \qquad 5.9$$

where the extra term r takes into account the higher order of the unknown (Wang, 2003). It can be noticed that stress does not converge as quickly as the displacement for a given degree of interpolation; this translates into practical applications by considering that coarser mesh might be sufficient for the analysis of displacements while more refined mesh would be required for accurate stress analysis (Lepi, 1998).

5.4.3.1 Mesh settings for gear performance analysis

The use of an adequate finite element mesh is crucial for the quality of numerical results. An adequate mesh consists of an appropriate discretization of the model as already described, coupled with the use of proper elements. For the study of 2D solid elastic models, also for the case of non-linear analyses, quadrilateral elements are the most appropriate, especially for the case of complex geometries as they are able to adapt closely to the curved profiles and represent the model in its entirety. The rate of adaptation to the underlying surface increases with the order of the elements such that quadratic elements follow the geometry better than similarly sized linear elements (ANSYS®, 2016; Lepi, 1998).

In this study, the finite element model of the gear pair is created using PLANE183 elements shown in Figure 5.4. They are quadratic elements defined by 8 nodes having two DoF at each node: translations in the nodal X and Y directions (ANSYS®, 2016).

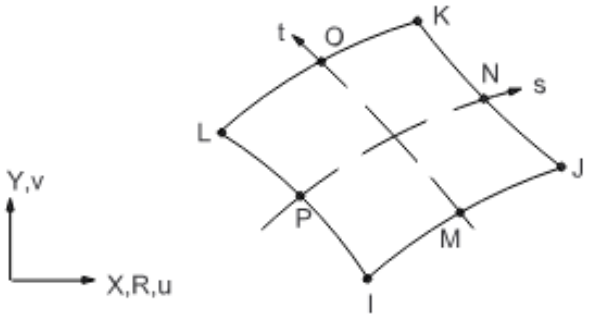

Figure 5.4 – PLANE 183 element (ANSYS®, 2016).

In order to model the contact regions with sufficient accuracy, as the location of the contact point changes while gears rotate, the entire tooth flank surface requires a refined mesh. The other area necessitating a finer mesh is the one near the root fillet of the tooth that is carrying the load. For the remaining part of the gear, which includes the area around the gear hub and the teeth far away from the contacting area, a minor refined mesh is required. By following the mesh convergence analysis outcomes, for all the analysis in the following parametric study, the element side length of 0.001 mm was used to discretize the area of contact and the root fillet of interest coupled with a coarser mesh (0.01 mm) for the neighbouring area. A coarser mesh, with an element side length

of 0.1 mm was used for the gear hub and teeth away from the contacting area. The resulting mesh is illustrated in Figure 5.5 and consists of a 171,330 quadrilateral elements. A detailed diagram of the area marked as “D”, which is the highly refined mesh distributed along the tooth flank and root fillet of the contacting teeth, is shown in Figure 5.6.

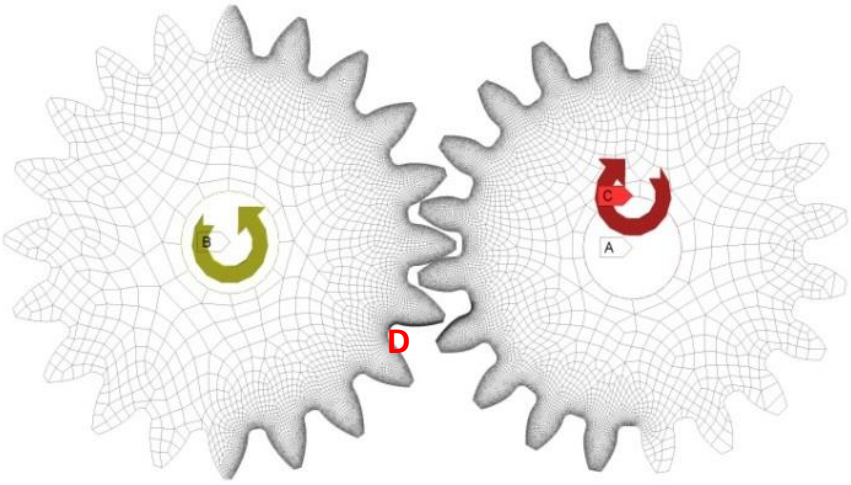

Figure 5.5 – 2D model of the reference spur gear pair after element discretization and with applied boundary conditions.

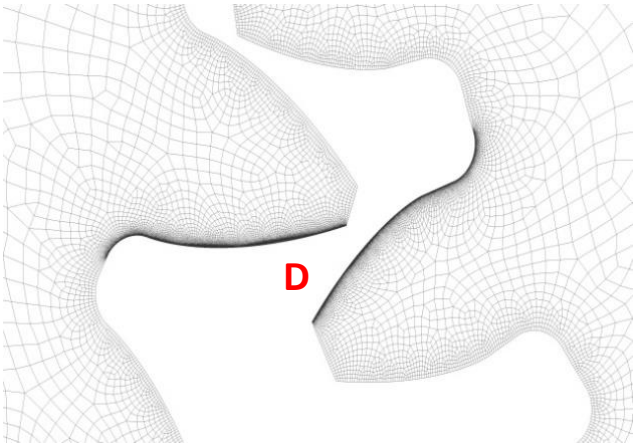

Figure 5.6 – Detailed view of the refined mesh area around D.

5.4.3.2 Mesh convergence study

A mesh convergence study has been carried out with respect to flank contact stress, root bending stress and total displacement in order to find an acceptable compromise between computational cost and time, and accuracy of results for a gear pair with standard proportions. It involves a number of 2D FEM calculations of a pair of mating gears with characteristics listed in Table 5.2.

Table 5.2 –FEA model's Gear parameters for driving and driven gears including material properties

Parameter	Driving	Driven
Number of teeth N	20	20
Module m [mm]	1	1
Facewidth L [mm]	5	5
Pressure angle α [°]	20	20
Profile shift coeff. *x*	0	0
Addendum factor h_a	1	1
Dedendum factor h_f	1.25	1.25
Young's modulus E [MPa]	$2x10^5$	$2x10^5$
Poisson ratio ν	0.3	0.3
density ρ [kg/m^3]	7850	7850
mass [kg]	0.0225	0.0225

The gear model is positioned such that the contact occurs at the highest point of contact for a single tooth pair. The gear wheel is constrained at the inner hub while the pinion is free to rotate around its own axis (constraints B and C in Figure 5.5). A moment of 500 Nmm (C in Figure 5.5) is applied to the pinion inner hub.

Two critical stresses were calculated: Maximum Von Mises contact stress (σMXc) at the area of contact, and Maximum Von Mises bending stress (σMXb) at the root fillet of the driven gear. Total displacement (U_{tot}) of the tooth in contact has been evaluated for the point at the centre of tooth top land as shown in Figure 5.7.

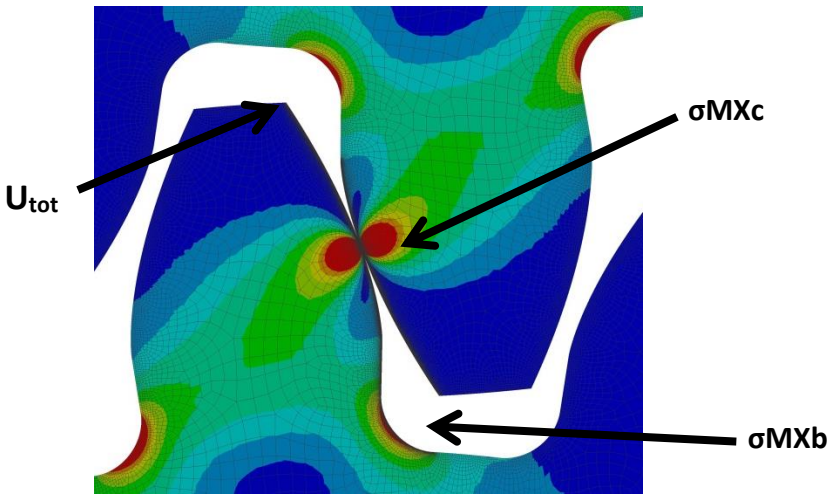

Figure 5.7 – Plot of Von Mises stress distribution for a single tooth pair in contact at the pitch circle. The area of maximum bending stress occurring at the tooth root is indicated by σMXb while the area of maximum contact stress occurring on the tooth flank is indicated by σMXc. U_{tot} indicates the node where the total displacement is measured.

Table 5.3 reports the results for a number of mesh densities from a coarse mesh model with 51,966 nodes to the final model with a highly refined mesh of 877,232 nodes. The controlled variable was the element side length in proximity to the area of contact and root fillet, as shown in Figure 5.6 and reported in Table 5.3.

Table 5.3: FEA calculation results for the mesh convergence study

Element side length [mm]	Node no.	(σMXc) [MPa]	(σMXb) [MPa]	U_{tot} [mmx10^{-4}]
0.0001	877232	429.3744384	38.916	8.158
0.00025	450000	429.0316049	38.903	8.1582
0.0005	299054	429.5017765	39.818	8.1584
0.00075	213306	429.8935862	38.917	8.1583
0.001	171330	428.93	38.918	8.1584
0.002	115000	426.0930323	38.9	8.158
0.003	85000	424.1339839	38.903	8.1579
0.005	72641	417.786667	38.903	8.1576
0.0075	65402	410.263921	38.906	8.1583
0.01	61547	394.3172668	38.887	8.1589
0.025	54792	332.5190843	38.752	8.1564
0.03	54127	300.1262186	38.509	8.1485
0.0375	53430	301.477962	38.606	8.159
0.04	53373	262.2871983	38.43	8.1533
0.05	53459	191.477393	38.606	8.1999
0.075	52348	107.7378681	37.291	8.0985
0.1	51966	88.15130195	39.451	8.3245

The number of nodes demonstrates an exponential increase, as shown in Figure 5.8, as function of the element side length. By considering the computing time being directly dependent on the number of nodes/elements, an exponential increase is expected with a reduced element side length.

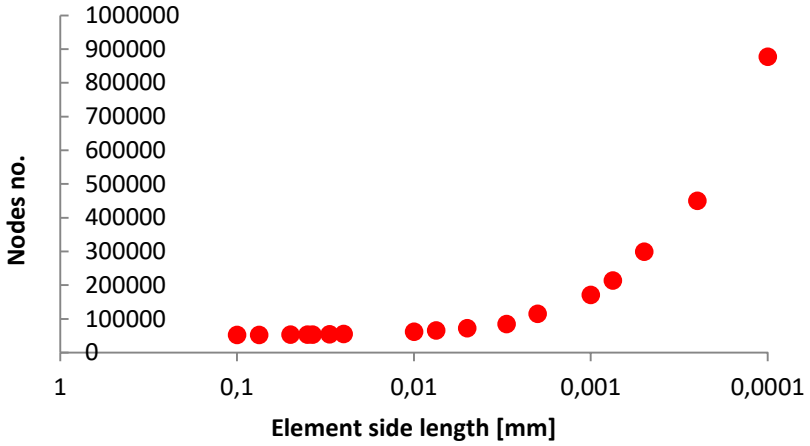

Figure 5.8 – Nodes number variation as function of element side length.

Figure 5.9 clearly shows that for an element side length just over 0.025 mm, corresponding to a model with 450000 nodes, the total displacement U_{tot} converges to a value of ≈ $8.15X10^{-4}$ mm. For the same mesh density, also the tooth root bending stress shows convergence to a value of ≈38.9 MPa (Figure 5.10). On the other hand, the stress at the contact point does not appear to have converged for the same mesh density. Figure 5.11 shows the asymptotic trend followed by σMXc that stabilises to a value of ≈ 429 MPa for an element side length of 0.001 mm.

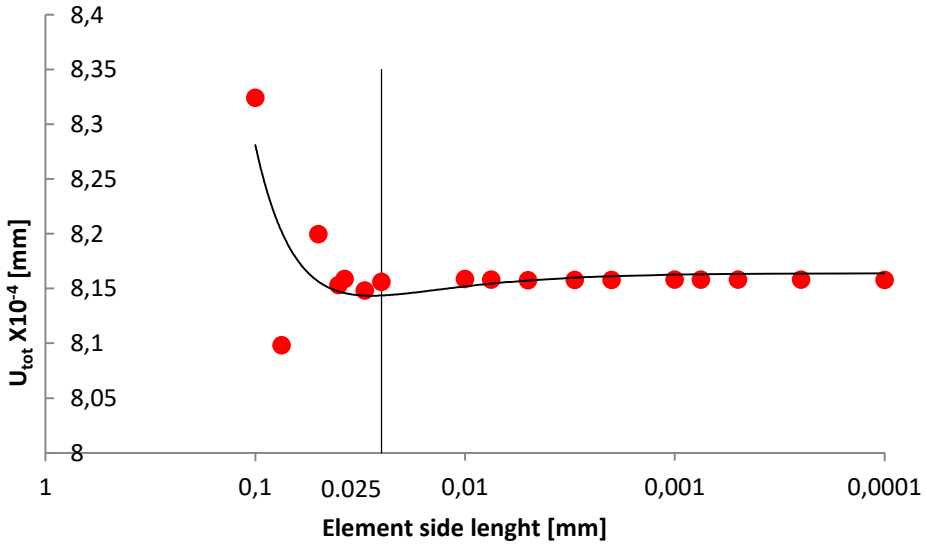

Figure 5.9 – Tooth tip total deformation as a function of element side length.

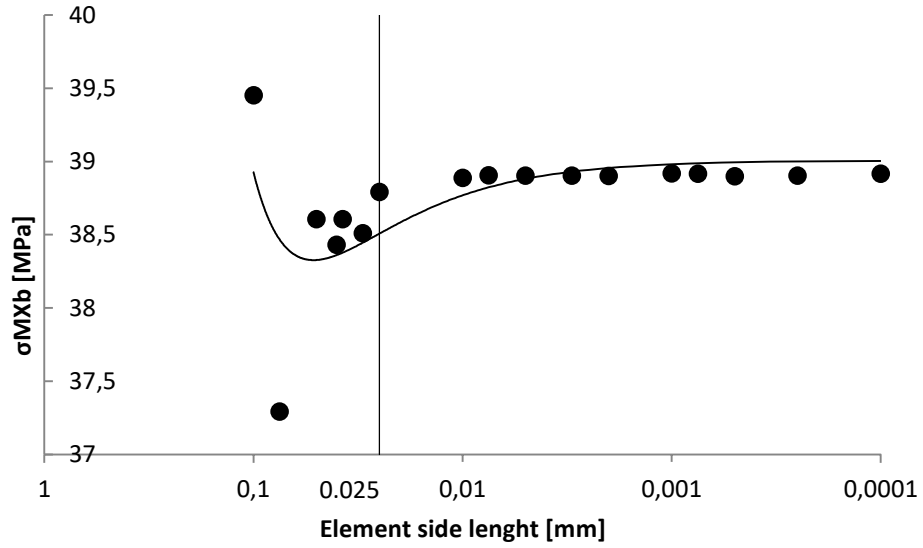

Figure 5.10 – Von Mises bending stress at the tooth root as a function of element side length.

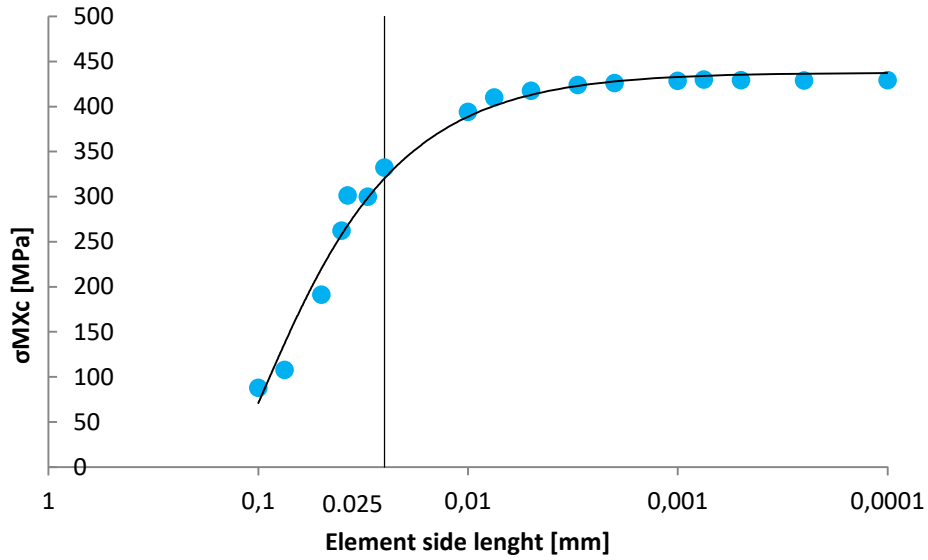

Figure 5.11 – Von Mises flank contact stress as a function of element side length.

5.4.4 Finite element Contact Model

The next type of elements necessary to completely define the behaviour of an actual gear pair using a finite element model are contact elements. These special elements allow various parts of the model to interact and share loads and constraints. For the analysis of mating gears, contact conditions are of primary importance as the power transmission from one member to the other occurs through them. A gear system is characterized by highly non-linear contact behaviour and for this reason it represents

the major cause of solution non-convergence. The point of contact (which in reality becomes an area if the elasticity of the material is considered) continuously moves along the mesh area with a mixed pure rolling and sliding motion condition. Moreover, it transfers from the current mating tooth pair to the next in the cycle. For these complex contact conditions, appropriate contact element formulations are necessary in order to achieve the most accurate solution possible.

5.4.4.1 Contact settings for gear performance analysis

Finite Element Analysis simulates the condition of contact by means of special elements placed in between contacting components. Contact modelling starts with the definition of parts in contact. For the case of 2D gear analysis, the tooth flank surface is replaced by an edge to edge contact. 5 edges for each gear corresponding to the tooth flanks that would experience contact during the mesh cycle across the 36° of rotation of the wheels where selected.

After the contact surfaces are created, the next step is to define the functions to determine their reciprocal interactions. First in order of selection is the definition of contact type. For gears, the type of contact closest to reality is the one defined as frictional. With this setting, the two contacting geometries can carry shear stresses up to a certain magnitude across their interface before they start sliding relative to each other. The equivalent shear stress at which sliding begins is a fraction of the contact pressure. Once the shear stress is exceeded, the two geometries will slide relative to each other (ANSYS®, 2016). Based on this consideration, the contact regions between pinion and gear were defined as frictional, with a null coefficient of friction. The ANSYS contact elements that correspond to this setting are CONTA172 and TARGHE169. These are then generated over the underlying mesh already created on the gear surfaces. Contact and target element formulation define the characteristics of the contacting surfaces such that only the contact surface can penetrate the target surface between nodes as the surfaces come into contact. ANSYS (2016), in the section of its manual dedicated to contact mechanics, gives guidelines on how to define contacting surfaces in terms of either contact or target. The guidelines are based on the assumption that a difference in terms of material, refinement and/or order of the mesh, geometry and size of the components exists. Once in this case no differences exist between the contacting

surfaces, the pinion tooth flank was defined as contact and the gear tooth flank as target, based on the consideration that force is transferred from the pinion to the gear. To avoid mutual penetration between contact and target elements the “symmetric behaviour” option was selected. As part of the advanced contact options, the detection method played a crucial role in the quality of the obtained results. To explain the effect of this detection method an example is presented.

Figure 5.12 shows the contact stress distribution in the area around the lowest point of single tooth contact for a 28° pressure angle gear pair configuration. It can be noticed that results are highly affected by the contact detection method used, and depending on the formulation chosen, the degree of instability increases or decreases. The influences of mesh density and number of substeps have also been investigated for the “program controlled” option. Between all the possible detection methods available in ANSYS, the most appropriate result for the Contact stress distribution was found with the “Nodal-projected Normal from Contact” option with an element side length of 0.001mm (defined by the mesh convergence study), and 360 substeps as shown in Figure 5.12. In fact, in the region of single tooth pair in contact, between HPSTC and LPSTC, there is no geometrical and/or load variations that can justify a non-constant stress distribution which does not justify the random variation of the evaluated stress distribution in such area of the mesh cycle. Moreover, a value of Equivalent contact stress of 382 MPa for α=28° is in perfect agreement with the analytical result calculated by means of ISO 6336 B (2006).

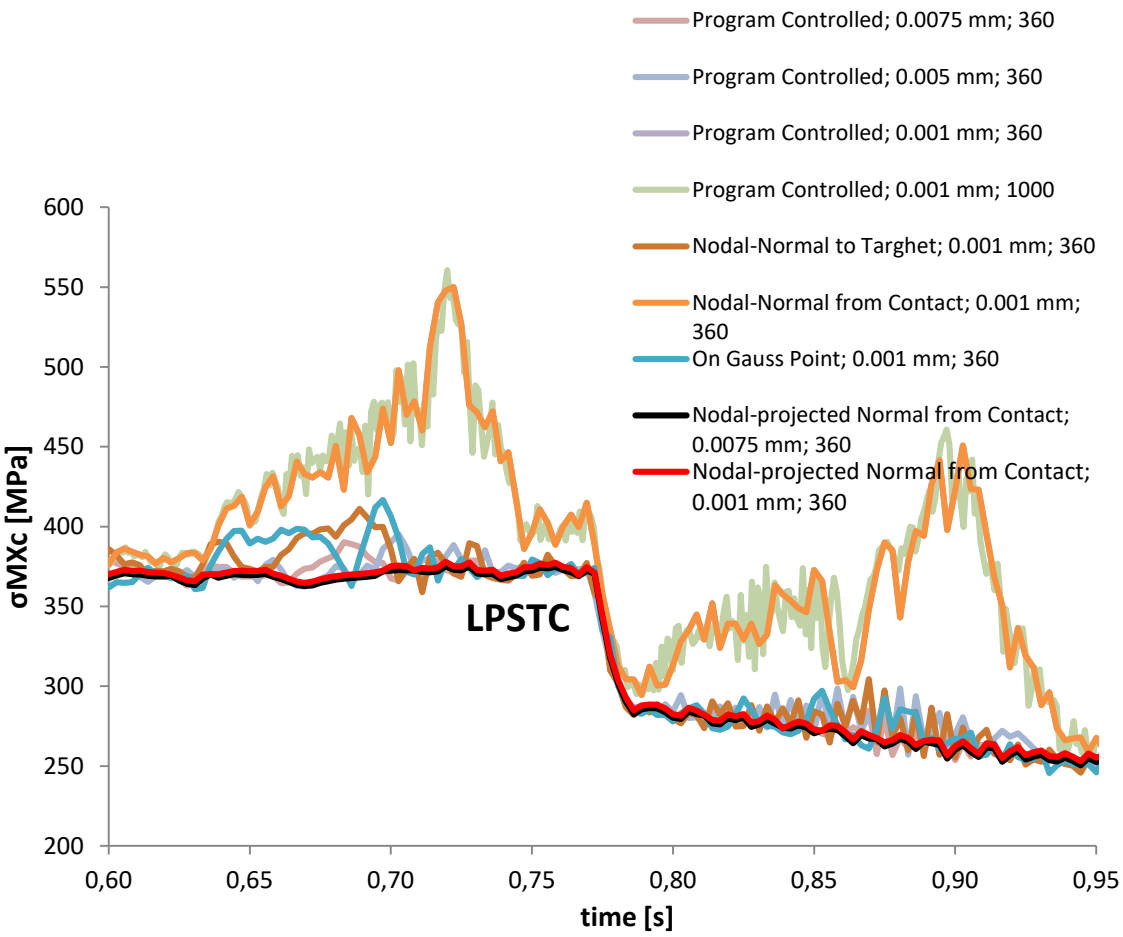

Figure 5.12 – Effect of FEA contact detection method on the quality of contact stress results for a mating spur gear pair for $N_{1,2}$=20, α=28°, $x_{1,2}$=0.

Within the list of advanced contact functions, the "interface treatment" had a major influence in overcoming convergence difficulties raised at the first instants of the simulation. The presence of any kind of penetration or gap between parts creates convergence difficulty as the contact condition is not correctly defined. In this circumstance the interface treatment is selected as "adjust to touch", and this helps to overcome the risk of convergence failure by reducing the initial penetration and/or closing any initial gap. A reduced degree of non-linearity, and the established initial stress free state, enhances the probability of convergence and hence success.

5.4.5 Time step Controls

For the numerical analysis of non-linear contact problems, ANSYS allows the user to define the number of load steps and the number of load increments within each load step. The automatic step control function also optimizes the solution time by adjusting the load increments based on the encountered degree of non-linearity. In this study it

was preferred to have a better control of the load increments in order to achieve a resolution of 0.1 degrees of rotation. The loading time has been divided in two steps of 0.25s and 1 s for a total time window of 1.25 s. The first step was used for system stabilization and to overcome initial convergence difficulties. The second step time window instead covers the entire cycle from engagement until disengagement of the tooth pair under investigation. For step 1 a number of load increments spanning from 20 to 90 has been used depending on whether solution was converging or not. Step 2 has a constant number of sub steps equal to 360 in order to achieve the 0.1° resolution over the 36° of gears rotation. In order to model the gear pair under the initial assumption of quasi-static behaviour, the Time Integration function is deactivated, so that inertial effects are not considered.

5.4.6 Boundary conditions

A constant rotational velocity is applied to the driven gear hub with a 45° rotation angle corresponding to 1.25 s in time. The angle is divided in 9° and 36° for the first and second load step respectively. The result is a constant rotational velocity of 6 rpm (0.628 rad/s) in a counter clockwise direction. The driving gear is loaded at the centre of the hub with a clockwise moment that ramps from 0 to 500 Nmm in 0.25 s, and is constant at 500 Nmm for the second load step. Both driving and driven gears are supported at the centre hub by means of a remote displacement that allows rotation about the Z axis only, while fixing the other 5 DoF. A graphical representation of the boundary conditions applied is shown in Figure 5.10 where moment and rotation are displayed in red and yellow respectively.

5.4.7 Validation of results

The absence of an experimental test rig to test and validate numerical data from the modelling work done has led to find an alternative validation methodology results based on International Design Standards. ISO 6336 Method B, briefly described in the 5.3 above, is currently the most used design and calculation method for gears and gear trains. Many studies have been published regarding the effectiveness of analytical calculations to determine stress state, load sharing ratio, dynamic effects and any aspect that has to be evaluated at the design stage of a gear transmission. Rating standards are

based on analytical calculations corrected by coefficients determined empirically by means of repeated testing campaigns. As consequence, accurate results are given for standardised geometries as they are highly tested and analysed, instead, for non-standard geometries, the method is less accurate and results can only be considered estimations of the effective stress state. This aspect is clearly indicated in the ISO 6336 Part 1 (2006) which suggests that users confirm their results by experience when operating pressure angles exceed 25° (McVittie, 1998). This statement confirms that when the geometry reaches a certain level of modification, the calculation method is inaccurate due to the inappropriate correction coefficients. Rating standards have reached a high level of precision in predicting the stress state of standard profiles as shown by La Bath et Al., (2004) and Lisle et Al., (2016) after comparing the generated stress state on a 20° pressure angle profile with experimental and Finite Element Method results. Both analytical and numerical method in this case were found in good agreement with the experiment outcomes. On this basis, it has been decided to validate the Finite element approach used with the standardised profile ISO 53 Profile B against the results of calculations in accordance with ISO 6336 B performed by means of the machine design software KISSsoft. Later in this paragraph, it will be seen that a perfect agreement between analytical and numerical methods is achieved for standard profiles, while, for non-standard geometries the gap increases with the amount of modification applied.

5.5 Evaluation of Contact Stress for a spur gear pair

During the meshing process, the forces shared between the two surfaces in contact modify the profile geometry due to the Hertzian elastic deformation experienced by the material (Wang, 2003). Locally limited to the theoretical point of contact, the surface profiles change their geometry, creating an area of contact on which the transmitting force is distributed, hence generating a pressure. The deformation modifies the tooth flank profile's geometry modifying it from the perfect involute condition. In an ideal system, perfectly manufactured and assembled, without errors such as axis misalignment and centre distance variation and without taking into account the stress concentration occurring at the sharp edges, contact stress is uniformly distributed along

the tooth facewidth and varies in magnitude across the mesh cycle. The contact stress variation is visible in Figure 5.13 where the stress distribution field for three meshing positions, respectively at beginning of contact, highest point of single tooth contact and end of contact are shown.

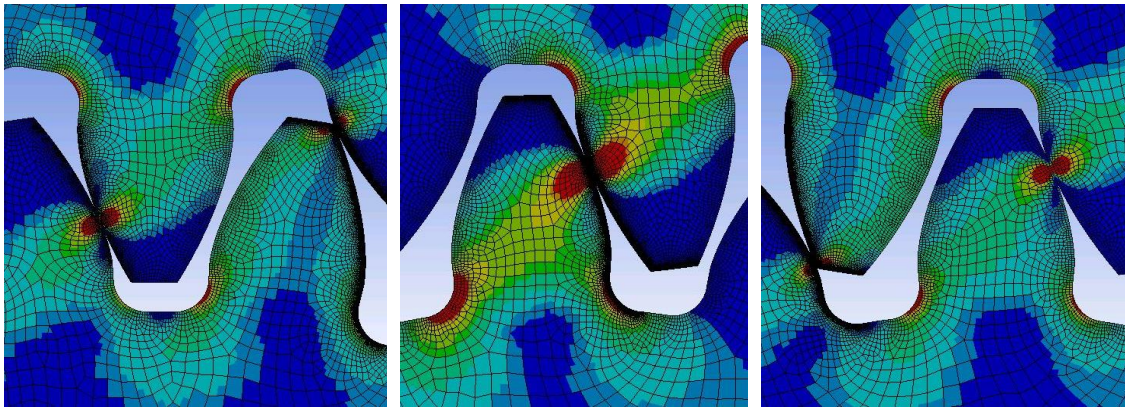

Figure 5.13 – Generated stress field for three meshing positions: beginning of contact, highest point of single contact, end of the mesh cycle.

Two main reasons can be found to justify the continuous variation of contact stress; the two-step oscillation is accounted for by the variation in number of tooth pairs in contact within the mesh cycle as consequence of the gear rotation. This effect in Figure 5.14 is indicated by the sharp rise in contact stress at A^{I} B and $D^{I}C$ corresponding to the beginning and end of the single tooth pair contact phase. The second reason is due to the continuous variation of the area of contact, $A_{c,}$ as the contact point moves along the tooth flank. The effect corresponds to the variation of contact stress in the intervals AA^{I}, BC, and $D^{I}D$ in Figure 5.14. An explanation can be given by taking into consideration the pressure acting on the tooth flank for any contact position in the mesh cycle. Contact pressure and consequently stress is function of the instantaneous force locally applied and the instantaneous area of contact generated as consequence of the applied force. Since the force varies as function of the contact position as described by the load distribution, and the area of contact follows the non-linear localized contact deflection (Wang, 2003) the ratio F/A_c is not constant determining a non-constant stress state.

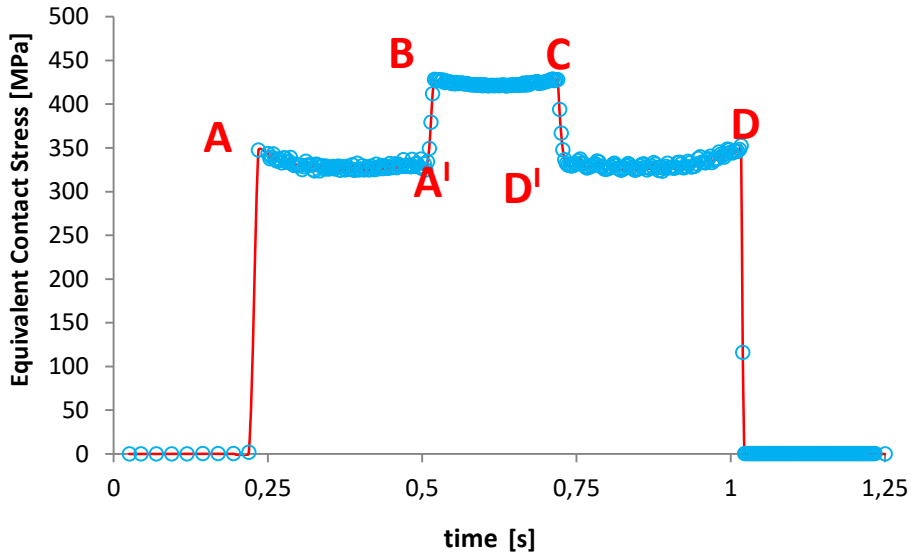

Figure 5.14 - Equivalent tooth flank Contact stress distribution during the entire mesh cycle for the reference spur gear pair.

5.5.1 Load distribution

The load distribution indicates the amount of load shared between two mating teeth at any position of the mesh cycle. Local surface deflection and global tooth deflection coupled with the mesh stiffness due to the variation of contacting tooth pairs, determine a continuous variation of transmitted load along the mesh cycle. Only for the phase when a single tooth pair is in contact the sharing load is constant and equal to the maximum value. The numerical result of contact force distribution among the mesh cycle for the reference gear pair loaded with a 500 Nmm torque is shown in Figure 5.15.

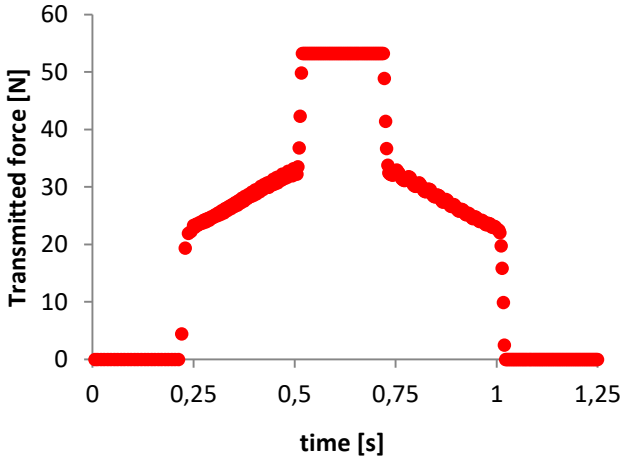

Figure 5.15 – Effective load distribution for the entire mesh cycle calculated by means of FEA.

The effective load distribution is of main importance for the analytical calculation of the instantaneous area of contact, and to analytically evaluate the stress state at any positions of the mesh cycle different than the ones at the HPSTC diameter or at the pitch diameter prescribed by the rating standards.

5.5.2 Influence of reference pressure angle α

The variation of numerical contact stress is calculated by means of quasi-static FEM for a range 20°<α<32°. Figure 5.16 shows the time-varying contact stresses for all values of α in the given range. This enables the overall stress reduction, given by an increase of pressure angle, to be visualised in comparison with that for the standard 20°. Each trend of the plotted numerical contact stresses assumes an almost concentric arc shape in the interval BC, where a single tooth pair is carrying the load. The equivalence in shape is not confirmed for the "legs" AB and CD of the contact stress variation. As visible in Figure 5.16, for α=20°, the contact stress is decreasing in the approach phase and increasing during the recess. This trend is not found in any other case studied. For higher pressure angle geometries intervals AB and CD see an increasing contact stress and the gradient increases with the pressure angle. A similar decreasing/increasing trend for a 20° pressure angle gear pair was found by Olguner (2014).

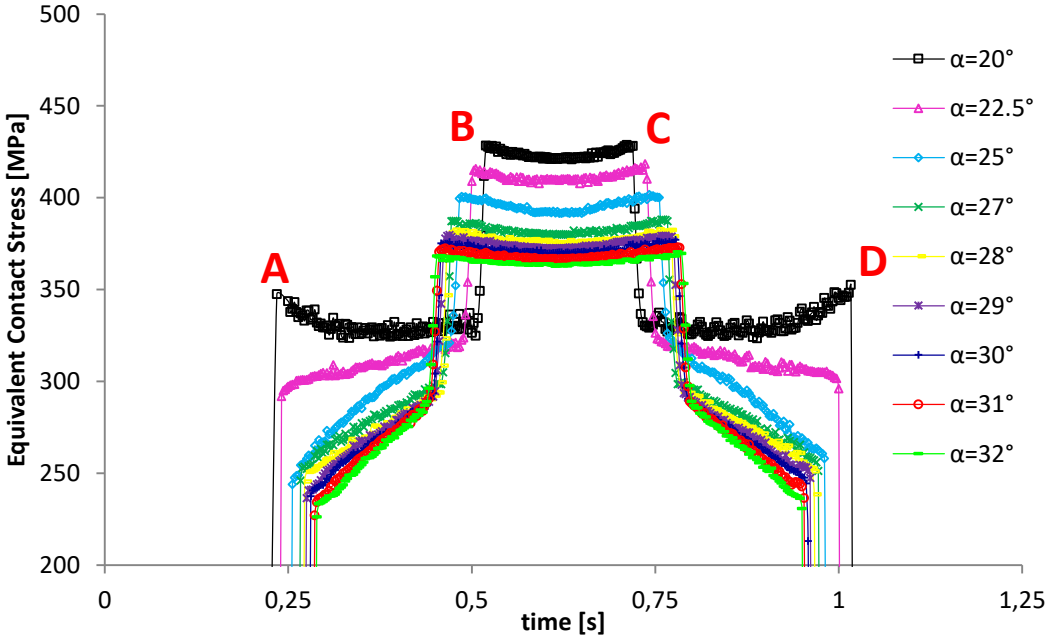

Figure 5.16 – Variation in equivalent contact stress for a complete mesh cycle for a range of 20° <α< 32°.

By collecting the maximum values of contact stresses given in Figure 5.16 for the nine geometrical configurations tested, the contact stress variation as function of pressure angle can be estimated.

Figure 5.17 shows the variation of maximum values of equivalent contact stress for corresponding values of pressure angle. Numerical results are plotted against analytical result calculations following the standard ISO 6336 method B (2006). For both numerical and analytical results, contact stress decreases almost linearly with an increase in pressure angle from a maximum of 403 MPa for α=20°, to a minimum for α=32° of 370.37 or 381.2 MPa if numerical or analytical results are considered. This linearity can be explained considering the size of the area of contact and its variation with pressure angle. Generally an increase in pressure angle determines a linear increase of the tooth profile's radius of curvature (Maitra, 2012)and a consequent linear increase of the area of contact as shown in Figure 5.18. For the geometrical configurations tested, the increase in pressure angle from the standard 20° to 32° would increase the load carrying capacity of the tooth flank by 13% if numerical results are considered and 10.5% if based on analytical results. A similar percentage reduction was found by (Marimuthu, 2016) by increasing the pressure angle of the drive side of an asymmetric gear from 23° to 33°. It can be noticed in Figure 5.17 that numerical and analytical results are very close for α=20°, 25°, 28° while, for other values in the considered range, a gap of maximum 2.9% is shown for α=32°. Values calculated by means of ISO 6336-B are generally more conservative than the numerical ones.

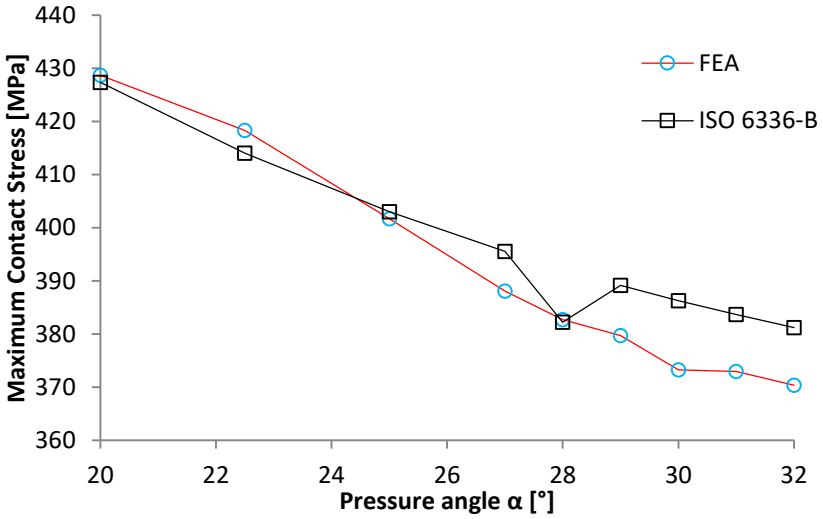

Figure 5.17 – Maximum values of Contact stresses for varying pressure angles (α) compared to nominal contact stress calculated using ISO 6336-B.

5.5.3 Area of contact

In contact mechanics contact stresses are usually estimated through the use of Hertzian theory. The most relevant standards in the field: ISO 6336-2 (2006) and ANSI/AGMA 2101/D04 (2016) apply the Hertz theory to gears with the addition of correction factors determined empirically. Involute tooth flanks are approximated as two cylinders pressed against each other, with the radii of the two cylinders simulating the two involutes at the instantaneous point of contact. During the meshing process, the forces shared between the two surfaces modify the profile geometry due to elastic deformation of the material. Locally, around the theoretical point of contact, the surface profiles change their geometry creating an area over which the applied load is distributed. The area has a rectangular shape with length equal to the gear facewidth (L) and width (b) that can be calculated according to the elastic Hertz theory with the following Equation (Maitra, 2012):

$$\boldsymbol{b} = \sqrt{\frac{8\mathrm{F}\left[\frac{1-\mathrm{v}_1^2}{\mathrm{E}_1}+\frac{1-\mathrm{v}_2^2}{\mathrm{E}_2}\right]}{\pi\mathrm{L}\left(\frac{1}{\mathrm{R}_1}+\frac{1}{\mathrm{R}_2}\right)}} \qquad 5.14$$

The size of the area of contact in Equation 5.10 is function of material and radius of curvature of the contacting surfaces for a constant value of facewidth. In Figure 5.18 the instantaneous radii of curvature at the pitch point are plotted against pressure angle, as well as the area of contact at the pitch point.

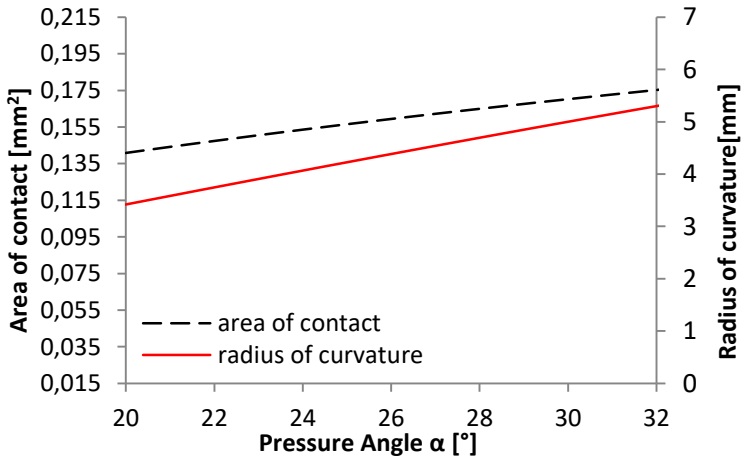

Figure 5.18 – Effect of pressure angle (α) on the area of contact (Ac) and instantaneous radius of curvature (R) at the pitch diameter.

A further analysis of the area of contact has been carried out in order to investigate its local variation as function of the contact point position on the tooth flank. Also for this case the FEA analysis result was compared to the analytical method based on the Hertz theory and calculated accordingly to Equation 5.10. The time varying area of contact was analytically determined by considering the instantaneous radii of curvature as function of the relative position of the two mating profiles and the instantaneous transmitted force numerically determined in the load distribution analysis as shown in Figure 5.15. The results plotted in Figure 5.19 show the time varying contact area for both analytical and numerical methods

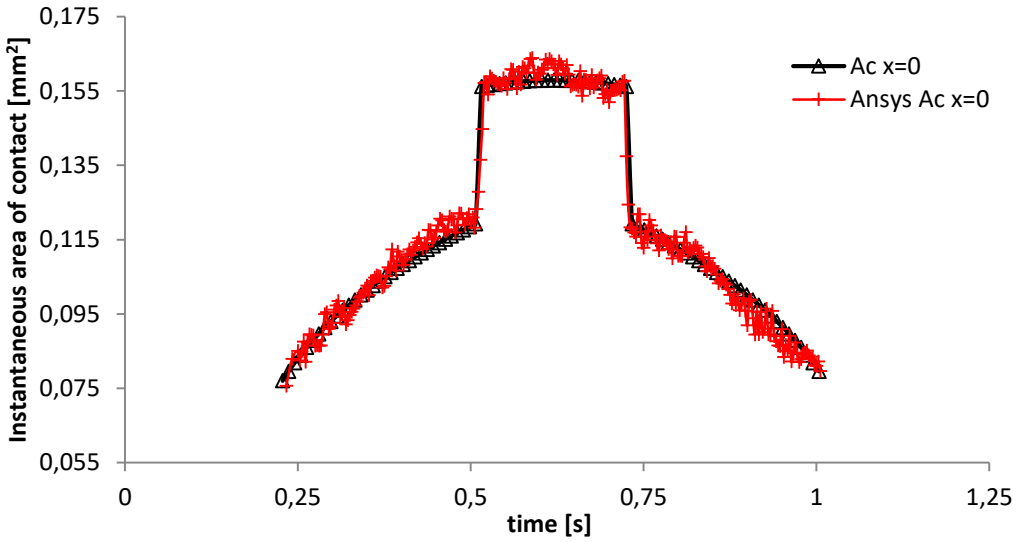

Figure 5.19 – Time varying instantaneous area of contact for a complete mesh cycle calculated by means of numerical and analytical procedures for the reference gear pair.

5.5.4 Influence of profile shift coefficient *x* on tooth flank Contact Stress

The aim in this section is to investigate the change in contact stress due to differing values of profile shift coefficients. To this end, it was important to avoid the influence of any possible compensation, by only applying the modification to the driven gear, leaving the driver with standard proportions. The range of variation of profile shift was limited to a lower value of x=-0.2 by the undercutting condition, and to an upper value of x=+0.5 to avoid the condition of the pointed tooth tip. It is also known that an unbalanced profile shift alters the centre distance, with a consequent modification in operating pressure angle. For the range of profile shifts used here, the working pressure angle α_w varies from 19.1° for x=-0.2, to 23.3° for x=0.5. Equivalent contact stress for the

combination of modified profiles listed in Table 5.1 is plotted in Figure 5.20. FEM results show a variation of equivalent contact stress when a single pair of teeth is in contact. Within the segment BC, contact stress shows a different behaviour, depending on whether the modification is positive, null or negative. For positively corrected profiles the stress state is lower because of the overall increase of operating pressure angles (Miler et Al., 2017). Moreover, a further reduction is visible when the point of contact moves towards point C. The opposite happens for negatively corrected profiles, for which a higher stress state is followed by a further increase when the point of contact moves from B to C. A similar variation was not shown for the case of two standard profiles in mesh for which the generated stress in the $\overline{BC}$ time interval shows a slight concavity, with the two extremes at the same stress value. The cause can be explained by taking into consideration the size of the instantaneous area of contact during the time interval between the HPSTC and the LPSTC (Gurumani et Al., 2011).

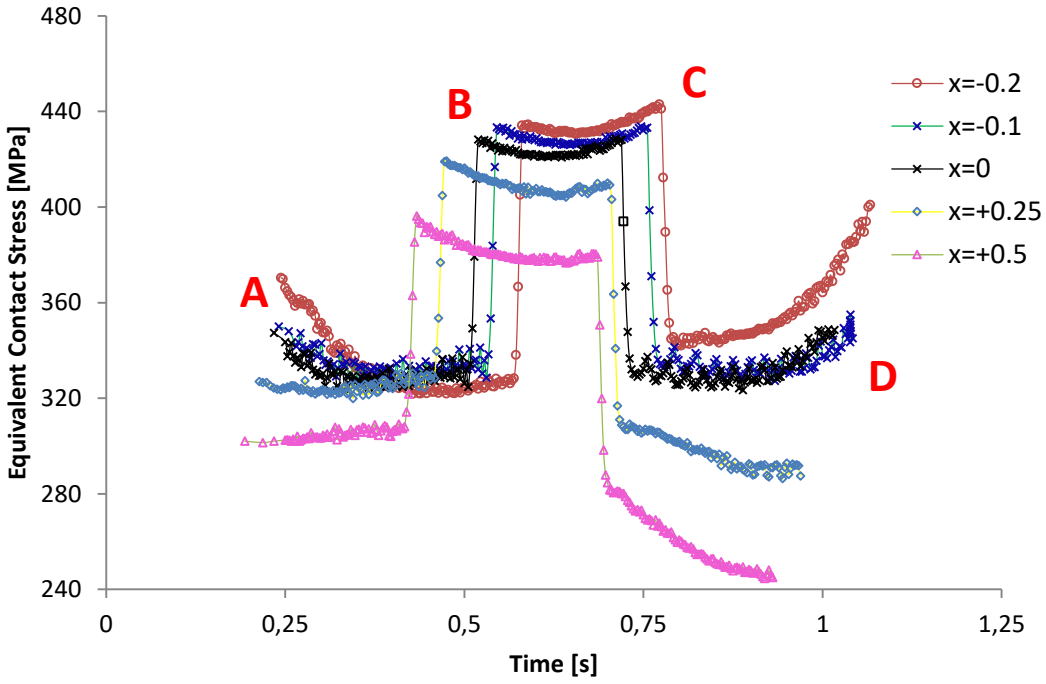

Figure 5.20 – Time varying Contact stress for a complete mesh cycle for different profile shift coefficients (-0.2<x<0.5).

Figure 5.21 shows the evolution of the area of contact along a complete mesh cycle. Points B and C and the section in between have been highlighted for the three most relevant conditions under study. For the profile with *x*=+ 0.5 as the point of contact moves from B towards C, the area of contact increases up to a point that corresponds

to the maximum area of contact and then has a slight decrease as C lies on the descending part of the curve BC. For the case without modifications, points B and C are placed symmetrically relative to the highest point of the curve BC. The small variation between the extreme points and the maximum explains the slight concave trend shown by the stress state for *x*=0. For the negatively corrected profile, point B is placed just before the highest point while point C lies on the descending part of the curve. In this case the trend followed by the contact stress between HPSTC and LPSTC is descending at the beginning and then increases towards C. while the point of contact is moving towards LPSTC. Also in this case, the area of contact and generated contact stress show the same trend.

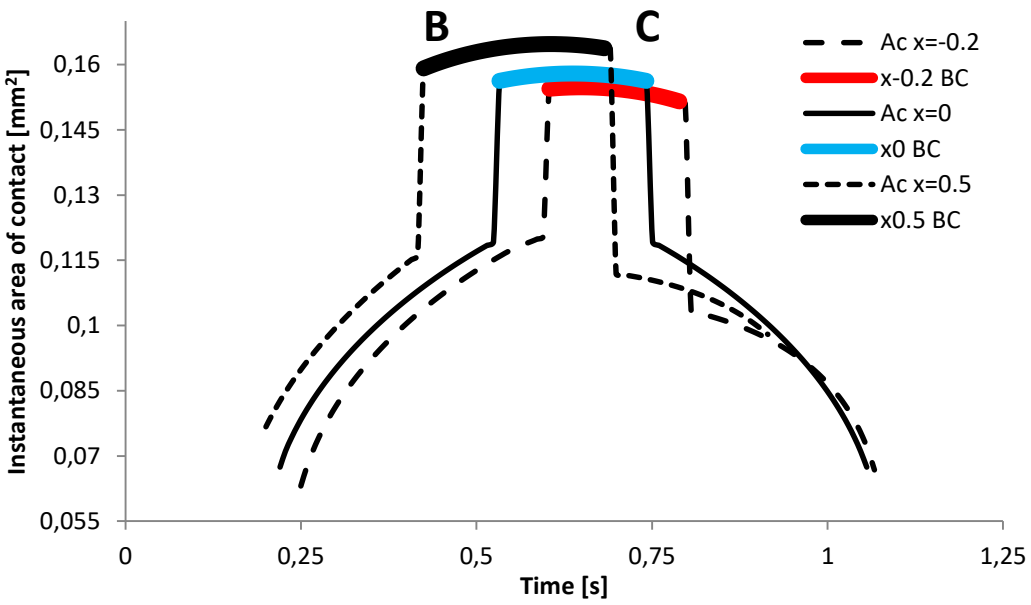

Figure 5.21 – Instantaneous area of contact as a function of time (for one complete mesh cycle), highlighting the region where a single tooth pair is in contact for *x*=-0.2, *x*=0 and *x*=0.5.

Numerical and analytical values of maximum contact stress are plotted against profile shift coefficients in Figure 5.22. The two trend lines decrease almost constantly as the profile shift increases. For values below x=0 numerical results are in perfect agreement with ISO 6336-B while for x=0.25 and x=0.5 a small deviation can be seen. As both α and *x* have a similar effect on tooth geometry, the results are in agreement with the ones shown in the previous Section (5.4.7.2) where an increase in pressure angle leads to a

reduction in contact stress (Olguner et Al., 2014). A comparison between the standard profile with *x*=0 and the two extremes considered leads to an increase of contact stress of 3%, resulting from both analytical and numerical calculations, when the negative modification (*x*=-0.2) is applied. On the other side, the positive profile shift *x*=+0.5 generates a contact stress reduction of 7.5% calculated by means of FEA and 5.8% if numerical results are considered.

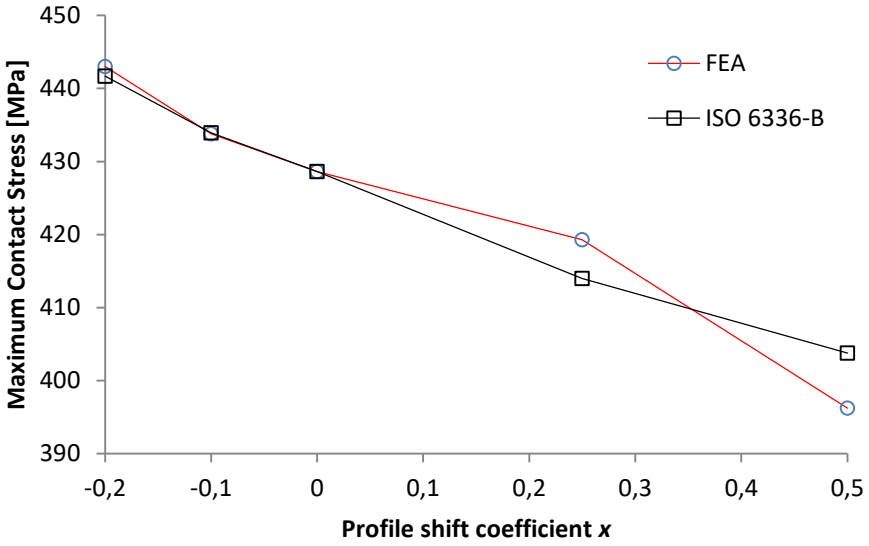

Figure 5.22 – Maximum values of Contact stress versus profile shift coefficient (*x*) compared to nominal contact stress from ISO 6336-B.

5.5.5 Influence of addendum factor h_a on tooth flank Contact Stress

The Addendum factor, h_a, affects the tooth involute profile in the region above the pitch circle. By modifying the addendum factor the gear tip diameter changes but flank curvature and tooth thickness remain unchanged as shown in Figure 5.1. While this modification does not affect the instantaneous radii of curvature, it varies the position of point A or first point of contact and the position of point C when a new pair of teeth engages and the time interval of single tooth pair in mesh ends. The point relocation within the mesh cycle generates a shift of the segment BC along the line of action making the contact eventually occurring where area of contacts are smaller and the resulting contact stresses are higher. FEM results for the variation in addendum factor are shown in Figure 5.23, where it is clearly visible how the contact stress maximum values increase and persist for a longer interval of time as h_a decreases.

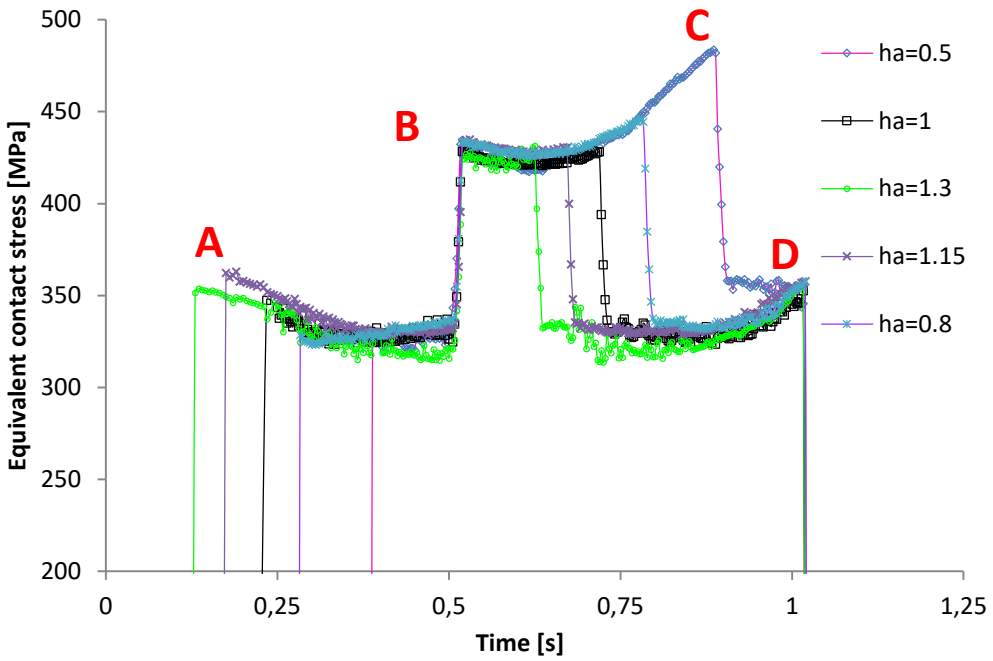

Figure 5.23 – Time varying equivalent contact stress for a complete mesh cycle for different values of addendum coefficient, $0.5<h_a<1.3$.

Increasing the driven gear outside diameter by increasing the addendum length increases the approach action: point A moves to the left as the addendum factor increases. In Figure 5.23 the recess stays constant as the last point of contact, corresponding to point D, for all the combinations tested, always occurs at time 1.01 s. Another consideration with regards to addendum factor is about its influence on contact ratio. Whilst point B is fixed, point C moves from the left to the right as the addendum factor decreases; this is the result of a reduction of the average number of teeth simultaneously in contact. Having two pairs of teeth in contact that share the load for longer time intervals reduces the exposure of the tooth profile to high stress states. In Figure 5.24 the contact time duration for a single tooth pair in contact are plotted, as well as the contact ratio as a function of the addendum factor ha. This plot shows how much the addendum length modifies the contact ratio, and consequently the time interval when a single pair of teeth is in contact, which is associated to a prolonged high stress level.

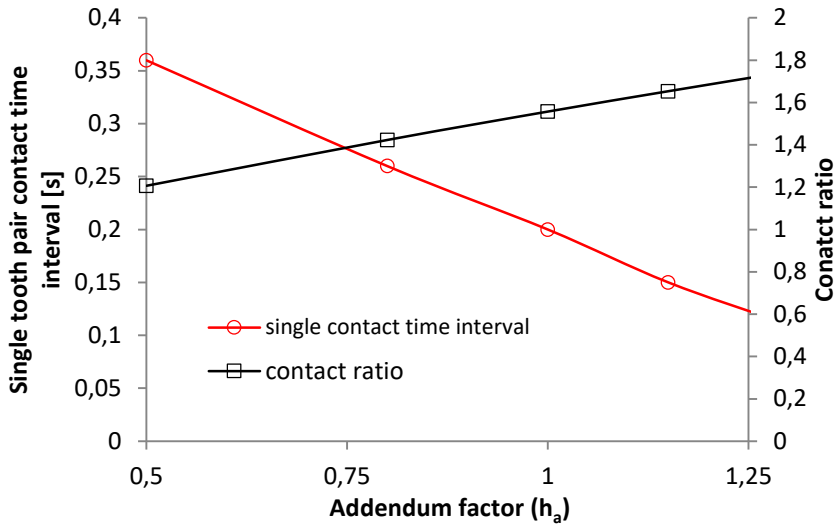

Figure 5.24 – Single tooth pair contact time interval and contact ratio (ε) as function of addendum factor (h_a).

5.6 Evaluation of root bending stress for a spur gear pair

Root bending stress is the result of the transmitting force applied to a generic point along the tooth flank that generates a moment at the root where the tooth is attached to the gear rim. The time-varying equivalent bending stress generated at the tooth root for the entire mesh cycle is plotted in Figure 5.25. Root bending stress depends entirely on two factors: the applied force and the distance between the tooth root and the position where the force is applied. At point A of Figure 5.25 the contact on the driven gear profile occurs in correspondence of the tip point while another tooth pair is simultaneously in contact. In the interval AA^I the Equivalent bending stress shows a constant trend that is the result of the product between the increasing shared force shown in Figure 5.15 and the progressive reduction of the bending arm as the force application point moves from the tip towards the root as shown in Figure 5.13. In the time interval BC only one pair of teeth is in contact and carries the entire load applied. The stress state is clearly higher in such an interval and decreases because the bending arm progressively decreases while the transmitted force is constant (Figure 5.15). The recess action D^ID sees the root bending stress decreasing due to the simultaneous reduction of the applied force and bending arm as the contact point is moving towards D, where the considered tooth pair disengages.

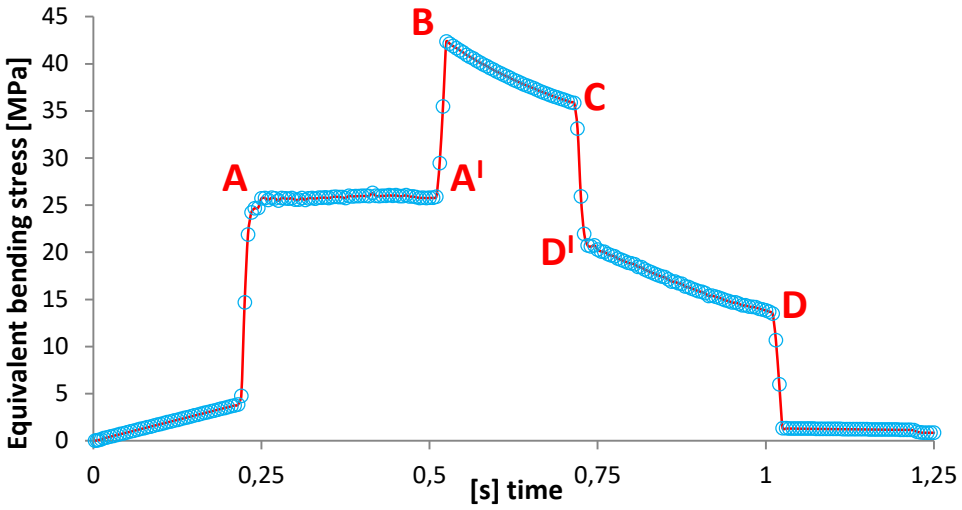

Figure 5.25 - Time varying Von Mises root fillet stress along the entire mesh cycle for the reference gear pair.

5.6.1 Effect of pressure angle

The quasi-static FE method was also used to evaluate the generated root bending stress for different pressure angles in the range 20°<α<32°. Plots of nodal time-varying Equivalent root fillet stress are shown in Figure 5.26. Also for the case of root bending stress, the sudden change in values corresponding to the beginning and end of the single tooth pair in contact is shown, and its duration (interval BC in Figure 5.26) varies as function of pressure angle. Increasing the pressure angle reduces the contact ratio that corresponds to an increase of the segment length, BC. From the full root bending stress spectrum, it can be noticed that an increase of α corresponds to a lower stress state in the interval where a single tooth pair are in contact but also to a longer exposure to a higher stress state when two pairs of teeth are in contact.

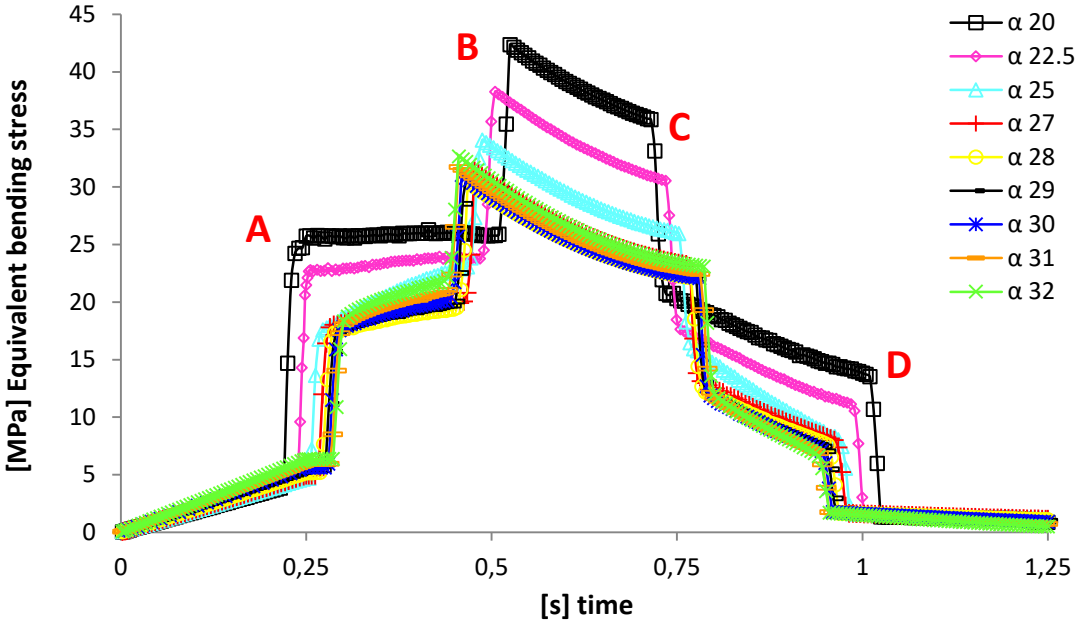

Figure 5.26 - Time varying Von Mises root fillet stress along the entire mesh cycle for 20°<α<32°.

Maximum values of bending stress at the root fillet are shown in Figure 5.28 as function of pressure angle. The trend indicates a minimum for bending stress corresponding to a 28° pressure angle. This result can be explained by taking into consideration the tooth fillet radius and its necessary variation for values of pressure angle above 28°. By making a geometric consideration based on Figure 5.1 it can be seen that to an increase in pressure angle corresponds a thicker tooth base with a consequent reduced space between two adjacent teeth. Furthermore, for α=28° the base circle is close to the root circle reducing the space available for the fillet. The consequence is that the root fillet radius decreases as shown in Figure 5.27 and effects of stress concentration start to be evident. The standard root fillet radius for the standard ISO 53 Profile A fixed at 0.38 mm is maintained for values of α up to 28°. For α=30° ρ_f is reduced to 0.30 mm and the minimum is for α=32° where the root fillet radius is 0.22 mm.

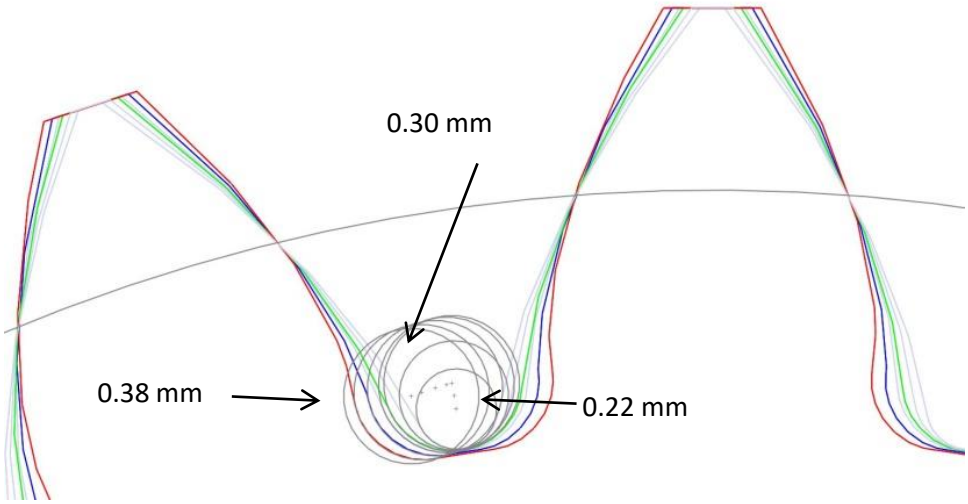

Figure 5.27 - Comparison between tooth profiles and root fillet radii for 20°<α<32°.

If a balance between the positive effect of a thicker tooth base and the negative effect of a small root fillet radius on the bending stress reduction can be made, the 28° pressure angle geometry would be the transition point. Up to α=28° the effect of a thicker tooth base overcomes the negative effect of a higher stress concentration at the root fillet. For bigger values of α, the stress concentration effect overcomes the beneficial effect given by a thicker tooth base, so the root bending stress inverts the trend and starts to increase. Numerical and analytical methods give different results for the considered analysis as shown in Figure 5.28. The concave trend followed by numerical values is not replicated by analytical results. ISO 6336 shows almost a linear decreasing trend going from the standard α=20° to α=32° with a small increase for values above 28° and gives more conservative results compared to FEA (Lisle et Al., 2017). The inaccuracy in the calculation of the stress state for high pressure angle gear pairs is confirmed in the ISO 6336 Part 1 which suggests that users confirm their results by experience when operating pressure angles exceed 25° (McVittie, 1998). For numerical results, the maximum gap of root bending stress occurs between α=20° and α=28° with a reduction of 28.2% for α=28°. If the same comparison is made by considering numerical calculations a reduction of 13.9% is seen. The maximum gap resulting from the numerical analysis occurs between α=20° and α=32° and is equal to 17%.

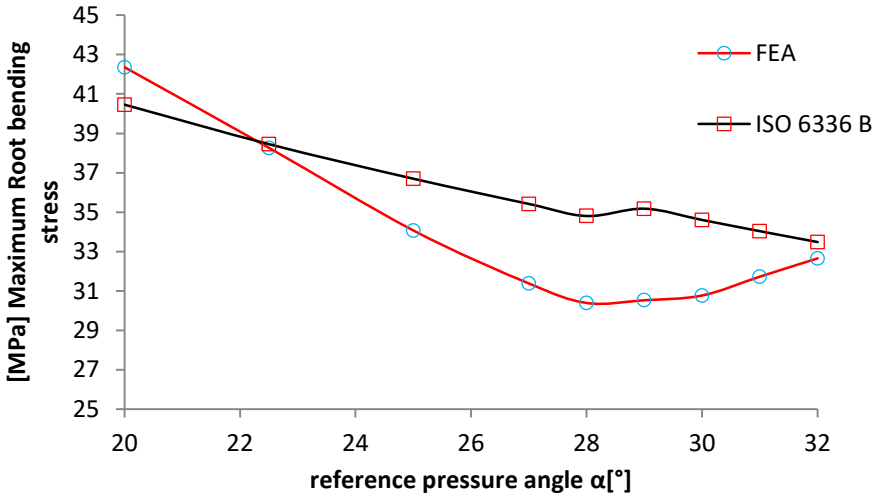

Figure 5.28 – Maximum values of root bending stress for varying pressure angles (α) compared to nominal root stress from ISO 6336-B.

5.6.2 Effect of profile shift coefficient on root bending stress

The parametric study has also been carried out with regards to the variation of profile shift coefficient on root bending stress. The resulting time-varying root bending stresses along the mesh cycle calculated by quasi-static FEM for five different profile shifts are shown in Figure 5.29. Time-varying stresses for the analysed cases see almost parallel trends that decrease as the profile shift increases. By referring to the standard geometry with x=0 it can be noticed that negative shifts are responsible for higher stress states while positive shifts give a stress reduction. Another aspect that can be noticed in Figure 5.29 is the variation of approach and recess actions: Positive profile shifts on the driven gear bring a reduced approach and an extended recess, inversely negative values for x imply a longer approach. This determines the shift for all the time-varying plots towards the left where the first point of contact A occurs. Profile shift modifies contact ratio in the same way as for the case of pressure angle, the time interval BC of single tooth contact increases with positive profile shifts. The variation in length in this case is not symmetric as it was for the pressure angle in Figure 5.26.

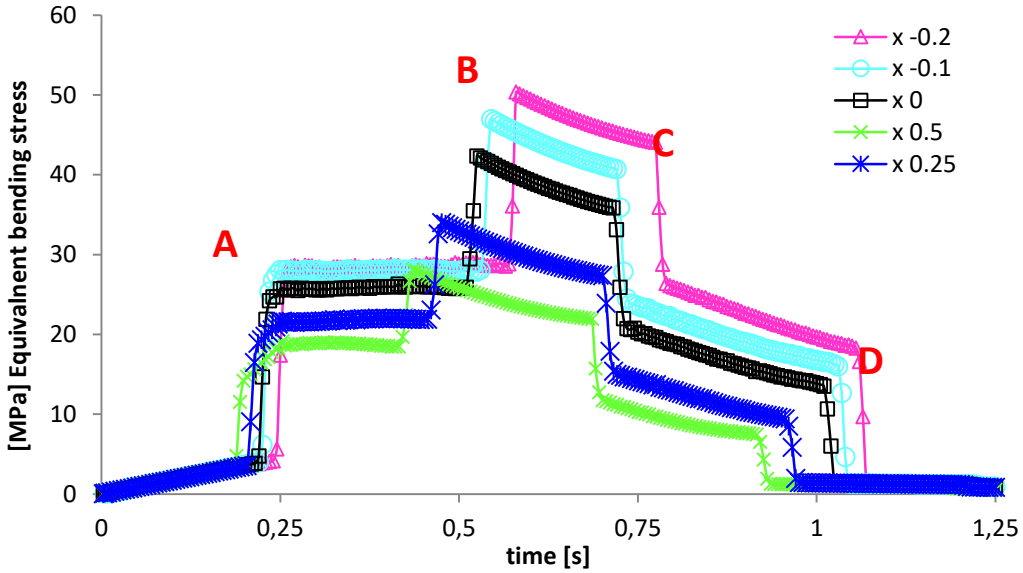

Figure 5.29 - Root bending stress along the mesh cycle for varying profile shift coefficients -0.2<x>0.5.

Also for this case, the maximum values of bending stress were plotted against profile shift coefficient, as shown in Figure 5.30. The values show a linear decreasing trend in maximum bending stress as the profile shift coefficient increases. Given the similarities that profile shift has with pressure angle on the tooth geometry, limited to the range of profile shifts used, α_w varies from 19.1° for x=-0.2, to 23.3° for x=0.5. As expected, the trend shown in Figure 5.30 is similar to the initial part of the one presented in Figure 5.28. Analytical results also show a linear decreasing trend for the variation of x from negative to positive values being in close accordance with that found by means of FEA.

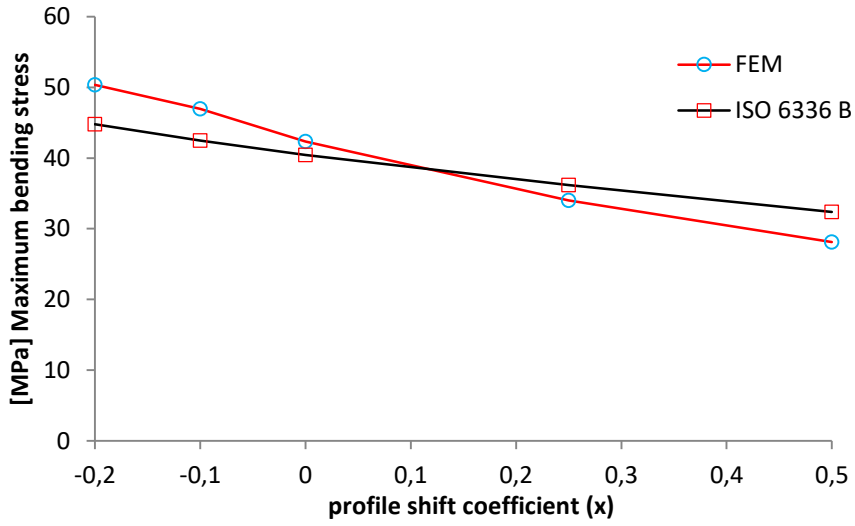

Figure 5.30 - Effect of varying profile coefficient on maximum root bending stress.

5.6.3 Effect of dedendum factor h_f on root bending stress

The time varying maximum bending stress is also evaluated for the case of a variation in dedendum factor in the range $1<h_f<1.5$. Dedendum factor has an effect on the region of the tooth below the pitch diameter. An increase in h_f results in an increased tooth length with negative effects on the maximum bending stress because of the increased moment applied to the tooth root. Plots of variation of nodal Von Mises stress along a complete mesh cycle are shown in Figure 5.31.

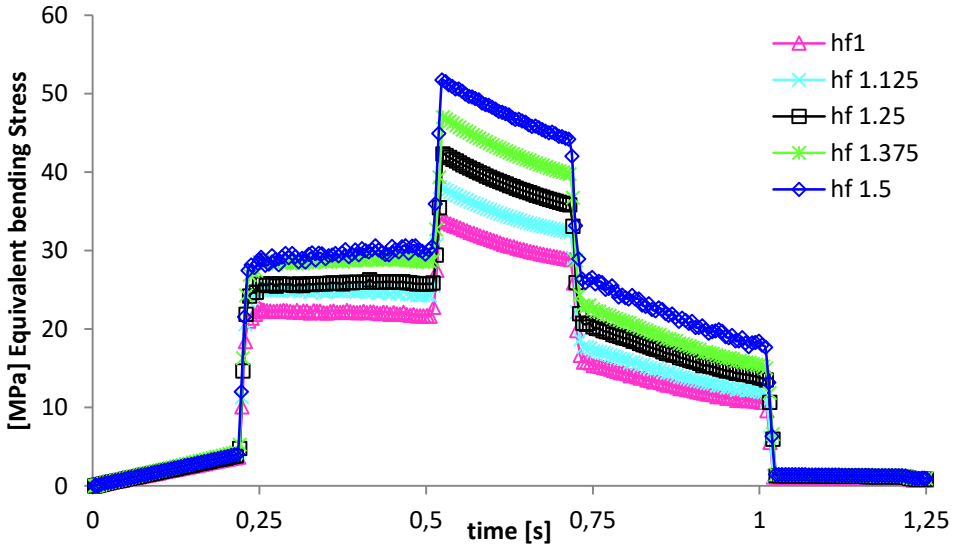

Figure 5.31 - Maximum root bending stress as function of dedendum coefficient for 1<hf<1.5.

By comparing the entire spectrum of root bending stress for the five cases tested it can be seen that position of all the characteristic points in the cycle are fixed as consequence of the constant contact ratio. Variations in terms of stress magnitude are accentuated in the area of single tooth pair in contact and result smaller when two pairs are simultaneously in contact. Also for this case, maximum values of equivalent root filet stress are plotted in Figure 5.32 and compared with analytical results. The outcome is a linear increasing trend as the dedendum coefficient increases for both calculation methods, although the numerical analysis results are slightly more conservative than the ones according to ISO 6336 (2006).

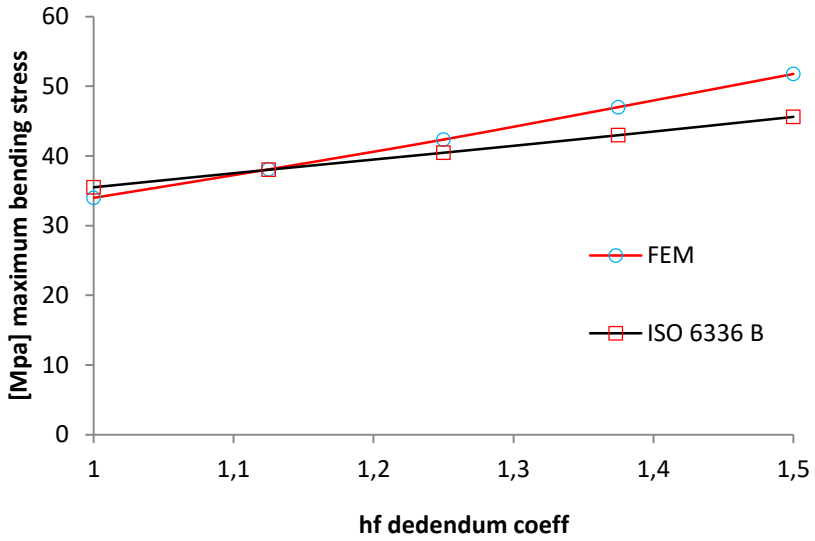

Figure 5.32 - Effect of dedendum factor on bending stress.

5.6.4 Effect of addendum factor h_a on root bending stress

The addendum factor, h_a, has an effect on tooth geometry in the region above the pitch diameter. Despite an increase in tooth length, in this case the maximum bending stress result from FEA does not show any variation in terms of peak value, as shown in Figure 5.33. This effect can be addressed by the fact that the addendum factor, in this study, is varied only for one of the mating gears. To clarify this aspect, the addendum factor has also been varied for the pinion in order to achieve a long addendum profile for the two gears in mesh. A further increase was not possible due to the occurrence of tip root interference condition. Root fillet maximum bending stress results for this last case are also plotted in Figure 5.33 with a red line, and show a reduction of bending stress peak value of 9.5% compared to all the other cases in which the modification was applied only to the driven gear. The addendum factor also has an effect on the time interval during which the maximum range of values occur as explained in 5.8.4. As the average number of teeth in contact increases with the addendum coefficient, the time interval for a single pair of teeth in contact decreases, reducing prolonged high stress states acting on the gear. The contact ratio varied from ε=1.207 for h_a=0.5, to ε=1.746 for h_a 1.3. For the case in which the modification was applied to both pinion and gear, the contact ratio was ε=1.941.

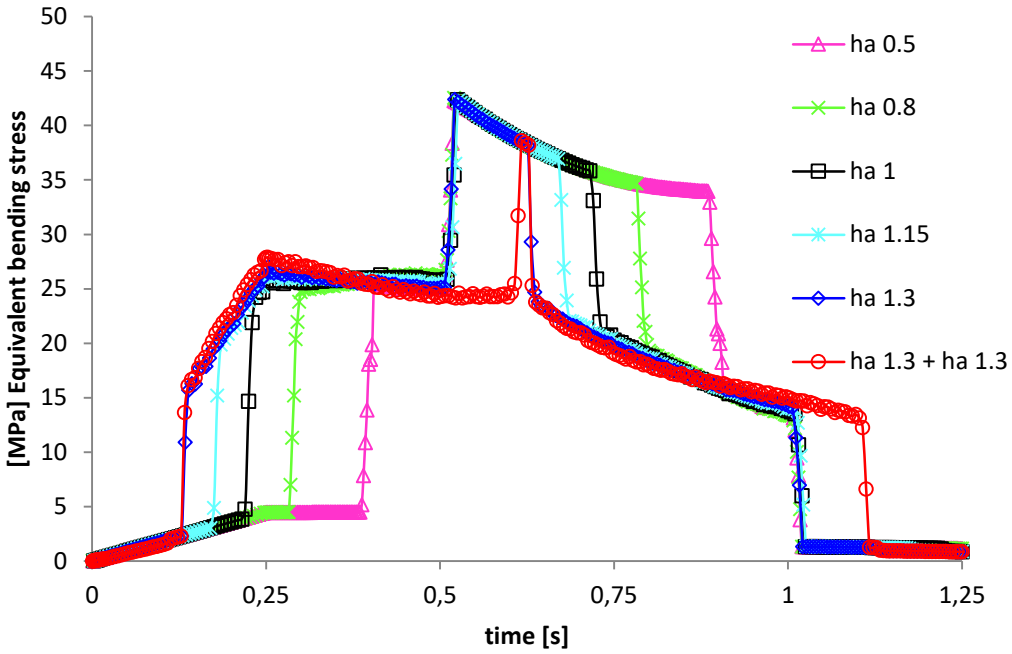

Figure 5.33 - Equivalent root bending stress as function of addendum coefficient for $0.5<h_a<1.3$.

5.7 Conclusion

This chapter focuses on the influence of relevant geometrical parameters on the contact and bending stresses that develop in loaded mating involute profile gears. Von Mises contact and bending stresses have been estimated by means of finite element analysis and compared to analytical values calculated in accordance to the ISO 6336 Standard. An established procedure to overcome convergence difficulties due to the high degree of non-linearity of the mating gear system is used. Moreover, the effect of contact detection methods, which contribute to the quality of the achievements, is investigated and the optimal setting proposed. A number of gear geometries characterised by pressure angles, profile shift coefficients, addendum and dedendum factors were studied with respect to the effective contact and bending stress distribution during a complete mesh cycle of a tooth pair. Results have shown the role played by the geometrical parameters investigated in terms of highest stress magnitude and duration. The following observations can be made on the basis of this parametric study:

- For a given combination of geometrical parameters with fixed module and number of teeth, an increase in pressure angle and profile shift coefficient has resulted in an overall reduction of the stress state.
- FEM results show a constant decreasing trend of contact stresses from 428.63 or 427.3 MPa to 427.3 or 381.21 MPa for numerical and analytical results respectively when the pressure angle is increased in the range $20°<\alpha<32°$. This trend is comparable to the one generated with analytical results. While the numerical analysis shows a linear decreasing trend, the analytical one, following the ISO 6336 standard, displays a trend which is linear with a discontinuity for $\alpha=28°$ (382.21 MPa).
- FEM result of the equivalent bending stress occurring at the tooth root fillet shows (in the range $20°<\alpha<32°$) a clear minimum of 30.40 MPa for a pressure angle of 28° which is 28.2% lower than 42.35 MPa corresponding to $\alpha=20°$ and 6.9% lower than 32.66 MPa for $\alpha=32°$. The minimum is not confirmed by analytical calculations according to ISO 6336 as they generate an almost linear trend from 40.45 MPa to 33.49 MPa.
- Given that a positive profile shift coefficient leads to an increase in operating pressure angle, it also contributes to a reduction in contact stress and bending stress. In a range of profile shift between X=-0.2 mm and X=+0.5 mm the minimum value of contact and bending stress is found for X=+0.5 mm where the maximum value of operating pressure angle occurs. Numerical and analytical results are comparable for the case of profile shift variation for both contact and bending stress and show an overall decreasing trend with a minimum of 403.75 or 396.22 MPa for contact and 32.37 or 28 MPa for bending stress if analytical or numerical analyses are considered.
- Addendum factor has an effect on contact stress distribution by affecting the contact ratio. The addendum factor variation modifies the time interval when the tooth profile is subjected to a higher stress state. Moreover, by reducing the driven gear outside diameter, an increase of maximum contact stress in the area of single tooth pair contact is registered. Also for the case of bending stress,

varying the addendum coefficient affects the duration of the maximum bending stress interval but without having any influence on its magnitude.

- Dedendum factor does not have any influence on the contact stress values. On the other hand, bending stress is directly affected by a dedendum factor variation and increases with h_f. The linear trend shown by FEA results is confirmed by analytical calculations and shows its minimum of 35.49 MPa for h_f=1 and the maximum value of 51.75 or 45.6 MPa if FEA or ISO 6336 are used for h_f=1.5.
- Numerical and analytical results are generally in good agreement for the calculation of Equivalent contact stress. Also with regards to Equivalent root bending stress a good agreement is seen for values of $\alpha<25°$ while for higher values of pressure angles the difference between results calculated from ISO 6336-B is generally because these are more conservative than the ones calculated by means of FEA.

The outcome of the parametric study gives clear guidance of how to enhance the load carrying capacity of a gear pair, through the variation of what are often considered as standard parameters.

6 High pressure angle planetary drives

Epicyclic gear arrangements are generally known for their improved power to weight ratios and maximised power density compared to traditional parallel axis gearboxes. Epicyclic gearboxes are traditionally used in hand tools (Figure 6.1) as their main requirements are compactness and lightweight. These devices are typically used for tightening and loosening fastenings on wind turbine assemblies, oil and gas pipeline installations, and in general for applications in which an accurate and quick tightening of high number of fasteners is required. The gear system provides the power transmission from the user to the output device achieving a mechanical advantage when a high amount of torque is required, especially in limited workspaces. In those cases, epicyclic gear trains are the most viable solution due to their concentric axes physical disposition that provides weight reduction and compactness as consequence of an improved power density (Höhn et Al., 2013; Kapelevich et Al., 2011).

Figure 6.1 - Single and multiple stages hand torque multipliers. Part number 16012 from the NORBAR® catalogue (Norbar Torque Tools ltd., 2018).

Despite the large amount of literature available on epicyclic transmissions there is very little information about applications with low rotational speed and high levels of transmitted torque. For these specific conditions, the only standard entirely dedicated to Epicyclic gearboxes ANSI/AGMA 6123-B06 (2006), confirms the gap in knowledge, underlining the necessity of undertaking a detailed engineering study in order to satisfy the requirements for the design of epicyclic devices. In this part of the study, an attempt

to further increase the load carrying capacity of planetary transmissions has been attempted by applying the concept of “high pressure angle gears” previously determined.

This chapter will cover critical design considerations for epicyclic gear arrangements. The design space for internal mating gears has been defined and further constraints typical of epicyclic configurations have been included. A case study was conducted in order to investigate the simultaneous influence of non-standard geometrical parameters on the distribution of stresses and load carrying capacity in planetary drives.

6.1 Geometrical arrangement of epicyclic drives

Basic Epicyclic gearing configurations consist of four different members. The simplest arrangement is composed by the planets engaged with the sun which is placed at the centre of the system and with the ring gear that includes all the mating components working as casing. The planets are held in their relative position by a carrier connected with the output shaft as Shown in Figure 6.2. Usually two or more planets are used to distribute evenly the transmitted load and balance the dynamic forces. The term epicyclic derives from the mathematical function epicycloid, which is the shape of the curve traced by a generic point of the planet gear when it rolls around the sun while is carried by the planet carrier (ANSI/AGMA 6123-B06 2006). In (non-differential) Epicyclic systems, depending on which member if fixed, the resulting arrangement is designated by a different name. We refer to “solar” systems when the sun is fixed with the ring gear and planet carrier working differently as input and output. If the carrier is the fixed element, the arrangement is called “star”. It is interesting to notice that for this configuration the planet does not follow an epicycloid because it is prevented from rotating about the axis of the system, and is only free to rotate about its own axis. Nevertheless, it is common to consider star configurations as epicyclic gearings. The third possible configuration involves a fixed ring gear and is called “planetary”. In a planetary configuration, with the internal gear prevented from rotating, the planets orbit around the sun gear and provide the output torque through the carrier. Depending on the arrangement of the transmission, speed ratio and rotational direction change

accordingly. From now on, the investigation will focus on the planetary arrangement as it is the appropriate configuration for the use in hand tools products.

The speed ratio output/input of a planetary gear train with the sun gear being the input and the planet carrier the output members is determined by Equation 6.1 where N_s and N_R are number of teeth of sun and ring gear respectively (ANSI/AGMA 6123-B06 2006, Ferguson 1983, KHK 2015):

$$i = \frac{\frac{N_s}{N_R}}{1 + \frac{N_s}{N_R}} = \frac{1}{\frac{N_R}{N_s} + 1} \qquad 6.1$$

Input and output members rotate in the same direction.

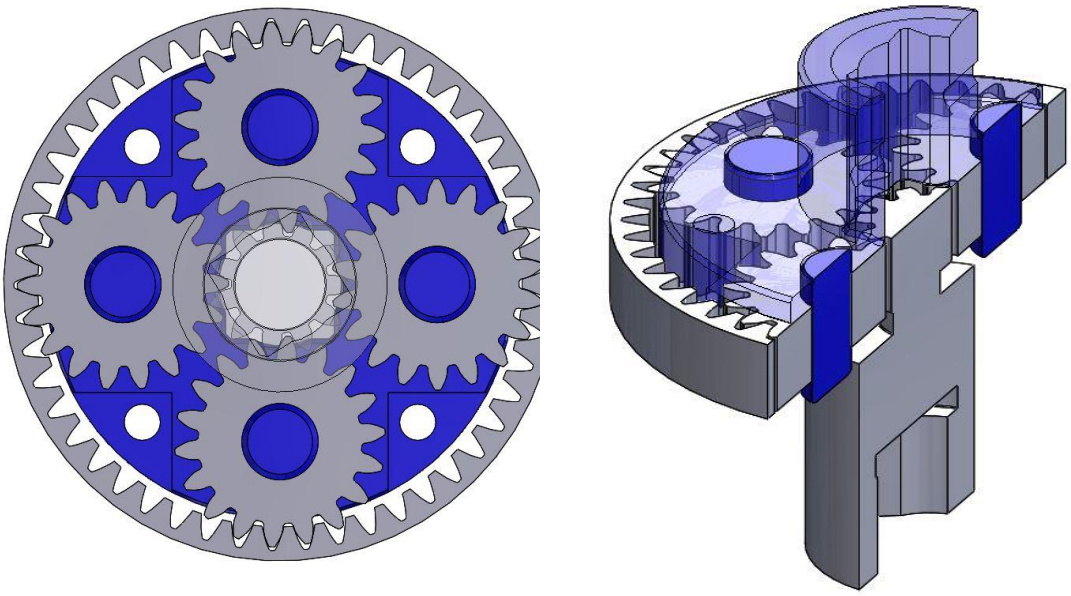

Figure 6.2 - Frontal view and trimetric cross-sectional view of a 5:1 reduction ratio, four planet, single stage epicyclic speed reduction system.

6.1.1 Meshing and assembly requirements

Epicyclic gear systems, due to the simultaneous mesh between multiple components, can be considered higher order systems compared to classical parallel axis arrangements. The geometrical disposition of mating elements, that involves multiple planet gears simultaneously in mesh with the sun gear and enclosed within the ring gear, imposes further constraints over the ones typically addressed for parallel axis systems.

For an epicyclic configuration centre distance and number of planets have to be considered in order to allow a correct assembly and meshing conditions. Three main conditions have to be fulfilled in order to determine a relation between the number of teeth of sun, planet and ring gears (ANSI/AGMA 6123-B06 2006, KHK 2015).

- First, the equality of centre distances between sun /planet and planet/ring must be guaranteed: a_{we}= a_{wi}. This is a general condition and is valid for both standard and non-standard geometries.
- The second condition to satisfy is related to the even distribution of planets around the sun gear which is expressed by the following relation:

$$\frac{(N_s + N_r)}{n} = integer$$

- The last condition ensures that adjacent planets are not so close as to interfere with each other during assembling and working operations. The general rule, valid for both standard and non-standard geometries is expressed by the inequality:

$$d_{ap} < 2a_w \sin\beta \qquad 6.2$$

  Where d_{ap} is the tip diameter of the planet gear and β is half of the angle between adjacent planets.

The above mentioned constraints, impose limitations on the number of teeth that can be chosen and directly affect the maximum speed ratio that can be achieved. The ANSI/AGMA 6123-B06 standard reports the maximum values of gear ratio achievable with standard profiles for the different epicyclic arrangements. For the case of simple planetary configurations, the maximum achievable gear ratio is reported as being 12.5 and can be achieve by using 3 planets only. As the number of planets increases the maximum overall ratio decreases up to a value of *i*=2.7 if 8 planets are used. As this is a guideline only valid for standard profiles, by means of non-standard corrected tooth geometries and non-standard centre distances it is possible to achieve different gear ratios and match the requirements of specific applications by varying these other parameters.

In addition to the three basic constraints above, the geometrical limits of internal gears also have to be taken into consideration.

6.2 Internal gears geometry definition

The most frequent applications of internal gears is in epicyclic gear systems. Due to the peculiar characteristic of internal mating gears, that determine a reduced centre distance compared to an equivalent external gear pair, a more compact design is achieved for any particular reduction ratio. Also the concave/convex contact interface gives a reduction in contact stress, and the wider tooth base is responsible for reduced bending stresses. The internal mesh also determines a longer line of action which results into an increased contact ratio with consequent distribution of the transmitted load over more teeth in simultaneous contact.

In order to define the geometry of internal gears, the same considerations already applied in Chapter 3 with regards to external gears can be used after appropriate modifications that take into account the inverted profile of teeth. A sketch of two gears in internal mesh is shown in Figure 6.3. As can be seen, the basic geometric quantities are inverted compared to external mating gears: tip diameter is smaller than pitch and root diameter. For the case of internal gears pitch and base diameters are calculated in the same way as for external gears by Equations 3.26 and 3.37. The tip and root diameters are calculated as follows:

$$d_{ai} = d - 2(h_{ai} - x_i)m \tag{6.3}$$

$$d_{fi} = d + 2\left(h_{fi} + x_i\right)m \tag{6.4}$$

From this, addendum and dedendum lengths [mm] are derived and equal to:

$$H_{ai=(h_{ai}-x_i)m} \tag{6.5}$$

$$H_{fi=\left(h_{fi}+x_i\right)m} \tag{6.6}$$

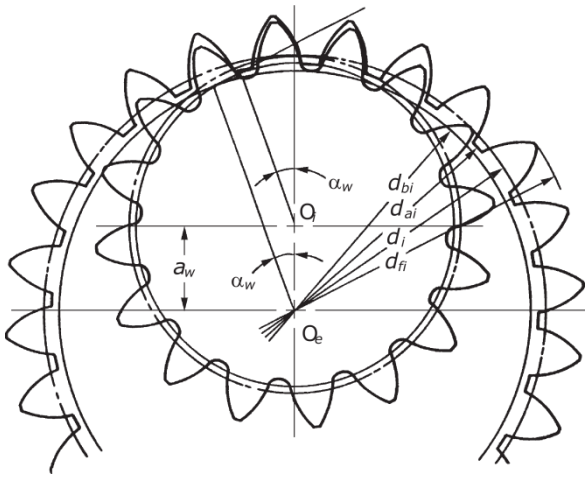

Figure 6.3 – Graphical representation of internal mating gears with highlighted basic geometrical quantities of internal gears: d_{bi} base diameter; d_{ai} tip diameter; d_i pitch diameter; d_{fi} root diameter.

Figure 6.3 also shows the distance between centres of the two gears in internal mesh. In this case the external gear is placed inside the internal gear so centre distance $\overline{O_i O_e}$ is not the sum of the working pitch radii as for the case of mating external gears (Equation 3.35) but rather the difference, as given in Equation 6.7 for a non-corrected gear pair.

$$a = m\frac{(N_i - N_e)}{2} \qquad 6.7$$

If a profile shift coefficient is applied, also in this case, the diameter of the pitch circles changes and becomes a working quantity to be calculated with Equations 3.33 and 3.34. Profile shift in internal gears is considered positive when the shift is applied in the opposite direction of the centre while the negative profile shifts are applied towards the gear centre. The choice of such reference systems helps in the calculations as it makes the shift direction consistent with the one used for external gears. For such a configuration, if the profile shift applied to the two mating gears is both positive and of the same quantity, then the modification will be balanced and no centre distance variation will occur. For the sake of clarity, KISSsoft applies profile shifts in the opposite directions compared to the ones defined here. If $+x_1 \neq +x_2$, then the working pitch radii require α_w to be calculated. The iterative method for the determination of the working pressure angle from the involute function is the same as the one explained in 3.2.3 for

external mating gears. The involute function is adjusted for the case of internal mating gears as given in Equation 6.8

$$inv\alpha_{wi} = m\frac{(x_i - x_e)\tan\alpha}{\frac{(N_i - N_e)}{2}} + inv\alpha \qquad 6.8$$

The working centre distance for unbalanced profile shifts applied to internal mating gears can now be calculated as follows:

$$a_w = a\frac{\cos\alpha}{\cos\alpha_w} = (r_i - r_e)\frac{\cos\alpha}{\cos\alpha_w}m \qquad 6.9$$

6.2.1 Internal gearing geometrical and operational boundaries

Manufacturing and operational boundaries can be defined also for the case of internal mating gears. The involved parameters do not differ from the ones defined for external gearing except for the fact that the "negative" of the tooth profile has to be taken into consideration. The existing relations between geometrical parameters and their mutual influence allow an area to be defined where a feasible combination of parameters determines the geometry of involute internal spur gear profiles. The relations that determine the boundaries of the feasible $x_{i,e}$ domain for internal gears are given as follows.

6.2.1.1 Geometrical Interference

The geometrical Interference defined in Section 3.3.3 with regards to external gears is replaced, in the case of internal mating gears, by three different types of interference namely: Involute, Trochoid and Trimming interference as shown in Figure 6.4.

- Involute interference occurs between the addendum of the internal gear and the dedendum of external gear and is comparable to the condition of non-undercutting of external gears in Section 3.3.1. This type of interference is relevant when the number of teeth of the external gear is small. The limiting condition that expresses the interference of the involute is given in the Equation below:

$$d_e \geq d_i\tan\alpha_w - d_i\tan\alpha_{ai} \qquad 6.10$$

Where α_w is the working pressure angle and α_{ai} is the pressure angle at the tip diameter of the internal gear tooth, and is calculated as follows:

$$\alpha_{a1} = \cos^{-1}\left(\frac{d_{bi}}{d_{ai}}\right) \tag{6.11}$$

- Trochoid Interference occurs between the addendum of the external gear and the addendum of internal gear. This interfering condition tends to happen when the difference in the number of teeth between the two gears is small. The limiting condition is expressed by Equation 6.12:

$$\theta_{ai} \leq \theta_{ae}\frac{d_e}{d_i} inv\alpha_w - inv\alpha_{ai} \tag{6.12}$$

In which, angles $\theta_{a,i}$ refers to the sketch in Figure 6.4 for the part relative to the trochoid interference.

$$\theta_{ae} = \cos^{-1}\left(\frac{r_{ai}^2 - r_{ae}^2 - a^2}{2ar_{ae}}\right) + inv\alpha_{ae} - inv\alpha_w \tag{6.13}$$

$$\theta_{ai} = \cos^{-1}\left(\frac{r_{ai}^2 - r_{ae}^2 + a^2}{2ar_{ai}}\right) \tag{6.14}$$

- Trimming Interference refers to the manufacturing process of internal gears by means of pinion cutter and also to the assembly process of the internal/external gear pair. When one of the two gears is moved in a radial relative motion with respect to the other, the addendum of the external gear might interfere with the addendum of the mating internal gear. The limiting condition for the trimming interference is expressed by:

$$\theta_{ae} + inv\alpha_{ae} - inv\alpha_w \geq \frac{d_i}{d_e}(\theta_{ai} + inv\alpha_{ai} - inv\alpha_w) \tag{6.15}$$

Where $\theta_{a,i}$ related to the trimming interference condition shown in Figure 6.4 are:

$$\theta_{ae} = \sin^{-1}\sqrt{\frac{1 - (\cos\alpha_{ae}/\cos\alpha_{ai})^2}{1 - \left(\frac{d_e}{d_i}\right)^2}} \tag{6.16}$$

$$\theta_{ai} = \sin^{-1} \sqrt{\frac{1 - (\cos \alpha_{ai} / \cos \alpha_{ae})^2}{\left(\frac{d_i}{d_e}\right)^2 - 1}} \qquad 6.17$$

The equations presented in this paragraph are derived from the following sources (KHK 2015, Litvin 1989, Maitra 2012, Savage et al 1986).

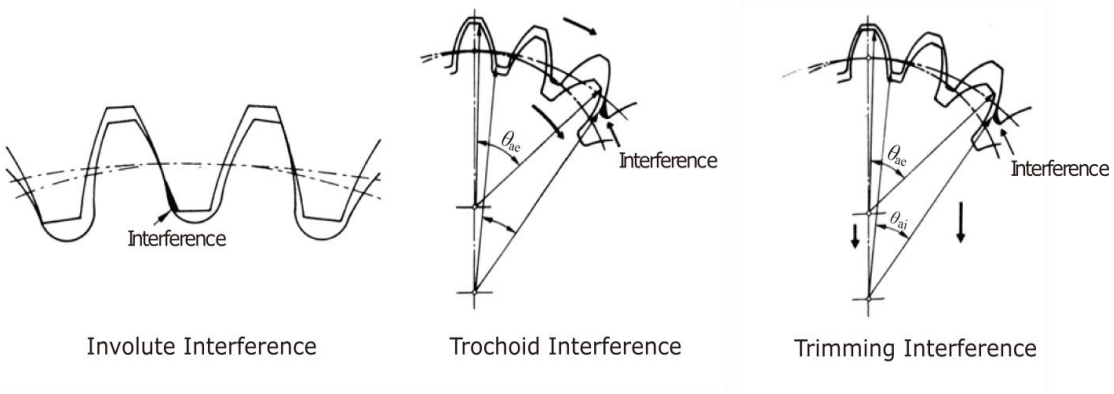

Figure 6.4 - Involute, Trochoid and trimming interference conditions occurring in internal mating gears.

6.2.1.2 Top land thickness and root space between adjacent teeth

The unwanted condition of a tooth top land that results in it being brittle and is a possible cause of early breakage due to reduced thickness also exists for internal gears. The literature suggests a range of minimum values for the coefficient of top land thickness of internal gears s_{ai} that spans from 0.2 to 0.4 depending on material, geometry and operational conditions (ANSI/AGMA 2101/D04, 2016; Kapelevich, 2013; Maitra, 2012). The thickness at the top land of internal gears can be found by geometrical considerations based on the parameters shown in Figure 6.5 (Tomori et Al., 2016). Starting with the profile pressure angle at the tip circle of the internal gear α_{ai}, derived from the following relation between tip and base radii.

$$r_{ai} \cos \alpha_{ai} = r_{bi} \qquad 6.18$$

$$\cos \alpha_{ai} = \frac{r_i \cos \alpha}{r_{ai}} \qquad 6.19$$

which yields:

$$\alpha_{ai} = \cos^{-1}\left(\frac{N_i m}{d_{a_i}}\cos\alpha\right) \tag{6.20}$$

The tooth thickness at the pitch circle:

$$S_i = \frac{m\pi}{2} - 2xm\tan\alpha \tag{6.21}$$

is related to the tooth thickness at the tip circle of internal gears by means of the profile angle σ_i as follows:

$$\sigma_i = \frac{S_i}{2r_i} - inv\alpha = \frac{S_{ai}}{2r_{ai}} - inv\alpha_{ai} \tag{6.22}$$

By rearranging 6.22, the top land thickness S_{ai} is determined in the equation below:

$$S_{ai} = 2r_{ai}\left(\frac{S_i}{2r_i} + inv\alpha - inv\alpha_{ai}\right) \tag{6.23}$$

And by substituting Equations 6.18 and 6.20 into 6.23, the tooth thickness at the tip circle of internal gears is expressed by:

$$S_{ai} = d_{ai}\left\{\frac{\pi}{2N_i} - \frac{2x_i}{N_i}\tan\alpha - inv\alpha + inv\left[\cos^{-1}\left(\frac{N_i m}{d_{a_i}}\cos\alpha\right)\right]\right\} \tag{6.24}$$

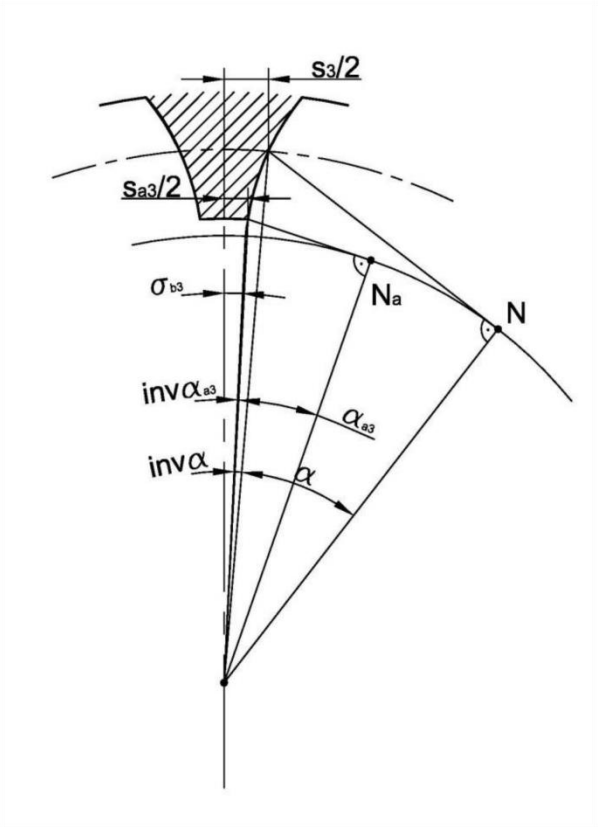

Figure 6.5 –Schematic diagram for the calculation of the top land thickness S_{a3} in internal gears;. α is the profile angle at the pitch circle; α_{a2} is the profile angle at the tip circle.

When the top land thickness of internal gears is plotted as a function of profile shift it follows a concave trend as shown in Figure 6.6. Differently from the case of external gears where a reduction in top land thickness was the result of an increase in pressure angle and/or profile shift coefficient, here, once the minimum value is derived and this results in values being above the imposed limit, then the profile shift can be changed without restrictions with respect to this limiting parameter. On the other hand, the pressure angle affects the top land thickness. The combined effect of simultaneous variations of α and *x* on s_{ai} is shown in Figure 6.6. It can be seen that for a given profile shift, as the pressure angle increases the top land thickness decreases linearly. This consideration suggests that the top land thickness of internal gears is a less strict limitation than the equivalent for external gears, and usually does not limit design choices unless very high values of pressure angle, α are used.

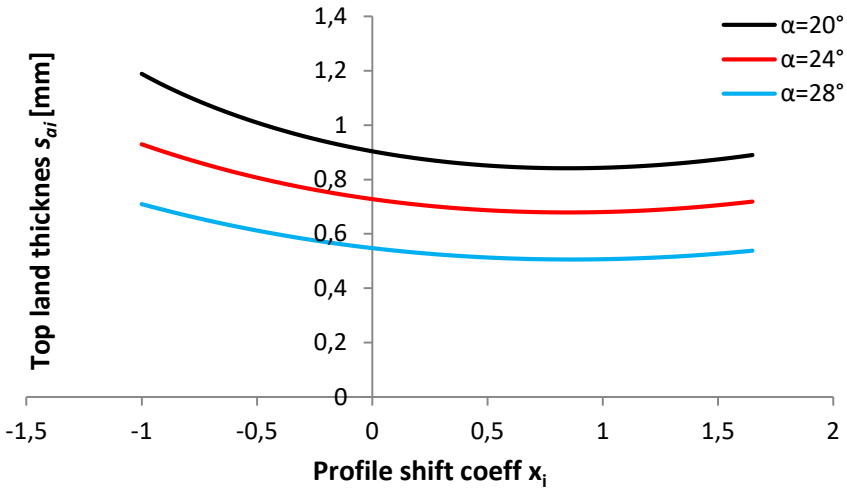

Figure 6.6 – Top Land Thickness of an internal gear, S_{ai}, as function of profile shift coefficient, x_i, for three pressure angles α (N=71; m=1).

Tooth space at the root of internal gears S_{fi} is equivalent to the top land thickness calculated for external gears with Equation 3.51. The only modification required involves the change of the tip diameter d_a in 3.51 with the actual root diameter d_{fi} of internal gears. Hence, the final Equation for the determination of S_{fi} is given as:

$$S_{fi} = d_{fi}\left\{\frac{\pi}{2N_i} + \frac{2x_i}{N_i}\tan\alpha + inv\alpha - inv\left[\cos^{-1}\left(\frac{N_i m}{d_{fi}}\cos\alpha\right)\right]\right\} \qquad 6.25$$

The space at the root of internal gears between two adjacent teeth is a parameter that has not been standardised so there is no information about the range of possible values. The only source found is in KISSsoft which suggests values for S_{fi} bigger than 0.2*m. A reduced space at the root may be the source of manufacturing problems and an area of stress concentrations due to the resulting pointed shape.

6.2.1.3 Contact ratio in internal gears

The contact ratio in internal gears is usually greater than the equivalent for external gears. Due to the geometrical configuration and the meshing process of internal mating gears, in which the external gear teeth are entirely covered by the internal gear teeth, the line of action is longer and in comparison more teeth are in simultaneous contact within a mesh cycle. An example can be considered by comparing the contact ratios of internal and external mating gears equivalent in geometry; if the values N_1=16, N_2=71,

α=20°, $x_{1,2}$=0 are compared to N_e=16, N_i=71, α=20°, $x_{1,2}$=0, the resulting contact ratio is for the external couple ε=1.65 while for the internal couple ε_i=1.88.

The geometrical explanation of contact ratio for internal gears is based on Figure 6.7 and differs from the one given in Equation 3.79, because of the position of the external gear that is placed inside the external one. In this approach the contact ratio ε is defined by the ratio between the length of the line of action AD and the base pitch.

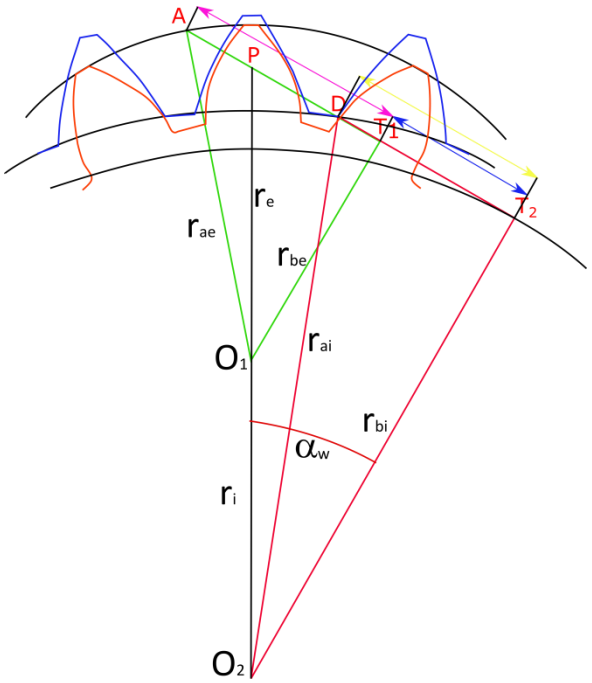

Figure 6.7 – Geometrical description of path of contact AD for internal gears.

In order to derive the length AD it is necessary to know the position of five fundamental points that lie on the line of contact highlighted in Figure 6.7. Point A is placed at the intersection between the line of contact and the tip circle of the external gear r_{ae}; point D lies on the line of contact at the intersection with the tip circle of the internal gear r_{ai}; T_1 and T_2 are the points where the line of contact is tangent to the base circle of external (r_{be}) and internal (r_{bi}) gears respectively; P is the pitch point where the pitch circles of the mating gears are in mutual tangency. Once the position of the above-mentioned points is known, the segments AT_1, T_1T_2 and T_2D can be calculated accordingly to Figure 6.7 as follows:

$$AT_1 = \sqrt{r_{ae}^2 - r_{be}^2} \qquad 6.26$$

$$DT_2 = \sqrt{r_{ai}^2 - r_{bi}^2} \tag{6.27}$$

$$T_1T_2 = (r_i - r_e)\sin\alpha_w \tag{6.28}$$

Which yields:

$$AD = AT_1 - (DT_2 - T_1T_2) \tag{6.29}$$

Now, by considering the initial assumption also valid for external mating gears:

$$\varepsilon = \frac{AD}{p_b} \tag{6.30}$$

And by substituting Equations 6.29 and 3.24 into 6.30 and rearranging it, yields the contact ratio for internal gears:

$$\varepsilon_i = \frac{\sqrt{r_{ae}^2 - r_{be}^2} - \sqrt{r_{ai}^2 - r_{bi}^2} + (r_i - r_e)\sin\alpha_w}{\pi m \cos a} \tag{6.31}$$

Also for this case, if the path of contact $\overline{AD}$ is equal to the base pitch p_b, the contact ratio would be 1.

The contact Ratio for internal mating gears varies as a function of pressure angle and profile shift as shown in Figure 6.8. Similarly, for the case of external gears, an increase in α corresponds to a decrease in contact ratio. Profile shift also plays a role with regards to contact ratio and in particular, as can be seen in Figure 6.8, the application of a positive profile shift translates the curve ε-α towards lower values of ε; inversely, if negative shifts are used, higher values of contact ratio will be obtained. Also for this case, the theoretical minimum contact ratio that can be achieved is 1, but when manufacturing tolerances and assembly errors are taking into account then the actual minimum to consider is ε_i=1.2.

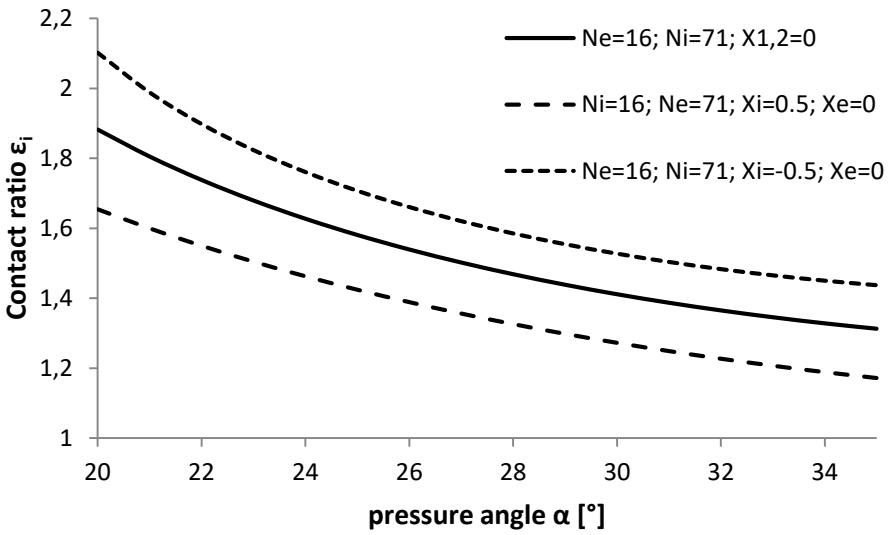

Figure 6.8 - Dependency of contact ratio for internal gears on pressure angle and profile shift.

6.3 Case study

The case study considered here is the design of the last stage of a multiple-stage planetary transmission gearbox produced by NORBAR®, for several hand power tools in their production range (Figure 6.9). Hand power tools demand compact gearboxes to meet safe handling requirements. A very compact transmission with high load carrying capacity is essential to reduce weight and volume, and improve power-to-weight ratio. For these applications, weight and physical compactness are the most effective characteristics to make the products attractive on the market. The design choices undertaken were aimed at reducing the stress on the components in order to evaluate the possibility of downsizing the existing design for the same amount of maximum torque transmitted. The size constraints listed in Table 6.1 were based on the original design of the power tool code n°18033-PT2000 produced by Norbar shown in Figure 6.9 (Norbar Torque Tools ltd., 2018).

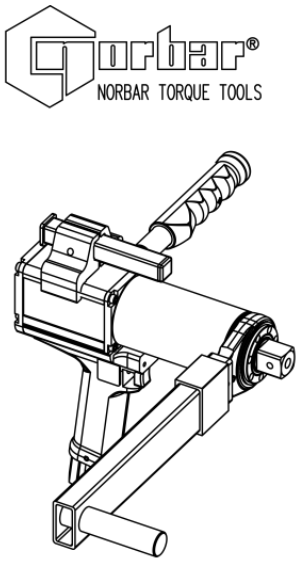

Figure 6.9 – Technical drawing of a power tool PT2000 designed by NORBAR® (Norbar Torque Tools ltd. 2018b).

Table 6.1 – Design constraints of a planetary drive for power tools applications

Torque ratio *i*	5.5±2%
Input Speed v_i [rpm]	13±5%
Centre distance [mm]	22
Number of planets	4
Facewidth [mm]	15
Ring gear OD [mm]	80

6.3.1 Design process

The following design process has been undertaken to model three epicyclic transmissions with a combination of standard and non-standard parameters. Once the design constraints and boundary conditions were defined, the design procedure was guided by the pressure angle with the aim to achieve a value of α_w as close as possible to 28° at the sun/planet interface where the highest stress levels occur. The choice of such value is dictated by the outcomes of the performance analysis in Chapter 5 from which it is evident that 28° pressure angle gives the best response in terms of root bending stress which contributes to the reduction of tooth flank contact stress. This

choice is further justified by the slow rotational speeds involved. Since a high value of pressure angle reduces the contact ratio with a consequent reduction on the smoothness of the mesh, vibration and noise then normally become important design constraints. In this case, and for other applications in which low speed rates are involved, as the dynamic load can be considered negligible, vibration and consequent noise are not relevant so that the stress level dominates the design process (Kapelevich, 2016; Novikov et Al., 2008).

The determination of the number of teeth for sun, planet and ring (internal gear) requires the fulfilment of multiple design constraints such as speed ratio, centre distance and outside diameter. In addition, the geometrical constraints imposed by planetary arrangements, and the geometrical constraints for external and internal gears have to be simultaneously considered.

Since transmission ratio, centre distance and overall transmission diameter were pre imposed design constraints, a combination of number of teeth that satisfied those constraints was determined as follow. Starting from the sun gear, the number of teeth has been chosen in consideration of the condition of undercutting. As shown in Figure 3.19, for a module m=1 mm, the minimum number of teeth that do not experience undercutting is 17. However, N_s=16 is a valid candidate as the amount of undercutting is negligible, only 0.064 mm, while it helps minimising the gear diameter. Once the number of teeth for the sun gear has been determined, the planet gear is a direct consequence dictated by the centre distance. In order to achieve the imposed condition a=22 mm, N_p=28 is the only option possible if no profile shifts are applied. The third mating component, the internal gear, has to fulfil the condition imposed by the centre distance as it is concentric with the sun and the condition imposed by the speed ratio listed in in Table 6.1. The number N_R that fulfils the two conditions is N_R=72. Nevertheless, N_R=72 does not fulfil the condition of trochoid interference expressed by Equations 6.12, 6.13, 6.14 in Section 6.2.1.1, due to an excessive thickness of the internal gear teeth. To overcome the interference condition, it has been decided to reduce the number of teeth to N_R=71 and apply a positive profile shift that in order to both reduce the tooth thickness and increase the working centre distance to a_w=22 mm. The module chosen was 1 mm. The design process for all the remaining parameters follows the method based on the blocking contour construction covered in Chapter 4 for the

external gears and previously in this chapter with regards to internal mating gears. Considering all the parameters described above and their mutual interaction, three different gear sets have been generated fulfilling the constraints imposed by planetary gear systems. Two gear sets had a resulting 28° working pressure angle at the sun/planet interface and above 30° at the planet/ring interface. This result is partially in compliance with the AGMA 6123-B06 (2006) standard in which it is stated that "best strength to weight ratio is achieved with high operating pressure angles at the sun to planet mesh and low operating pressure angles at the planet to ring mesh". A third gear set with a standard 20°/23.3° working pressure angle was also modelled for comparison purposes.

The design process described above can be schematised through a flow chart as shown in Figure 6.10. The diagram starts with a block containing basic design constraints addressed to the transmission system such as gearing ratio, centre distance and external diameter. The second step regards the selection of module and reference pressure angle which plays a crucial role on the gear properties and mechanical characteristics of the drive. The number of teeth of the sun gear are defined on the basis of manufacturing and geometrical constraints typical of external spur gears such as undercutting and pointed tooth tip. If one of the constraints is violated, given the value for module and pressure angle chosen in the previous step, there is the need to step back and adjust the pressure angle accordingly. Otherwise, when the design parameters are in a feasible range, the design routine can proceed to the next phase. With regard to the number of teeth of the planet gears, both limitations imposed by geometrical and manufacturing parameters and by the pre-imposed working centre distance a_w have to be considered. As for the previous step, if undercutting and/or pointed tooth tips happen, a step back to modify the reference pressure angle is necessary. Moreover, given that centre distance is function of module, number of teeth and profile shift, if a deviation from the pre-determined a_w is obtained then a modification of module and/or profile shift of sun and planet is required. The last design step is about the determination of the number of teeth that constitute the ring gear. The value of number of teeth in this case is function of two parameters already defined: gearing ratio (Eq. 6.1) and centre distance given the existing condition for epicyclic arrangements $a_{we} \equiv a_{wi}$. Internal gears are subjected mainly to operational and geometrical constraints such as conditions of interference and

sharp tooth fillet edges. In this case, given the impossibility to modify the profile shift fixed by the centre distance limitation, if interference or pointed tooth roots occur, a modification of pressure angle is necessary to make the gears working and mesh properly. By following the steps listed above, it is possible to design an epicyclic gear system involving either standard or non-standard gears.

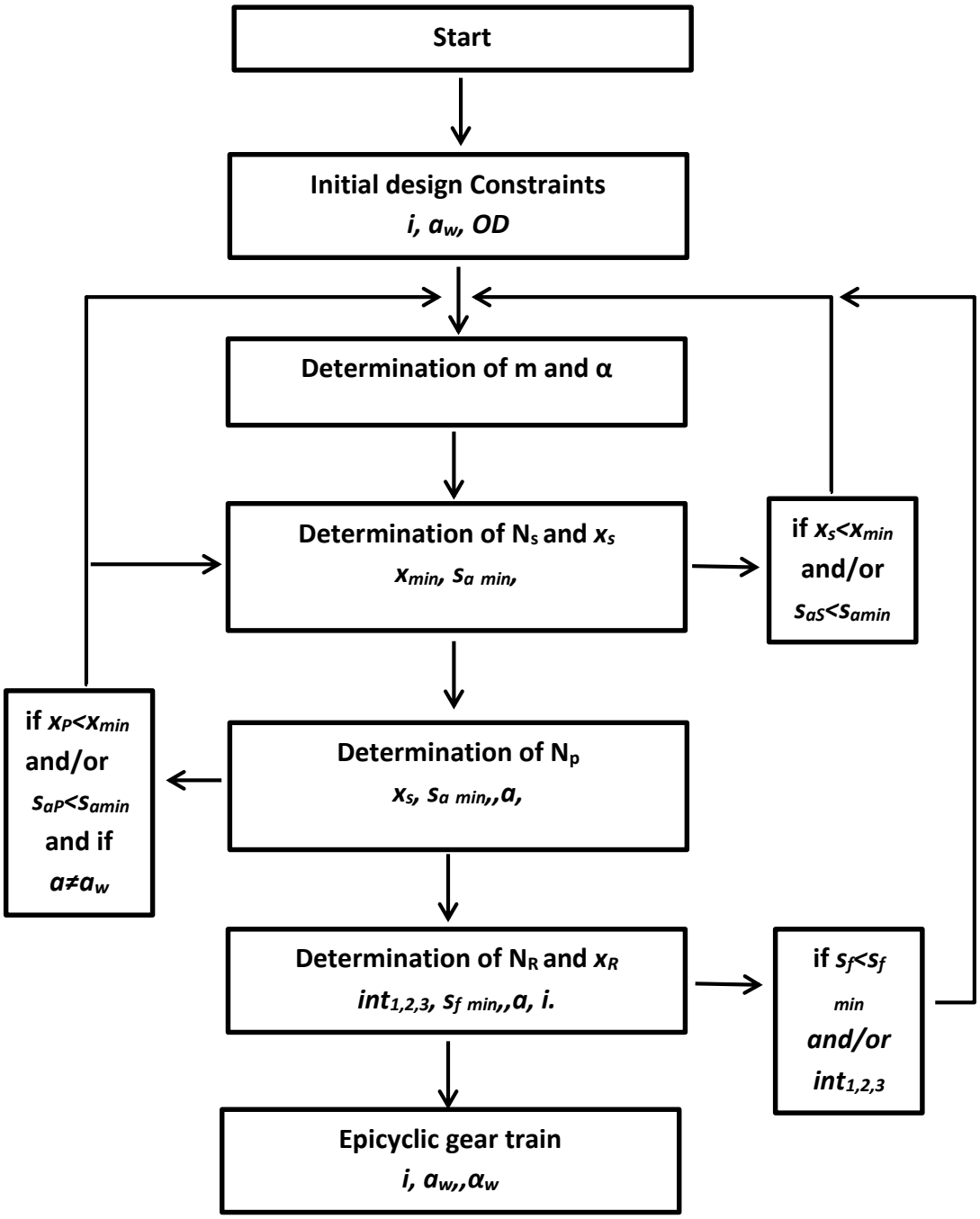

Figure 6.10 - Flow chart of the design process of epicyclic gear transmissions step by step in a logical order.

6.3.2 Geometry-based external/internal contour plots

Based on the equations given in the previous paragraphs, a multi-parametric design space was generated in order to study the geometrical properties of a gear train that includes an internal/external mesh as for the planetary configuration. In this paragraph, contour plots for the geometries studied are presented both for the external sun/planet and the internal planet/ring meshes. The design process, based on the concept explained in Chapter 4, is applied here in order to determine the necessary combination of geometrical parameters and fulfil the condition imposed by manufacturing and operational boundaries with the considerations of the extra assembly constraints imposed by the physical arrangement of epicyclic gears. The design process for epicyclic transmissions by means of the blocking contour technique has been attempted for the first time here. The literature survey in the field has not shown any study previously carried out with such a technique for the determination of internal gear parameters and even more for the geometrical definition of gears for epicyclic systems. The closest research work available is the one published by Goldfarb et Al. (2005) in which the authors explain the generation of blocking contours for external mating gears and attempt to further apply the contour blocking technique to internal mating gears.

To follow, the plots for the three cases studied are shown in the range of Figures 6.11 – 6.19 and a detailed analysis of the considerations involved is given. Starting with the standard 20° pressure angle system used as baseline for comparison, the first geometrical analysis considers planet and sun in external mesh. The plot in Figure 6.11, shows the area of feasible combination of geometrical parameters in the x_1x_2 domain where 1 and 2 refer to sun and planet respectively. The enclosed area, highlighted in grey, exists only in the second and third quarters of the diagram and is confined by the minimum contact ratio, minimum top land thickness for the sun, the limiting condition for undercutting for both sun and planet and corner interference occurring at the sun gear root fillet. The condition for $x_1=0$ is not available due to the number of teeth $N_1=16$ being below the minimum of 17 for $\alpha=20°$. Given the imposed constraint centre distance a=22 mm, the possible combinations x_1x_2 lie on the inclined line for constant a=22 mm passing through the centre and being coincident with the line representing the constant pressure angle $\alpha=20°$. The $x_1=0.065$ and $x_2=-0.065$ combination chosen had to be

reciprocal in order to maintain the imposed centre distance and the desired condition of a working pressure angle α_w=20°. The value of x_1 was chosen according to the boundary geometrical limit in order to avoid the occurrence of undercutting while the negative *x* applied to the planet allows the profile shift to be balanced while maintaining a constant centre distance equal to 22 mm.

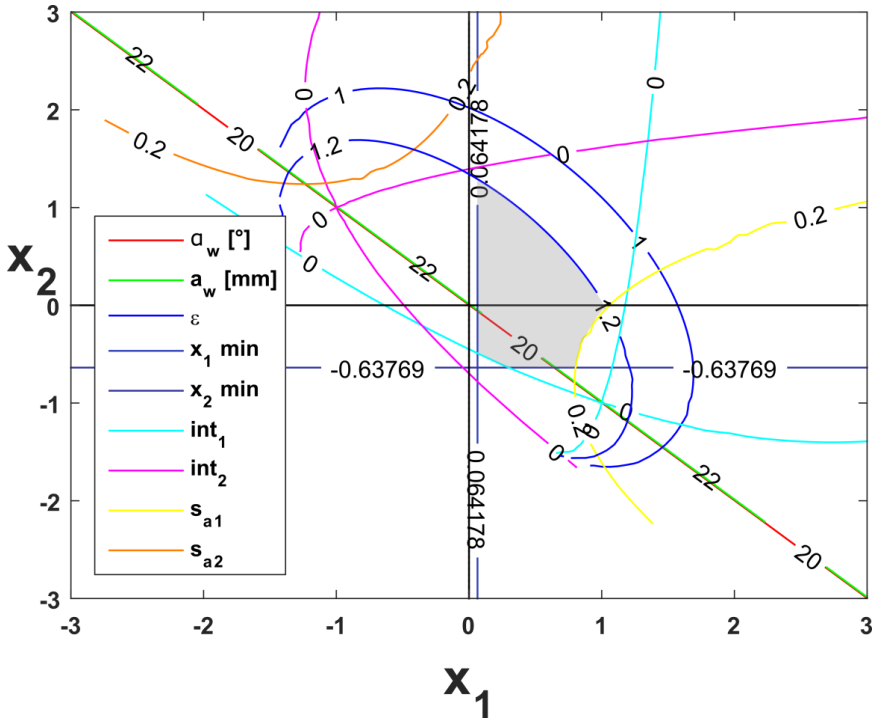

Figure 6.11 – Feasible domain for involute spur gears in external mesh with α=20°, N_1=16, N_2=28, m=1, $h_{a1,2}$=1, $h_{f1,2}$=1.25.

Once the $x_{1,2}$ combination is defined and fulfil all the imposed restrictions the plot in Figure 6.12 representing the planet/ring meshing conditions can be considered. In this case the area of feasible $x_{e,i}$ combinations is bounded by the limit of undercutting and minimum top land thickness of the planet gear, with corner interference occurring at the dedendum of the planet, trochoid interference and minimum contact ratio. As the profile shift for the planet is known from the considerations above, it can be used with the plot for x_e= -0.065, which intersects the line of constant a_w=22 mm, allowing the amount of profile shift to be applied to the internal gear in order to maintain the desired centre distance; in this case x_i=0.4757. For the determined parameters it can be seen that, due to the unbalanced profile shift conditions and an overall positive value x_e+x_i=0.5407, the resulting working pressure angle is higher than the reference α and is

equal to 23.31°, as indicated by the red line. Figure 6.12 also shows the line indicating the minimum top land thickness of the internal gear. In fact, the function s_{ai} follows a concave trend presenting a minimum for a particular value of x_i as shown in Figure 6.6. This condition ensures that top land thickness for all the possible combinations $x_{e,i}$ within the feasible area would not be smaller than 0.841 which is above the suggested range of limit values.

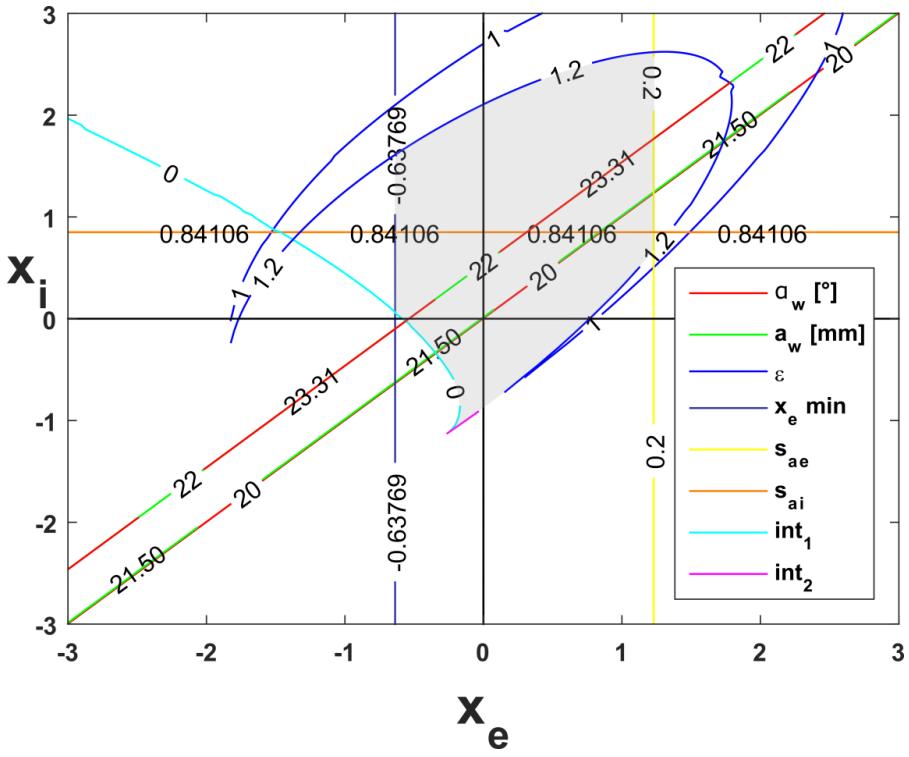

Figure 6.12 – Feasible domain for involute spur gears in internal mesh with α=20°, N_e=28, N_i=71, m=1, $h_{ae,i}$=1, $h_{fe,i}$=1.25.

The same design method has been followed for the geometry definition of the 28° pressure angle system, as shown in Figure 6.13. This gives a considerably smaller area when compared with the one for the case of α=20° previously considered. The reason is mainly because of the reduction in tooth top land thicknesses of the two mating gears because of of the increased pressure angle. Also the contact ratio is reduced and so the curve for constant ε=1.2 is closer to the centre. The increased limit for the undercutting of the two gears determines a shift of the feasible area towards negative values of $x_{1,2}$, resulting in the feasible are being located almost at the centre of the plot. For this case, given that the line indicating the constant centre distance a=22 mm crosses the grey area, and passes through the plot centre $x_{1,2}$=0, then no profile shifts were used.

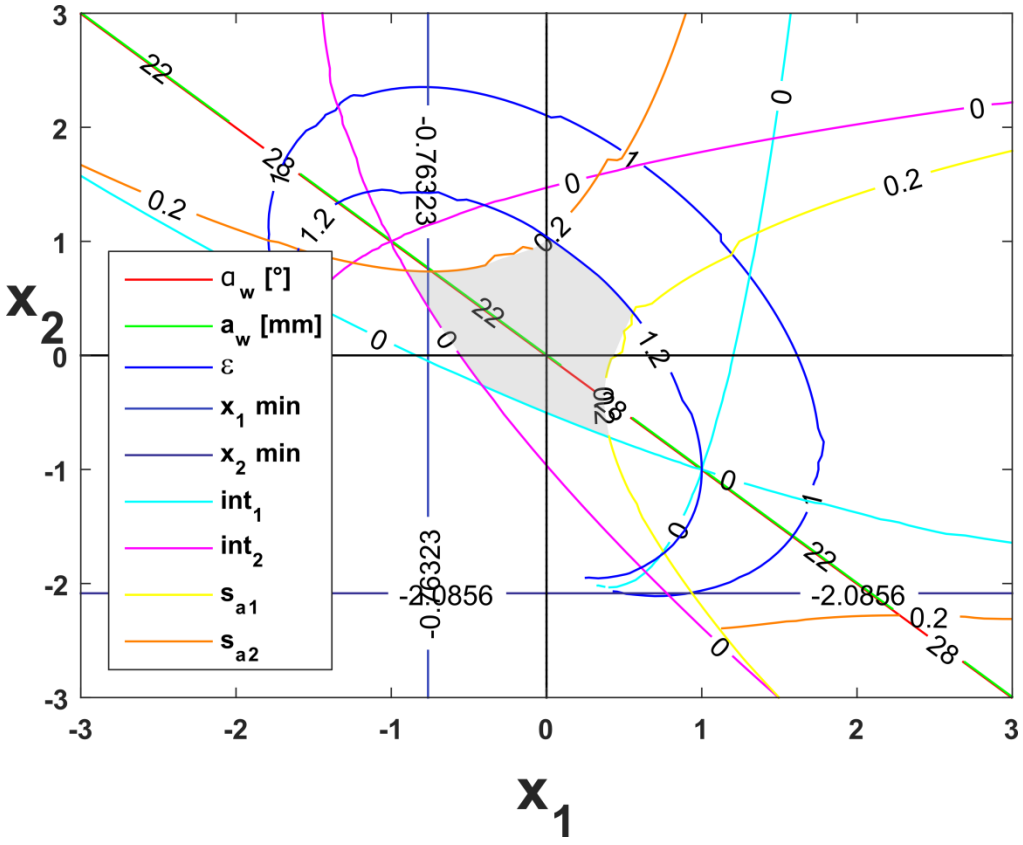

Figure 6.13 – Feasible domain for a high pressure angle involute spur gear pair in external mesh with α=28°, N_1=16, N_2=28, m=1, $h_{a1,2}$=1, $h_{f1,2}$=1.25.

The design continues with the geometric definition of the internal ring gear by means of the plot in Figure 6.13. Also for this case the feasible area is shifted towards the third quarter and includes the condition for x_e=0 that corresponds to the one for x_2=0 previously determined. The area is still limited by minimum contact ratio, minimum top land thickness for the planet, corner interference and by a new introduced coefficient s_{fi} that describes the distance between two adjacent flanks at the root of internal gears. An increase in pressure angle, as known, increases the tooth thickness at the tooth root and consequently reduces the width of the space between two adjacent teeth. If the space is too small, manufacturing problems arise and stress concentration becomes more evident. The limit imposed for s_{fi} is 0.2 (KISSsoft, 2017). By entering the plot with x_e=0, the corresponding x_i is found at the intersection between x_e=0 and a_w=22 mm. This combination returns a value of x_i=0.5196 which corresponds to a working pressure angle α_w=30.36°.

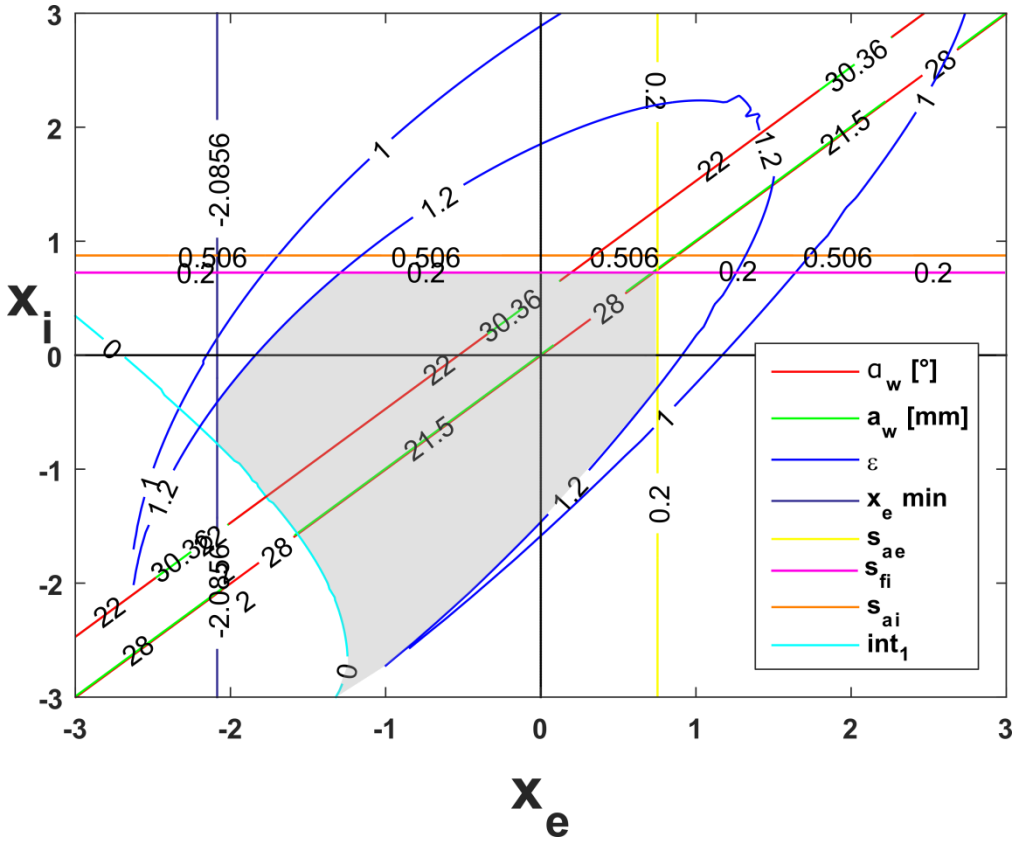

Figure 6.14 – Feasible domain for high pressure angle involute spur gear pair in internal mesh with α=28°, N_e=28, N_i=71, m=1, $h_{ae,i}$=1, $h_{fe,i}$=1.25.

The last of the three design choices regards the definition of geometrical parameters for a 24° pressure angle planetary system with the aim of achieving a working pressure angle of approximately 28° at the interface between the sun and planet. The plot in Figure 6.15 shows the area of feasible combinations for the case considered here. The line of constant centre distance crosses the area of feasibility, and determines the existence of a $x_{1,2}$ combinations that fulfil the imposed a=22 mm condition. On the other hand, it is shown that the line for constant pressure angle α_w=28° is parallel to the one for a=22 mm and coincident with a line giving a working centre distance a_w=22.74 mm. The condition of non-coincidence implies that with the set of parameters chosen, the two pre-imposed constraints a_w=22 mm and α_w=28° cannot be fulfilled.

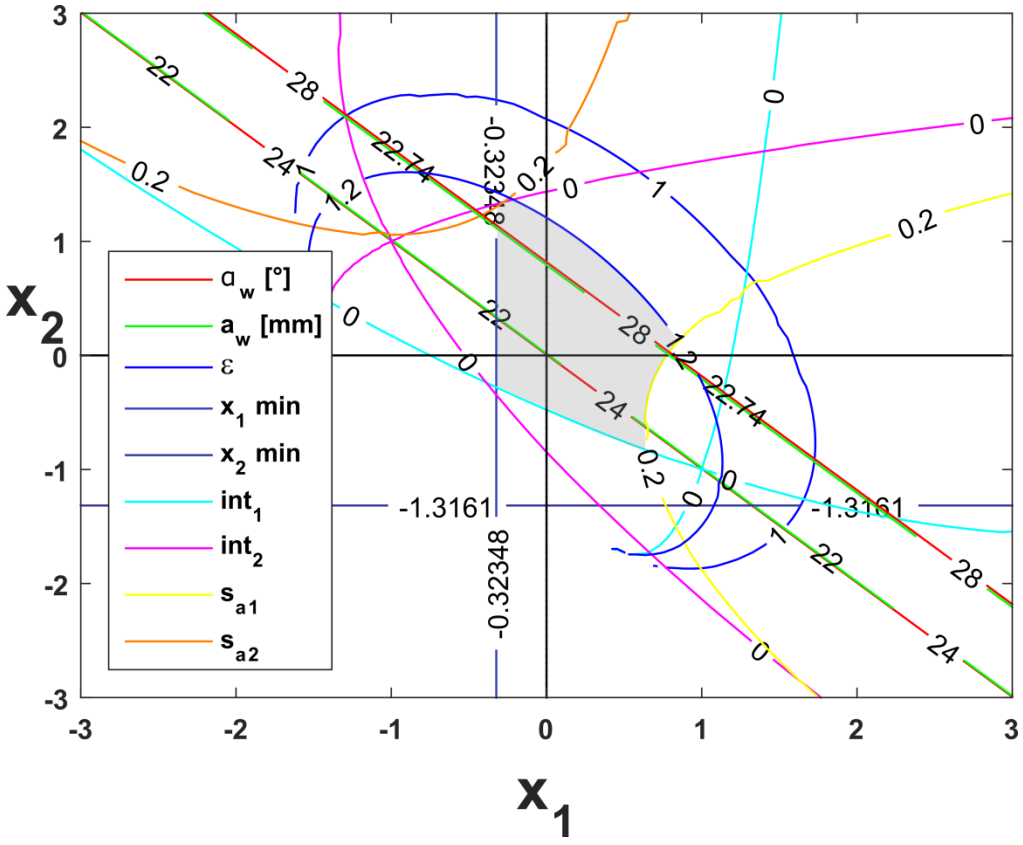

Figure 6.15 – Feasible domain for involute spur gears in external mesh with α=24°, N_1=16, N_2=28, m=1, $h_{a1,2}$=1, $h_{f1,2}$=1.25.

By taking into consideration that centre distance is related to gear size, it can be seen that it is necessary to reduce gear diameters in order to match the desired parameters. To do so, the number of teeth and/or module must be modified. Although the number of teeth was fixed in order to match the required transmission ratio, the module was not constrained by any of the pre-imposed conditions. The value for the module, initially set to 1, was reduced to the point where the line for a=22mm was coincident with the line for α_w=28° (actual value 28.15°) as shown in Figure 6.15. The confined area determined for the new configuration, with a module of 0.956 mm, is geometrically equivalent to the one shown in Figure 6.15 confirming the assumption that the module has the effect of a scale factor for gear parameters. For the case with the modified module, all the points lying on the lines for a_w=22 mm and α_w=28° in the portion within the feasible domain $x_{1,2}$ satisfy the required design constraints. The point actually chosen is defined by the coordinates x_1=0.592 and x_2=0.2727, and is based on the consideration that a positive profile shift applied to the gear with the smallest number of teeth (sun) returns an increased load carrying capacity, with improvements for both

root bending and flank contact stresses. In order to balance the potentially improved performance of the sun gear, a positive but less pronounced profile shift has also been applied to the planet gear resulting in the abovementioned $x_{1,2}$ combination.

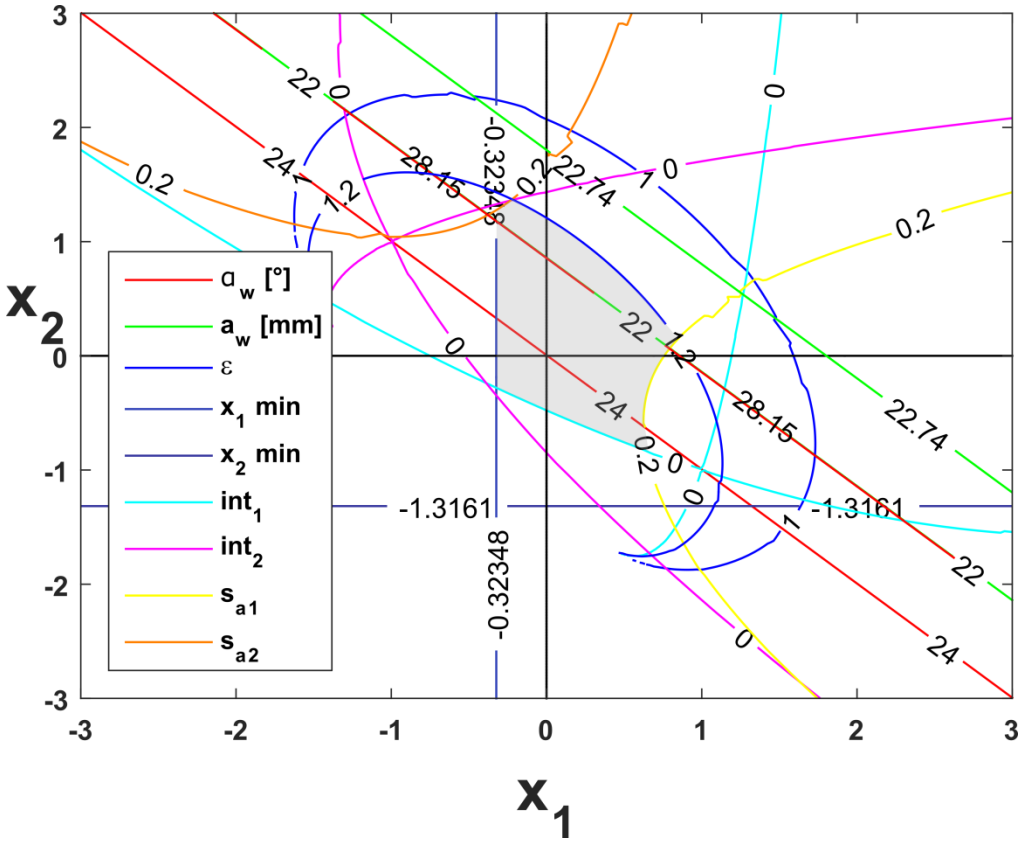

Figure 6.16 – Feasible domain for involute spur gears in external mesh with α=24°, N_1=16, N_2=28, m=0.965, $h_{a1,2}$=1, $h_{f1,2}$=1.25.

As for the previous cases, the plot in Figure 6.17, representing the geometrical parameters of the gears in internal mesh and defined for m=0.965, is accessed from the X axis with the value determined above $x_2=x_e=0.2727$. It can be noticed that the candidate point with coordinates $x_e=0.2727$ and $x_i=1.7424$ determined at the intersection between $x_e=0.2727$ and the line for a=22 mm is outside the area of feasible parameters. For the combination of geometrical factors considered here, the limiting condition related to the root space width of internal gears s_{fi} limits the area from above reducing the range of possible value that fulfil the desired a_w=22 mm condition.

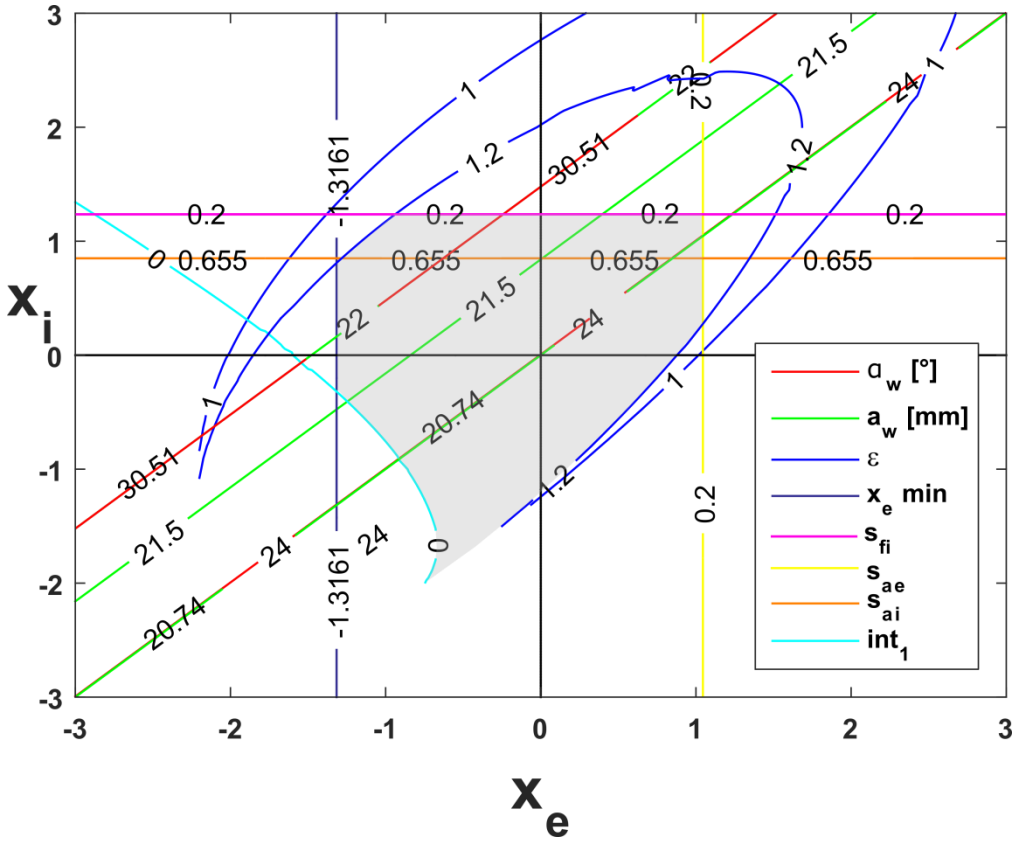

Figure 6.17 – Feasible domain for a involute spur gears in internal mesh with α=24°, N_e=28, N_i=71, m=0.965, $h_{ae,i}$=1, $h_{fe,i}$=1.25.

In order to increase the feasible domain in the upper region of the plot, the dedendum coefficient h_f of the internal gear was reduced until the point of interest was lying on the line that describes the limit for s_{fi}=0.2 as shown in Figure 6.18. The value of h_f after this consideration was reduced from the standard 1.25 to 1.05. The resulting working pressure angle for such modified parameters is α_w=30.51° as indicated by the red line coincident with the line for a_w=22 mm in Figure 6.17.

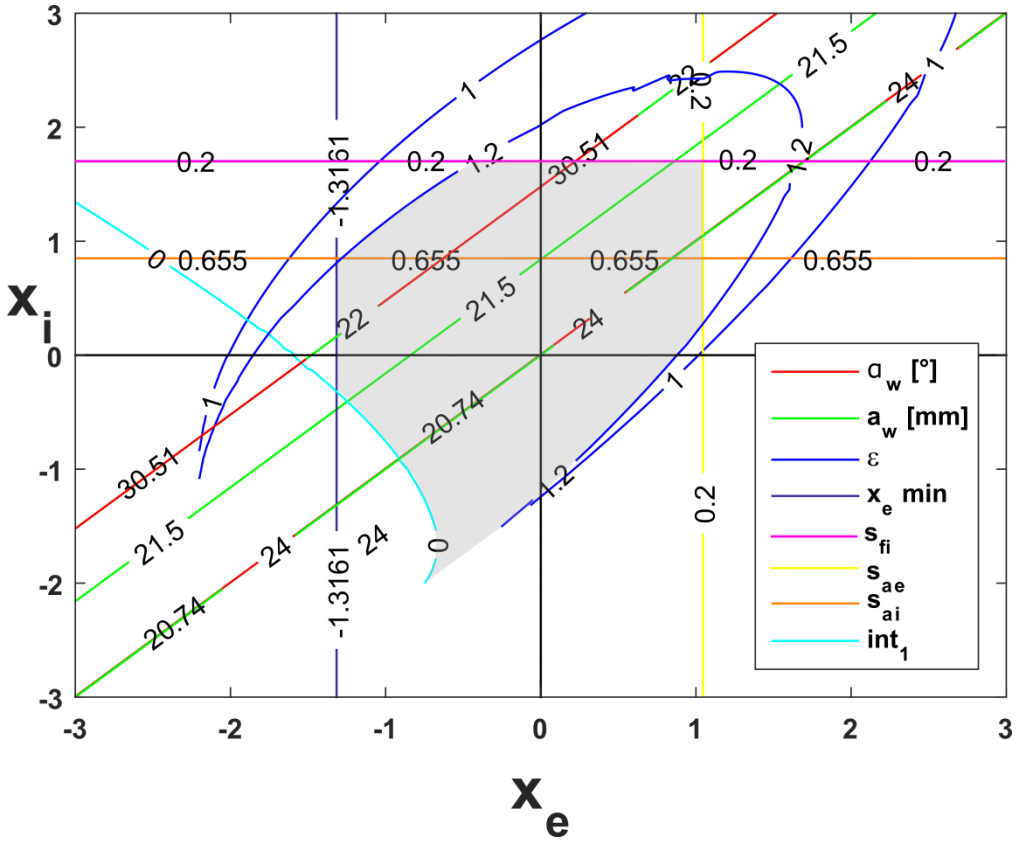

Figure 6.18 – Feasible domain for involute spur gears in internal mesh with α=24°, N_e=28, N_i=71, m=0.965, $h_{ae,i}$=1, h_{fe}=1.25, h_{fi}=1.05.

All the geometrical values determined above and listed in Table 6.2 uniquely define the tooth profile shapes. The result of the application of these parameters on the physical tooth geometries is shown in Figure 6.19 where tooth traces of sun, planet and ring gear are plotted against each other for comparison purposes.

All the plots above were generated by means of a Matlab® program written for the specific case of internal mating gears. The program and the related functions are listed in Appendix B.

Table 6.2 – Geometrical and functional parameters for sun, planet and ring for chosen design cases

Gear/Parameter	Sun	Plan	Ring	Sun	Plan	Ring	Sun	Plan	Ring
Reference pressure angle α [°]	20°			28°			24°		
Module [mm]	1			1			0.965		
Number of teeth N	16	28	71	16	28	71	16	28	71
Profile shift coeff *x*	0.065	-0.065	0.4757	0	0	0.5196	0.592	0.2727	1.7424
Addendum factor h_a	1	1	1	1	1	1	1	1	1
Dedendum factor h_f	1.25	1.25	1.25	1.25	1.25	1.25	1.25	1.25	1.05
Working pressure angle α_w [°]	20°	23.31°		28°	30.36°		28.16°	30.51°	
Contact Ratio ε	1.56	1.79		1.35	1.44		1.32	1.30	
Tooth base thickness S_b [mm]	1.81	1.97	2.83	2.12	2.37	3.19	2.26	2.22	2.97
Root fillet radius ρ_f [mm]	0.38	0.38	0.35	0.38	0.38	0.24	0.37	0.37	0.2
Overall transmission ratio *i*	5.438								

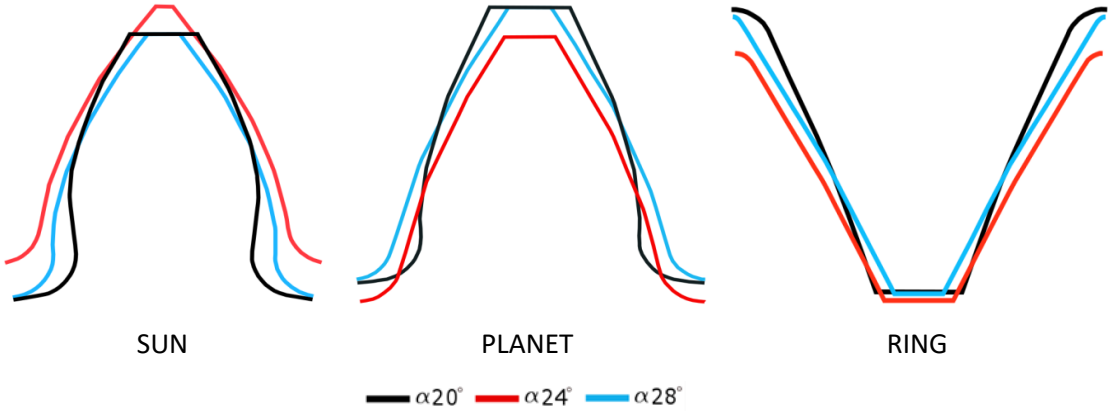

Figure 6.19- Comparison between tooth profile traces for the geometries listed in Table 6.2. Sun, Planet and Ring gear profiles for the three pressure angle configurations α=20°, 24° and 28°are shown respectively in black, red and blue.

6.4 Planetary drive modelling

The modelling of the three planetary systems resulting from the design process undertaken has followed the process described in section 5.2 which involves a multi-step routine in order to create the 3D models of single gears, assembling them into a planetary arrangement and then downgrading them from 3D to 2D for the subsequent FE analysis. The combinations of parameter given in Table 6.2 have also been modelled in the Machine Design Software KISSsoft®. Successively, 3D gear models were exported through a direct interface into SolidWorks for assembling together in a full system model, as shown in Figure 6.19. Also a "motion study" has been performed to observe whether any physical interference was occurring during the meshing process. Due to the computational weight of the systems as consequence of the high number of nodes and the complex contact conditions, it was decided to model only one of the four planets as shown in Figure 6.20.

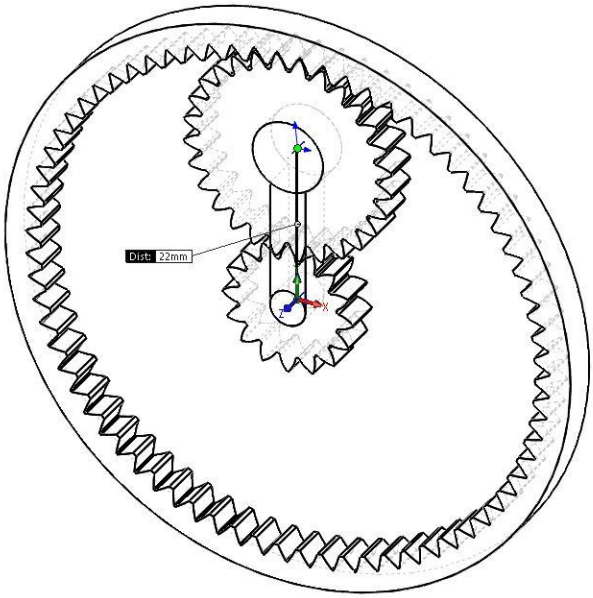

Figure 6.20 – Isometric view of the 3D assembly of the designed planetary gear train showing only a single planet configuration.

From this, all the models are exported into the ANSYS FEA environment first for the extraction of 2D surfaces and successive FE Analysis.

6.5 Finite Element Analysis

The planetary gear systems designed as described in the previous section have been analysed by means of Finite Element Analysis with the aim of understanding how the stresses induced within the system were distributed among the components. The FEA procedure follows the same steps as for the performance analysis of spur gears described in detail in Section 5.4. The 2D mesh density used in that case, based on an element side length of 0.001 mm for the elements near to the contact areas, has also been used for this case. This was based on the size of the area of contact and by considering that the smallest area of contact, shown in Figure 6.28, is comparable but generally bigger than the one shown in Figure 5.19 in Chapter 5. Hence it is assumed that the discretization would produce results as accurate as the ones previously achieved. By using an element side length of 0.001 mm, a higher level of discretization is achieved as can be seen in Figure 6.20. The remaining part of the model has been discretized with elements with side lengths of 0.03 mm.

Also with regards to the definition of the contact elements, the settings described in 5.4.4 were used. In this case contact elements were placed at the sun/planet interface and planet/ring interface and were defined as frictional. Another contacting area is at the interface between the carrier and planet gear where the formulation used for the contact elements was “frictionless” in order to simulate the presence of a bearing.

The material used for the analysis was a structural steel with characteristics listed in the Table below.

Table 6.3 –FEA model’s material properties

Young’s modulus E [MPa]	$2x10^5$	$2x10^5$
Poisson ratio ν	0.3	0.3
density ρ [kg/m^3]	7850	7850

6.5.1 Time step Controls

The analysis history has been divided in two steps of 0.25 s and 0.75 s for a total time frame of 1s. For the first step, the automatic step control function available in ANSYS has been used in order to optimize the number of load increments necessary for the solution to converge. For the second step that covers the mesh cycles of interest, a constant number of substeps equal to 600 was used in order to achieve a resolution of ≈0.1° over the 54.38° of rotation of the sun relatively to the carrier and a resolution of 0.025° over 15.35° degrees of planet rotation.

6.5.2 Boundary conditions

The system has been loaded through the sun gear by applying a ramped moment from 0 to 1.5 Nm in the 0.25s of the first time step and then kept constant for the entire second substep of 0.75s. The rotational velocity has been simulated by applying at the carrier a rotation angle of 5° for the first time step, and a successive angle of 10° for the second time step. The resulting average rotational speed over the 1s time frame is 2.5 rpm for the carrier while 13.6 rpm was the resulting sun input speed as required by the specifications in Table 6.1.

The sun gear is supported by a cylindrical support that allows only rotations about its own axis. Also the planet carrier is supported by a cylindrical support concentric with

the one applied to the sun gear. The planet gear is supported by the carrier and, in this configuration, can replicate the compound motion divided into rotation about the central axis of the system and the rotation about its own axis. The outer face of the ring gear was defined as rigidly constrained. A summary of the boundary conditions applied is shown in Figure 6.21.

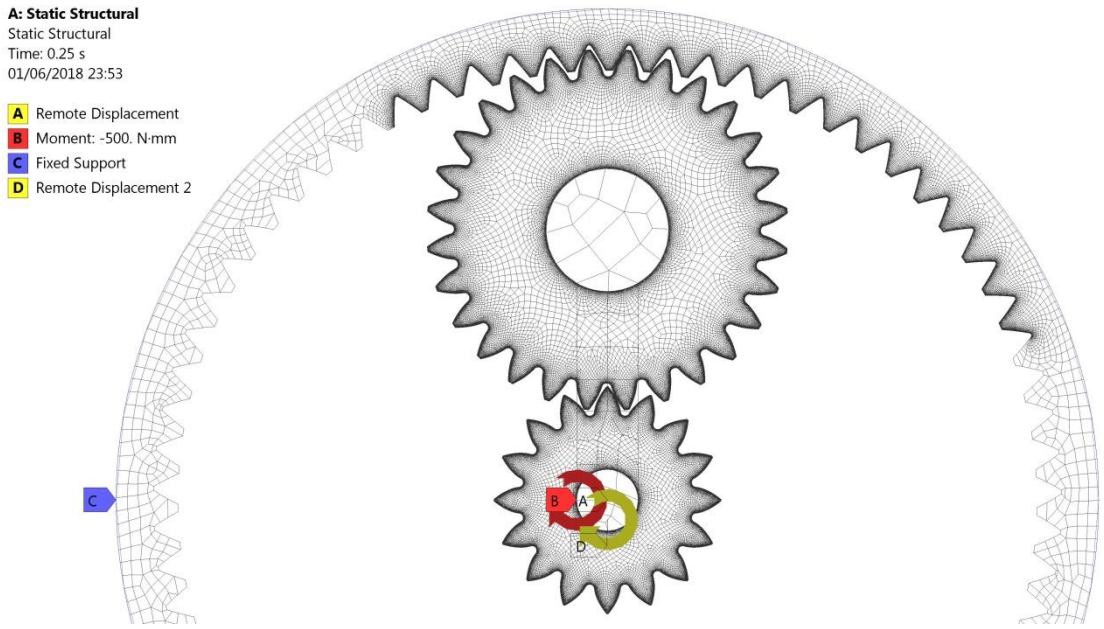

Figure 6.21 – 2D model of the plant gear mesh with boundary conditions applied.

6.6 Results and Discussion

The application of quasi-static FEA for the study of the stress distribution among components in a planetary gear train has returned a time-varying stress distribution at the two mating points through which the input load is simultaneously transmitted within the system. Both equivalent contact and bending stresses have been evaluated for a total meshing time of 1 s. Such a time of engagement for the considered rotational velocity corresponds locally at the mating points, to two complete mesh cycles of sun/planet and planet/ring contacting profiles for each condition tested. The evaluation of root bending stress involves the study of stresses at the root of each gear in mesh that, because of the different geometry, reacts differently to the applied force. On the other hand, contact stress is evaluated at the point of contact of the mating tooth flanks and is equally distributed between the two contacting components. For this reason, only

the contact stress at the interface between sun and planet gear and at the interface between planet and ring gear are needed to determine the entire contact stress distribution field for the three components in simultaneous contact. Figure 6.22 shows the Von Mises stress distribution within the system as a consequence of the applied input moment to the sun gear and the resistance at the carrier applied by the imposed rotation. In can be seen that, because of the distribution of forces, while the sun pushes the planet in the anti-clockwise direction, the planet, subjected to the rotational motion about its own axis shares forces with the ring gear which also reacts by pushing the planet clockwise. The sum of the two tangential components of the forces applied to the planet is opposed by the force due to the reaction torque applied from the carrier to the planet. This force acts in the anti-clockwise direction, determining an area of compressive stresses at the planet/carrier interface. It is also interesting to notice that due to the difference in working pressure angles occurring at the two contact interfaces, and being generally higher for the mating couple planet/ring than for planet/sun, the radial component of the force at planet/ring interface is higher than the one at the sun/planet interface resulting in an unbalanced radial component acting on the planet bearing and pointing towards the centre. This force has to be taken into consideration for the design of the planet carrier.

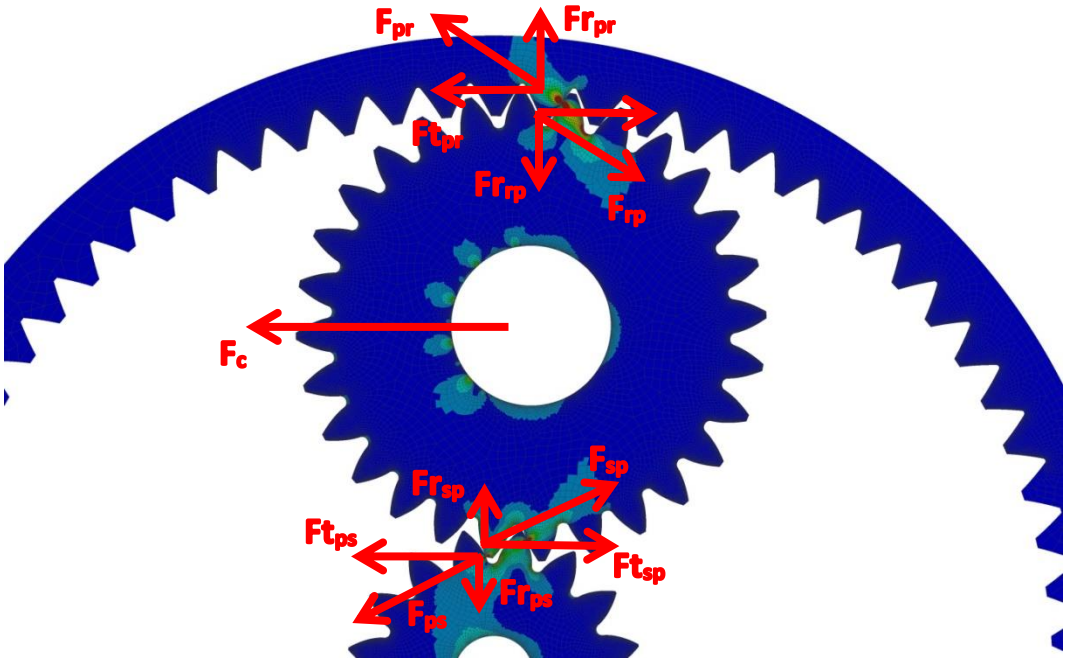

Figure 6.22 - Von Mises stress distribution among the planetary system subjected to applied torque at the sun gear and reaction torque at the planet carrier.

This study focuses on the stress distribution that occurs at the mating tooth. Root bending stresses were recorded at the tooth root fillet of adjacent teeth during the entire arc spanned by the planet position for the time of the analysis, in order to follow the time-varying meshing progress and the related stress variation. Similarly, for the detection of contact stresses, nodal solutions of equivalent stress were recorded along the tooth flanks of adjacent teeth in mesh, in order to follow the progress of the contact point over the entire time of the analysis.

6.6.1 Bending stress

Starting from the sun gear through which the input torque is transmitted to the system, the time-varying equivalent stress distribution for the three geometrical configurations studied is shown in Figure 6.23. The plot shows the typical root bending stress distribution explained in detail in Section 5.6 for a single mesh cycle. In this case, as the investigated time frame of 1s covers two entire mesh cycles, the stress distribution at the tooth root is repeated twice. No evident differences between the first and the second mesh cycle have been detected. The time intervals between one and two tooth pairs in simultaneous contact follows the variation of contact ratio which is maximum for α=20°, decreases for α=28° and is minimum for α=24° as listed in Table 6.2. For the case of α=24° the contact ratio is lower compared to the other two models due to the simultaneous use of a higher reference pressure angle and a sizeable positive profile shift that have been shown as having a concurrent effect on the reduction of contact ratio (Section 3.3.4). Because of the variation of ε, the time interval in which the mating gears are subjected to these high stresses varies accordingly.

By analysing the equivalent root bending stress results occurring at the sun gear, it is found that the gear designed with α=20° is the one subjected to the maximum stress state compared to the other two models. This is accounted for by the higher tangential component of the force $Ft_{ps.}$ Because of the resulting working pressure angle α_w=20° at the sun/planet interface, when the transmitted force F_{ps} is decomposed into the radial and tangential components, the second of these, responsible for the root bending stress, is higher when compared to the other two cases designed with $\alpha_w \approx 28°$. Moreover, as the amount of profile shift used is equal to the minimum geometrical

boundary to avoid undercutting, the tooth thickness at the base is equal to 1.81 mm, which is considerably smaller when compared to the two other geometries. The combination of a higher tangential force and a reduced tooth thickness are the causes responsible for the increase in root bending stress. Lower values of root bending stress are found for the geometry designed when the reference pressure angle equals to 28°. In this case the tangential force Ft_{ps} is lower at the expense of the radial component Fr_{ps}. The higher radial component, which is undesirable because this generates an extra load on the sun gear support, contributes to the reduction of root bending stress due to the induced localized compressive stress state which is subtracted from the tensile component responsible for the bending stress. To this, a tooth base thickness of 2.12 mm has to be added in order to justify the stress reduction compared to the standard case α=20°.

The third model tested was built with the intention of taking into account both higher pressure angles and positive profile shifts in order to achieve a working pressure angle at the sun/planet interface of ≈28° (α_w=28.13°). Interestingly, the root bending stress for the geometry of this model gives lower results compared to the other two cases despite the lower module adopted: 0.965 instead of 1 mm. The combination of a non-standard reference pressure angle α=24° and positive x_1, x_2 generates a tooth geometry with the largest tooth base of the three, equal to 2.26 mm. The shared forces are equivalent to the previous case as the resulting pressure angle here is α_w=28.13°. The slightly smaller root fillet radius due to the reduced module does not affect the root bending stress. Arguably, the stress concentration at the root fillet is not that high to overcome the benefits of a thicker tooth base for the reduction of bending stress.

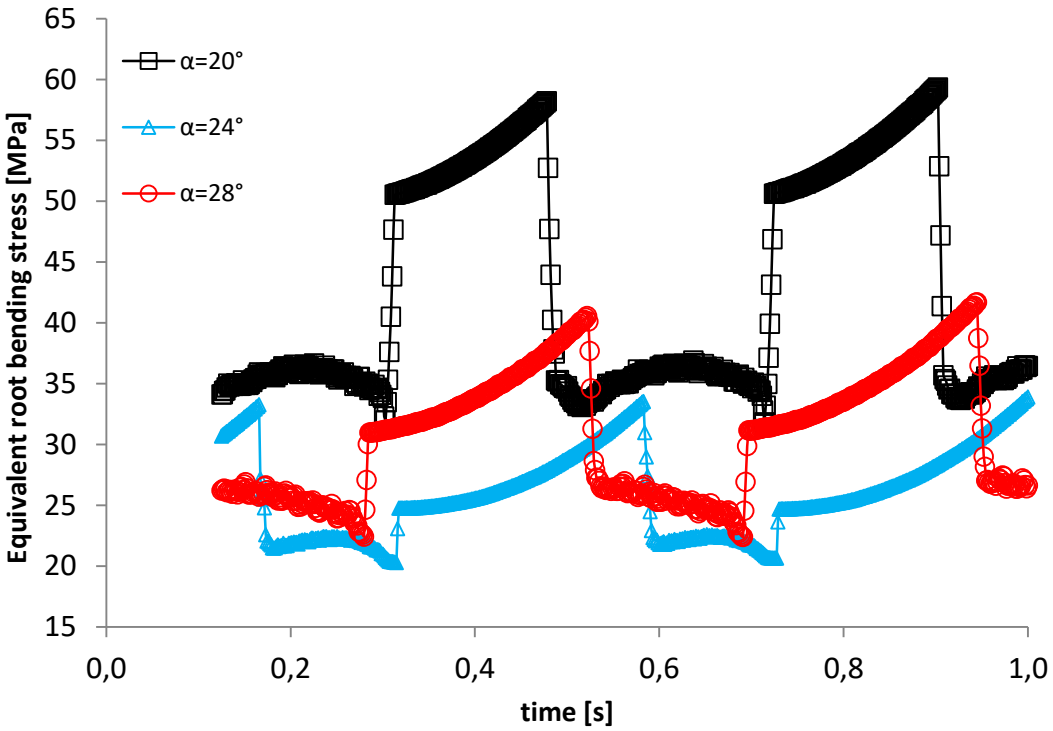

Figure 6.23 - Equivalent root bending stress for the sun gear for two consecutive mesh cycles.

Similar considerations can be made for the study of root bending stress for the planet gear at the planet/sun mesh interface. Compared to the sun gear, the planet has a higher number of teeth which implies for the same module, larger pitch, tip and root diameters according to Equations 3.26 and 3.27. A larger root diameter implies teeth with thicker bases. The 28 tooth planet, even in presence of a small negative shift of -0.065 mm for α=20°, has a tooth base thickness of 1.97 mm. This geometrical characteristic determines the reduction in root bending stress from 68.25 MPa acting on the sun to 56.07 MPa acting on the planet for the same amount of shared force, as shown in Figure 6.24. In the analysis of root bending stress for the planets, for the two non-standard geometries, unlike the previous result for the sun gear, the more stressed geometry is the one with α=24°. Also in this case the reduced tooth base thickness is the quantity that accounts for this result; the reference pressure angle α=24° and the positive shift of 0.2727 mm generate a tooth geometry with a tooth base thickness of 2.22 mm while the geometry with α=28° and no shift applied has S_b=2.37 mm. As the contact ratio is obviously the same as the one described for the sun gear, in this plot the time intervals that correspond to a single and double pair of teeth in contact are equivalent to the ones shown in Figure 6.24.

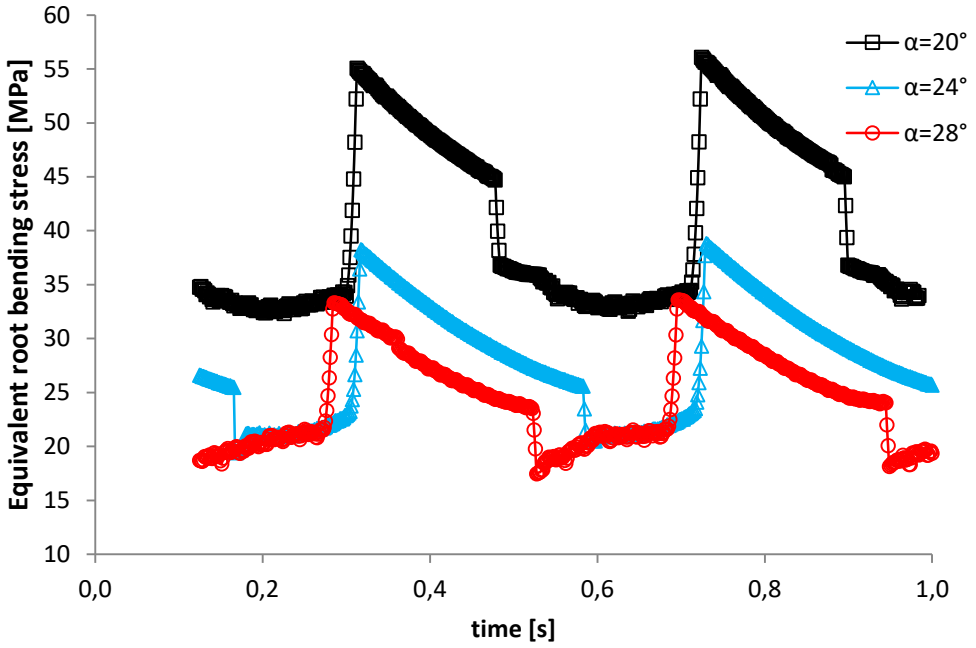

Figure 6.24 - Equivalent root bending stress at the planet gear at the planet/sun interface for two consecutive mesh cycles.

In the epicyclic arrangement the planet gear is in simultaneous mesh both at the sun/planet interface and at the planet/ring interface. In figure 6.25 it can be seen that the time interval corresponding to a double pair of teeth in contact is considerably longer, especially for the case with α=20°, then the ones previously described for the sun and planet in mesh. This is due to the higher contact ratio ε=1.79 for α=20°. For α=28° there is a drop of contact ratio to a value of 1.44, and the resulting working pressure angle is α_w=30.36°. Because of such a high value of α_w, the tangential component of the reaction force Ft_{rp} applied to the planet as consequence of the planet/ring load sharing, is smaller in value compared to the one occurring at the sun/planet mesh. The combination of the reduced tangential and increased radial components of the transmitted force, along with a tooth base thickness of 2.37 mm, gives a reduction of the maximum value of root bending stress compared to the standard case with α=20° (α_w=23.31° and S_b=1.97 mm).

The last case to consider, with a reference pressure angle α=24°, due to a very high profile shift coefficient of 1.7424 (*0.956) applied to the ring gear, gives a working pressure angle of 30.51° similar to the one found for the previously considered case for

α=28°. This configuration, due to a tooth base thickness of 2.22 mm, is subjected to a root bending stress between the other two condition tested.

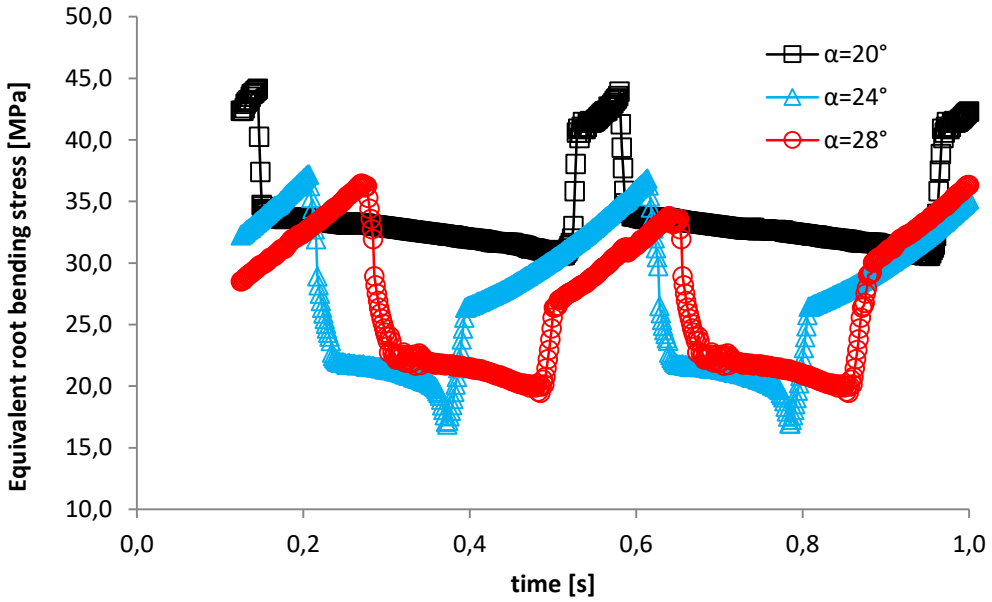

Figure 6.25 - Equivalent root bending stress at the planet gear at the planet/ring interface for two consecutive mesh cycles.

The last gear to analyse is the ring gear. For this component, the same considerations made for the case of the planet gear at the planet/ring mesh regarding contact ratio and working pressure angle are valid. Also the force F_{pr} is equal to the F_{rp} previously analysed. The bending stresses occurring at the tooth root of the internal gear are on average 32% lower compared to the ones acting on the planet at the same mating interface. This is due to the stronger tooth form of internal gears than those of the corresponding external gears (Maitra 2012). Stronger teeth mean having a thicker tooth base compared to their equivalent external profile. For the case of α=20°, a S_b=2.83 mm coupled with a generous root fillet radius of 0.35 mm gives a root bending stress of 27.74 MPa as shown in Figure 6.26. A similar value of bending stress is also found for the case of α=24°. For this case, the high value of the working pressure angle α_w=30.51°, and the increased tooth base thickness of 2.97 mm as a result of a 24° reference pressure angle and positive profile shift coefficient of 1.7424, do not compensate the reduced root fillet radius ρ_{fi} of only 0.2 mm. The root radius coefficient of the internal gear may arguably be considered the source of the increased bending stress due to stress concentrations

occurring at the tooth root. The tooth profiles of the ring gear required an addendum reduction in order to meet the minimum required space between adjacent teeth s_{fi}=0.2. The last configuration tested, with α=28°, presents the thicker tooth base of the three configurations, equal to 3.19 mm, which is the result of the high reference pressure angle and the positive X_i=0.5196 mm applied. The expected drop of root bending stress due to the thicker tooth base did not take place; evidently a reduced root fillet radius of only 0.24 mm accounts for the presence of stress concentration at the toot root.

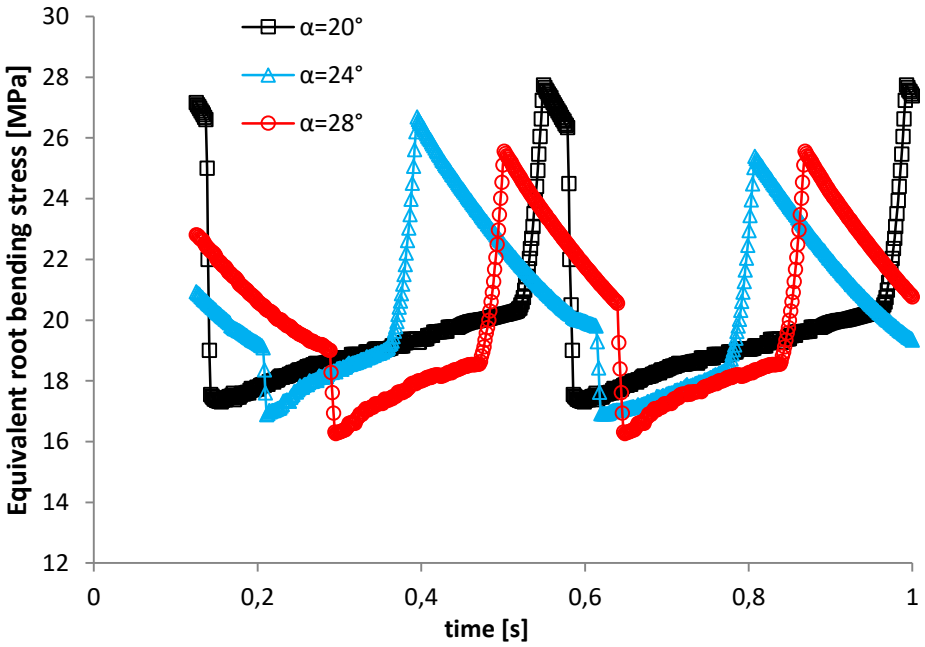

Figure 6.26 - Equivalent root bending stress at the ring gear at the ring/planet interface for two consecutive mesh cycles.

6.6.2 Contact stress

Contact stress is directly related to the size of the area of contact as already explained in Section 5.8. In turn, the area of contact depends on the radii of curvature of the mating tooth profiles and so on pressure angle and profile shifts applied. Figure 6.27 shows the time-varying tooth flank contact stress for the three tested geometries of the external mating gears. By starting with the analysis of the standard α=20° geometrical configurations, it was expected that this would give the highest stress. The maximum value of equivalent tooth flank contact stress over the two mesh cycles is equal to 504.55 MPa and about 18% higher compared to the other two cases investigated. In fact, both the non-standard geometries have a resulting working pressure angle ≈28° due to the

combination of reference pressure angle and profile shift applied. This circumstance gives a corresponding change in maximum flank contact stress to 417.05 MPa for α=24° and 402.57 MPa for α=28°.

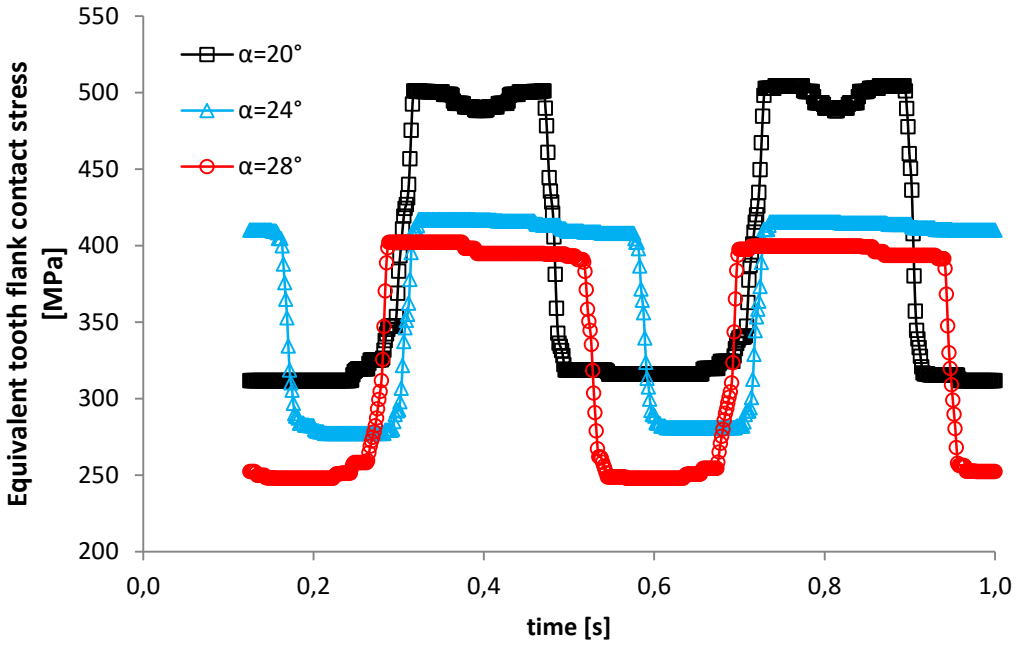

Figure 6.27 - Equivalent tooth flank contact stress at the sun/planet interface for two consecutive mesh cycles.

In epicyclic gear systems the planet gear is in simultaneous contact with the sun and the ring gears. However, a substantial difference occurs at the interface between mating components depending on the meshing condition and on whether these are external or internal gears. Gears in external mesh, as for the case of the sun and planet, have convex tooth profiles that create an area of contact A_c, responsible for the generated contact stress, as described in Section 5.8.2.1. On the other hand, when internal gears are meshing, the contact occurs between convex and concave profiles. The resulting contact area, responsible for the stress state at the contact point, is larger compared to a convex/convex contact interface. The surfaces in contact in this case can be approximated to a cylinder pressed against a cylindrical groove. By applying Hertzian theory to the case of convex/concave contacting surfaces, Equation 5.10 is adjusted by modifying the radius of curvature R_2 at the instantaneous point of contact with R_2 valid for the case of concave profiles as in Equation 6.32.

$$\boldsymbol{b_i} = \sqrt{\frac{8\mathrm{F}\left[\frac{1-\mathrm{v}_1^2}{\mathrm{E}_1}+\frac{1-\mathrm{v}_2^2}{\mathrm{E}_2}\right]}{\pi\mathrm{L}\left(\frac{1}{\mathrm{R}_1}+\frac{1}{(-\mathrm{R}_2)}\right)}} \qquad 6.32$$

Once the width of the contact area is known, the instantaneous area of contact generated at the planet/ring interface can be calculated as:

$$A_{ci} = b_i L \qquad 6.33$$

An example of how the area of contact calculated at the pitch point for both external and internal gears in mesh varies as function of pressure angle is shown in Figure 6.28.

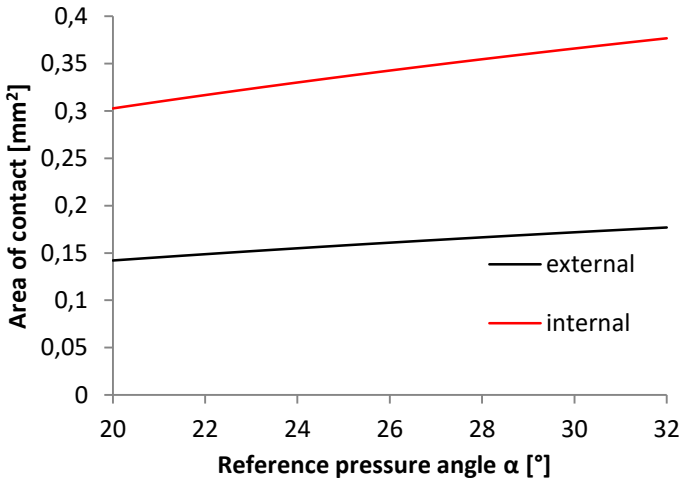

Figure 6.28 - Comparison between the area of contact at the pitch point of the internal and external mating gears as function of pressure angle; N_1=16, $N_{2,e}$=28, N_i=71, m=1, x_1=0, $x_{2/e}$=0, x_i=0.

Such a difference in the value of the area of contact explains the difference in magnitude of contact stress shown between Figures 6.27 and 6.29 respectively at the sun/planet and planet/ring interfaces. The average reduction of ≈50% reflects the increase in the area of contact shown in Figure 6.28 between external and internal mating gears.

The analysis of the time-varying flank contact stress at the ring/planet in internal mesh is shown in Figure 6.29. Also for this case the Maximum values of equivalent contact stress depends entirely on the pressure angle. Due to the combination of α and *x*, the working pressure angle at the internal mating gears assumes values of 23.31°, 30.36° and 30.51° respectively for the reference α=20° and the non-standard values α=28° and α=24°. Therefore, a sizeable difference of maximum values of contact stress between

standard profiles and profiles generated with non-standard combination of parameters was expected. This is evident in Figure 6.29 in which an average reduction of ≈11% between the nodal results for α=20° and the results for the other two configurations can be appreciated. For the three cases, Maximum contact stress occurs at the initial point of the single tooth pair interval and reduces towards the end of this interval.

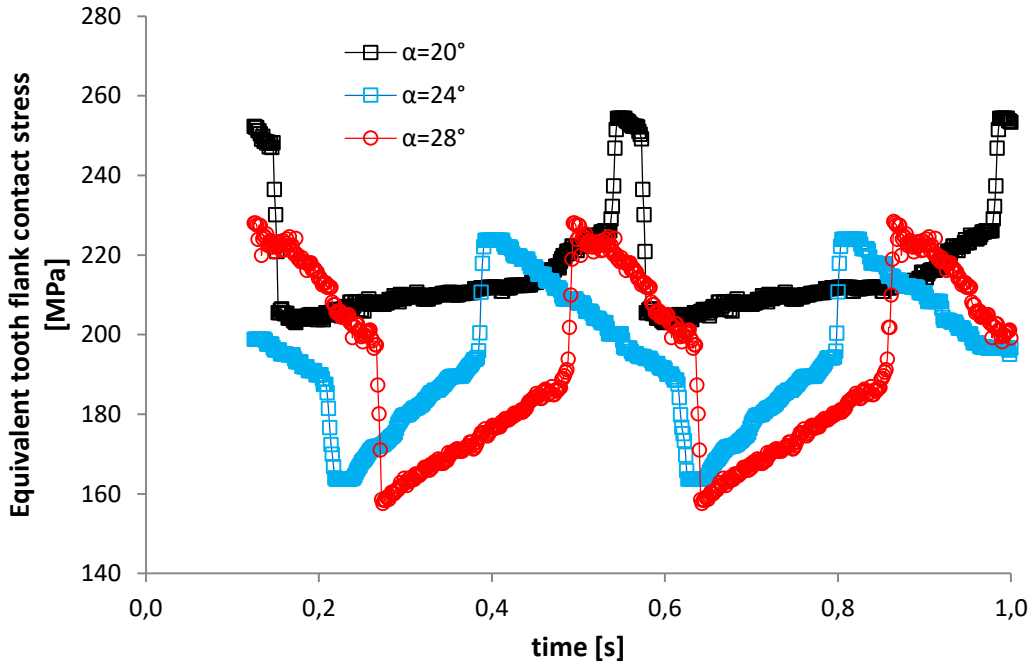

Figure 6.29 - Equivalent tooth flank contact stress at the planet/ring interface for two consecutive mesh cycles.

After results of the numerical analyses were produced, peak values of Equivalent root bending stress and flank contact stress across the two mesh cycles and for the three tested geometries were compared to analytical results calculated in accordance with the standard ISO 6336 by means of KISSsoft. The results are summarised in Table 6.4 and 6.5 for Bending and Contact stress respectively.

Table 6.4 - Maximum Root Bending stress [MPa]

Bending	FEA			KISSsoft (ISO)			Variation %		
	20°	24°	28°	20°	24°	28°	20°	24°	28°
SUN	59.35	33.93	41.69	51.29	40.84	46.01	13.6	-20.4	-10.4
PLANET/SUN	56.07	38.81	33.56	48.53	45.42	40.71	13.4	-17	-21.3
PLANET/RING	44.17	37.24	36.45	43.31	45.96	38.28	1.9	-23.4	-5
RING	27.74	26.68	25.56	31.16	31.78	29.03	-12.3	-10.3	-13.5

Table 6.5 - Maximum Flank Contact stress [MPa]

Contact	FEA			KISSsoft (ISO)			Variation %		
	20°	24°	28°	20°	24°	28°	20°	24°	28°
SUN/PLANET	504.55	417.05	402.57	472.96	435.5	434.15	6.2	4.4	-7.8
PLANET/RING	254.29	223.75	228.44	194.45	195.51	190.74	23.5	12.6	16.5

The values listed in Tables 6.4 and 6.5, where the comparison between stresses calculated by means of FEA and ISO 6336 B is done, show a discrepancy between results obtained with the two methods. Interestingly with regards to Equivalent root bending stress FEA results for the non-standard configurations are always smaller than analytical results. On the other hand, for the standard α=20° design, the numerical results are generally and sometimes considerably higher than the ones calculated according to the standard.

FEA results for tooth flank contact stress are generally more conservative than numerical ones. Also for this case the maximum difference occurs for α=20° at the ring gear and is equal to 23.5%.

The ISO 6336 part 3, suggests the use of a mesh load factor K_γ to take into consideration the uneven distribution of load over the individual meshes when the evaluation of the stress state in an epicyclic arrangement is attempted. In part 1 (ISO 6336-1, 2006) it is stated that when a gear drive has two or more mating gears simultaneously in contact it is necessary to include the factor K_γ for the evaluation of the tooth root stress. The standard suggests determining K_γ by measurement or alternatively to estimate its value from literature, but no further indications are given. ANSI/AGMA 6123-B06 (2006) is dedicated to enclosed epicyclic drives, and gives suggestions for the value of K_γ (mesh load factor) in a table as a function of operating conditions and gear manufacturing quality. It also states that if the system contains more than one planet gear, than it is recommended to use values of mesh load factor according to the given table. For an epicyclic arrangement with one planet gear the suggested mesh load factor is 1. Suggested values are based on the general assumption that the used reference pressure angle is the standard α=20°.

After this analysis, for the standard configuration α=20°, a value of K_γ=1.2 even for the case of single planet gear seems appropriate in order to reduce the difference between results calculated by numerical and analytical methods. For standard gears in external mesh, after applying a mesh load factor of 1.2, the % difference drops from 13.6% to -3.7% for the sun and from 13.4% to -3.8% for the planet gear.

6.7 Conclusions

This chapter has presented the application of the "high pressure angles" to planetary gear trains with the aim of increasing the load carrying capacity of such systems for their applications in hand tools. The design process followed was based on the blocking contours technique that, in order to be applied to the case of planetary transmissions, requires the novel determination of the area of feasible combinations for the case of internal gearing. To this end, the analytical determination of the limiting conditions typical of internal gears was presented. The design process undertaken started with the determination of geometrical parameters for the external mating gears. The profile shift value chosen for the planet was then used as input parameter for the determination of *x* to apply to the internal gear. The outcome of the design process was three planetary systems equivalent in terms of centre distance and number of teeth but differing in the geometrical parameters that define the tooth profiles. The generated models were analysed by means of quasi-static FEM and the time-varying nodal stress results acting on each component were plotted for the three considered geometries for comparison purposes. For the same configurations, stresses were calculated according to ISO 6336 method. Differences between the numerical and analytical results were also highlighted by means of a calculated percentage variation in Table 6.5. The designs involving non-standard parameters have shown improvements in the load carrying capacity as both contact and bending stresses were reduced compared to the configuration characterised by a standard 20° reference pressure angle. The two non-standard configurations have shown a similar behaviour, sign that the effect of the working pressure angle (equal for both configurations) has a predominant effect compared to the other geometrical parameters.

The outcome can be considered a suitable suggestion for the design of planetary systems for enhanced torque carrying capacity and physical packaging volume reduction, for applications characterized by low speed conditions. Norbar Torque Tools has implemented the findings of this work in their production by designing a new torque multiplier suitable for the application on power tools. The comparison between the new (grey) and old (red) designs in Figure 6.29 is explanatory of the achieved improvement in terms of compactness for the same rated torque and working life.

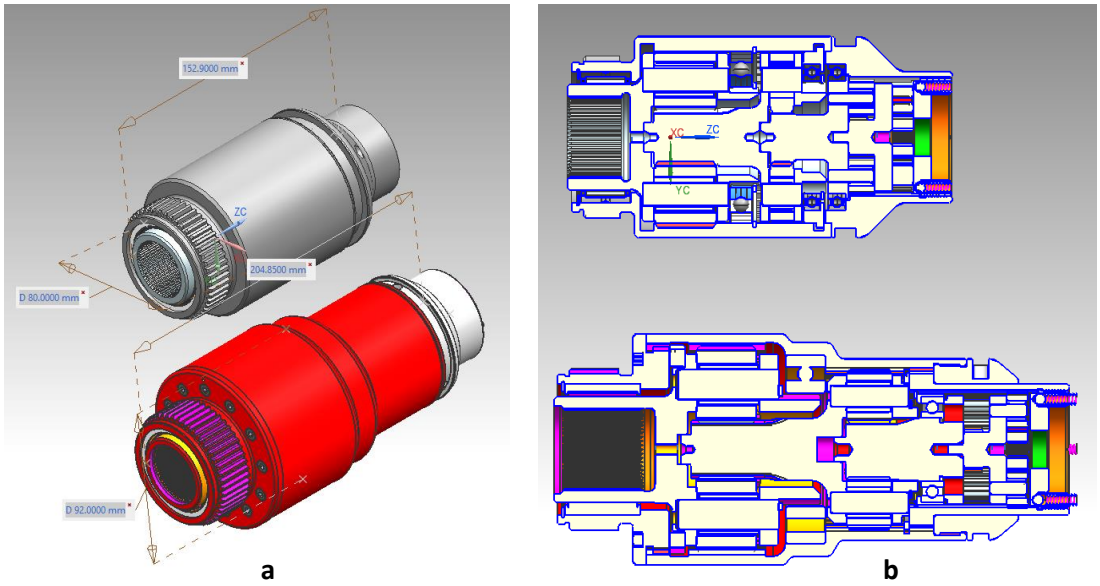

Figure 6.30 - Comparison between two 4 stage planetary drives that differs for the value of gear profile pressure angle but are equivalent in terms of speed ratio and output torque. a) isometric view of the two models with highlighted overall dimensions; b) longitudinal section view of the two models.

Both the devices are four stages planetary transmissions with a velocity ratio *i*=1:280 and capable of a maximum output torque of 2700 Nm. For the design of the new model a profile pressure angle α=25° has been used in combination of positive profile shift in order to achieve a working pressure angle $\alpha_w \approx 28°$. The new device features a volume reduction of 43% compared to the old design with standard 20° pressure angle. This demonstrates the existence of room for improvements of this class of devices when non-standard combination of parameters is used.

7 Design and analysis of a cycloidal speed reducer

The mechanical advantage of multiplying the torque can be achieved through a variety of devices based on different concepts. In the previous chapter, an epicyclic geared transmission arranged in a planetary configuration has been analysed on geometrical and performance bases. In this chapter, the alternative category of cycloidal speed reducers is analysed because considered a viable solution for the torque multiplication in industrial applications (Hwang et Al., 2006). The motivation to investigate this further category of mechanical reduction systems was given by Norbar Torque Tools Ltd. Traditional epicyclic single and multi-stage gearboxes are at the basis of Norbar production and an investigation of the alternatives to the universally used epicyclic gearing was required and attempted. The aim was to design a gearbox capable of an improved torque to weight ratio by maintaining the same characteristics of robustness and reliability provided by the well-known epicyclic systems.

Despite the increasing popularity of cycloidal drives, only few literature sources are available. Moreover, the absence of a dedicated design standard makes the design process complex and requires the use of numerical and experimental approaches for the evaluation of performance.

In a Cycloidal system, the principal component, the cycloid disk, in its interaction with the external pins replaces the multiple contacts between gears occurring in epicyclic gear trains (Braren, 1928; Braren, 1932). As the main component of a cycloidal transmission is the cycloidal wheel, the geometrical relations of the cycloidal profile are investigated in this chapter. The theoretical findings were then applied to practice with the design of a 1:15 gearing ratio cycloidal speed reducer. The designed model, exploded in Figure 7.1, was used for numerical analyses aimed to evaluate the time-varying stress distribution acting on the cycloidal disk at the interface with the annulus pins. The model has also been manufactured by Norbar Torque Tools Ltd. for testing purposes.

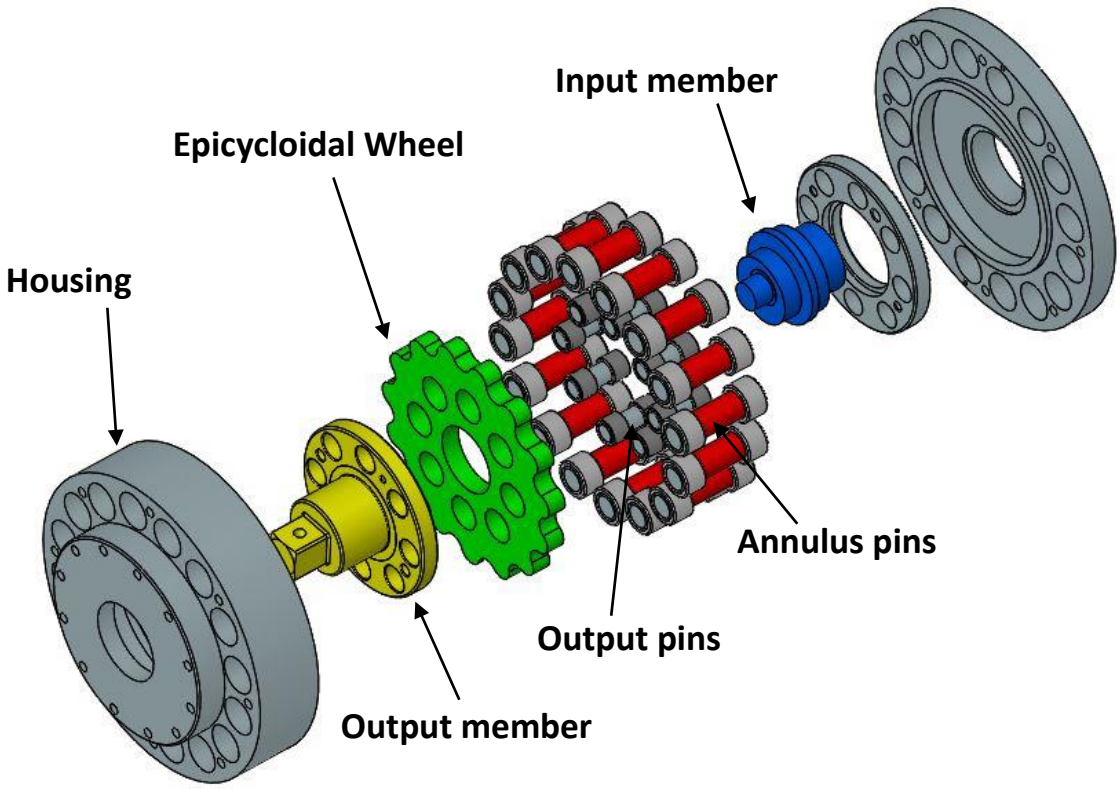

Figure 7.1 – Exploded view of the designed cycloidal transmission.

7.1 Geometrical arrangement of a cycloidal speed reducer

A cycloidal speed reducer in its simplest arrangement is made by four basic components namely: input eccentric shaft, cycloidal disk, ring gear and output shaft. The cycloidal disk is driven by the eccentric cam which is rigidly connected to the input high speed shaft and provides the power to the system. The eccentric cam, by rotating inside the central bore of the cycloidal disk, determines a conversion of the rotating motion into a reciprocating motion of the cycloidal disk. This is the result of the interaction between the lobes lying around the external circumference of the disk and the pins evenly distributed along the internal circumference of the ring gear. The reciprocating motion of the cycloidal disk is then converted into a rotational motion by means of an output shaft. The continuous tangency between the pins flanged to the output shaft and the output holes on the cycloidal disk ensures a constant rotational velocity of the output shaft concentric to the input shaft. For each revolution of the high speed shaft, the cycloidal disk steps one position in the ring gear housing in the opposite direction with

respect to the input shaft (Shin et Al., 2006). The number of revolutions of the input shaft in order to make the cycloidal disk completing an entire cycle within the ring gear depends on the gear ratio.

7.2 Geometrical analysis

A cycloidal curve finds an engineering application in cycloidal gear trains. These types of devices have their principal component, the cycloidal disk, with the external profile shaped following an epicycloidal curve. In the following paragraph the parametric equations of the basic cycloid curve and subsequently of the epicycloid are determined and applied to the design of a cycloidal gear train.

7.2.1 Parametric Equation of a cycloidal curve

A *common* cycloidal is the curve created by tracing the trajectory of a point *P* fixed on a circle that rolls without slipping on a straight line as shown in Figure 7.2. As the circle rolls, the point of tangency between the circle and the line which is also the centre of instantaneous rotation (*C)* is moving of the same distance along the line so that the distance travelled by the point *P* on the straight line is equal to the arc length *k* described on the circle by point *P* due to the pure rolling condition.

Although the cycloidal curve can be expressed by an explicit equation, especially for engineering applications, a parametric equation is simpler to use. In this formulation, equations for x and y, coordinates of the curve, are produced relative to a single parameter θ, corresponding to the angle of rotation of the circle. Figure 7.2 shows a portion of the cycloid curve and its generating circle after it has experienced a rotation θ from the origin *C.*

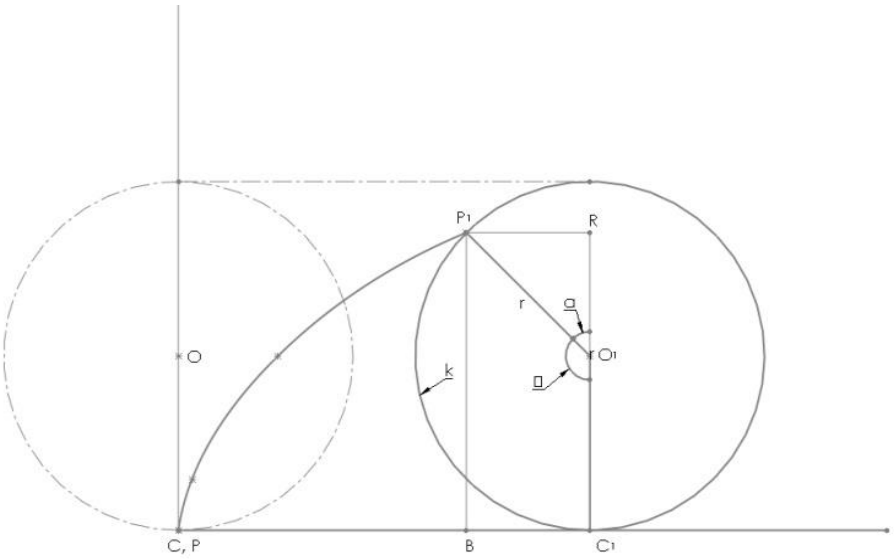

Figure 7.2 – Generation process of a cycloidal curve.

After θ revolutions, the centre of the circle at the instantaneous position has been named O_1 and a triangle $\widehat{O_1P_1R}$ is formed as shown in Figure 7.2. The horizontal and vertical sides of the triangle represent the distance of P_1 from the centre O_1.

The coordinates of O_1 are (C_1,r), where the distance C_1, corresponding to the x coordinate, is equal to the arc length k.

By using the right triangle trigonometry on triangle $\widehat{O_1P_1R}$ and the following geometrical relations between distances:

$$r \sin \alpha = \overline{P_1R} \tag{7.1}$$

$$r \cos \alpha = \overline{RO_1} \tag{7.2}$$

$$\theta = 180 - \alpha \tag{7.3}$$

And by considering the following trigonometric identity:

$$\sin(180 - \alpha) = \sin \alpha \tag{7.4}$$

and the relation:

$$\sin \theta = \sin \alpha = \frac{\overline{P_1R}}{r} \tag{7.5}$$

It is possible to parametrise the coordinates of P(x, y) in terms of the angle ϑ.

Since the coordinates x and y of P_1 are equal to:

$$x(P_1) = k - \overline{P_1R} \tag{7.6}$$

$$y(P_1) = r + \overline{O_1 R} \tag{7.7}$$

and including the following relations:

$$k = r\vartheta = \overline{CC_1} \tag{7.8}$$

$$\overline{CB} = \overline{CC_1} - \overline{BC_1} = r\theta - r\sin\theta \tag{7.9}$$

$$\overline{BP_1} = r + \overline{O_1 R} = r - r\cos\theta \tag{7.10}$$

It yields the parametric equations for the cycloidal geometry:

$$x(\theta) = r(\theta - \sin\theta) \tag{7.11}$$

$$y(\theta) = r(1 - \cos\theta) \tag{7.12}$$

The graph traced by point P after θ rotations is a periodic function and repeats every 2π*r. In the simplified case of radius *r* equal to 1, since point *P* traces the cycloid, it takes one complete revolution or 2π to find again the x-axis as shown in Figure 7.3.

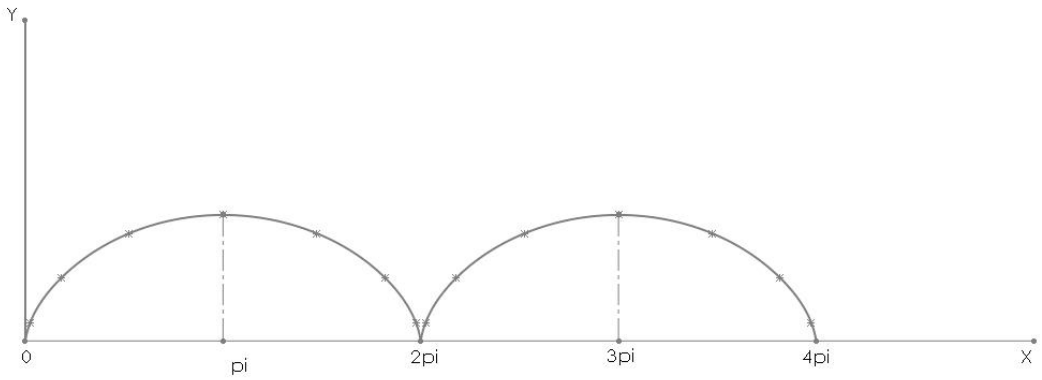

Figure 7.3 – Repeated cycloidal curves showing a period of 2π.

The graph shows smooth and continuous curves between the sharp turns in which a minimum of the function occurs. Moreover, relative maximum points may occur at the turning point 2π and 3π when the trend changes from ascendant to descendent.

7.2.2 Parametric equation of an epicycloid curve

From the definition of the cycloid curve as above, it is possible to move on to the epicycloid curve. The epicycloid, as for the case of the cycloid, is a cyclic curve used in engineering to shape the lobes of an epicycloidal disk or also called cycloidal disk.

The epicycloid is defined as the curve generated by the trajectory of a point fixed to a circle, called epicycle, which rolls without slipping on a fixed circle of radius r.

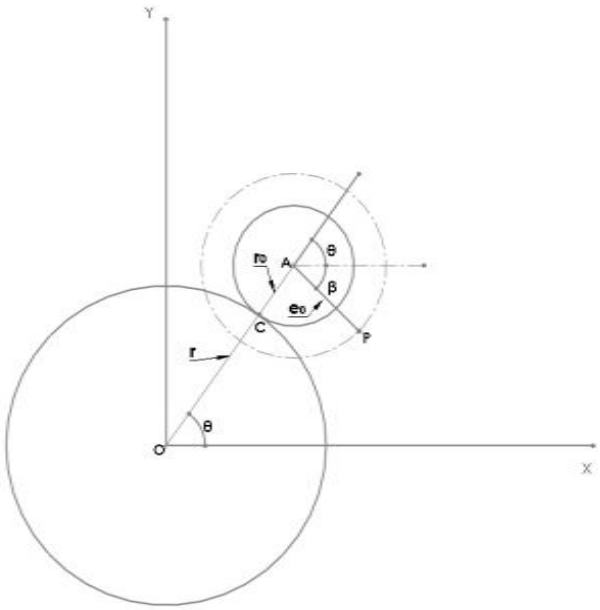

Figure 7.4 – Generation process of an extended epicycloid.

As shown in Figure 7.4, the epicycloid is obtained by tracing the path of point P rigidly connected to the rolling circle of radius r_0 that rolls without slipping on a fixed circle of radius r. θ indicates the angle of rotation between two successive positions of the circle of radius r_0.

In order to work out the coordinates of point *P* (x_p, y_p) as a function of angle θ, the trajectory of point *P* is defined by the superimposition of the two motions: P in terms of A, centre of the mobile circle, and A in terms of O, centre of the fixed circle.

$$P(x,y) \rightarrow \begin{cases} x = e_0 cos\beta \\ y = e_0 sin\beta \end{cases} \quad 7.13$$

$$A(x,y) \rightarrow \begin{cases} x = (r_0 + r) cos\theta \\ y = (r_0 + r) sin\theta \end{cases} \quad 7.14$$

Due to the pure rolling condition of motion between the two circles of radii r_0 and r, and by considering C the instantaneous centre of rotation, it is possible to define the following relations between angles:

$$r\theta = \widehat{OAP}r_{\,0} \rightarrow \widehat{OAP} = \frac{r}{r_0}\theta \tag{7.15}$$

$$\widehat{OAP} - \beta + \theta = \pi \tag{7.16}$$

$$\beta = \widehat{OAP} + \theta - \pi \tag{7.17}$$

Using the information from above and after transformations we obtain the following equations:

$$P(A)\begin{cases} x = e_0 \cos\left(\frac{r}{r_0}\theta + \theta - \pi\right) \\ y = e_0 \sin\left(\frac{r}{r_0}\theta + \theta - \pi\right) \end{cases} \rightarrow \begin{cases} x = -e_0 \cos[\theta\left(1 + \frac{r}{r_0}\right)] \\ y = -e_0 \sin[\theta\left(1 + \frac{r}{r_0}\right)] \end{cases} \tag{7.18}$$

And after combining P and A coordinates it yields the parametric equation of an extended epicycloid as function of the parameter θ where the radii r_0, r and the distance e_0 are known parameters.

$$\begin{aligned} X_P &= (r_0 + r)cos\theta - e_0 \cos[\theta\left(1 + \frac{r}{r_0}\right)] \\ Y_P &= (r_0 + r)sin\theta - e_0 \sin[\theta\left(1 + \frac{r}{r_0}\right)] \end{aligned} \tag{7.19}$$

Depending on the position of generating point *P* relative to the rolling circle r_0, different geometrical configurations can be achieved:

- If P lies on the edge of the circle (e_0=r_0), the generated curve will be a *normal epicycloid.*
- If P is placed anywhere inside the circle (e_0< r_0), it will generate a *shortened epicycloid.*
- If P is outside but still rigidly connected to the circle (e_0> r_0), the resulting curve will be an *extended epicycloid.*

The three possible configurations are shown in the Figure 7.5 below.

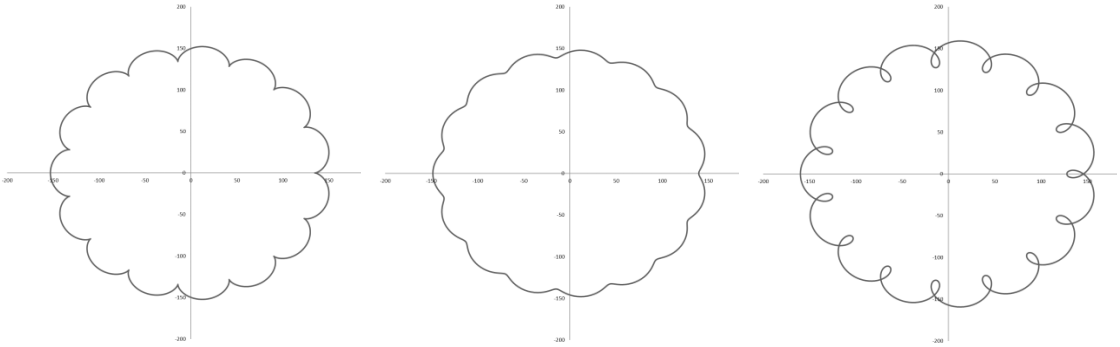

Figure 7.5 - Comparison between a normal (left), shorten (centre) and extended (right) epicycloid profiles.

If we consider that the circle of radius r_0 has rotated of an angle $\widehat{OAP} = 2\pi$ by making a complete rotation, then equation 7.15 can be rewritten as follow:

$$\theta = 2\pi \frac{r_0}{r} \tag{7.20}$$

After a complete rotation of the circle r_0, one entire lobe of the cycloidal profile is generated. The process continues until the lobes are evenly distributed along the fixed circle r. Therefore, the epicycle of radius r_0 has to complete a number of rotations before it covers the entire perimeter of the fixed circle; this entails that the length of the arc $2\pi r$ is a multiple of $2\pi r_0$ and their ratio defines the number of lobes of the epicycloid profile as follows:

$$\frac{r}{r_0} = N_l \tag{7.21}$$

It is an obvious consideration that the number of lobes must be an integer in order to generate a closed and continuous curve suitable for mechanical applications.

7.2.3 Epicycloid working profile

The profile generated by the coordinates Xp and Yp as above, is termed as *Theoretical* because it is not functional for engineering applications such as cycloidal gears. As explained by Alipiev (1998), the reason is attributed to the sharp turning points between the end and the beginning of two adjacent lobes. As the force in such systems is shared between the lobes on the cycloidal disk and the pins placed circumferentially on the annulus, the radius of curvature of the concave portion of the epicycloidal profile has to be always bigger than the radius of the annulus pins in order to avoid motion discontinuities and intermittent torque delivery which are unacceptable conditions for a speed reducer. This introduces the necessity of modifying the theoretical profile with

an equivalent geometry that does not exhibit unwanted characteristics but that still satisfies the law of gearing.

In order to prove that the epicycloidal profile is conjugate to the pins, Figure 7.6 shows the normal to the epicycloidal profile (dashed red line) at point O_c^I that passes through the point of instantaneous rotation or pitch point P_o^I and divides the line of rotation centres $O_1O_0^I$ in the two segments $O_1P_o^I$ and $P_o^IO_0^I$ such that:

$$\frac{\overline{O_1P_0^I}}{\overline{P_0^IO_0^I}} = \frac{\omega_0}{\omega_1} = i \qquad 7.22$$

Therefore, the vector velocity of the point O_C^i is always tangent to the epicycloidal curve and normal to the line connecting O_C^i and the centre of instantaneous rotation P_o^i. This condition satisfies the law of gearing and determines the two surfaces being conjugate (Litvin 1989, Litvin et Al., 2004).

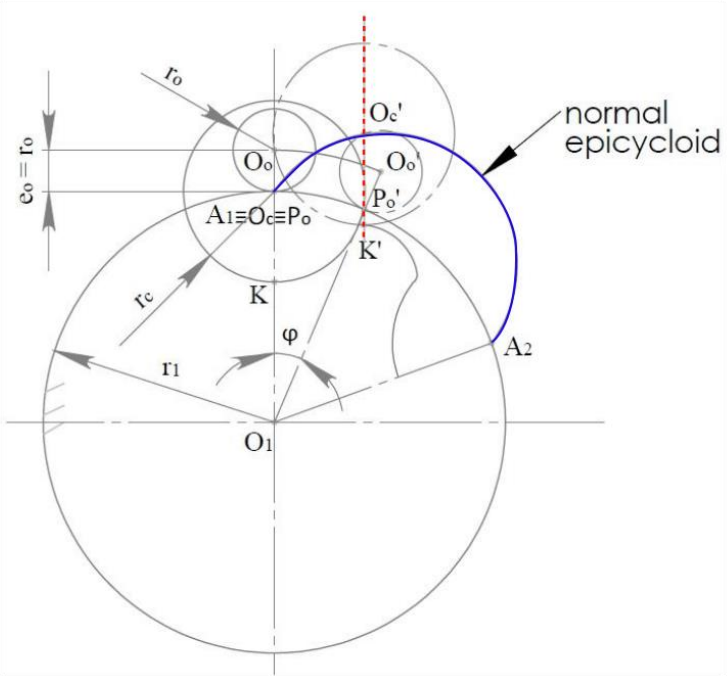

Figure 7.6 - Schematics of the profile generation process. The normal to the profile (dashed red) passes through the instantaneous pitch point K^I. Source (Alipiev, 1988) modified by the author.

By combining Equations 7.21 and 7.22 and after considering that for cycloidal systems the difference between number of annulus pins and number of cycloidal disk lobes is equal to 1, the following important relations are found:

$$i = N_l = N_p - 1 \qquad 7.23$$

7.2.3.1 Parametric equations of the cycloidal working profile

The tooth profile of the epicycloidal disk is defined by starting from the theoretical profile T-T in Figure 7.7. If a circle is selected, which moves fixed to the epicyclic (red circle) that rolls without slipping on the pitch circle (green), it creates a curve equidistant to the theoretical called working profile and identified in Figure 7.7 with W-W. The selected circle can be considered as a profile generating geometry for the working profile of epicycloidal disks, equivalent to the rack cutter in involute gears.

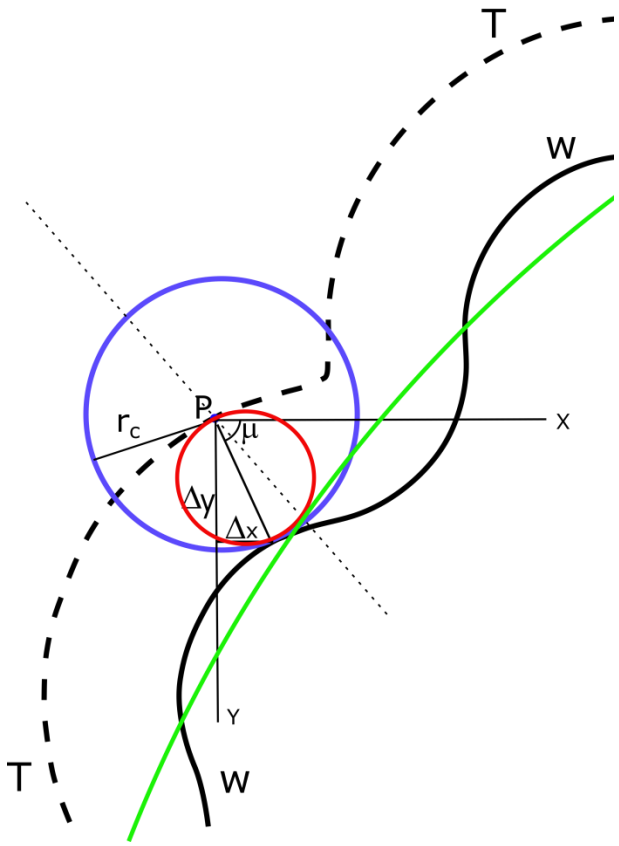

Figure 7.7 - Generation process of the working profile W-W by starting from the theoretical profile T-T. In red the epicycle of radius r_0, in green the pitch circle of radius r and in blue the generating circle of radius r_c and centre P. The dashed line is the normal to the profile passing through the pitch point. $\Delta_{x,y}$ determine the position of the equidistant curve WW from the original TT.

In order to define the coordinates of the new generating point *P'(x, y),* it is necessary to introduce two factors $\Delta_{x,y}$ that take into account the displacement of the curve from the original theoretical profile.

$$X_w = X_P + \Delta_X \quad 7.24$$

$$Y_w = Y_P + \Delta_Y \quad 7.25$$

The quantities $\Delta_{x,y}$ can be calculated by using the unit normal vector to the theoretical profile multiplied by the radius of the generating circle r_c that indicates the actual distance between the two equidistant curves.

$$\Delta_X = r_c \overrightarrow{Pnx} \quad 7.26$$

$$\Delta_y = r_c \overrightarrow{Pny} \quad 7.27$$

The unit normal vector of components is obtained by deriving the tangent vector components:

$$\overrightarrow{P_t} = (x_p, y_p) \quad 7.28$$

as function of the turning angle θ. In order to complete the coordinate transformation, the order of the components has to be inverted and the sign of one of them has to be changed as follow:

$$\overrightarrow{P_n} = (-\frac{\partial y_p}{\partial \theta}, \frac{\partial x_p}{\partial \theta}) \quad 7.29$$

The two components of the normal vector $\overrightarrow{P_n}$ corresponds respectively to the horizontal and vertical sides of a right triangle of which the hypotenuse is oriented in the normal direction to the curve as schematised in Figure 7.8.

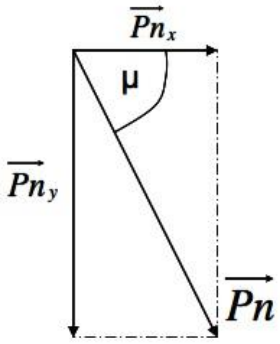

Figure 7.8 - Normal vector unit and its components along the x and y axes.

By applying the right triangle relations and by considering the following components:

$$\overrightarrow{Pnx} = -\frac{\delta y_p}{\delta\theta};\ \overrightarrow{Pny} = \frac{\delta x_p}{\delta\theta} \tag{7.30}$$

It yields:

$$\overrightarrow{Pn} = \sqrt{(-\frac{\delta y_p}{\delta\theta})^2 + (\frac{\delta x_p}{\delta\theta})^2} \tag{7.31}$$

And by considering the relation below:

$$\overrightarrow{Pn}\cos\mu = -\frac{\delta y_p}{\delta\theta} \tag{7.32}$$

$$\overrightarrow{Pn}\sin\mu = \frac{\delta x_p}{\delta\theta} \tag{7.33}$$

After substitution and transformation of both the equations it yields:

$$cos\mu = \frac{-\frac{\delta y_p}{\delta\theta}}{\sqrt{(-\frac{\delta y_p}{\delta\theta})^2 + (\frac{\delta x_p}{\delta\theta})^2}} \tag{7.34}$$

$$sin\mu = \frac{\frac{\delta x_p}{\delta\theta}}{\sqrt{(-\frac{\delta y_p}{\delta\theta})^2 + (\frac{\delta x_p}{\delta\theta})^2}} \tag{7.35}$$

Once both $sin\mu$ and $cos\mu$ are known values, the equations that describe the coordinates of the modified curve result as follow:

$$X_W = X_p + r_c\frac{-\frac{\delta y_p}{\delta\theta}}{\sqrt{(-\frac{\delta y_p}{\delta\theta})^2 + (\frac{\delta x_p}{\delta\theta})^2}} \tag{7.36}$$

$$Y_W = Y_p + r_c\frac{\frac{\delta x_p}{\delta\theta}}{\sqrt{(-\frac{\delta y_p}{\delta\theta})^2 + (\frac{\delta x_p}{\delta\theta})^2}} \tag{7.37}$$

Where the terms $-\frac{\delta y_p}{\delta\theta}$ and $\frac{\delta x_p}{\delta\theta}$ are respectively:

$$-\frac{\delta y_p}{\delta \theta} = (r_0 + r)\sin\theta + e_0\left(1 + \frac{r}{r_0}\right)\sin\theta\left(1 + \frac{r}{r_0}\right)] \quad 7.38$$

$$\frac{\delta x_p}{\delta \theta} = (r_0 + r)\cos\theta - e_0\left(1 + \frac{r}{r_0}\right)\cos\theta\,[\theta\left(1 + \frac{r}{r_0}\right)] \quad 7.39$$

The equations above describe the working profile of an epicycloid and can be used for geometrical modelling of cycloidal disks. This profile construction method allows the minimum radius of curvature being always bigger than the pin radius, which is as seen the basic requirement for the application of an epicycloid in gearing applications. The resulting geometry and a comparison between a theoretical profile and its corresponding working profile are shown in Figure 7.9:

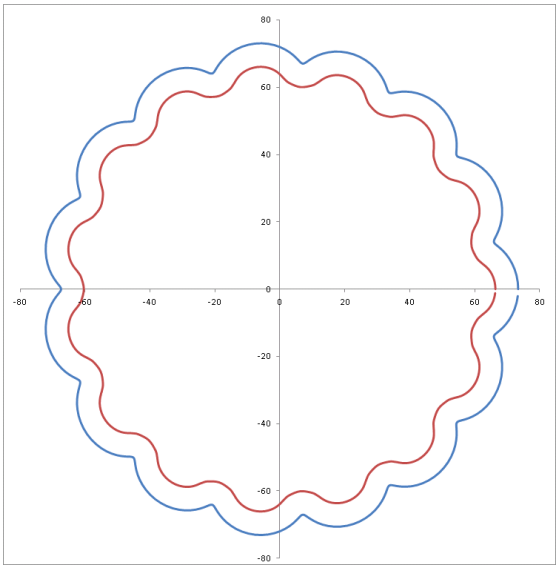

Figure 7.9 - Comparison between epicycloidal theoretical profile in blue and the corresponding working profile for the set of parameters of Table 7.1 and 7.2.

7.2.3.2 Design considerations

Some considerations can be done based on the analytical relations determined in the previous paragraph. It can be seen that the geometry of the cycloidal disk is based on some independent variables. The values to be attributed to these variables follow considerations in order to guarantee a correct mesh between cycloidal disk and the mating annulus pins.

To follow, an explanation of the physical meaning of these variables and their geometrical relations:

- Radius of the annulus pins r_p;
- Radius of the pitch circle r;
- Gearing ratio i;
- Eccentricity e_0;

The radius of the annulus pins r_p has to be equal to the radius of the generating circle r_c in Figure 7.7. This guarantees a correct mesh condition due to the fact that the epicycloidal profile is shaped by means of the generating circle.

The imposition of the gearing ratio i, univocally determines the second reference geometry, namely the epicycle or circle of radius r_0 given the relation $i = \frac{r}{r_0}$. Moreover, by following the relations 7.21 and 7.23, the number of annulus pins and cycloidal disk lobes is univocally defined.

The eccentricity e_0 is the fundamental parameters for the generation of cycloidal disks as it determines the type of epicycloidal if shortened, normal or extended. Moreover, the value e_0 corresponds to the centre distance between the cycloidal disk and the input/output shafts and determines the wobbling motion of the wheel within the annulus.

7.2.4 Design process and geometrical considerations

In this paragraph geometrical considerations for the design of the cycloidal drive are discussed and the calculated geometrical parameters necessary for the modelling of the considered components listed.

7.2.4.1 Cycloidal disk

The cycloidal disk represents the principal component of the cycloidal transmission system and characterises this type of devices from the more common geared systems. The disk is in simultaneous contact with three mating components allowing the power transmission from the input to the output shaft. The external contact occurs with the annulus pins; internally it is driven by the eccentric input shaft and midways it is in contact with the output pins. In order to guarantee a correct mesh between the cycloidal

disk and the annulus pins the appropriate geometry has to be determined as explained in the previous paragraph.

The design of the cycloidal disk started with a number of considerations based on the size of the device:

- The first decision made was with regards to the gearing ratio. Norbar has suggested a 15:1 overall ratio as the idea was to expand their HT4 series with a device capable of transmitting a considerable torque within a relative compact size (Norbar Torque Tools ltd., 2018).
- Secondly, the diameter of the annulus pins was predetermined as they were available in stock at Norbar in diameter of 14 mm.
- Thirdly, the pitch circle radius was determined by following considerations based on a size factor. The pitch circle radius of 66 mm was determined after few iterations by considering the limiting condition $e_0=r/N_p$ (Shin et Al., 2006), the gearing ratio i=15:1 and the dependent variable r_0. In fact, in order to obtain a shortened epicycloidal profile as suggested by Alipiev (1988) and Litvin (1989), the relation between the eccentricity and the radius of the epicycle needs to be such that: $e_0<r_0$. This condition allows the construction of a working profile without undercutting and geometrical singularities that would make the profile unusable for mechanical applications (Litvin et Al., 2004).

  Once the independent variables have been assigned, the values of dependent parameters have been determined with the following geometrical relations:

Theoretical addendum circle radius	$\rightarrow r_{at} = r + r_0 + e_0$	7.40
Theoretical dedendum circle radius	$\rightarrow r_{dt} = r + r_0 - e_0$	7.41
Working addendum circle radius	$\rightarrow r_{aw} = r_{at} - r_0 - r_p$	7.42
Working dedendum circle radius	$\rightarrow r_{dw} = r_{dt} - r_0 - r_p$	7.43
Tooth depth	$\rightarrow h = r_{aw} - r_{dw} = 2e_0$	7.44

The geometrical values listed in Tables 7.1 and 7.2 define univocally the cycloidal disk profile. The result of the application of those parameters on the physical geometry is shown in Figure 7.10 where the sketch of the cycloidal wheel is shown.

Table 7.1 – Theoretical Cycloidal Profile parameters

Independent		Dependent	
Gearing ratio *i*	15	**Epicycle radius r_0**	4.4 [mm]
Pitch circle radius *r*	66 [mm]	**Addendum radius r_{at}**	74.4 [mm]
Eccentricity e_0	4 [mm]	**Dedendum radius r_{dt}**	66.4 [mm]
		Number of lobes N_l	15

Table 7.2 – Working Cycloidal Profile parameters

Independent		Dependent	
Gearing ratio *i*	15	**Number of lobes N_l**	15
Pitch circle radius *r*	66 [mm]	**Number of pins N_p**	16
Annulus pin radius r_p	7 [mm]	**Addendum radius r_{aw}**	63 [mm]
Eccentricity e_0	4 [mm]	**Dedendum radius r_{dw}**	55 [mm]
		Tooth depth *h*	8 [mm]

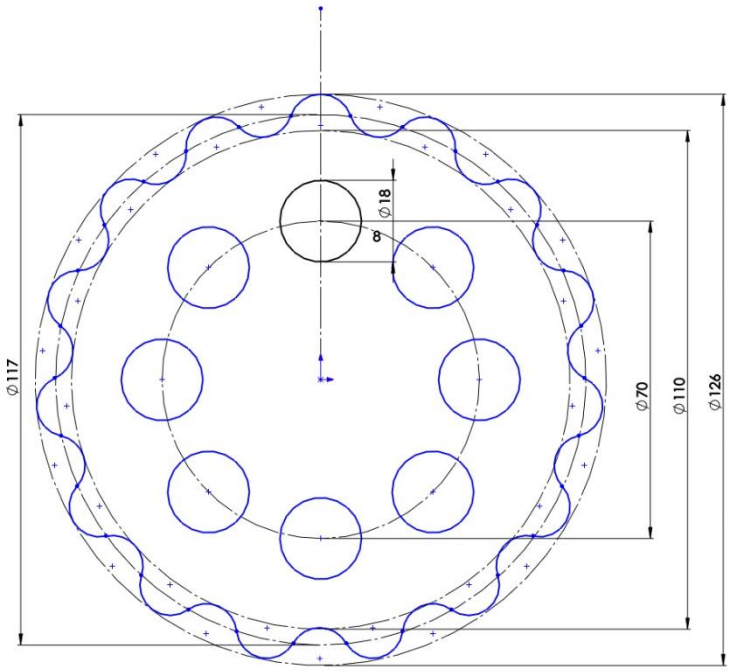

Figure 7.10 – Frontal view of the cycloidal dick with indicated relevant measures.

7.2.4.2 Annulus

Consequently, the annulus included into the housing was designed. Also for this case, geometrical relations based on the same independent variables as before, allow to determine the basic geometry of the part. The following geometrical relations were used:

Annulus pitch circle radius $\rightarrow r_2 = r_1 = 2r_{aw} - 2e_0 + 2r_p$ 7.45

Annulus dedendum circle radius $\rightarrow r_{da} = r_2 - r_0 + r_p$ 7.46

Annulus addendum circle radius $\rightarrow r_{aa} = r_2 - r_0 - r_p$ 7.47

The values resulting from the calculations are listed in Table 7.3 and the corresponding model is shown in Figure 7.11.

Table 7.3 – Annulus Design parameters

Independent		Dependent	
Gearing ratio *i*	15	**Epicycle radius r_0**	4.4 [mm]
Pitch circle radius *r*	66 [mm]	**Pitch circle radius r_2**	66 [mm]
Eccentricity e_0	4 [mm]	**Addendum radius r_{aa}**	59 [mm]
		Dedendum radius r_{da}	73 [mm]
		Number of lobes N_l	15

It can be noticed that for the case of nominal dimension, the radii of cycloidal dedendum circle and annulus addendum circle are coincident and equal to 55 mm.

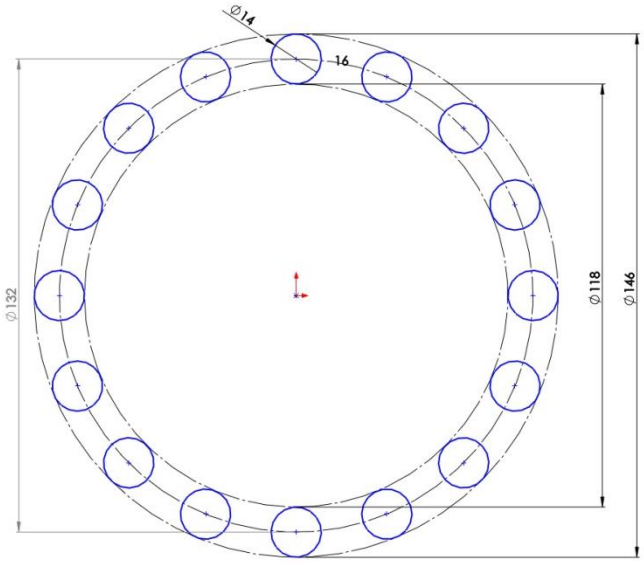

Figure 7.11 – Frontal view of the annulus pins.

7.2.4.3 Output shaft

The output member has the task of transmitting the power from the system to the user. The power transmission is required to be as smooth and linear as possible in order to avoid the start of unwanted vibrations during working operations. In a cycloidal system,

the load is transmitted from the cycloidal disk to the output shaft by means of the contact between holes placed in the internal circumference of the cycloidal disk and pins rigidly connected to the output member. The pins are placed on a pitch circle concentric to the shaft axis. Once the diameter of the output pins d_{op} has been determined, the diameter of the corresponding holes d_h on the cycloidal disk follows the relation:

$$d_h = d_{op} + 2e_0 \qquad 7.48$$

The frontal view of the output shaft is shown in Figure 7.12.

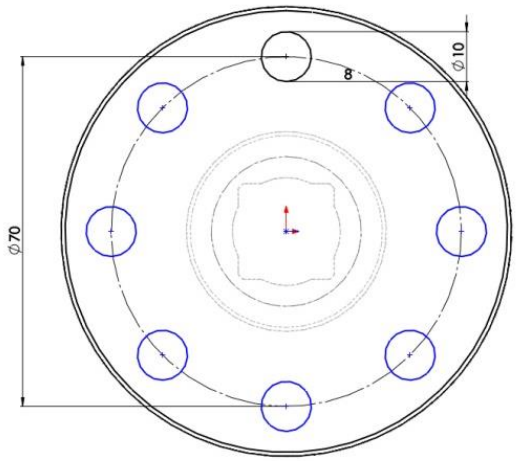

Figure 7.12 – Frontal view of the output shaft with indicated relevant measures.

7.2.4.4 Input Shaft

The input shaft, as indicated by the name, is the member connected to the power source. Industrial speed reducers are for most cases connected and driven by electric motors and have the function of converting their typical high rotational speed in a higher torque level. For the case of cycloidal reducers, the input shaft needs to provide the required eccentricity in order to properly move the cycloidal disk. The component is designed in such a way that the main axis is concentric with the output and annulus members and an eccentric cam put the cycloidal disks in motion. Even though using a single disk is not ideal due to the resulting unbalanced centripetal forces, the choice was dictated by the manufacturing considerations.

The frontal view of the designed Input shaft is shown in Figure 7.13.

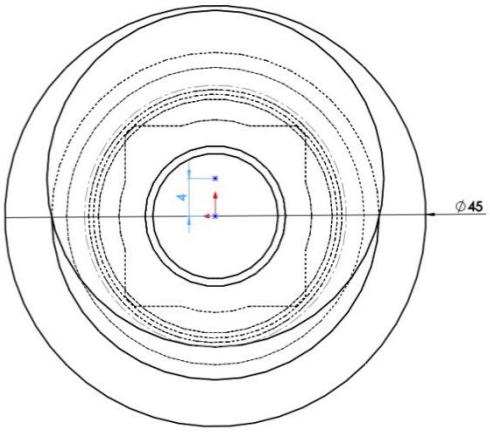

Figure 7.13 – Frontal view of the input shaft drawing in which the measures of overall diameter and eccentricity are shown.

7.2.4.5 Secondary components

After the geometry of the main parts of the system was defined, the drawings were forwarded to the engineering group at Norbar for considerations on thickness of the components and sizing of the remaining parts. It was decided to support the annulus and output pins by roller bearings in order to make the pins rotating and minimise the sliding friction at the contact. The input and output shafts are supported by roller bearings as shown in the section view in Figure 7.14.

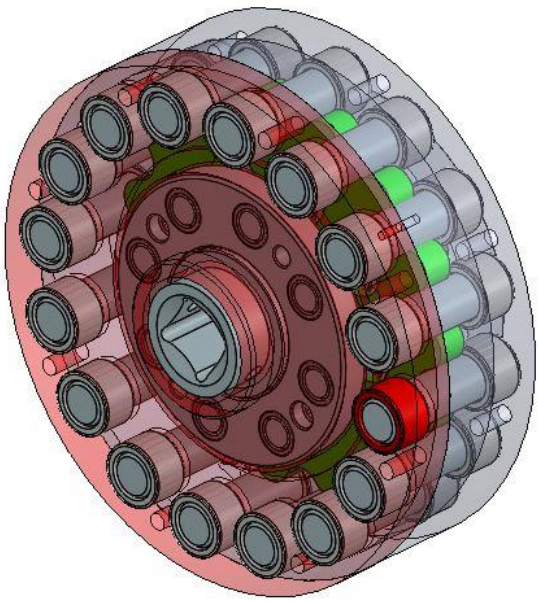

Figure 7.14 - Isometric view of the 3D cycloidal transmission model.

7.2.4.6 Manufacturing

The material and the specific heat treatments were decided for each component and tolerances were given. All the relevant information is included in the technical drawings in Appendix C. Figures 7.15 and 7.16 show the manufactured components and the top view of the assembled cycloidal drive.

Figure 7.15 – Manufactured components of the designed cycloidal transmission including housing, cycloidal plate, roller bearings and input and output shafts.

Figure 7.16 – Top view of the designed cycloidal components after the assembly operations.

7.3 Cycloidal drive modelling

The modelling of the cycloidal systems resulting from the design process undertaken started with the generation of 3D models of each component then assembled into a cycloidal arrangement and successively used for the FE analysis. Each part has been modelled in SolidWorks by using the reference dimensions in table 7.2, 7.3. The cycloidal disk profile was created by means of the function implemented in Solidworks called “equation driven curve”. Such command allows drawing a curve by inserting a parametric equation of the wanted geometry rather than constructing it by single points then manually joined with a spline curve. After the whole model was assembled as shown in Figure 7.14, a “motion study” has been performed in order to observe whether any interference was occurring during the meshing process. The model built with nominal dimensions has resulted interference free.

The successive step of the analysis was with regards to performance by means the FEA analysis. In order to conduct the numerical analysis, given the complexity of the geometry, it was decided to use a simplified version of the cycloidal gear train, still able to represent entirely the dynamics and kinematics of the system but, at the same time, lighter from a computational point of view. The simplified model is shown in Figure 7.17.

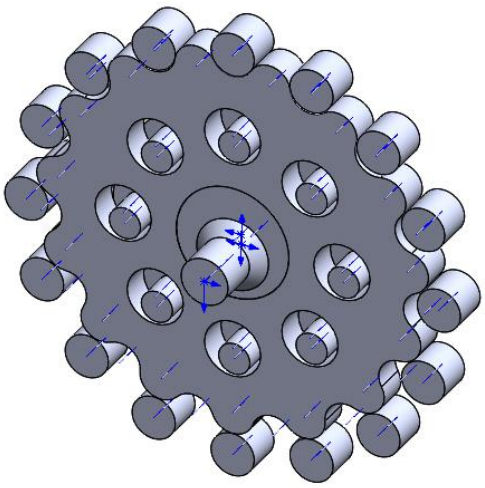

Figure 7.17 - Isometric view of the 3D assembly of a simplified version of the designed cycloidal gear train.

From this, all the models are exported into the ANSYS FEA environment for the successive 3D FE Analysis.

7.3.1 Finite Element Analysis

The cycloidal system designed as described in the previous section was the object of a preliminary study by means of Finite Element Analysis with the aim of understanding the stress state occurring at the interface between the cycloidal disk and the annulus pins. The FEA procedure follows the same quasi-static approach used for the performance analysis of a spur gear pair in Chapter 5 and the investigation on planetary gear trains in Chapter 6 in order to evaluate the time varying stress among the entire mesh cycle with the only difference that for this case a 3D model was used instead of a 2D model as for the previous cases.

7.3.1.1 3D Finite Element Mesh

Since a 3D model was used for the numerical analysis of the designed cycloidal transmission, a 3D mesh was required in order to discretise the entire geometry in elements of volume. The use of an adequate finite element mesh is crucial for the quality of numerical results and guarantees an appropriate discretization of the model coupled with the use of proper elements is the key to achieve accurate results as already described in 5.4.2. For the study of 3D solid elastic models, hexahedral elements are the most appropriate especially for the case of complex geometries, as they are able to adapt closely to the curved profiles and represent the model in its entirety. The rate of adaption to the underlying surface increases with the order of the elements such that quadratic elements follow the geometry better than similarly sized linear elements (ANSYS®, 2016; Lepi, 1998).

In this study, the finite element model of the gear pair is created using SOLID186 elements shown in Figure 7.18. They are quadratic elements defined by 20 nodes having three DoF at each node: translations in the nodal X,Y and Z directions (ANSYS®,. 2016).

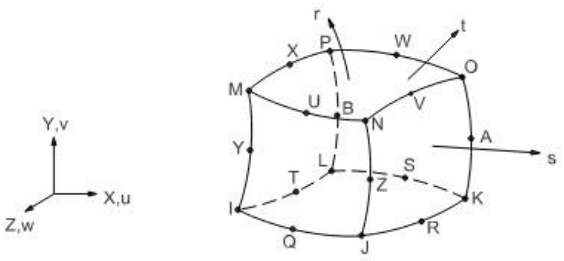

Figure 7.18– SOLID186 element (ANSYS®, 2016).

In order to model the contact regions with sufficient accuracy, as the location of the contact point changes the entire surface requires a refined mesh. Unfortunately, due to the high computational cost induced by the complex contact condition in the system and the limited computational resources a refined mesh was not possible. In order to balance the required solution time with a reasonable quality of results, a refined mesh with element side lengths of 1 mm was used to discretize the cycloidal disk and the annulus pins while input and output shafts were discretised with elements with a side length of 2 mm. This was the limit found for the computational resources available as for any further refinement of the step the solver was not able to perform the solution due to a lack of memory. The resulting mesh is illustrated in Figure 7.19 and is composed of 832179 nodes and 188230 elements.

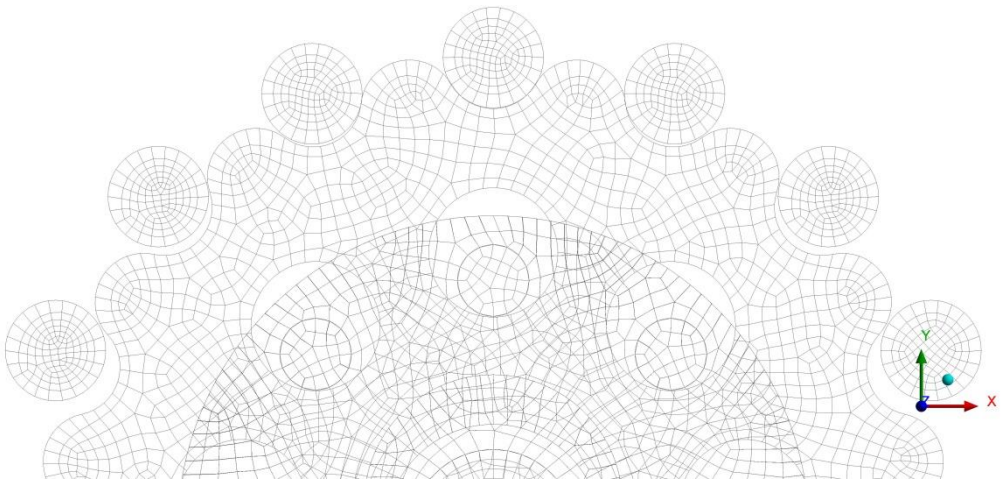

Figure 7.19 – 3D mesh of the cycloidal system model.

7.3.1.2 Finite Element 3D Contact model

The next type of elements necessary to completely define the finite element model is contact elements. For the analysis of a cycloidal gear train, contact conditions are of primary importance as the power transmission from one member to the other occurs through the interaction of various parts of the model. Contact modelling starts with the definition of parts in contact. For the case of a 3D model, the cycloidal disks thickness is selected as a contact surface as it would experience contact with the mesh cycle. The mating part is represented by the annulus pins of which, the external face has been selected as target. Input shaft and cycloidal gear have also been selected as contacting surfaces being the eccentric cam the contact and the inner surface of the central hole of the cycloidal gear, the target. A representation of the selected contacting surfaces is shown in Figure 7.20.

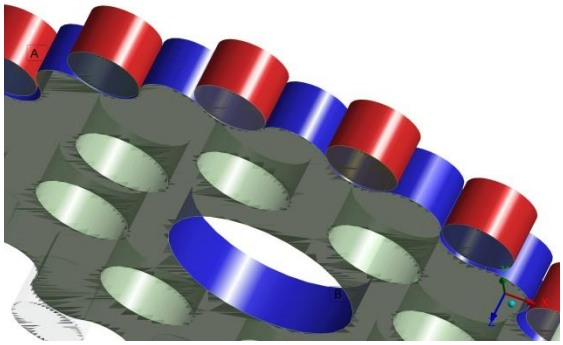

Figure 7.20 – Selection of contact and target surface between cycloidal disk and annulus pins and eccentric cam (hidden) and cycloidal disk.

After the contact surfaces are created, the next step is to define the functions to determine their reciprocal interactions. The Contact regions between cycloidal disk and annulus pins were defined as frictional with a null coefficient of friction. Instead, for the input shaft/cycloidal interface a frictionless contact formulation was used in order to simulate the presence of a bearing which eliminates the frictional forces. For contact and target elements a “symmetric behaviour” option was selected as explained in 5.5. For the current analysis, the “program controlled” option was selected in order to control the the advanced contact functions except for the “interface treatment” that

was set as “adjust to touch” to overcome the risk of convergence failure by reducing the initial penetration and/or closing any initial gap between contacting parts.

7.3.1.3 Time step Controls

The loading history has been divided in three steps, two of 1.5 s and one of 3 s for a total time frame of 6s. For the first step, the automatic step control function available in ANSYS has been used in order to optimize the number of load increments necessary for the solution to converge. For the second step, a constant number of substeps equal to 180 was used in order to achieve a resolution of =0.5° over the 90° of rotation of the input shaft. For the third step, 360 substeps cover a rotation angle of the input shaft equal to 180° for a corresponding resolution of 0.5°. The total angle of rotation across the 6s time frame is 360°.

7.3.1.4 Boundary conditions

The system has been loaded through input shaft by applying a ramped moment in counter clockwise direction from 0 to 50 Nm in 1.5s for the first time step and then kept constant for the following substeps. The rotational velocity has been simulated by applying at the input shaft a rotation angle of 90° for the first time step and a successive total 270° across the second and third substeps. The resulting input shaft average rotational speed over the 6s time frame is 10 rpm.

The output shaft was rotated in accordance with the overall gearing ratio i=15:1 of a total angle of 24° across the 6s time frame. The assigned rotational direction is clockwise, opposite to the input shaft one. In order to simulate the physical constraints given by bearings and flanged supports, the following configuration was used. The input shaft is supported by a cylindrical support that allows only rotations about its own axis. Also the output shaft is supported by a cylindrical support concentric with the input shaft. The annulus pins are kept in their spatial position by a fixed support applied to the free ends while the entire pin is subjected to the force applied perpendicularly by the cycloidal disk. And finally, the cycloidal disk is kept in place by a translational support which allows the component to move free on the XY plane constraining any displacement along the Z axis. The cycloidal disk is then moved by the eccentric cam and by the reaction forces due to its interaction with the annulus pins. In this configuration,

the cycloidal disk can replicate the wobbling motion divided into rotation about its own central axis and a translation on the XY plane. A summary of the boundary conditions applied is shown in Figure 7.21 and the mechanical characteristics of the material used for the analysis are listed in table 7.4.

Table 7.4 –Cycloidal system FEA model material properties.

Young's modulus E [MPa]	$2x10^5$	$2x10^5$
Poisson ratio ν	0.3	0.3
density ρ [kg/m^3]	7850	7850

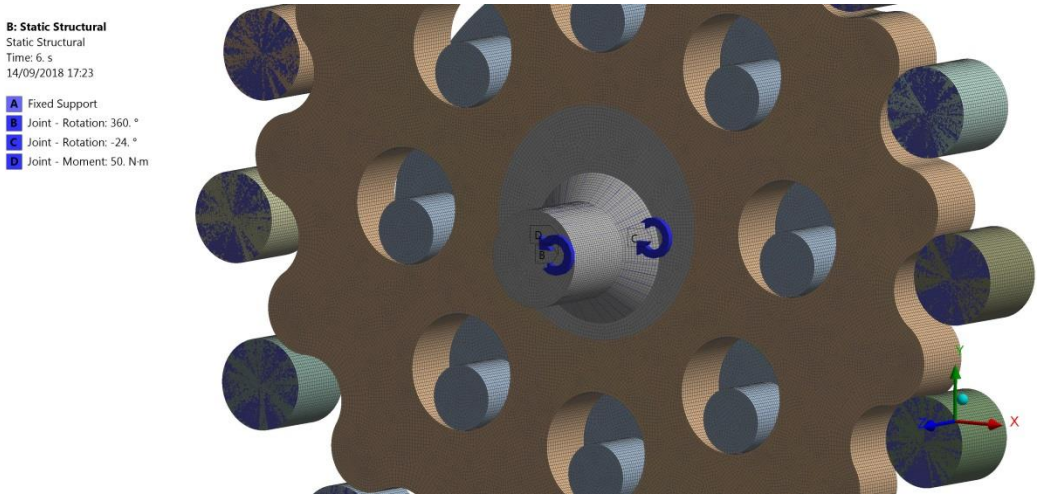

Figure 7.21 – Simplified 3D model for numerical analysis with boundary conditions applied.

7.3.1.5 Results and Discussion

The application of quasi-static FEA for the study of the stress distribution within the cycloidal gear train has returned the time-varying stress distribution occurring on the cycloidal disk and annulus pins. The Von Mises induced stress state has been evaluated for a total meshing time of 6 s corresponding to one rotation of the input shaft. Such meshing time for the considered rotational velocity corresponds, locally at the mating points, to the change in position of the cycloidal disk from one pin to the immediate next. Unfortunately, due to the coarse mesh used as consequence of the limited computational results, stress values cannot be considered accurate. In fact, an element side length of 1 mm is not small enough in order to model the area of contact generated by the force shared between the two mating components. Based on this consideration,

it was decided to normalise the values of stress and plot them in percentage of the maximum load.

Figure 7.22 shows the Von Mises stress distribution within the system as consequence of the applied input moment and the resistance at the output given by the imposed rotation. By the resulting stress distribution, it can be seen that, while the eccentric cam rotates anti-clockwise and pushes the cycloidal plate against the annulus pins, at the same time, the disk is subjected to a reaction force from the annulus pins. This reaction force generates a moment in the clockwise direction around the cycloidal disk axis that is transferred to the output shaft through output pins in continuous contact with the holes placed on the cycloidal disk.

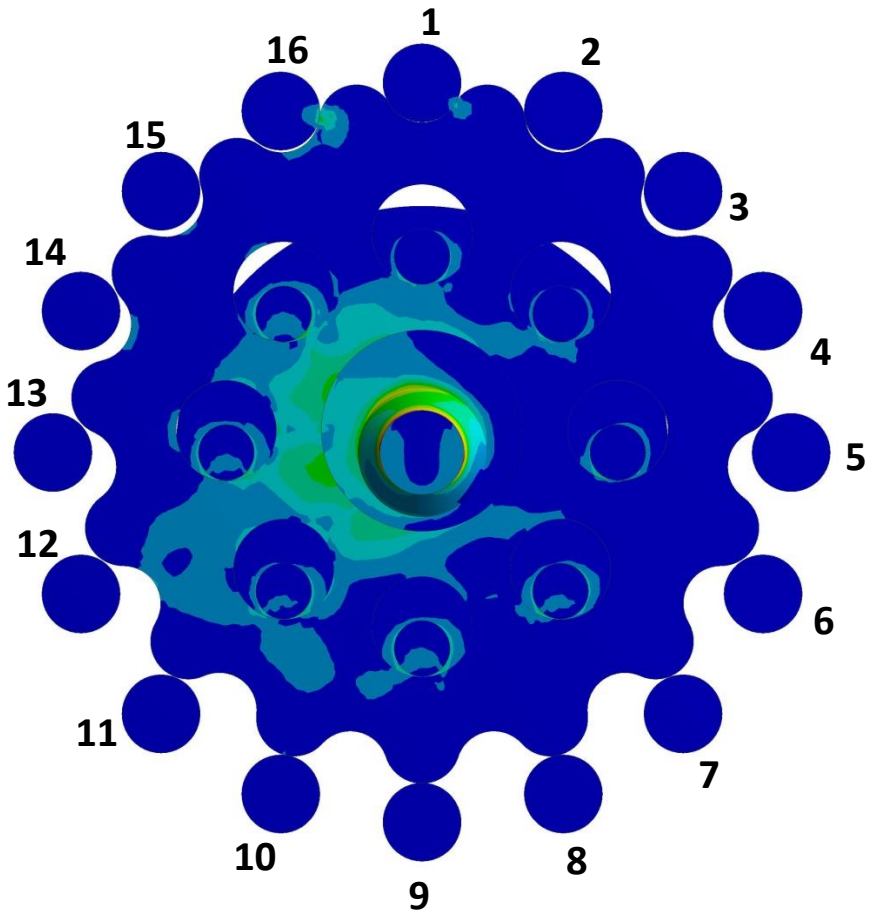

Figure 7.22 – Von Mises stress distribution at t=5.9 s among the cycloidal system subjected to applied torque at the eccentric cam and reaction torque at the output shaft.

This study mainly focuses on the stress distribution that occurs at the interface between the mating surfaces. The Von Mises stress state was evaluated on each annulus pin

during the 360° rotation spanned by the eccentric input shaft for the time of the analysis in order to follow the time-varying meshing progress and the related stress variation.

As the main characteristic of cycloidal transmissions is the contact of multiple pins with the cycloidal disk, the evaluation of the stress state for the entire mesh cycle allows to quantify such interaction.

The study of the quasi-static FEA results started with the analysis of the time-varying stress distribution developed at the interface between the cycloidal disk and the annulus pin number 9 in Figure 7.22 for a complete mesh cycle. The time-varying stress distribution plotted in Figure 7.23 shows that pin number 9 is subjected to the maximum stress value at t=3.1 s which corresponds to a 180° rotation angle of the input shaft, when the eccentric cam is pointing towards pin 9. The graph also shows that the first interaction between the pin and the cycloidal disk occurs at t=1.85 s while the last point of contact is placed at t=4.56 s, when the pin and cycloidal disk disengage. Within this time interval, the stress fluctuates and 7 distinct peaks can be recognised. The peaks indicate the engagement and disengagement of the disk with other pins in the proximity of pin 9. As the force is shared between multiple pins in simultaneous contact, the shared force and consequently the generated stress first increases and then decreases almost symmetrically to the peak for t=3s. The first peak occurring at t=2.08 s corresponds to an angle of rotation of the input shaft of 126° for which pin 6 is fully engaged and is carrying the maximum load. After that, at t=2.45 s the second peak and at t=2.81 s the third peak occur. These peaks happen respectively for an angle of 144° and 167°, when pin 7 and then 8 are fully engaged. This trend shows that while the lobe of the eccentric input shaft is approaching the pin under consideration, the load to which the pin is subjected increases. After the instant of maximum stress, the time-varying stress distribution shows a decreasing trend almost symmetrical to the approaching part. In the descending part, pin 9 is still subjected to the stress generated by the contact with the cycloidal wheel as it still participates in sharing the load with other pins. At t=3.55 s, t=3.85 s and t=4.15 s, corresponding angles of the input shaft are 213°, 231° and 249°, while the pins that are carrying the majority of the load are 10, 11 and 12 respectively.

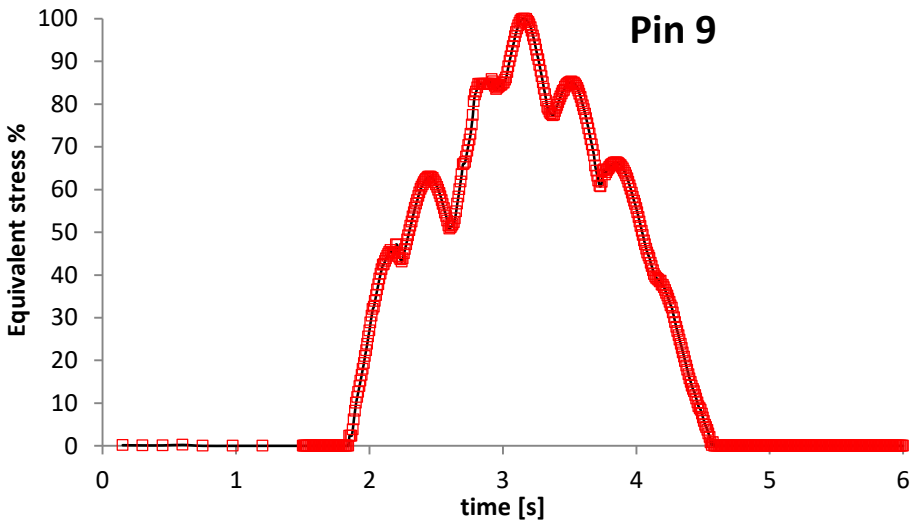

Figure 7.23 – Percentage distribution of the time-varying Equivalent stress state on the annulus pin number 9 for 360° rotation of the input shaft.

The combination of time-varying stress distributions for all pins is shown in Figure 7.24. In this case, as the investigated time frame of 6 s covers the entire rotation of the input shaft and all the pins come into contact with the cycloidal wheel, the stress distribution on the pins is repeated 16 times. No evident differences between the 16 mesh cycles are detected. The time intervals between two successive pins depends on the number of output pins and consequently, as asserted by Equation 7.23, on the gearing ratio. In Figure 7.24, if a vertical line is traced, then the number of curves encountered is equal to the number of pins in simultaneous contact at the time of interest.

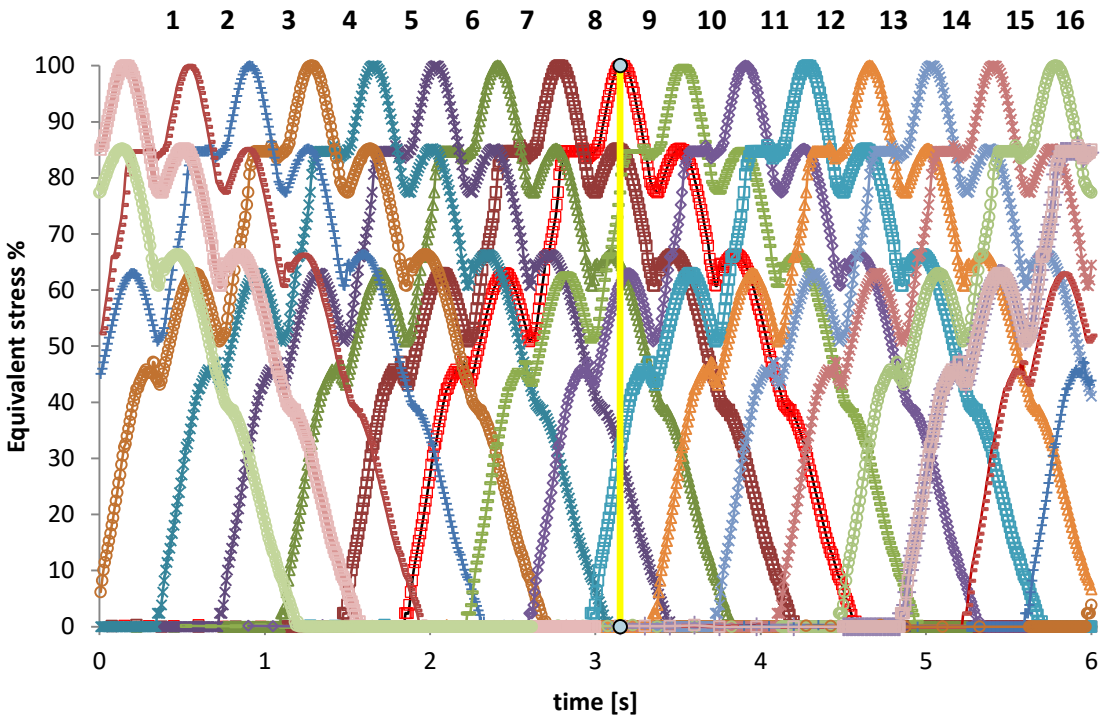

Figure 7.24 – Percentage distribution of the time-varying Equivalent stress for the 16 annulus pins for 360° rotation of the input shaft.

As already mentioned above in this paragraph, because of the interaction between multiple pins and multiple lobes of the cycloidal disk at the same time, the total transmitted force is distributed at each instant over a number of contacts. The effect of such distribution is shown in Figure 7.25 in which, at t=3.1 s, the total force is simultaneously shared between 7 pins, from pin n° 7 to pin n° 12, resulting into a convenient loading conditions as no components in the system are loaded with 100% of the applied force. From Figure 7.25 it can be seen that pin 9 is loaded with a 20.5% of the entire shared force while the pins in the proximity are subjected to lower values, down to 9% for pin 6 and 8% for pin 12. The considerable number of component that share simultaneously the load is a characteristic feature of cycloidal gear trains that determines their high power density and advantageous power to weight ratio compared to their direct competitor, the epicyclic transmission.

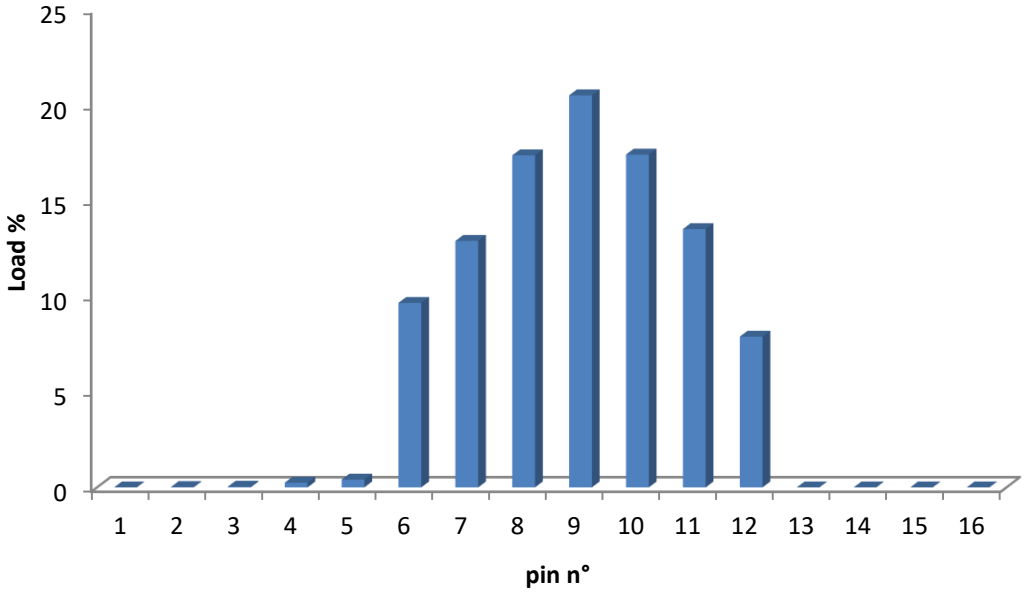

Figure 7.25 –Percentage distribution of the total load simultaneously shared between multiple annulus pins.

7.4 Conclusion

This chapter presented the entire process of designing a cycloidal transmission from the preliminary geometrical calculations, to the manufacturing stage. The design process included the definition of the epicycloidal profile, from theoretical to the actual working profile of cycloidal disks. The parametric equation of the cycloidal profile was determined as function of basic parameters of the gearing system and allowed defining the appropriate geometry for the required characteristics. From the definition of the cycloidal disk, the appropriate annulus and the input shaft geometries were determined.

Once the profile of the cycloidal disk and the geometry of the mating parts were known, a prototype system was manufactured at Norbar Torque Tools Ltd. Considerations on the most suitable manufacturing process, applied tolerances and materials were also made.

A simplified version of the model was used to perform a quasi-static 3D FE study to determine the amount of load shared between the annulus pins and the actual stress distribution at the cycloidal disk/annulus pins interface. The outcome, due to the limited computational resources, is not considered accurate in terms of absolute value of

shared loads and generated stresses. Therefore, the time-varying stress distribution found has been analysed in terms of percentage of the maximum value. The results have shown that for an entire mesh cycle corresponding to 360° rotation of the input shaft, each pin is loaded 7 times. The time-varying stress occurring on the annulus pin 9 has shown 7 peaks of stress. The stress distribution follows an increasing-decreasing trend, symmetric to the maximum value which occurs when the eccentric cam is oriented in the direction of the considered pin. The transmission force was shared simultaneously among 7 over the total of 16 pins. The maximum force applied on a single pin is only the 20% of the total force, while the remaining 80% is shared between 6 other pins in the immediate proximity.

In general, the approach used has been shown to be appropriate for the design of a cycloidal transmission. Further investigation is needed to establish the magnitude of the generated stress and to determine the maximum performance of the transmission. Experimental testing is also necessary to validate the numerical approach.

8 Conclusions and future research

The thesis focuses on the improvement of mechanical characteristics of geared mechanical transmission systems. As Norbar Torque Tools Ltd. bases its business on the production of hand tools torque multipliers for a vast range of industrial applications, the aim was to improve the characteristics of such systems in order to achieve an advantageous power to weight ratio that would increase the competitiveness of their products on the market.
An alternative solution to the epicyclic systems for the use in torque multipliers was attempted with the design and a preliminary analysis of a cycloidal transmission.

8.1 General conclusion

This thesis presented the application of a validated numerical approach for predicting the mechanical characteristics of spur gears in mesh for various combinations of profile geometrical parameters. The numerical model was able to analyse the entire mesh cycle providing detailed information of the variation of stress as consequence of the change in contact status.

Various gear tooth profiles were investigated and compared to a standardised design. Non-standard gear profiles have also worked with epicyclic transmissions showing an average stress state reduction of 11% for both contact and bending stress conditions. The same approach was used for the analysis of epicyclic gear trains. The baseline consists of a standardised profile in accordance with the ISO 6336 Profile B which is almost entirely used in industrial gearing applications. A modification of such geometry has shown room of improvement with an optimum showing 13% of flank contact stress and 28% of bending stress reduction.

The work on tooth profile modifications investigated the effects on the contact and bending stress distribution of various type of profile modifications. The gear geometry was defined by applying the blocking contour technique in which a combination of lines defines a enclosed design space and represents an area of feasible combination of parameters. Each line is the physical representation of a boundary condition or a

physical constraint. The multi-parametric design space considers the simultaneous effect of pressure angle, module, addendum, dedendum, and number of teeth of the mating gears. In accordance with the limitations found, seventeen gear pairs with different geometrical characteristics have been modelled. They include a range of pressure angles from the standard 20° to very high values for symmetric gears of 32°; short, intermediate and long addendum and dedendum; a range of profile shifts spanning from negative to positive values. The contour plot technique, in primis developed by Goldfarb et Al., (1998), has been modified to define non-standard gear profiles. This further development can be considered a novelty in the filed as it has been attempted for the first time and successfully implemented as gear design tool.

The same approach of developing an area of feasible combination of geometrical parameters has been used for the determination of gears for epicyclic transmission systems. For this case, the design procedure undertaken consisted in a multiple step process. First, the design space for the two gear in external mesh has been defined; then, the design space for the internal mating gears has been developed and the fundamental relations valid for epicyclic systems have been taken under consideration. This process has resulted into the determination of a design tool for epicyclic transmissions that takes into account geometrical, operational and manufacturing constraints and is able to return any possible combination of geometrical parameter within the defined area. The newly developed methodology was implemented for the design of three planetary systems equivalent in terms of centre distance and number of teeth but differing in the tooth profile geometry. In this part of the research two novelties can be clearly identified: one consists in the definition of a design area for internal mating gears, while the other regards the use of high pressure angles in epicyclic transmissions. In fact, there is no mention in the available literature of symmetric spur gears arranged in epicyclic configurations designed with values of pressure angle above 25°. The current cases under investigation with $\alpha_w \approx 28°$ represent a novelty in the field.

Gear models and systems have been analysed by means of numerical methods based on the software package ANSYS®. A procedure to overcome convergence difficulties due to the high degree of non-linearity of the mating gear system is proposed. Moreover, the effect of contact detection methods, which contribute to the quality of the

achievements, is investigated and an optimal setting for the analysis of mating gears is established. A wide range of FEA problems were solved in order to study the effective stress distribution for a complete mesh cycle of a number of gear geometries characterised by alteration of pressure angles, profile shift coefficients, addendum and dedendum factors. The numerical results have shown that the working pressure angle plays a crucial role in the reduction of the contact and bending stress state.

The effect of generating pressure angle α has been found to be the critical parameter to control in order to affect the bending and contact stress distributions. Generally, to higher working pressure angles correspond lower stress states as highlighted by the analysis results. In particular, a linear reduction of contact stress has been found as consequence of an increase in pressure angle from a maximum of 403 MPa for α=20°, to a minimum for α=32° of 370.37 MPa which, in percentage terms, corresponds to a substantial 13% reduction of the stress acting on the tooth flank. The same effect is seen when the profile shift and its relation with the working pressure angle is studied. For the range of profile shifts used, α_w varies from 19.1° for x=-0.2, to 23.3° for x=0.5. A comparison between the standard profile with x=0 and the two extremes considered led to an increase of contact stress of 3% when the negative modification (x=-0.2) is applied and a reduction of 7.5% when x=+0.5.

The quasi-static FE method was also used to evaluate the generated root bending stress for the same range of profile modifications as above. In this case an asymmetric concave trend has been determined with a maximum, again for α=20°, of 42.35 MPa and a minimum, for α=28°, of 32.66° MPa resulting in a percentage root bending stress reduction of 13.9%. The evaluated stress for α=32° is 32.66 MPa.

Further analyses on the tooth profile modification include the effect of addendum and dedendum length on the occurring stress state and the duration of the high stress stage. While dedendum has not shown any influence on the generated contact stress, a reduced addendum h_a=0.5 implies a contact stress of 558 MPa which is 22% higher compared to the standard h_a=1 (433.61 MPa). On the other hand, dedendum length has an effect on the root bending stress and in particular, increasing the dedendum leads to an increase from 42,35 MPa for the standard h_f=1.25 to 51,75 MPa when h_f=1.

High pressure angles gears were also used for the generation of planetary gear trains with the end to increase the load carrying capacity. 3D models were analysed by means of quasi-static Finite Element Model and numerical contact and bending stresses compared to analytical results obtained by the application of the ISO 6336 standard. As result, the designs involving non-standard parameters have shown improvements in the load carrying capacity as both contact and bending stress were reduced if compared to the standard configuration with 20° reference pressure angle. This study has shown again that the working pressure angle is the critical parameter that influences the contact and bending stress state. More in detail, it has shown that both methods to increase $\alpha_{w,}$ either by modifying the profile pressure angle or by changing the profile shift, are effective and lead to a stress reduction. The standard of the three models, with α=20°, has seen a maximum tooth flank contact stress at the sun/planet interface of 501 MPa, about 18% higher compared to the other two cases investigated with equivalent $\alpha_w \approx 28°$. An even more pronunced stress reduction occurs with regards to the root bending stress on the sun gear that drops from 58 MPa to 48 MPa by changing α_w from 20° to 28°. A drop of 41% of root bending stress also occurs for the same geometrical configurations on the planet gear while a 23% reduction is seen at the tooth root of the internal gear. As a consequence of the global reduction of the stress state acting on the tooth profile the load carrying capacity of such gears results increased and permits to achieve a mechanical advantage for the entire transmission system.

For validation and comparison purposes, for each geometrical configuration analysed, equivalent contact and bending stresses have been estimated by means of the ISO standard 6336 method B (ISO 6336 2006). The result of such comparison has shown that current standards are not well suited to the application and analysis of High Pressure angle gears. On average, a difference of 7% can be appreciated between numerical and analytical methods, with values calculated by means of ISO 6336-B being generally more conservative than numerical results.

The parametric study gives clear guidance on how to enhance the load carrying capacity of a gear pair through the variation of what are often considered standard parameters

and can be considered a suitable suggestion for the design of planetary systems for enhanced torque carrying capacity and physical packaging volume reduction.

In order to give a valid alternative to epicyclic systems, cycloidal transmissions have been studied. Given the fact that no design standards are available for this class of devices, the profile geometry has been derived and implemented in order to create the physical model of the cycloidal transmission. A full scale prototype was manufactured at Norbar Torque Tools ltd and a simplified model was used to perform a quasi-static 3D Finite Element study. The outcome, consisting in the time-varying stress distribution, has shown that for an entire mesh cycle corresponding to 360° of the input shaft rotation, each pin is loaded 7 times and subjected to 7 peaks of stress across the entire mesh cycle. Each pin carries a maximum 20% of the total applied force while the remaining 80% is shared between 6 other pins in the immediate proximity. In general, the followed approach has shown to be appropriate for the design of a cycloidal transmission. Although it is not possible to extrapolate absolute values of stress from the performed analyses, general considerations can be done with respect to the improvements given by the cycloidal system compared to a planetary system. As seen, in a 16-pins cycloidal transmission, the load is shared between 7 pins allowing a consistent repartition of the generated stress. A possible analogy is with the number of planets in an epicyclic transmission through which the load is simultaneously shared. However, the number of planets is usually in a range between 3 and 5 making the number of load sharing positions modest compared to cycloidal systems where the higher the transmission ratio the higher the number of pins and so the entity of load distribution.

Further investigations are needed in order to establish the magnitude of the generated stress and determine the maximum performance of the transmission.

8.2 Future Work

The following points summarise the areas that, in the light of this thesis, necessitate of further research.

- Definition of a 3D domain of existence by including the variation of a third variable. This would generate a volume of feasible values of geometrical parameters within which any combination fulfils all the imposed boundaries and constraints.
- The point above necessitate of a further addition consisting of iso-performance lines in order to allow the user to predict the working performance of a given geometrical configuration. This would determine a performance based domain of existence which allows the designer to predict performance for any of the possible combinations.
- Also for the case of cycloidal transmission the definition of a design space would simplify the design process. Limiting conditions of eccentricity and annulus pins radii should be determined and used as boundaries of a dominium of feasible combinations of geometrical design parameters.
- Further numerical method investigation and study should be conducted on full-scale 3D models in order to evaluate the stress state along the face width without making the simplistic assumption of plane-stress state.
- Further Finite Element analysis should be conducted under dynamic loading conditions including the inertial effect that would reduce the amount of approximation introduced with the quasi-static analysis.
- Further numerical analysis should be conducted for the study of cycloidal gear trains. An appropriate 3D mesh is required for the evaluation of stresses occurring on the cycloidal disk lobes and on the annulus pins.
- Experimental testing is necessary and should be carried out in order to provide further validation of the outcome of the study of high pressure angle configurations.
- Further experimental testing should be carried out on non-standards epicyclic systems in order to evaluate the failure mechanisms due to higher pressure angles configurations.
- Further testing of cycloidal gear train at low-speed high-torque conditions should be carried out for the evaluation of the maximum transmittable torque. The evaluation of the stress distribution on the cycloidal disk and annulus pins

by means of strain gauges would help to validate numerical results which in this case result difficult to compare given the absence of rating standards and established calculation methods for this category of devices.

Appendix A: Contour plot generator for external mating gears

```
clear all
close all
clc


m=1;     %module
z1=16;   %pinion
z2=28;   %gear


alpha_degree=20;   %reference pressure angle
alph=alpha_degree/180*pi;

ha1_c=1; %pinion addendum factor
ha2_c=1; %gear addendum factor

hau=ha1_c;   %pinion producing cutter dedendum factor
had=1;       %pinion producing cutter addendum factor
hl=hau+had; %heigth factor of the rectilinear sector of pinion
producing cutter

% working pressure angle
al_deg=alpha_degree;
al_deg1=28.15;
al_deg2=28.48;

% working centre distance
aw=22;
aw1=22.74;
% aw2=21.02;

n=240;
xx1=linspace(3,-3,n);
xx2=linspace(3,-3,n);
[X1,X2]=meshgrid(xx1,xx2);

for i=1:n
    for j=1:n
        i;
        j;
        x1=xx1(j);
        x2=xx2(i);
        Alphaw(i,j)=inv_alpha2(x1,x2,z1,z2,alph);
    end
end



db1=m.*z1.*cos(alph);  %base diameter pinion
db2=m.*z2.*cos(alph);  %base diameter gear

y=(z1+z2)./2.*(cos(alph)./cos(Alphaw)-1); %centre distance
modification coefficient
```

```
ha1=(ha1_c+y-X2).*m;   %addendum pinion
ha2=(ha2_c+y-X1).*m;   %addendum gear


da1=m.*z1+2.*ha1;      %tip diameter pinion
da2=m.*z2+2.*ha2;      %tip diameter gear

a_w=(((z1+z2)/2)+y).*m; %working centre distance



% atest=(((z1+z2)/2)+((z1+z2)./2.*(cos(alpha)./cos(20/(180*pi))-
1))).*m

%%%%%%%%%%%%%%%%%%%%%%%%%%%%%%%%%%%%%%%%%%%%%%%%%%%%%%%%%%%%%%%%%%%%%%%
%%%%%%%%%%%%%%%%%%%%%%%%%%%%%%%%%%%%%%%%%%%%%%%%%%%%%%%%%%%%%%%%%%%%%%%

Q1=db1./da1;
Q1(Q1>1 | Q1<-1)=nan;
Q2=db2./da2;
Q2(Q2>1 | Q2<-1)=nan;
alpha_a1=acos(Q1);  %pinion tooth profile angle at the tip diameter
alpha_a2=acos(Q2);  %gear tooth profile angle at the tip diameter

inv_alpha=tan(alph)-alph;          %inverse involute functions
inv_alpha_a1=tan(alpha_a1)-alpha_a1;
inv_alpha_a2=tan(alpha_a2)-alpha_a2;
inv_alphaw=tan(Alphaw)-Alphaw;
%%%%%%%%%%%%%%%%%%%%%%%%%%%%%%%%%%%%%%%%%%%%%%%%%%%%%%%%%%%%%%%%%%%%%%%
%%%%%%%%%%%

%%%%%%%%%%%%%%%%%%%% working pressure angle

Alpha_deg=Alphaw*(180/pi);

figure(1)
contour (X1,X2, Alpha_deg, [al_deg al_deg],'r','ShowText',
'on','DisplayName','\alpha_w [°]');
hold on

% title('area of feasible combinations');
set(gca,'fontweight','bold','fontsize',10);
xlabel('x_1','fontweight','bold','fontsize',20);
ylabel('x_2','fontweight','bold','fontsize',20);
set(get(gca,'ylabel'),'rotation',0)

%%%%%%%%%%%%%%%%%% working centre distance


contour (X1,X2, a_w, [aw aw],'g','ShowText','on','DisplayName','a_w');
hold on

%%%%%%%%%%%%%%%%%%%%%%%%%%%%%%%%%%%%%%%%%%%%%%%%%%%%%%%%%%%%%%%%%%%%%%%
%%%%%%%%%%%

%%%%%%%%%%%%%%%%% contact ratio
```

```
eps_a=1;
eps_a1=1.2;
eps_a2=1.4;

%constant value of contact ratio

CR=1./(2.*pi).*(z1.*tan(alpha_a1)+z2.*tan(alpha_a2)-
(z1+z2).*tan(Alphaw));

contour(X1,X2,CR,[eps_a
eps_a],'b','ShowText','on','DisplayName','\epsilon');
hold on

%%%%%%%%%%%%%%%%%%%%%%%%%%%%%%%%%%%%%%%%%%%%%%%%%%%%%%%%%%%%%%%%%%%%%%%%%%%%%%%%
%%%%%%%%%%

%condition of non undercutting


x1_undercut=(hl-hau)-(1/2).*z1.*sin(alph)^2
x2_undercut=ha2_c-(1/2).*z2.*sin(alph)^2;

contour(X1,X2,X1,[x1_undercut
x1_undercut],'ShowText','on','DisplayName','x_1 min');
hold on
contour(X1,X2,X2,[x2_undercut
x2_undercut],'ShowText','on','DisplayName','x_2 min');
hold on

%%%%%%%%%%%%%%%%%%%%%%%%%%%%%%%%%%%%%%%%%%%%%%%%%%%%%%%%%%%%%%%%%%%%%%%%%%%%%%%%
%%%%%%%%%%

%Isograms of interference

INT_p=-z2.*cos(alph)*tan(alpha_a2)+(z1+z2)*cos(alph)*tan(Alphaw)-
z1*sin(alph)+2*(((hl-hau)-X1))/sin(alph);

INT_g=-z1.*cos(alph)*tan(alpha_a1)+(z1+z2)*cos(alph)*tan(Alphaw)-
z2*sin(alph)+2*((ha2_c-X2))/sin(alph);

contour(X1,X2,INT_p,[0 0],'c','ShowText','on','DisplayName','int_1');
hold on
% contour(X1,X2,INT_p,[0.3 0.3],'ShowText', 'on');
% hold on
contour(X1,X2,INT_g,[0 0],'m','ShowText','on','DisplayName','int_2');
hold on
% contour(X1,X2,INT_g,[0.3 0.3],'ShowText', 'on');
% hold on
%%%%%%%%%%%%%%%%%%%%%%%%%%%%%%%%%%%%%%%%%%%%%%%%%%%%%%%%%%%%%%%%%%%%%%%%%%%%%%%%
%%%%%%%%%%

% tooth thickness

Sa1=0.2;
Sa2=0.2;
Sa11=0;
Sa22=0;
Sa111=0.4;
```

```
Sa222=0.4;

TT_p=da1.*((pi./(2*z1))+((2*X1/z1)*tan(alph))+inv_alpha-inv_alpha_a1);

TT_g=da2.*((pi./(2*z2))+((2*X2/z2)*tan(alph))+inv_alpha-inv_alpha_a2);


contour(X1,X2,TT_p,[Sa1
Sa1],'y','ShowText','on','DisplayName','s_a_1');
hold on
contour(X1,X2,TT_g,[Sa2 Sa2],'Color',[1 0.5
0],'ShowText','on','DisplayName','s_a_2');
hold on
%%%%%%%%%%%%%%%%%%%%%%%%%%%%%%%%%%%%%%%%%%%%%%%%%%%%%%%%%%%%%%%%%%%%%%%%%%%%%%%%
%%%%%%%%%%
legend('\alpha_w [°]','a_w [mm]','\epsilon','x_1 min','x_2
min','int_1','int_2','s_a_1','s_a_2','Location','southwest');
% legend('s_a_1','s_a_2','Location','southwest');
%%%%%%%%%%%%%%%%%%%%%%%%%%%%%%%%%%%%%%%%%%%%%%%%%%%%%%%%%%%%%%%%%%%%%%%%%%%%%%%%
%%%%%%%%%%

x1_xaxis=0;
x2_yaxis=0;

contour(X1,X2,X1,[x1_xaxis x1_xaxis],'k');
hold on
contour(X1,X2,X2,[x2_yaxis x2_yaxis],'k');
hold on
contour (X1,X2, Alpha_deg, [al_deg1 al_deg1],'r','ShowText',
'on','DisplayName','\alpha_w [°]');
hold on
% contour (X1,X2, Alpha_deg, [al_deg2 al_deg2],'r','ShowText',
'on','DisplayName','\alpha_w [°]');
hold on
contour (X1,X2, a_w, [aw1 aw1],'g','ShowText',
'on','DisplayName','a_w');
hold on
% contour (X1,X2, a_w, [aw2 aw2],'g','ShowText',
'on','DisplayName','a_w');
hold on
contour(X1,X2,CR,[eps_a1
eps_a1],'b','ShowText','on','DisplayName','\epsilon');
hold on
```

Where the MATLAB function inv_alpha2 calculates the working pressure angle for external mating gears.

```
function [alphaw]=inv_alpha2(x1,x2,z1,z2,alpha)

TOLL=1e-3;
invalphaw=2*(x1+x2)/(z1+z2)*tan(alpha)+tan(alpha)-alpha;
alphaw=1;
```

```
for i=1:1000
    alphaw_new=alphaw+(invalphaw-tan(alphaw)+alphaw)/tan(alphaw^2);
    if abs(alphaw_new-alphaw)<TOLL
        break;
    end
    alphaw=alphaw_new;
end

if i==1000
    alphaw=nan;
end
    alphaw(find(alphaw<0))=nan;
```

Appendix B: Contour plot generator for internal mating gears

```
clear all
close all
clc

m=0.965;     %module
z1=28;
z2=71;
i=z2/z1; %gearing ratio
alpha_degree=24;   %reference pressure angle
alpha=alpha_degree/180*pi;
ha1_c=1; %rack addendum coefficient
ha2_c=1;
hf2_c=1.25;

n=241;
xx1=linspace(-3,3,n);
xx2=linspace(-3,3,n);
[X1,X2]=meshgrid(xx1,xx2);

for i=1:n
    for j=1:n
        i;
        j;
        x1=xx1(j);
        x2=xx2(i);
        Alphaw(i,j)=inv_alpha2_int(x1,x2,z1,z2,alpha);
    end
end


db1=m.*z1.*cos(alpha);  %base diameter pinion
db2=m.*z2.*cos(alpha);  %base diameter gear
y=(z2-z1)./2.*(cos(alpha)-cos(Alphaw))./cos(Alphaw); %centre distance
modification coefficient
ha1=(ha1_c+X1).*m;   %addendum pinion
ha2=(ha2_c-X2).*m;   %addendum gear
hr2=(hf2_c+X2).*m;
da1=m.*z1+2.*ha1;    %tip diameter pinion
da2=m.*z2-2.*ha2;    %tip diameter gear
dr2=(z2+(2.*(hf2_c+X2)).*m);
a_w=(((z2-z1)/2)+y).*m; %working centre distance

%%%%%%%%%%%%%%%%%%%%%%%%%%%%%%%%%%%%%%%%%%%%%%%%%%%%%%%%%%%%%%%%%%%%%%%%

Q1=db1./da1;
Q1(Q1>1 | Q1<-1)=nan;
Q2=db2./da2;
Q2(Q2>1 | Q2<-1)=nan;
alpha_a1=acos(Q1);  %pinion tooth profile angle at the tip diameter
alpha_a2=acos(Q2);  %gear tooth profile angle at the tip diameter

%%%%%%%%%%%%%%%%%%%%%%%%%%%%%%%%%%%%%%%%%%%%%%%%%%%%%%%%%%%%%%%%%%%%%%%%

L1=db2./dr2;
L1(L1>1 | L1<-1)=nan;
```

```
alpha_a3=acos(L1);

%%%%%%%%%%%%%%%%%%%%%%%%%%%%%%%%%%%%%%%%%%%%%%%%%%%%%%%%%%%%%%%%%%%%%%%

inv_alpha=tan(alpha)-alpha;          %inverse involute functions
inv_alpha_a1=tan(alpha_a1)-alpha_a1;
inv_alpha_a2=tan(alpha_a2)-alpha_a2;
inv_alphaw=tan(Alphaw)-Alphaw;
inv_alpha_a3=tan(alpha_a3)-alpha_a3;

%%%%%%%%%%%%%%%%%%%%%%%%%%%%%%%%%%%%%%%%%%%%%%%%%%%%%%%%%%%%%%%%%%%%%%%
%%%%%%%%%%%
figure(1)


% working pressure angle

al_deg=alpha_degree;
al_deg1=30.51;
Alpha_deg=Alphaw*(180/pi);

contour (X1,X2, Alpha_deg, [al_deg al_deg],'r','ShowText',
'on','DisplayName','Alpha_deg');
hold on

set(gca,'fontweight','bold','fontsize',10);
xlabel('x_e','fontweight','bold','fontsize',20);
ylabel('x_i','fontweight','bold','fontsize',20);
set(get(gca,'ylabel'),'rotation',0)

% working centre distance

aw1=21.50;
aw2=22;
aw3=20.74;

contour (X1,X2, a_w, [aw1
aw1],'g','ShowText','on','DisplayName','a_w');
hold on



%%%%%%%%%%%%%%%%%%%%%%%%%%%%%%%%%%%%%%%%%%%%%%%%%%%%%%%%%%%%%%%%%%%%%%%
%%%%%%%%%%

%contact ratio

eps_a=1.0;    %constant value of contact ratio
eps_a1=1.2;
CR=1./(2.*pi).*(z1.*tan(alpha_a1)-z2.*tan(alpha_a2)+(z2-
z1).*tan(Alphaw));

contour(X1,X2,CR,[eps_a
eps_a],'b','ShowText','on','DisplayName','eps');
hold on
%%%%%%%%%%%%%%%%%%%%%%%%%%%%%%%%%%%%%%%%%%%%%%%%%%%%%%%%%%%%%%%%%%%%%%%
```

```
%condition of non undercutting

x1_undercut=ha1_c-(1/2).*z1.*sin(alpha)^2;

contour(X1,X2,X1,[x1_undercut
x1_undercut],'ShowText','on','DisplayName','und_2');
hold on

%%%%%%%%%%%%%%%%%%%%%%%%%%%%%%%%%%%%%%%%%%%%%%%%%%%%%%%%%%%%%%%%%%%%%%%%%%%%%%%%
%%%%%%%%%%%

%tooth thickness
% eta=cos(z2*m*cos(alpha)./da2)
Sa1=0.2;
Sa2=0.2;


TT_p=da1.*((pi./(2*z1))+((2*X1/z1)*tan(alpha))+inv_alpha-
inv_alpha_a1);
TT_p(find(TT_p<0))=nan;

TT_r=(dr2.*((pi./(2*z2))+((2*(X2)/z2)*tan(alpha))+inv_alpha-
inv_alpha_a3)).*m;

TT_g=da2.*((pi./(2*z2))-((2*X2/z2)*tan(alpha))-
inv_alpha+inv_alpha_a2);
TT_g(find(TT_g<0))=nan;

M=min(TT_g);
L=min(M)
N=L+0.0000001
contour(X1,X2,TT_p,[Sa1
Sa1],'y','ShowText','on','DisplayName','TT_2');
hold on
contour(X1,X2,TT_r,[Sa2 Sa2],'ShowText','on','DisplayName','TT_r');
hold on
contour(X1,X2,TT_g,[N N],'color',[1 0.5
0],'ShowText','on','DisplayName','TT_3');
hold on

%%%%%%%%%%%%%%%%%%%%%%%%%%%%%%%%%%%%%%%%%%%%%%%%%%%%%%%%%%%%%%%%%%%%%%%%%%%%%%%%
%%%%%%%%%%%

% % Isograms of interference
Int_1=(z1/z2)-1+tan(alpha_a2)./tan(Alphaw);

contour(X1,X2,Int_1,[0 0],'c','ShowText','on','DisplayName','Int_1');
hold on

k=((da2.^2-da1.^2-4.*a_w.^2)./(4.*a_w.*da1));
k(find(k>1))=nan;
p=acos(k);
teta1=p+inv_alpha_a1-inv_alphaw;

b=(4.*a_w.^2+da2.^2-da1.^2)./(4.*a_w.*da2);
b(find(b>1))=nan;
teta2=acos(b);
```

```
Int_2=(teta1.*(z1./z2)+inv_alphaw-inv_alpha_a2)-teta2;

contour(X1,X2,Int_2,[0 0],'m','ShowText','on','DisplayName','Int_2');
hold on

%%%%%%%%%%%%%%%%%%%%%%%%%%%%%%%%%%%%%%%%%%%%%%%%%%%%%%%%%%%%%%%%%%%%%%%%%%%%%%%%
%%%%%%%%%%%%%%%

legend('\alpha_w [°]','a_w [mm]','\epsilon','x_e
min','s_a_e','s_a_i','int_1','int_2','Location','southeast');

contour (X1,X2, a_w, [aw2
aw2],'g','ShowText','on','DisplayName','a_w');
hold on
contour (X1,X2, a_w, [aw3
aw3],'g','ShowText','on','DisplayName','a_w');
hold on
contour(X1,X2,CR,[eps_a1
eps_a1],'b','ShowText','on','DisplayName','CR');
hold on
contour (X1,X2, Alpha_deg, [al_deg1 al_deg1],'r','ShowText',
'on','DisplayName','Alpha_[deg]');
hold on

x1_xaxis=0;
x2_yaxis=0;

contour(X1,X2,X1,[x1_xaxis x1_xaxis],'k')%,'DisplayName','X1');
hold on
contour(X1,X2,X2,[x2_yaxis x2_yaxis],'k')%,'DisplayName','X2');
hold on
```

Where the the MATLAB function inv_alpha2_int calculates the working pressure angle for internal mating gears:

```
function [alphaw]=inv_alpha2_int(x1,x2,z1,z2,alpha)

TOLL=1e-3;
invalphaw=2*(x2-x1)/(z2-z1)*tan(alpha)+tan(alpha)-alpha;
alphaw=1;

for i=1:1000
    alphaw_new=alphaw+(invalphaw-tan(alphaw)+alphaw)/tan(alphaw^2);
    if abs(alphaw_new-alphaw)<TOLL
        break;
    end
    alphaw=alphaw_new;
end

if i==1000
    alphaw=nan;
end

alphaw(find(alphaw<0))=nan;
```

Appendix C: Cycloidal drive, technical drawings

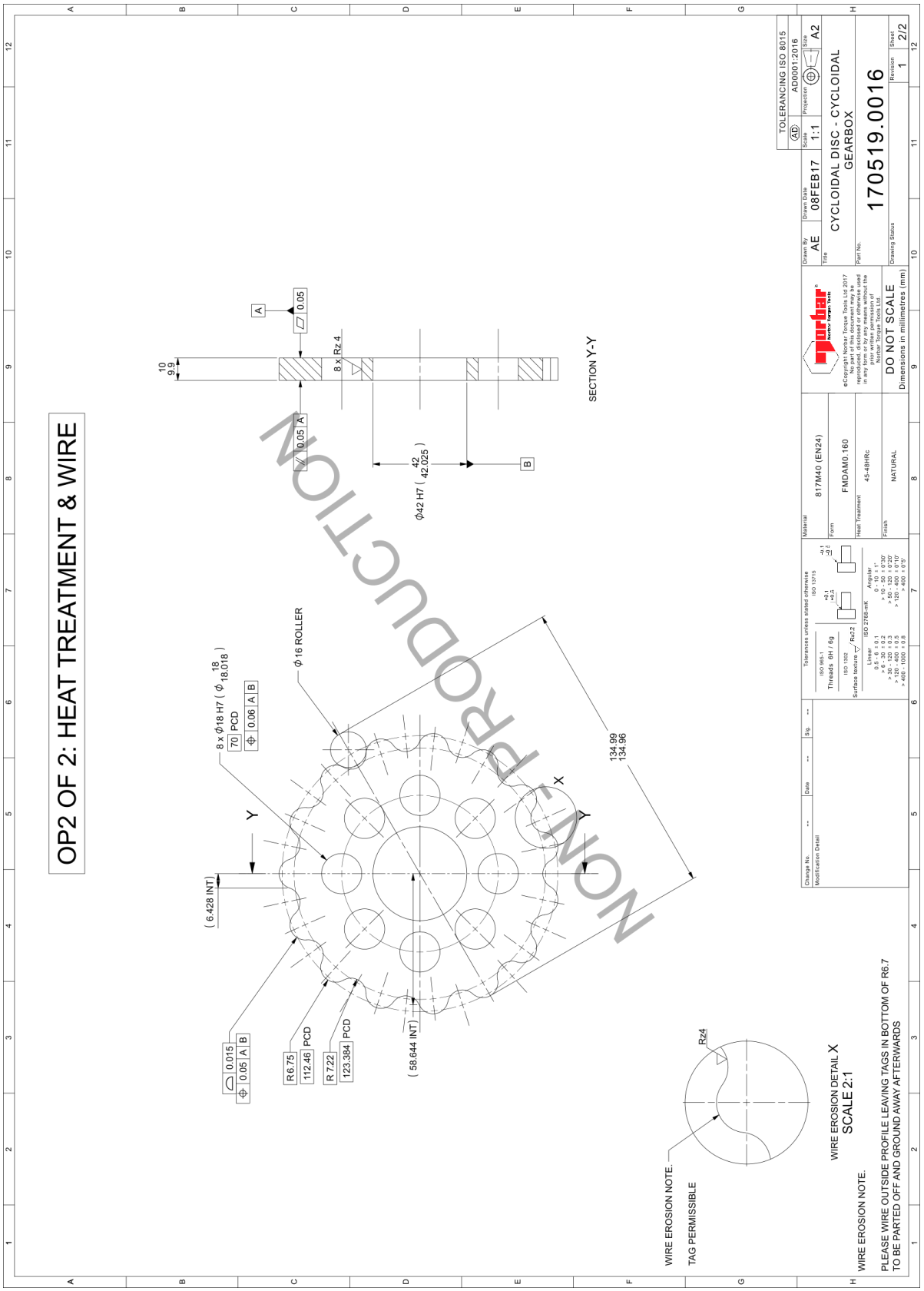

OP1 OF 2: TURN AND MILL SQUARE

SCALE 1:2

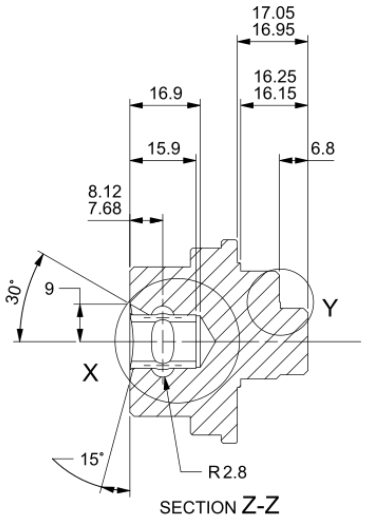

SECTION Z-Z

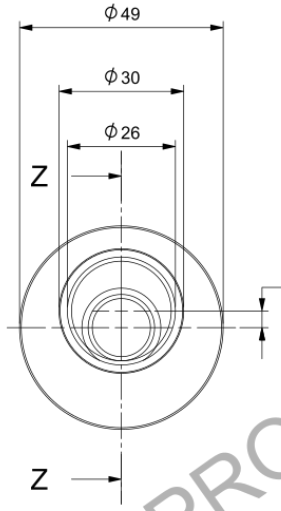

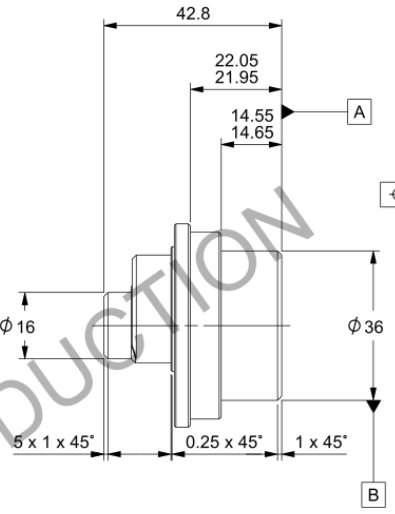

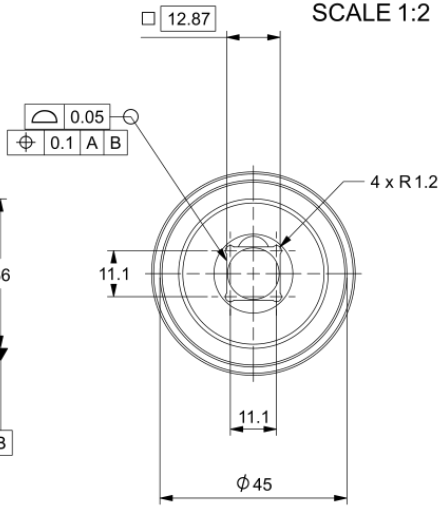

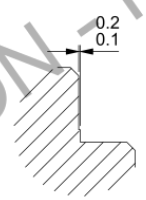

DETAIL Y
SCALE 2:1

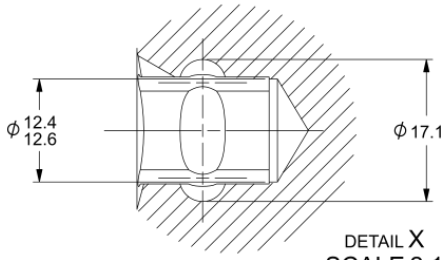

DETAIL X
SCALE 2:1

Change No. --	Date --	Sig. --
Modification Detail		

Tolerances unless stated otherwise

ISO 965-1
Threads 6H / 6g

ISO 1302
Surface texture Ra1.2

ISO 13715

ISO 2768-mK

Linear	Angular
0.5 - 6 ± 0.1	0 - 10 ± 1°
> 6 - 30 ± 0.2	> 10 - 50 ± 0°30'
> 30 - 120 ± 0.3	> 50 - 120 ± 0°20'
> 120 - 400 ± 0.5	> 120 - 400 ± 0°10'
> 400 - 1000 ± 0.8	> 400 ± 0°5'

Material: 817M40 (EN24)

Form: FMDAM0.055

Heat Treatment: 45-48HRc

Finish: HOT CHEMICAL BLACK

DO NOT SCALE
Dimensions in millimetres (mm)

TOLERANCING ISO 8015
AD AD0001:2016

Drawn By	Drawn Date	Scale	Projection	Size
AE	03FEB17	1:1		A3

Title: ECCENTRIC INPUT SHAFT - CYCLOIDAL GEARBOX

Part No.: 170519.0015

Drawing Status

Revision	Sheet
1	1/2

OP1 OF 1: WIRE ERODE HOLES

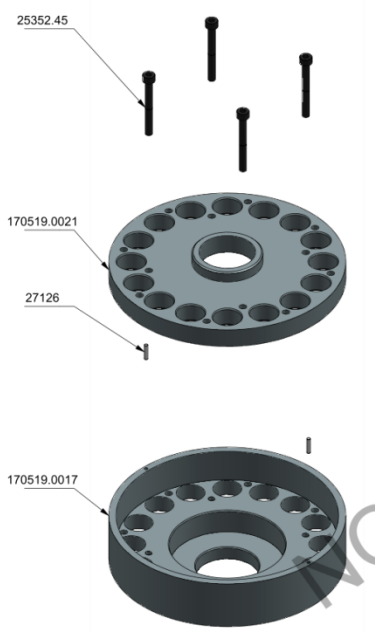

SCALE 1:2

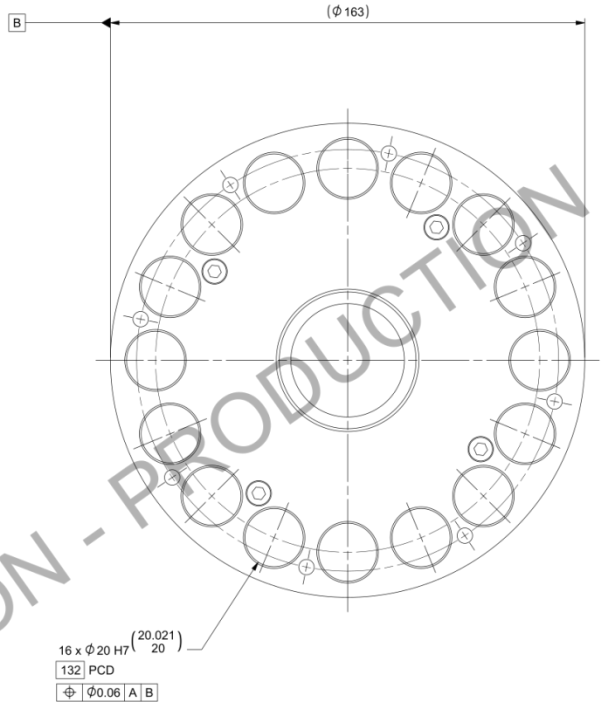

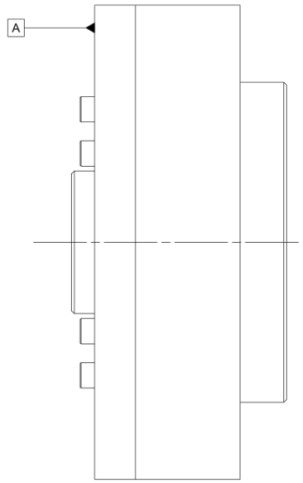

Part No	Qty	Description
170519.0017	1	ANNULUS - CYCLOIDAL GEARBOX
170519.0021	1	ANNULUS TOP PLATE - CYCLOIDAL GEARBOX
25352.45	4	SHCS M5 x 45 - 12.9 TO ISO 4762
27126	2	NEEDLE ROLLER NRA 2.5 DIA X 11.8 LG G2

Change No. -- Date -- Sig. --
Modification Detail

Tolerances unless stated otherwise
ISO 965-1 Threads 6H / 6g
ISO 1302 Surface texture Ra3.2
ISO 13715
ISO 2768-mK

Linear	Angular
0.5 - 6 ± 0.1	0 - 10 ± 1°
> 6 - 30 ± 0.2	> 10 - 50 ± 0°30'
> 30 - 120 ± 0.3	> 50 - 120 ± 0°20'
> 120 - 400 ± 0.5	> 120 - 400 ± 0°10'
> 400 - 1000 ± 0.8	> 400 ± 0°5'

Material: VARIOUS
Form: ASSEMBLY
Heat Treatment: N/A
Finish: NATURAL

DO NOT SCALE
Dimensions in millimetres (mm)

TOLERANCING ISO 8015
AD0001:2016

Drawn By	Drawn Date	Scale	Projection	Size
AE	23FEB17	1:1		A2

Title: ANNULUS WIRING ASSEMBLY - CYCLOIDAL GEARBOX

Part No. 170519.0029

Drawing Status	Revision	Sheet
	1	1/1

OP1 OF 1: WIRE ERODE HOLES

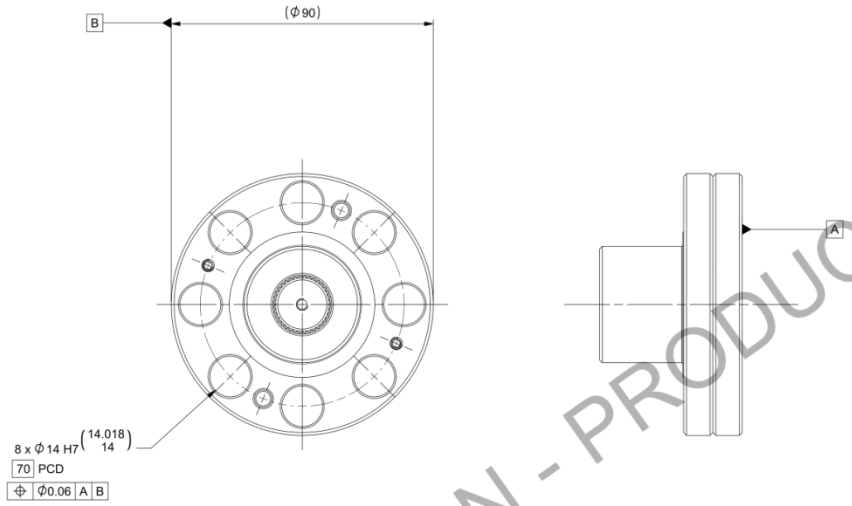

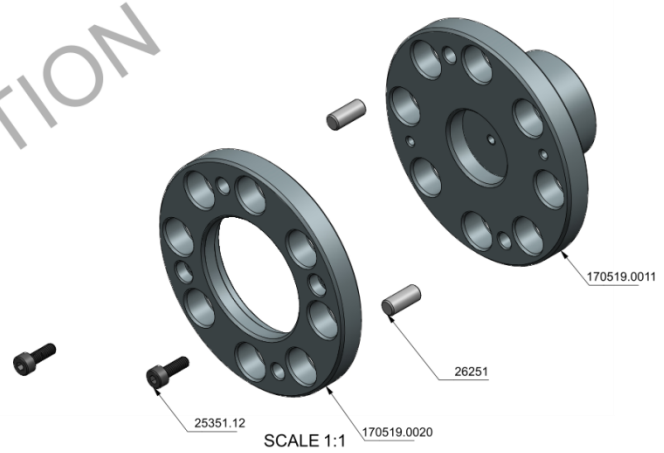

SCALE 1:1

Part No	Qty	Description
170519.0011	1	OUTPUT DRIVE PLATE - CYCLOIDAL GEARBOX
170519.0020	1	INTERMIDIATE OUTPUT SUPPORT PLATE - CYCLOIDAL GEARBOX
25351.12	2	SHCS M4 x 12 - 12.9 TO ISO 4762
26251	2	PIN DOWEL 6 DIA X 14

Change No. -- | Date -- | Sig. --
Modification Detail

Tolerances unless stated otherwise
ISO 965-1 Threads 6H / 6g
ISO 1302 Surface texture Ra3.2
ISO 13715
ISO 2768-mK

Linear	Angular
0.5 - 6 ± 0.1	0 - 10 ± 1°
> 6 - 30 ± 0.2	> 10 - 50 ± 0°30'
> 30 - 120 ± 0.3	> 50 - 120 ± 0°20'
> 120 - 400 ± 0.5	> 120 - 400 ± 0°10'
> 400 - 1000 ± 0.8	> 400 ± 0°5'

Material: VARIOUS
Form: ASSEMBLY
Heat Treatment: N/A
Finish: NATURAL

DO NOT SCALE
Dimensions in millimetres (mm)

TOLERANCING ISO 8015
AD0001:2016

Drawn By	Drawn Date	Scale	Projection	Size
AE	23FEB17	1:1		A2

Title: OUTPUT DRIVE WIRING ASSEMBLY - CYCLOIDAL GEARBOX

Part No. 170519.0028

Drawing Status | Revision 1 | Sheet 1/1

Bibliography

ANSI/AGMA 6123-B06 (2006): "Design Manual for Enclosed Epicyclic Gear Drives. American Gear Manufacturers Association (AGMA)".

Alaci S., Amarandei D., (2008) Simulation of Gear Rack Generation of Involute Spur Gears", Fascicle of Management and Technological Engineering, Volume VII (XVII).

Alipiev O., (1988): "Geometry and Forming of Epi and Hypo-Cycloidal Toothed Wheels in Modified Cyclo-Transmission" . .

Anon (2014): "A New Approach for Designing Gear Profiles using Closed Complex Equations". *Acta Polytechnica Hungarica* 11(6). Available at: http://www.uni-obuda.hu/journal/Laczik_Zentay_Horvath_52.pdf (accessed 29/04/18).

ANSYS® (2016): "ANSYS® Mechanical Structural Nonlinearities: introduction to contact".

ANSYS® (2016): "*ANSYS® Academic Research Mechanical", Release 16*. .

ANSYS® (2016): "ANSYS® Mechanical Structural Nonlinearities: introduction to contact."

ANSYS 15.0 (2015): "Transient Analyis -Linear and Nonlinear Dynamics - Lecture 9". Ansys Mechanical.

Arafa MH., Megahed MM., (1999): "Evaluation of spur gear mesh compliance using the finite element method". *Proceedings of the Institution of Mechanical Engineers*.

Alipiev O., (2011): "Geometric design of involute spur gear drives with symmetric and asymmetric teeth using the Realized Potential Method". *Mechanism and Machine Theory* 46(1): 10–32.

Alipiev O., Antonov S., Grozeva T., (2013): "Generalized model of undercutting of involute spur gears generated by rack-cutters". *Mechanism and Machine Theory* 64: 39–52.

Amani A, Spitas C., Spitas V., (2017): "Generalised non-dimensional multi-parametric involute spur gear design model considering manufacturability and geometrical compatibility". *Mechanism and Machine Theory* 109: 250–277.

Andrews JD., (1991): "A finite element analysis of bending stresses induced in external and internal involute spur gears". *The Journal of Strain Analysis for Engineering Design* 26(3): 153–163.

ANSI/AGMA 2101/D04 (2016): "Fundamental Rating Factors and Calculation Methods for Involute Spur and Helical Gear Teeth (Metric Edition)". American Gear Manufacturers Association (AGMA).

Archard JF., (1953): "Contact and Rubbing of Flat Surfaces". *Journal of Applied Physics*.

Bonori G., (2005): "Static and Dynamic Modelling of Gear Transmissions". Modena, Italy.

Beard J., Yannitell D., Pennock G., (1992): "The effects of the generating pin size and placement on the curvature and displacement of epitrochoidal gerotors". *Mechanism and Machine Theory* 27(4): 373–389.

Blagojevic M., (2014): "Analysis of Clearances and Deformations at Cycloid Disc". *Machine Design* 6.

Blagojevic M., Marjanovic N., Djordjevic Z., Stojanovic B., Marjanovic V., Vujanac R., Disic A., (2014): "Numerical and Experimental Analysis of the Cycloid Disc Stress State".

Botsiber A., KingstonL., (1956): "Design and performance of cycloid speed reducer". *Machine Design* 65–69.

Braren L., (1928): "Patent US1694031 - Gear Transmission". United States Patent Office.

Braren L., (1932): "Patent US1867492 - Gear Transmission". United States Patent Office.

BS 978 - 2 (1984): "Specification for fine pitch gears - Cycloidal type gears".

Coy JJ., Townsend DP., Zaretsky EV., (1985): "*Gearing"*. National aeronautics and space administration cleveland oh lewis research center.

Conrado E., Davoli P., (2007): "The “True” Bending Stress in Spur Gears".

Dai X., Cooley CG., Parker RG., (2015): "Prediction and Experimental Correlation of Tooth Root Strains in Spur Gear Pairs". ASME, V010T11A012. Available at: http://proceedings.asmedigitalcollection.asme.org/proceeding.aspx?doi=10.1115/DETC2015-47517 (accessed 18/01/18).

Dolan and Broghamer (1942): "A Photoelastic Study of Stresses in Gear Tooth Fillets". University of Illinois.

Dooner D., (2012): "*Kinematic Geometry of Gearing* (2nd edition)". Wiley.

Dudley D., (1969): "*The Evolution of the Gear Art"*. American Gear Manufacturers Association (AGMA).

Fetvaci C., (2012): "Computer Simulation of Involute Tooth Generation". In: Gokcek M (ed) *Mechanical Engineering*. InTech. Available at: *Gear Technology*.

Ferguson R., (1983): "Short Cuts For Analyzing Planetary Gearing". *Machine Design*.

Gavin H., (2016): "Numerical Integration in Structural Dynamics". CEE 541, Duke University.

Gerpen HV., Reece CK., (1989): "Form Diameter of Gears". *Gear Technology*.

Gopinath K and Mayuram M (2016) Gear Failure Lecture. Indian Institute of Technology Madras.

Gurumani R and Shanmugam S (2011) Modeling and contact analysis of crowned spur gear teeth. *Engineering Mechanics* 18(1): 65–78.

Höhn B-R, Stahl K and Gwinner P (2013) Light-weight design for planetary gear transmissions.“. *Gear Technology”, Sept*.

Handschuh RF and Zakrajsek AJ (2010) High pressure angle gears: preliminary testing results.

Handschuh RF and Zakrajsek AJ (2012) High pressure angle gears: comparison to typical gear designs. *NASA/TM* 216251/REV1.

Höhn B-R, Stahl K and Gwinner P (2013a) Light-weight design for planetary gear transmissions.“. *Gear Technology”, Sept*.

http://www.intechopen.com/books/mechanical-engineering/computer-simulation-of-involute-tooth-generation (accessed 29/04/18).

Hwang S-C, Lee J-H, Lee D-H, Han S-H and Lee K-H (2013) Contact stress analysis for a pair of mating gears. *Mathematical and Computer Modelling* 57(1–2): 40–49.

Hwang Y-W and Hsieh C-F (2006) GEOMETRY DESIGN AND ANALYSIS FOR TROCHOIDAL-TYPE SPEED REDUCERS: WITH CONJUGATE ENVELOPES. *Transactions of the Canadian Society for Mechanical Engineering* 30(2): 261–278.

Hwang Y-W and Hsieh C-F (2007) Determination of surface singularities of a cycloidal gear drive with inner meshing. *Mathematical and Computer Modelling* 45(3–4): 340–354.

ISO 6336-1 (2006) Calculation of load capacity of spur and helical gears - Part1: Basic principles, introduction and general influence factors. International Standards Organization (ISO).

ISO 6336-2 (2006) Calculation of load capacity of spur and helical gears - Part2: Calculation of surface durability (pitting). International Standards Organization (ISO).

ISO 6336-5 (2006) Calculation of load capacity of spur and helical gears - Part5: Strenght and quality of materials. International Standards Organization (ISO).

ISO 10825 (1995) Gears - Wear and damage to gear teeth - Terminology. International Standards Organization (ISO).

IS 3756 (2002) Method for Gear Correction - Addndum Modification for External Cylindrical Gears with Parallel Axes. Bureau of Indian Standards.

ISO 53 (1998) Cylindrical gears for general and heavy engineering - Standard basic rack tooth profile. International Standards Organization (ISO).

ISO 54 (1996) Cylindrical gears for general engineering and for heavy engineering - Modules. International Standards Organization (ISO).

ISO 21771 (2007) Cylindrical involute gears and gear pairs - Concepts and geometry. International Standards Organization (ISO).

ISO/TR 4467 (1982) Addendum modification of the teeth of cylindrical gears for speed-reducing and speed-increasing gear pairs. International Standards Organization (ISO).

Jiang YC and Hui WL (2015) Finite Element Analysis of the Dynamic Cintact Stress of Cycloid Gear of RV Reducer. paper presented at the 4th International Conference on Sensors, Measurements and Intelligent materials (ICSMIM 2015). Beijing, China: North China University of Technology.

Juvinall RC and Marshek KM (1983) *Fundamentals of Machine Component Design*. John Wiley and Sons.

Kapelevich A (2013) *Direct Gear Design*. CRC Press, Taylor and Francis Group.

Kapelevich A and Shekhtman Y (2010) Area of Existence of Involute Gears. *Gear Technology*.

Kapelevich AL and Ananiev VM (2011) Gear transmission density maximization. *Gear Technology* (6): 46–52.

Kapelevich A and Kleiss R (2002) direct Gear Design for Spur and Helical Involute Gears.pdf. *Gear Technology*.

Kawalec A, Wiktor J and Ceglarek D (2006a) Comparative Analysis of Tooth-Root Strength Using ISO and AGMA Standards in Spur and Helical Gears With FEM-based Verification. *Journal of Mechanical Design* 128(5): 1141.

Kapelevich A (2016) Analysis and Optimization of Asymmetric Epicyclic Gears. *Gear Solutions*.

Konter A (2000) *Undertake a Contact and Friction Analysis*. NAFEMS Ltd.

KHK (2015) Gear Technical reference. Kohara Gear Industry Co, Ltd.

Kuang JH and Yang YT (1992) An Estimate of Mesh Stiffness and Load Sharing Ratio of a Spur Gear Pair. *6th International Power Transmission and Gearing conference*. USA.

Lepi SM (1998) *Practical guide to finite elements: a solid mechanics approach*. New York: Marcel Dekker.

Lewicki DG and Ballarini R (1997) Effect of Rim Thickness on Gear Crack Propagation Path (119th edition). *Journal of Mechanical Design*.

Lewis W (1893) Investigation of the Strenght of Gear Teeth. Gear Technology.

Lias MR, Sharif Z, Awang M, Jailani A and Warap H (2017) Quasi-static Modelling of Spur Gear Time Varying Strenght Analysis. .

Lisle TJ, Shaw BA and Frazer RC (2017) External spur gear root bending stress: A comparison of ISO 6336:2006, AGMA 2101-D04, ANSYS finite element analysis and strain gauge techniques. *Mechanism and Machine Theory* 111: 1–9.

Litvin FL (1989) Theory of Gearing. NASA Reference Pubblication.

Litvin FL and Feng P-H (1996) Computerized design and generation of cycloidal gearings. *Mechanism and Machine Theory* 31(7): 891–911.

Litvin FL and Fuentes A (2004) *Gear geometry and applied theory*. Cambridge University Press.

Litvin FL and Hsiao CL (1993) Computerized Simulation of Meshing and Contact of Enveloping Gear Tooth Surfaces (102nd edition). *Computer Methods in Applied Mechanics and Engineering*.

Litvin FL and Seol IH (1996) Computerized Determination of Gear Tooth Surface as Envelope to Two Parameters Family of Surfaces (138th edition). *Computer Methods in Applied Mechanics and Engineering*.

Mondkar DP and Powell GH (1977) Finite Element Analysis of Non-Linear Static and Dynamic response. *International Journal for Numerical Methods in Engineering* 11: 499–520.

Litvin FL, Wang AG and Handschuh RF (1998) Computerized determination of singularities and envelopes to families of contact lines on gear tooth surfaces (158th edition). *Computer Methods in Applied Mechanics and Engineering*.

Maitra G (2012) *Handbook of Gear Deisgn* (2nd edition). .

Marimuthu P and Muthuveerappan G (2016) Design of asymmetric normal contact ratio spur gear drive through direct design to enhance the load carrying capacity. *Mechanism and Machine Theory* 95: 22–34.

Miler D, Lončar A, Žeželj D and Domitran Z (2017) Influence of profile shift on the spur gear pair optimization. *Mechanism and Machine Theory* 117: 189–197.

Miller R (2017) Designing Very Strong Gear Teeth by Means of High Pressure Angles. *Gear Technology*.

McVittie D (1998) Calculating Spur and Helical Gear Capacity with ISO 6336. .

Miler D, Lončar A, Žeželj D and Domitran Z (2017) Influence of profile shift on the spur gear pair optimization. *Mechanism and Machine Theory* 117: 189–197.

Moya JL, Machado AS, Goytisolo RA and Becerra AM (2009) The Finite Element Method in the Design Process of Spur Gears. ASME, 529–537. Available at: http://proceedings.asmedigitalcollection.asme.org/proceeding.aspx?articleid=1639092 (accessed 29/04/18).

Marimuthu P and Muthuveerappan G (2016) Design of asymmetric normal contact ratio spur gear drive through direct design to enhance the load carrying capacity. *Mechanism and*

Nabtesco Corporation (2016) Precision Reduction Gear RV Catalogue. Nabtesco Precision Europe GmbH.

Norbar Torque Tools ltd. (2018) Norbar Catalogue 2018 - Multiplier Section.pdf. .

Norbar Torque Tools ltd. (2018b) Norbar Catalogue 2018 - PowerTools Section.pdf. .

Nielsen CV (2013) Modeling of Thermo-Electro-Mechanical Manufacturing Processes. SpringerBriefs in Applied Sciences and Technology.

Niemann (1982) *Machine Elements: Gears* (1st edition). Springer-Varlag.

Novikov A, Paikin A, Dorofeyev V, Ananiev V and Kapelevich A (2008) Application of Gears with Asymmetric Teeth in Turboprop Engine Gearbox. *Gear Technology*.

Olguner S and Filiz IH (2014) A study on the design of asymmetric spur gears in gear pump applications. *International Gear Conference 2014: 26th–28th August 2014, Lyon*. Elsevier, 406–417. Available at: http://linkinghub.elsevier.com/retrieve/pii/B9781782421948500458 (accessed 29/01/18).

Olguner S., Filiz i., (2014): "Contact and Bending Stress Analysis of Spur Gear Drives". *16th international Conference on Machine Design and Production*.

Oysu C (2007): "Finite element and boundary element contact stress analysis with remeshing technique". *Applied Mathematical Modelling* 31(12): 2744–2753.

Patrick JR (2009): "*Euclideian and Non-Euclideian Geometry, An analytic approach* (International Student Edition.)". Singapore: Cambridge University Press.

Prueter PE, Parker RG., Cunliffe F., (2011): "A study of gear root strains in a multi-stage planetary wind turbine gear train using a three dimensional finite element/contact mechanics model and experiments". *ASME Power Transmission and Gearing Conference, Washington, DC, p. DETC2011–47451*.

Rameshkumar M, Sivakumar P, Sundaresh S., Gopinath K., (2010): "Load sharing analysis of high-contact-ratio spur gears in military tracked vehicle applications". *gear technology*.

Rameshkumar M, Venkatesan G., Sivakumar P., (2010): "Finite Element Analysis of High Contact Ratio Gear". *AGMA Technical Paper, 10FTM06*.

Regalado I (2007): "The Use of Nonstandard Tooth Proportions and Center Distance to Improve the Performance of Gear Trains". *Gear Technology*.

Radzevich S (2012): "*Theory of Gearing: Kinematics, Geometry, and Synthesis"*. CRC Press, Taylor and Francis Group.

Raptis K., Costopoulos T., Tsolakis A., (2012): "Comparison between niemann's and finite element method for the estimation of maximum allowable stress of meshing spur gear teeth at highest point of single tooth contact". *American Journal of Engineering and Applied Sciences* 5(2): 205–216.

Ristivojević M, Lazović T., Vencl A., (2013): "Studying the load carrying capacity of spur gear tooth flanks". *Mechanism and Machine Theory* 59: 125–137.

Richards RR (2001): "*Principles of Solid Mechanics*. Boca Raton". FL: CRC Press, Taylor and Francis Group.

Radzevich S (2012): "*Theory of Gearing: Kinematics, Geometry, and Synthesis"*. CRC Press, Taylor and Francis Group.

Sirichai S (1997): "Finite Element Analysis of Gears in Mesh". *5th International Conference on Sound and Vibration*. Australia.

Simionescu PA., (2008): "Interactive Involute Gear Analysis and Tooth Profile Generation Using Working Model 2D". American Society of Engineering Education.

Sánchez MB, Pleguezuelos M., Pedrero JI., (2016): "Calculation of tooth bending strength and surface durability of internal spur gear drives". *Mechanism and Machine Theory* 95: 102–113.

Sánchez MB., Pleguezuelos M., Pedrero JI., (2017): "Approximate equations for the meshing stiffness and the load sharing ratio of spur gears including hertzian effects". *Mechanism and Machine Theory* 109: 231–249.

Savage M, Coy JJ., Townsend DP., (1986): "The Optimal Design of Standard Gearsets". *NASA Grant NAG3-55* 25.

Shigley JE., Mischke CR., (2003): "*Mechanical Engineering Design".* (International ed. Sixth Metric Edition.). New York: McGraw-Hill.

Shin J-H., Kwon S-M., (2006): "On the lobe profile design in a cycloid reducer using instant velocity center". *Mechanism and Machine Theory* 41(5): 596–616.

Spitas C., Amani A., Rajabalinejad M., (2014): "Parametric investigation of the combined effect of whole depth and cutter tip radius on the bending strength of 20° involute gear teeth". *Springer Vienna*.

Spitas V., Spitas C., (2007): "Optimizing involute gear design for maximum bending strength and equivalent pitting resistance". *Proceedings of the Institution of Mechanical Engineers, Part C: Journal of Mechanical Engineering Science* 221(4): 479–488.

Sumitomo Drive Technologies (2017): "Cyclo 6000 Gearmotors Catalogue". Sumitomo Machinery Corporation of America.

Tomori Z., Bognár GVD., (2016): "Defining the Top Land Thickness of Involute Gears". *Multiscience*. paper presented at the XXX microCAD International MultidisciplinarySientific Conference. Hungary.

Thurman D., (1999): "Calculating Start Active Profile and True Involute Form". *Gear Technology*.

Thube SV., Bobak TR., (2012): "Dynamic Analysis of a Cycloidal Gearbox Using Finite Element Method". AGMA Technical Paper 12FTF18..

Tsetserukou DO., Basinuk VL., Mardosevich EI., Neviarouskaya AV., (2015): "Contact Force Distribution Among Pins of Trochoid Transmissions".

Yan H-S., Lai T-S., (2002): "Geometry design of an elementary planetary gear train with cylindrical tooth-profiles". *Mechanism and Machine Theory* 37(8): 757–767.

Ye S-Y., Tsai S-J., (2016): "A computerized method for loaded tooth contact analysis of high-contact-ratio spur gears with or without flank modification considering tip corner contact and shaft misalignment". *Mechanism and Machine Theory* 97: 190–214.

Wang J (2003): "Numerical and Experimental Analysis of Spur Gears in Mesh". Curtin University of Technology.

Wang JD., Howard IM., (2006): "Error Analysis on Finite Element Modeling of Involute Spur Gears". *Journal of Mechanical Design* 128: 90.

Zhan J., Fard M., Jazar R., (2015): "A quasi-static FEM for estimating gear load capacity".. *Measurement* 75: 40–49.

Zienkiewicz O., Taylor R., (2000): "*The finite element method"*. Oxford: Butterworth-Heinemann.Gear Technology.